Optimierung von Fotokatalysatoren und Fotoreaktoren für die Synthese solarer Kraftstoffe

Optimizing photocatalysts and photoreactors for solar fuel synthesis

Zur Erlangung des akademischen Grades eines

DOKTORS DER INGENIEURWISSENSCHAFTEN

von der KIT-Fakultät für Chemieingenieurwesen und Verfahrenstechnik des
Karlsruher Instituts für Technologie (KIT)
genehmigte

DISSERTATION

von

M. Sc. Paul Philipp Kant

Mein herzlicher Dank gilt all denjenigen, die mich auf meinem Weg begleitet haben, begleiten und begleiten werden. Er gilt ebenso all denjenigen, die ich habe begleiten dürfen, begleiten darf und werde begleiten dürfen, kurzum all denjenigen, die Geschichte mit mir teilen.

Kurzzusammenfassung

Heute bekannte Technologien zur Synthese solarer Energieträger weisen eine zu niedrige Energieeffizienz und zu hohe Kosten auf, um ökologisch und ökonomisch sinnvoll eingesetzt werden zu können. Die vorliegende Arbeit analysiert deshalb den Auslegungsprozess eines hocheffizienten fotokatalytischen Prozesses und stellt letztlich einen Versuch dar, Wege hin zu einem hocheffizienten und gleichzeitig kostengünstigen Prozess zur Herstellung von solaren Energieträgern aufzuzeigen.

Die dargestellte Analyse stellt zunächst die herausragende Wichtigkeit der optischen und reaktionstechnischen Eigenschaften der Lichtquelle, des Fotokatalysators und des Fotoreaktors im Auslegungsprozess eines hocheffizienten fotokatalytischen Prozesses dar. In dem Fall, in dem die Sonne als Lichtquelle dient, wie auch bei Prozessen zur Synthese solarer Kraftstoffe, konzentriert sich der Auslegungsprozess selbstverständlich auf das Fotokatalysatorsystem und den Fotoreaktor.

Das erste Ergebnis der vorliegenden Arbeit ist konsequenterweise ein Satz von Methoden zur optischen und reaktionstechnischen Charakterisierung von Fotokatalysatoren und Fotoreaktoren.

Von besonderer Bedeutung ist dabei das vorgestellte Konzept zur Bestimmung von Quantenausbeuten in Fotoreaktionen. Der vorgeschlagene Ansatz ermöglicht dabei eine Variation aller wichtigen Betriebsbedingungen, namentlich die Variation der Temperatur, der Konzentration der Reaktanten, der Wellenlänge und vor allem der lokalen volumetrischen Photonenabsorptionsrate. Die Quantenausbeute ist dabei von herausragender Bedeutung für den Auslegungsprozess eines hocheffizienten fotokatalytischen Prozesses. Sie setzt die Anzahl der Produktionsevents in Relation zur Anzahl der vom Fotokatalysatorsystem absorbierten Photonen und stellt damit die Effizienzmetrik auf der Fotokatalysatorebene dar. Die Quantenausbeute und ihre Abhängigkeit von der Wellenlänge definieren damit ein absolutes Limit für die erreichbare fotokatalytische Effizienz in einem sonnenlichtbasierten fotokatalytischen Prozess. Die Möglichkeit die Quantenausbeute als Funktion der Betriebsbedingungen zu bestimmen, unterstützt damit die Auswahl geeigneter Fotokatalysatoren

und Betriebsbedingungen in einem Produktionsprozess. Die Abhängigkeit der Quantenausbeute von der lokalen volumetrischen Photonenabsorptionsrate ist dabei von besonderer Bedeutung. Beim in der vorliegenden Arbeit entwickelten und eingesetzten Modellfotokatalysator nimmt die Quantenausbeute mit steigender lokaler Photonenabsorptionsrate systematisch ab. Eine solche Charakteristik zieht direkt die Notwendigkeit einer sorgfältigen optischen Auslegung von Produktionsreaktoren nach sich. Die Auslegung muss darauf abzielen, zur Erreichung einer maximalen fotokatalytischen Effizienz des Gesamtprozesses, Hotspots in der lokalen Photonenabsorptionsrate im Katalysatorbett zu vermeiden.

Die Vermeidung von Hotspots in der lokalen Photonenabsorptionsrate zu vermeiden, ist jedoch nur ein Teilaspekt im Auslegungsprozess eines hocheffizienten Produktionsfotoreaktors. Zusätzlich zu dieser ersten Anforderung, muss ein hocheffizienter Produktionsfotoreaktor eine hohe Transporteffizienz für Photonen von der Fotoreaktorapertur hin zum Fotokatalysator aufweisen. Beides gleichzeitig sicherzustellen, das Ausbleiben von Hotspots in der lokalen Photonenabsorptionsrate und eine hohe Effizienz des Strahlungstransports von der Fotoreaktorapertur ins Reaktionsvolumen, ist eine substanzielle Herausforderung. Dies gilt besonders für den Fall des Einsatzes von partikelbasierten Fotokatalysatoren, die Licht typischerweise stark streuen. Die Herausforderung zu meistern, setzt die Fähigkeit voraus den Strahlungstransport in einem Fotoreaktor genau kontrollieren zu können. Möglich ist das durch eine geschickte Materialauswahl, das Einstellen der optischer Transporteigenschaften derselben und das Design geeigneter Fotoreaktorgeometrien. Die vorliegende Arbeit führt konsequenterweise sowohl ein Satz von Methoden zur Herstellung optischer Komponenten mit präzise eingestellten optischen Transporteigenschaften für den Bau von Fotoreaktorprototypen als auch Methoden zur Herstellung von optisch verdünnten Fotokatalysatoren auf Basis von transluzenten Pulvern aus Silica-basiertem Aerogel ein. Eine optische Verdünnung des Fotokatalysators ist dabei für fast alle Fotokatalysatoren essenziell, da das intensive Absorptions- und Streuverhalten des Fotokatalysators im unverdünnten Zustand in nahezu allen Aufbauten zu extremen Hotspots in der lokalen Photonenabsorptionsrate nahe der beleuchteten Oberfläche führt. Die eingeführte Strategie zur optischen Verdünnung ist dabei geradlinig und leicht auf viele Fotokatalysatorsysteme übertragbar. Die eingeführten Strategien zur Fertigung von Fotoreaktorkomponenten basieren auf additiver Fertigung bzw. 3D Druck, was einen flexiblen Designprozess mit einem hohen Freiheitsgrad in der Geometrie erlaubt. Eine detaillierte Analyse der optischen Transporteigenschaften der gedruckten Komponenten

zeigt jedoch, dass additive Fertigung nur eingeschränkt zur Herstellung optischer Bauteile geeignet ist. Dies ergibt sich aus der typischerweise hohen Oberflächenrauigkeit gedruckter Bauteile und der daraus resultierenden Notwendigkeit einer zeitaufwändigen Nachbearbeitung nach dem Druckprozess. Zum Abschluss wird im Rahmen der vorliegenden Arbeit über die materialbezogenen Aspekte hinaus ein neuartiges Fotoreaktorkonzept eingeführt, das bei korrekter Auslegung sowohl eine homogene Ausleuchtung der Reaktionszone, als auch eine hohe Effizienz des Strahlungstransports von der Reaktorapertur ins Reaktionsvolumen sicherstellt. Zusammengenommen resultieren diese beiden Eigenschaften in einer maximalen fotokatalytischen Effizienz eines sonnenlichtbasierten Gesamtprozesses. Der beschriebene Auslegungsprozess wird dabei durch eine Simulationsumgebung zur Abbildung von Strahlungstransportprozessen in voller räumlicher Auflösung unterstützt. Die Implementierung basiert auf einer Monte Carlo Ray Tracing Methode und ist objektorientiert in MATLAB® geschrieben. Die Implementierung ist speziell auf die Anforderungen der vorliegenden Arbeit angepasst. Das sich im Auslegungsprozess ergebende Fotoreaktordesign weist eine ausgeprägte Robustheit gegenüber der Richtung einfallendes Lichtes auf, die sich in sonnenlichtbasierten Prozessen inhärent aus dem Tageslauf der Sonne am Himmel ergibt. Bemerkungswerterweise wird diese Eigenschaft ohne eine mechanische Sonnennachführung erreicht. Dies ergibt eine minimale Systemkomplexität und daraus resultierend niedrige Systemkosten, sowohl in der Herstellung als auch im Betrieb, was in eine Vielzahl von möglichen Anwendungsszenarien mündet. Denkbar sind sowohl Anwendungen auf Hausdächern als auch in Sonnenfarmen. Darüber hinaus besteht das vorgeschlagene Fotoreaktordesign lediglich aus zwei Bauteilen, die aus Kunststoff und mit etablierten Massenfertigungsverfahren, Polymerextrusion und Polymerspritzguss, herstellbar sind. Dieser Aspekt ermöglicht eine standardisierte, kostengünstige und vor allem skalierbare Produktion des Fotoreaktordesigns. Zuletzt liefert die die im Rahmen der Arbeit durchgeführte Analyse zu erreichbaren Limits und Verlustmechanismen im vorgeschlagenen Fotoreaktordesign ein detailliertes Verständnis für Optimierungspotentiale und mündet in einer Auslegungsrichtlinie, die eine weitere Entwicklung und Anpassung des vorgeschlagenen Fotoreaktordesigns an andere Fotokatalysatorsysteme deutlich erleichtert.

Zusammenfassend stellt die vorliegende Arbeit eine signifikante Unterstützung für die weitere Entwicklung von hocheffizienten fotokatalytischen Prozessen dar. Die entwickelten Methoden ermöglichen detaillierte reaktionstechnische Untersuchungen von Fotokatalysatorsystemen, was eine funda-

mentale Voraussetzung für die Auswahl geeigneter Fotokatalysatoren und den anschließenden Auslegungsprozess eines hocheffizienten Fotoreaktors darstellt. Die dargestellten Methoden zur optischen Verdünnung von Fotokatalysatoren bereiten die Basis für die Einstellung von optischen Transporteigenschaften im Fotokatalysatorbett und sind einfach auf andere Systeme übertragbar. Die entwickelten Strategien zur Herstellung von Fotoreaktoren über 3D-Druckverfahren erweisen sich als praktikabel für die Herstellung von Prototypen. Ihre Anwendung ist lediglich durch die erreichbaren Oberflächengüten limitiert. Die implementierte Simulationsumgebung zur Abbildung von Strahlungstransport in voller räumlicher Auflösung kann für eine Vielzahl von Herausforderungen im Bereich der Fotoreaktionstechnik eingesetzt werden. Besonders geeignet ist sie zur Unterstützung des Auslegungsprozesses von neuartigen Fotoreaktorkonzepten. Zuletzt sind das entwickelte Fotoreaktorkonzept und die dazugehörige Auslegungsrichtlinie eine Richtschnur für Wege hin zu kostengünstigen fotokatalytischen Prozessen, Prozesse zur Synthese von solaren Energieträgern mit eingenommen.

Obwohl solare Energieträger und damit umso mehr die vorliegende Arbeit nur ein kleiner Teil in der Gesamtherausforderung sind, so stellen solare Energieträger und vielleicht auch die vorliegende Arbeit doch einen Beitrag im Weg hin zu einer nachhaltig lebenden Weltgemeinschaft dar. Einen langen Weg gilt es hier jedoch noch zu meistern, sowohl auf einer technologischen Ebene als auch auf einer gesellschaftlichen.

Short summary

Solar fuel technologies available today typically exhibit a solar to fuel efficiency too low and a capital and operational cost too high to be ecologically and economically reasonable. The work presented herein, therefore, analyses the design processes of high efficiency photocatalytic processes and lastly attempts to work out ways towards the goal of a high efficiency and low-cost photocatalytic process delivering a solar fuel.

The analysis first addresses the outstanding importance of the optical and reaction engineering properties of (1) the light source, (2) the photocatalyst, and (3) the photoreactor in the design process of a high efficiency photocatalytic process. If the sun represents the light source, as is the case in solar fuel processes, the design process naturally focuses on the photocatalyst and the photoreactor.

Consequently, the first result of the work presented herein is a method toolbox with experimental and simulation-based tools for the determination of optical and reaction engineering properties of photocatalysts and photoreactors.

Of especial relevance is the presented concept for the reliable, and especially precise determination of the quantum yield in photocatalytic reactions as a function of the operating conditions, namely the temperature, the reactants' concentration, the wavelength, and the local volumetric rate of photon absorption. The relevance of the introduced approach emanates from the pivotal role of the quantum yield in high efficiency photoreactor design. The quantum yield represents the efficiency metric on a photocatalyst level by relating the number of production events to the number of photons absorbed by the photocatalyst. The quantum yield and its dependency on the wavelength, therewith, set the ultimate limit for the achievable photocatalytic efficiency in a photocatalytic process driven by sunlight. The ability of the introduced approach to map the quantum yield as function of the operating conditions, consequently, provides the basis for the selection of suitable photocatalysts, and operating conditions in a production process. The dependency of the quantum yield on the local volumetric rate of photon absorption, which translates to the process intensity, thereby, is of outstanding relevance for the

design of high efficiency photoreactors. In the photocatalytic model system developed and characterized in detail in the presented work, the quantum yield systematically decreases with an increasing local volumetric rate of photon absorption, or increasing process intensity, respectively. Such a trend in the quantum yield directly entails the need for a careful optical design of a production photoreactor that avoids photon absorption hot spots in the photocatalyst bed.

Avoiding photon absorption hot spots in the photocatalyst bed is only one requirement in high efficiency photoreactor design. In addition to this first requirement, most importantly, high efficiency photo reactors must ensure a high efficiency of radiation transport from the reactor aperture into the reaction volume. Achieving both at the same time, well defined operating conditions, and a high efficiency of radiation transport, may be a significant challenge. This especially holds for systems in which particulate photo-catalysts are employed that tend to scatter light strongly. Addressing this challenge requires the skill to precisely control radiation transport in a pho-toreactor. This is possible via the selection of suitable materials, the tuning of their optical transport properties, and the design of suitable photoreactor geometries.

The work presented herein, therefore, introduces strategies for the fabrication of optical components for photoreactor prototypes with tuned optical trans-port properties, and strategies for an optical dilution of photocatalysts via supporting of photocatalysts on translucent silica aerogel powders. The latter is of high relevance in most photocatalyst systems, since they strongly absorb (and scatter) light and therefore tend to develop absorption hot spots close to the illuminated surface if employed without dilution in a photoreactor. The introduced optical dilution strategy is straight forward and applicable to many particulate photocatalysts. The introduced photoreactor component fabrication strategies are based on additive manufacturing, or 3D-printing, respectively, which allows a flexible design process with a high degree of shape freedom. A detailed analysis of optical transport properties of printed optical components, however, reveals that additive manufacturing has a lim-ited suitability for the fabrication of optical components. The latter emanates from the high surface roughness of printed components and the resulting need for time-consuming post-print treatments.

To complete the analysis and method toolbox, beyond the material related aspects, with the present work, a reflective multi-pass photoreactor design concept is presented that, if properly adapted to the employed photocatalyst, can guarantee both a homogeneous illumination of the reaction volume, and

a high efficiency of radiation transport from the reactor aperture into the reaction volume. Together, these two properties result in a maximum photocatalytic efficiency in a solar driven process. The described photoreactor design process, thereby, is supported by a 3D numerical model mapping radiation transport in the photoreactor. The model is Monte Carlo ray tracing-based and implemented in MATLAB®. The implementation is tuned to especially address the tasks of the present work. The resulting photoreactor design exhibits a pronounced tolerance towards different directions of incident light resulting from a moving sun in the sky. Noteworthy, this is achieved without relying on sun tracking. The latter entails a minimal system complexity and system cost, both in fabrication and operation, which allows to imagine a multitude of applications, for instance, on rooftops or in solar farms. The proposed photoreactor design further comprises two different parts only that are manufacturable in polymers via industry established polymer extrusion and injection moulding. This design aspect allows a standardized and as cheap as possible large-scale production of the proposed photoreactor design. Lastly, a detailed simulation-based analysis of the performance of the proposed photoreactor design permits a detailed understanding of achievable limits, prevalent loss mechanisms, and finally the derivation of a simple graphical design guideline. The later facilitates the adaptation and further development of the concept of reflective multi-pass photoreactors in various applications of photocatalysis.

Summarizing, the results of the work presented herein provide substantial support for the further development of low-cost, high efficiency photocatalytic processes. The methods introduced pave the way for detailed reaction engineering analysis of photocatalysts, which is a prerequisite for the selection of suitable photocatalysts and a subsequent photoreactor design process. The strategies introduced for the optical dilution of photocatalysts are simple and straight forward applicable to many photocatalysts. Additive manufacturing is shown to be a suitable tool for the fabrication of photoreactor protypes with some restrictions regarding achievable surface qualities. The implemented radiation transport simulation environment can be used for various task in the field of photochemical engineering, especially in the development and validation of different photoreactor concepts. The proposed high-efficiency and low-cost photoreactor design concept and especially the developed design guideline, lastly, could become one corner stone for a low-cost photocatalytic process to produce solar fuels.

Even though only a small piece in the overall picture, high efficiency photocatalytic processes enabled by sophisticated photochemical engineering

might be one contribution in the endeavour leading towards a sustainable living human population. However, a long way remains to be mastered, both on a technological as well as on a societal level.

Bachelor and Master theses

In the framework of the presented work eight Bachelor and Master theses have been initiated and supervised by the author. Six of those theses addressed aspects of the presented work and are the basis of presented data. Especially, experimental results are based on these theses. The six theses giving the experimental basis for the presented work are:

Momme Rickmers, Interdependencies of radiation transport properties and performance metrics of silica aerogel-supported photocatalyst systems, Master thesis, 2021.

Shengzhi Liang, Experimental & simulative study of light transport in photoreactors, Master thesis, 2021.

Marius Riedinger, Photocatalytic CO_2 activation with aerogel-supported indiumoxide-based catalysts: catalyst preparation and catalytic characterization, Bachelor thesis, 2021.

Luca Heim, Development of an aerogel-supported Pd/TiO_2 catalyst system for photocatalytic water splitting, Bachelor thesis, 2021.

Validierung eines Strahlungstransportmodells für einen Fotoreaktor zur Bestimmung von Quantenausbeuten, Domenik Fischer, 2022.

Bestimmung der Quantenausbeute eines Modellfotokatalysators als Basis für die Auslegung von Fotoreaktoren, Nils Thorben Gensior, 2022.

Contents

1.   Introduction

The global challenge faced

The effects of progressing climate change are no longer abstract concepts [1]. Sea levels observably rise [2], age-old natural habitats disappear [3], once fertile land dries out [4], and disastrous weather extremes are observed more frequently [5]. The impacts of these changes on human life on earth are manifold – health issues [6], migration [7], political tensions [8, 9], just to name a few. Climate change with its multi-faceted nature, thus, represents a substantial threat to human life on earth, and its mitigation becomes an egoistic act of self-preservation for mankind.

The mechanisms governing the processes of climate change are not subject to speculations. There is no serious doubt that greenhouse gases accumulating in the earth's atmosphere drive climate change [1]. There also is no serious doubt that greenhouse gas accumulation is the consequence of human acting, more precisely, human-induced land use change, and the use of fossil energy carriers [1, 10]. It lies in humanities' hands – our hands. The direction that needs to be taken is clear: anthropogenic green house gas emissions must be reduced as fast as possible, but especially before tipping elements in earth's climate system actually do tip [11]. This challenge is a global challenge demanding human cooperation in a global framework. The Paris Agreement of 2015 is a first step in this endeavour [12]. Noteworthy, time is not on mankind's side. According to the Intergovernmental Panel on Climate Change (IPCC), global net green house gas emissions must be cut to zero until latest 2050, if the goals defined in the Paris Agreement shall not fail [13].

Reducing anthropogenic green house gas emissions to net zero in such a short period of time is a political, societal, and technological challenge. No political framework alone will guarantee success. No behavioural change alone will make technological changes obsolete. But especially no technology alone will permit to continue business as usual. The change desperately needed to mitigate the consequences that climate change imposes on human life

on earth pervades societies in nearly all their aspects. Of course, a special focus lies on economy, mainly on the chemistry, the mobility, and the energy sector together being responsible for more than 70 % of accumulated historic anthropogenic green house gas emissions [14].

The technological challenges ahead

Today, roughly 80 % of the annually emitted anthropogenic green house gases result from the use of fossil energy carriers – natural gas, oil, and coal [10]. Renewable energy sources that are greenhouse gas neutral and fossil independent – namely wind, solar, and hydro – are therefore envisioned as the future energy backbone of the world economy. Substantial efforts are undertaken to intensify their exploitation via installation of wind turbines, photovoltaic fields, and hydro power plants delivering renewable electrical energy. Nevertheless, until 2020, renewable electrical energy remained a scarce resource with a share of only 12.6 % in the global primary energy mix [15]. Fortunately, the trend indicates a steady increase of this currently sobering number [16, 15]. However, with an increasing share of renewable electrical energy in the energy mix, transportation and storage of electrical energy becomes a major challenge. Technological development in the field of short and long term electrical energy storage is urgently needed. The most promising options currently in the portfolio are electrochemical energy storage solutions – batteries – and chemical energy storage solutions – namely power-to-x processes that deliver chemical fuels in electrically driven, and carbon dioxide, nitrogen, and water-based fuel synthesis processes. Power-to-x processes are currently the most promising option for large-scale and long-term seasonal energy storage, as well as global energy transportation. Furthermore, they are the only reasonable option for long distance, heavy duty, and air transportation applications [17]. Additionally, carbon dioxide-based power-to-x processes are not only able to deliver an alternative carbon feedstock for non-transportation applications such as in the chemical industry [17] but also an option to serve as a temporary carbon dioxide sink when capturing carbon dioxide from the atmosphere or at least from non-avoidable point sources. Building on existing technologies, some power-to-x processes are close to an economic implementation [18, 19].

Even though being a promising energy storage and transportation technology, power-to-x processes are object to vivid discussions. Core of these debates

is the achievable efficiency in multiple regards – first, with regard to the energy efficiency of the often multi-step processes, and second with regard to the efficiency expressed as carbon dioxide emission reduction potential per amount of electrical energy or financial effort invested. If, for instance, the achievable carbon dioxide emission reduction potential per amount of renewable electrical energy invested was the metric of choice to decide how renewable electrical energy was used, not power-to-x processes but commercial electrical heat pumps replacing fossil fired boilers in residential heating would be the option of choice for timely prioritized implementation [20]. A similar conclusion can be drawn if power-to-x products and direct electrification approaches in residential heating and light transportation scenarios are compared with regard to the financial cost per avoided greenhouse gas emission [17]. These discussions line out that besides the need for electrical energy storage solutions, use conflicts for renewable electrical energy are a substantial challenge in the transition phase from a fossil-based economy towards a sustainable economy independent of fossil energy resources. The discussions thereby highlight on the one hand that the share of renewable electrical energy urgently needs to be increased and on the other hand that more alternative technologies for the replacement of fossil energy carriers are desirable. In best case, these additional options would not depend on the availability of vast amounts of renewable electrical energy. They thereby could appease use conflicts and facilitate the allocation of the scarce resource 'renewable electrical energy' amongst the various envisaged applications. Also, these fossil-fuel alternatives could additionally serve as backup fuels for electricity grid stabilization in case photovoltaic fields, hydro power plants, and wind parks were not able to provide a stable enough supply. One such option are solar fuels.

Basics of solar fuel processes

Instead of renewable electrical energy, processes delivering solar fuels use sunlight to drive photochemical conversions of carbon dioxide and/or water to yield energy carriers [21]. Solar fuel processes are, thereby, quite similar to natural photosynthesis that uses sunlight to convert carbon dioxide and water to carbohydrates. In comparison to power-to-x processes, solar fuel processes can only partially be build from existing technologies and are far

less developed. Even the latest benchmark systems only reach a solar to fuel energy efficiency of roughly 1 % (definition see 1.1) [22, 23].

$$\eta_{STF} = \frac{heating\ value\ of\ produced\ fuel}{energy\ incorporated\ via\ incident\ light} \tag{1.1}$$

To be economically interesting and thereby become a real option in the portfolio of measures in climate change mitigation, the solar-to-fuel energy efficiency of a solar fuel process must lie in the range of 5-10 % [24]. At the same time, having in mind that sunlight collectors for significant production would cover huge areas, the photoreactors employed must be cheap with regard to the cost per covered area. Naturally, this addresses both, the capital and operational expenses. As an illustrative example, to underline the need for low area-specific costs, assuming a 5 % solar-to-fuel energy efficiency, an area only slightly smaller than the German federal state of Saarland ($\approx$2300 km^2) would be required to produce the kerosene consumed annually by German airports[1].

Inefficient photon usage is a hurdle for all photocatalytic processes, not only solar fuel processes. In a broader context than solar fuels, the efficiency metric employed to assess a photocatalytic process with regard to its efficiency is the photocatalytic efficiency rather than the solar to fuel energy efficiency introduced with equation 1.1. The photocatalytic efficiency relates the number of production events, in case of photoredox reactions the number of transferred electrons, to the number of incident photons in the relevant optical band, definition in accordance to the recommendation by the International Union of Pure and Applied Chemistry (IUPAC) [27], equation (1.2). A photocatalytic efficiency equal to unity, accordingly, would imply that every incident photon was used to contribute to the desired production process.

$$\eta_p = \frac{\#of\ production\ events\ in\ a\ system}{\#of\ incident\ photons\ in\ specified\ optical\ band} \tag{1.2}$$

Improving the photocatalytic efficiency of a photocatalytic process, including solar fuel processes, is governed by the three core elements of any photocatalytic process:

1. The employed photocatalyst absorbing photons and driving the chemical reaction

---

[1] Assuming an average solar global irradiance of 1050 kW h m^{-2} a^{-1} [25], a heating value of kerosene equal to 40 MJ kg^{-1}, and an annual kerosene demand at German airports of 10 Mio. metric tons [26].

2. The employed photoreactor that guides incident photons towards the photocatalyst

3. The light source, that supplies the process with photons

If the sun represents the light source, as is the case for solar fuel processes, the engineering of a high efficiency photocatalytic process naturally focuses on the photocatalyst and the photoreactor.

Goal of this thesis

No doubt, the availability of economically and ecologically reasonable solar fuel processes would be an appealing option in climate change mitigation pathways. Synthesized in the global sun belt, they could be traded around the world as fossil energy carriers are traded today. If available in significant amounts, they could support the electrification of the world's economy by providing a backup for electricity grid stabilization and facilitating the allocation of renewable electrical energy. Unfortunately, in 2022, reported solar fuel processes lack in technology readiness to take a significant role. The achieved photocatalytic efficiencies and process costs of the latest benchmark systems are insufficient to be competitive with alternative approaches.

The goal of this thesis is, therefore, to examine in detail the challenges of high efficiency photocatalytic process design in the field of solar fuels under the constraint to economize the cost of the proposed photoreaction technology. The work, thereby, firstly analyses the current state of the art and lines out the important engineering challenges. Secondly, it focuses on the appropriate choice and characterization of materials, photocatalysts and photoreactor component materials included. The third part of the work comprises a proposed methodology for high efficiency photoreactor design, and describes and demonstrates a novel low-cost photoreactor design concept that could be a core component of a future commercial solar fuel processes.

2. Literature overview

2.1. Photocatalysts

Photocatalysts employed in solar fuels processes drive a relevant chemical reaction and basically comprise an active material which may be impregnated onto a suitable support material or structure.

2.1.1. Target reactions

Relevant reactions in solar fuel processes yield energy carriers in a broad perspective, including hydrogen [28], carbon monoxide [29], synthesis gas [22], methanol [30, 31], methane [32], but also higher alcohols, or hydrocarbons [33].
Direct photocatalytic reactions of carbon dioxide with water, for instance to yield methane or higher hydrocarbons [32], as pointed out in equation (2.1), include a multitude of reaction steps and are extremely challenging from a kinetic point of view.

$$CO_2 + 2\,H_2O \longrightarrow CH_4 + 2\,O_2 \quad \Delta_R H^0 \approx 891 \text{ kJ}\,\text{mol}^{-1} \tag{2.1}$$

Remarkably, carbonaceous target products like methane, alcohols, and higher hydrocarbons can also be obtained in thermal reactions of carbon dioxide and hydrogen or carbon monoxide and water. Since the activation of water or carbon dioxide alone is less challenging than reactions of carbon dioxide with water, many works in the field of solar fuels focus on hydrogen or carbon monoxide as target product [21]. Common photocatalytic reactions are, consequently, water splitting, see for instance [23, 34] and refer to equation (2.2), and carbon dioxide splitting, see for instance [34] and refer to equation (2.3).

$$H_2O \longrightarrow H_2 + \frac{1}{2}\,O_2 \quad \Delta_R H^0 \approx 285 \text{ kJ}\,\text{mol}^{-1} \tag{2.2}$$

$$CO_2 \longrightarrow CO + \frac{1}{2}O_2 \quad \Delta_R H^0 \approx 284 \text{ kJ mol}^{-1} \tag{2.3}$$
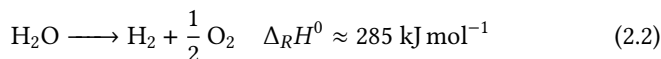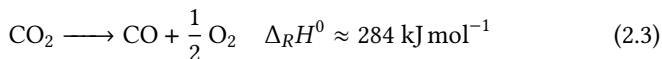
Still, photocatalytic water and carbon dioxide splitting are challenging reactions that need sophisticated catalyst systems and process designs, see for instance the co-catalyst modified water splitting catalyst system in [35], or the high temperature carbon dioxide activation process in [22]. Less challenging photocatalytic model reactions are methane dry reforming [36], refer to equation (2.4), the reverse water gas shift reaction [37], refer to equation (2.5), or methanol reforming [38], refer to equation (2.6).

$$CO_2 + CH_4 \longrightarrow 2\,H_2 + 2\,CO \quad \Delta_R H^0 \approx 247 \text{ kJ mol}^{-1} \tag{2.4}$$

$$CO_2 + H_2 \longrightarrow CO + H_2O \quad \Delta_R H^0 \approx 41 \text{ kJ mol}^{-1} \tag{2.5}$$

$$CH_3OH + H_2O \longrightarrow CO_2 + 3\,H_2 \quad \Delta_R H^0 \approx 49 \text{ kJ mol}^{-1} \tag{2.6}$$
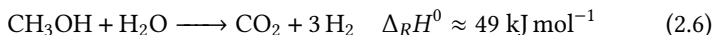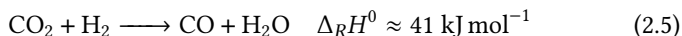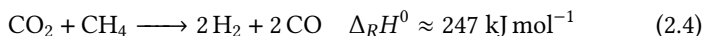
Noteworthy, these photocatalytic model reactions consume valuable reactants, methane, hydrogen, or methanol and are, therefore, less appealing in the bigger picture of solar fuel processes and climate change mitigation.

2.1.2. Active materials

An active material suitable for a solar fuel process drives one of the chemical reactions discussed briefly in section 2.1.1. Further, it uses the available photons efficiently to drive the chemical reaction, or with other words, exhibits a high quantum yield in the relevant optical band. The quantum yield is the efficiency metric of the active material and defined by IUPAC as the number of production events, which equals the number of transferred electrons in photoredox reactions, related to the number of photons absorbed by active material at a specific wavelength, equation (2.7) [27]. The 'relevant' optical band is defined by the emission spectrum of the employed light source. It equals the optical band in which the employed light source emits most of its photons.

$$\Phi = \frac{\#of\ production\ events}{\#of\ absorbed\ photons\ at\ specific\ wavelength} \tag{2.7}$$

Consequently, an active material suitable for a solar fuels application not only drives a relevant reaction yielding an energy carrier but especially exhibits a high quantum yield in the optical band in which the sun's emission spectrum
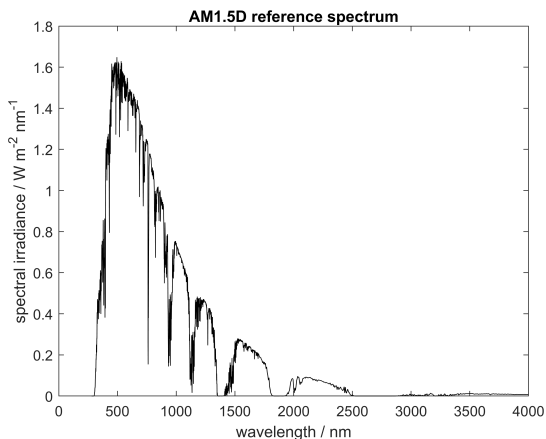
Figure 2.1.: Sunlight reference spectrum for direct illumination and 1.5 air masses (AM1.5D) according to ASTM G173-03 standard [39].

peaks, the ultra violet (UV, $\lambda < 400$ nm) and visible (Vis, $400\ nm < \lambda < 800$ nm) band, see sunlight reference spectrum in figure 2.1.

A quantum yield different from zero indicates that the considered active material is able to use photons productively in one or another way. Generally speaking, there are two main mechanisms how photons can be used to drive chemical reactions, a thermal and an electrochemical mechanism. In thermal pathways photons are used to generate heat that subsequently drives the chemical reaction. In electrochemical pathways, photons are used to separate and/or excite charge carriers that than provide the energy basis for the desired chemical reaction. Active materials can be grouped depending on which of the two mechanisms is assumed to be the major contributor. A rough grouping scheme comprises solar-driven thermal catalysis, photoelectro catalysis, and photothermal catalysis.

2.1.2.1. Solar-driven thermal catalysis

In solar-driven thermal catalysis, photons are used to generate heat that subsequently drives the desired chemical reaction [40]. An example for solar-driven thermal catalysis are high temperature redox cycles for water and/or carbon dioxide splitting [40], see scheme figure 2.2. In such redox cycles metal

oxides that decompose [41] or are partially reduced [34] at high temperatures are used as active materials. Typically the cycle comprises two steps. In the first step, the metal oxide, for instance Ceria (CeO_2) [34], is (partially) reduced at extreme temperature ($\approx$1500 °C), and the side product oxygen is released. Subsequently, the partially reduced metal oxide is used to split the reactants, carbon dioxide and/or water, at slightly lower temperature ($\approx$900 °C). In this second step, the metal oxide is obtained in its initial oxidation state and the products, carbon monoxide, hydrogen, or a mixture of both, are extracted.

The purely thermal mechanism in high temperature redox cycles entails a negligible sensitivity of the catalyst activity towards the wavelength of employed photons. Consequently, the whole solar spectrum from UV over Vis to infrared (IR) is of use in solar fuel processes that employ such thermally driven redox cycles [34]. Besides the obviously necessary material stability towards changing temperature and oxidation state, the challenges on the material side lie mostly on the reduceability, the reoxidizability, and the cycle capacity [42]. The material design/selection process aiming for a high overall process efficiency, thereby, is non-trivial and balancing high cycle capacities that allow a low cycle frequency reducing energy losses in the temperature swing itself, and favourable reaction kinetics in the reduction/oxidation step that keep the necessary temperature low and indirectly reduce heat losses induced by excess stripping gas feeds [42, 40].

2.1.2.2. Photoelectro catalysis

In photoelectro catalysis photons are used to separate charge carriers that subsequently drive the desired chemical reaction. An example for photoelectro catalysis are semiconductor-based active materials [28]. Photon absorption by the semiconductor, thereby, induces excitation of electrons from the valence band (VB) to the conduction band (CB) . Positively charged holes are left behind in the conduction band. Subsequently, if not recombined, electrons and holes migrate to the surface of the active material particle and induce reduction or oxidation reactions, respectively [28, 43]. For an illustration, see scheme figure 2.3.

Whether, or whether not a semiconductor can act as active material for a specific reaction is largely dependent on its electronic band structure [28]. There are two necessary, noteworthy not sufficient, preconditions: Firstly, the available photons must each carry enough energy to excite an electron
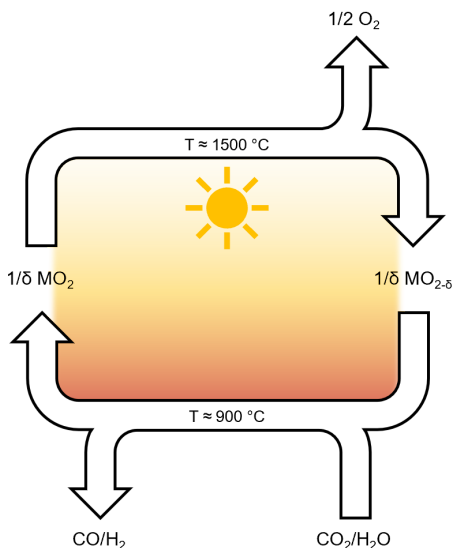
Figure 2.2.: Scheme of a solar-driven high temperature redox cycle comprising a metal oxide MO_2 as active material. The metal oxide is partially reduced releasing oxygen (O_2) at extreme temperature and subsequently employed to split water (H_2O) and/or carbon dioxide (CO_2) to yield hydrogen (H_2) and/or carbon monoxide (CO) at slightly lowered temperature. Presentation adapted from [34].

from the valence band to the conduction band or with other words, the photon energy equal to $h\nu$ must be equal or superior to the band gap energy of the employed semiconductor. Secondly, the band edge potentials, both, the valence, and the conduction band edge potentials, must be positive/negative enough to overcome the redox potential for the desired reaction [28]. For an illustration of these two hurdles, see scheme figure 2.3.

The first precondition, a photon energy bigger than the band gap energy, has decisive consequences for solar fuels applications. The precondition entails that all semiconductor-based active materials can only make use of the fraction of solar irradiation in which each photon carries enough energy to excite an electron from the valence to the conduction band. For many literature-reported, semiconductor-based photocatalysts only photons from the UV band fulfill this criterion, see for instance [44, 45]. This disadvantageous property of many reported photocatalysts limits their attractiveness for solar
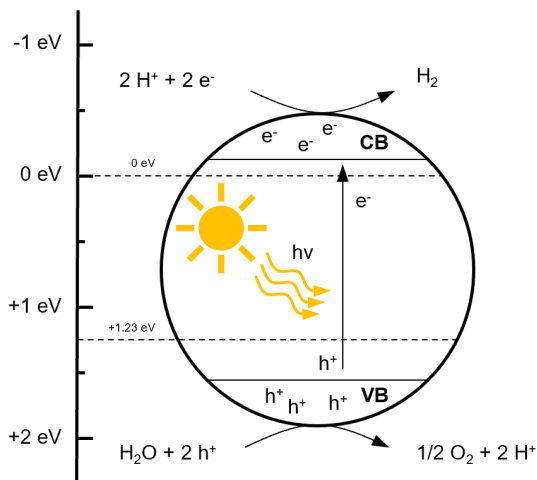
Figure 2.3.: Scheme of a semiconductor-based active material particle (circle) employed for water splitting. Photons are absorbed and excite electrons e^- from the valence band (VB) to the conduction band (CB). Positively charged holes (h^+) are left behind in the valence band. Electrons and holes subsequently migrate to the surface of the semiconductor particle and drive reduction and oxidation reactions, respectively. Importantly, the band edge potentials (thin solid lines) must be more negative/positive than the redox potentials of the desired reactions (thin dashed lines). For water splitting the band edge potential of the conduction band must be slightly more negative than the redox potential for the reduction of protons to hydrogen (0 eV) and the conduction band edge must be more positive than the redox potential for water oxidation (+1.23 eV). Figure based on [28].

fuel applications drastically, since only roughly 5 % of the solar irradiation on the earth's surface are in the UV band, see sunlight reference spectrum in figure 2.1.

The second named precondition, the band edge potentials, has decisive influence on the applicability of a semiconductor for a specific reaction. In the exemplary case of water splitting, at the first view, there are, for instance, many semiconductors whose band edge positions lie far enough apart that theoretically protons could be reduced and water molecules could be oxidized on one and the same semiconductor particle. The band gap in these potential active materials is wider than the thermodynamically necessary 1.23 eV for water splitting [28]. At the same time many of these potential active materials do not have both, a conduction band edge potential that is negative enough to reduce protons, and a valence band edge potential that is positive enough

to oxidize water molecules. These materials are, therefore, inactive for the water splitting reaction even though their band gap is wide enough [28].

For the sake of the outstanding relevance of the electronic band structure of a semiconductor, many works on photoelectro catalysis explore methods to influence the band gap and the band edge potentials, for instance through semiconductor doping with cations [46] and anions [47], or sensitization through coupling of the semiconductor with small band gap semiconductors [48] or dyes [49].

A very sophisticated way to overcome challenges that arise from unfavourable band edge potentials are Z-scheme active materials systems, see for instance [50, 51, 52]. In these active materials systems two semiconductors are employed. One of the two semiconductors drives the reduction reaction. It has a suitable conduction band edge potential. The second semiconductor drives the oxidation reaction. It has a suitable valence band edge potential. To ensure charge balance, the two semiconductors are coupled in order that electrons from the oxidation semiconductor can be transferred to the reduction semiconductor. The electrical coupling can either be realized via an electron conduction bridge, for instance a metal particle [50], or a redox shuttle mediating between the two semiconductors, for instance iodate/iodine in aqueous solution [51].

Noteworthy, a suitable band structure is not a sufficient condition for a semiconductor to be a promising active material. In order that the semiconductor drives a chemical reaction in consequence of photon absorption, electrons and holes must not recombine but rather must be transported to the active material particle's surface and have a lifetime on the surface long enough for charge carriers to be transferred to the reactants. The more efficient these two transport processes are, and the less significant recombination processes are in consequence, the higher is a potential quantum yield [35]. Typically, recombination and/or transportation of charge carriers to the surface of a semiconductor particle occurs in the time scale of pico- to nanoseconds, and charge transfer from the semiconductor particle to the reactants in the time scale of micro- to milliseconds [43]. Strategies to increase the quantum yield in a photoreaction by influencing the charge carrier dynamics, therefore, can be grouped in strategies that decrease the probability of charge carrier recombination and enhance charge carrier transport in the semiconductor bulk material, and strategies that extend the lifetime of charge carriers on the active material particle's surface.

Typically, a high crystallinity and purity of the semiconductor entails an advantageous mobility of electrons and holes and reduces the density of

recombination centers, such as lattice defects, in the bulk material [53, 54, 28]. By designing according materials, recombination is suppressed, and transportation to the semiconductor particle surface is facilitated.

Adding sacrificial agents that act as electron or hole scavengers [28, 55], or engineering of surface defects that act as electron or hole traps [43], extends the lifetime of charge carriers on the particle's surface.

Charge carrier transfer from the semiconductor particle surface to the reactants is the subsequent hurdle that influences achievable reaction rates and quantum yields. The design and appropriate deposition of co-catalysts reducing the over-potential necessary for charge transfer from the semiconductor surface to the reactants is, therefore, another strategy commonly employed to tailor active materials with high quantum yields [28]. An example for this strategy can commonly be found in titania-based photocatalysts employed for water splitting. In these catalyst systems, due to the only slightly negative conduction band edge potential of titania (relative to a standard hydrogen electrode), the reduction reaction of protons to hydrogen often is limiting [28]. Nobel metal co-catalysts reduce the over-potential for hydrogen evolution and, therefore, drastically enhance the photocatalytic hydrogen evolution rate on titania, see for instance [56, 57].

Even though extremely rare in literature, if all three discussed aspects, the electronic band structure of the employed photocatalyst, the charge carrier dynamics, and employed co-catalysts are engineered to perfection, even for challenging photocatalytic reactions like water splitting, quantum yields close to unity are feasible. Examples of such outstanding work are titania nanotube-based photocatalysts with a photodeposited carbon/platinum co-catalyst [45] or aluminum-doped strontium titanate-based photocatalysts ($SrTiO_3 : Al$) with photodeposited rhodium chrome oxide (Rh/Cr_2O_3) and cobalt oxide hydroxide ($CoOOH$) as co-catalysts [35].

Noteworthy, in addition to the material dominated mechanisms discussed in detail above, the operating conditions may also influence the achievable reaction rates and, especially, quantum yields.

For instance, charge carrier recombination in semiconductors is enhanced at elevated temperatures [53, 54] potentially inducing a decrease of the quantum yield with increasing temperature. The latter is one of the reasons for which most semiconductor-based photocatalysts are operated close to/at room temperature, see for instance [35, 45, 50]. In contrast, product adsorption/desorption and/or consecutive reactions of reaction intermediates towards the reaction products are enhanced as well with increasing temperature and may induce an increase of the quantum yield with increasing

temperature.

As a consequence of their influence on the charge carrier dynamics with their role as electron and hole scavengers, reactant concentrations on the surface of the catalyst, and, thereby, also the reactant concentration in the bulk, influence the reaction kinetics and quantum yields as well.

Last but not least, charge carrier recombination in semiconductors not only depends on the material properties, crystallinity, density of recombination centers like impurities, etc., and the temperature as commented above, but also on the density of photon induced charge carriers, which translates to the intensity of photon absorption, or the light intensity, respectively [53, 54]. Even though not clearly reported in current literature, the dependency on the density of photon induced charge carriers can entail a dependency of the quantum yield on the local volumetric rate of photon absorption, definition in accordance to IUPAC recommendations see equation (2.8) [27].

$$L^a_{p,\lambda} = \frac{\#\ of\ photons\ absorbed\ in\ control\ volume\ in\ given\ time}{control\ volume\ size\ \cdot\ time\ interval\ length} \qquad (2.8)$$

Consequently, quantum yields in semiconductor-based photocatalysis do not only exhibit the obvious dependency on wavelength [35, 45, 58], but also may exhibit a dependency on temperature [59], reactant concentration [55, 57], and local volumetric rate of photon absorption. For an experimental indication for the latter, see for instance [57].

2.1.2.3. Photothermal catalysis

In photothermal catalysis photons are used for the generation of both, charge carriers, and heat that together drive the desired chemical reaction [60]. Photothermal catalysis, therewith, represents the superposition of solar-driven thermal catalysis and photoelectro catalysis. It attempts to draw a benefit from the best of the two worlds, the ability to make use of the whole solar spectrum in solar-driven thermal catalysis, and the highly specific and potentially efficient reaction pathways achievable via photoelectro catalysis. Many catalyst systems tagged as photothermal catalysts are carbon dioxide hydrogenation catalysts, see for instance [61]. A common model reaction is the reverse water gas shift reaction, equation (2.2). Prominent examples of active materials are black indium oxide [37], silicon nano-wires decorated with non-stoichiometric partially hydroxylated indium oxide [62], or niobium oxide nano-rods decorated with palladium nano-crystals [63]. Importantly,

the heating mechanism in these examples is reported to be a localized heating mechanism focusing on the heating of the active sites rather than the bulk material, presumably more efficient and, thereby, less energy intensive than bulk heating. The delineation and experimental proof of a local heating effect, however, is difficult. For a discussion of this issue refer for instance to [63]. The bulk reaction temperatures in reported photothermal catalysis are consequently mild in comparison to reaction temperatures in traditional thermal catalysis for the same reactions. Typical reactor temperatures in photothermal catalysis of the reverse water gas shift reaction are, for instance, in the range from 100 °C to 300 °C [64, 63, 65] with local temperatures estimated to be as high as 570 °C [63] in contrast to reactor temperatures in the range from 500 °C [66] to 900°C [67] in traditional thermal catalysis of the reverse water gas shift reaction.

Material development strategies in photothermal catalysis focus on the search of material systems that show both, semiconducting properties, as well as broad band photon absorption. These demands contradict each other at first sight because of the intrinsic absorption characteristics of semiconductors that only absorb photons that carry enough energy to excite an electron from the valence to the conduction band. Photothermal catalysts are, therefore, exclusively precisely engineered hetero structures combining different materials each contributing to the functionality of the system [63, 37, 62]. Reported black indium oxide, for instance, is a core shell like nano-particle combining a crystalline indium oxide semiconductor in the core with a defect loaded indium oxide shell exhibiting broad band absorption due to induced mid band gap states [37]. Non-stoichiometric, partially hydroxylated indium oxide decorated silicon nano-rods assign the functionalities even clearer. Ultra black silicon nano-rods show broad band absorption, whereas non-stoichiometric, partially hydroxylated indium oxide shows a distinct band gap and semiconducting properties [68].

2.1.3. Supports

In most applications of heterogeneous catalysis, the active material is supported on a support material. The support material may be but is not necessarily inactive towards the chemical reactions occurring. In many cases the interactions between active material and support material are complex and open ways towards catalyst optimization. The primary motivation for supporting active materials on support materials emanate from the objectives

to use the (precious) active material effectively, to tune the selectivity in a reaction, and to reduce deactivation rates to an acceptable extend [69].

Since the desired chemical reactions occur primarily on the surface of the active material, effective use of the active material can be ensured by a fine dispersion of the active material on the (internal) surface of a support material. This results in a large active material surface area with a high density of active centers. Many catalysts exploiting this strategy are (noble-)metal catalysts like described for instance in [70, 71, 72]. Sintering of the finely dispersed active material particles either during the catalyst preparation (in calcination steps), or during catalyst operation, thereby, often deteriorates the activity of the catalyst, see for instance [72]. Choosing suitable support strategies can effectively hinder sintering by a nano-confinement of the active material particles. One example of a successful implementation of such nano-confinement described by Wu at al are noble metal catalysts encapsulated in LTA zeolite voids being stable towards oxidative sintering at temperatures as high as 600 ℃ [73].

An effective use of the active material is further only guaranteed if proper operating conditions are ensured throughout the whole volume of a porous catalyst particle or pellet [69]. This mainly addresses the reactant concentrations and the temperature. In this view, supporting the active material is a dilution strategy. High local reaction rates, which could entail mass transport hindrances in the catalyst particle and therefrom resulting low catalyst usages, are avoided through the dilution of the active material. The same argumentation holds for heat transport hindrances that could entail undesired hot/cold spots in the catalyst particle in exothermic/endothermic reactions.

Supporting active materials on support materials can further have a significant effect on the activity of active centers themselves. Works from Wang et al examining the activity of nickel-based carbon dioxide methanation catalysts reveal, for instance, that nickel catalysts supported in a lanthanum oxide matrix show significantly higher activities than pure nickel catalysts. According to density functional theory calculations, the reason for this might emanate from an increased adsorption strength of carbon dioxide molecules on the active sides on nickel particles in in the vicinity of lanthanum oxide [74].

The pore structure of support materials can have an effect on the selectivity in reactions with a broad product spectrum. One example for such spatial effects induced by the support material's pore structure, reported by Subramanian at al, are cobalt-based Fischer-Tropsch catalysts impregnated on a zeolite-based support [75]. The pore structure and size, thereby, affects the

observed selectivity especially with regard to higher hydrocarbons. Noteworthy, the zeolites employed in the work of Subramanian et al also act as acidic hydro-cracking catalyst, which highlights that support materials can also act as active materials themselves. The differentiation between active material and support material gets further blurred in such cases.

Summarizing, supporting active materials onto support materials can trigger complex mechanics, and can have effects on the activity of active sides, the rate of deactivation processes, the selectivity of reactions and catalyst particle-internal mass and heat transport processes. Obviously, in applications of photocatalysis, in addition to all the material-related and mass and heat transport-related aspects, impregnating the active material on a support material is a way to control radiation transport. With other words, supporting a photocatalytically active material onto a suitable support may be a way to guarantee that there are no limitations on the radiation transport side and the whole employed active material is accessible by photons.

As is the case in traditional thermal catalysis, supports for photocatalytic applications should (1) be stable, meaning they should be able to withstand the operating conditions and the chemical environment, (2) be chemically inert with regard to the target reaction or contribute in a desirable way, (3) provide a large surface area onto which the active material can be deposited, (4) be open porous and have favourable transport properties for the relevant species, and of course, (5) be of low-cost. Lastly, and of utmost importance, supports for photocatalytic applications must be transparent, at least translucent, in the relevant optical band. The latter includes a negligible parasitic absorption of the support. Even though this list of six criteria seems ambitious, there actually are support strategies that do fulfill the requirements. Amongst them are reticulated foams and aerogels.

2.1.3.1. Reticulated foams

Reticulated foams, example see figure 2.4, are one active material support option in applications of photocatalysis. The foam structure itself, typically, is made from metals [64], or ceramics [76, 77], in a template process. If the material is chosen appropriately, reticulated foams are stable in most chemical environments. With their open porosity but interconnected solid framework, reticulated foams allow deep penetration of light into the reaction volume [76, 77], provide good heat and mass transport properties [78], and have a large surface area for the deposition of active materials. The active material

Figure 2.4.: Photograph of a reticulated foam made from ceria and employed in a high temperature redox cycle splitting carbon dioxide to carbon monoxide and oxygen. Reprinted with permission from [76]. Copyright 2012 American Chemical Society.

can either be coated onto the inner surface of the foam [64] or, in case the active material was not precious, the foam itself can be made from the active material [76]. Coating of the active material onto the foam can be realized in manifold ways. Examples are direct growth of the active material on the foam surface [64], or simple wash/spin coating with a slurry containing the active material [79].

The crucial light penetration depth is predominantly shaped by the pore density or pore size respectively and lies in the range of millimeters to centimeters [77]. The lower the pore density/the bigger the pores respectively, the higher is the penetration depth and the smaller are gradients in the intensity of photon absorption [77].

2.1.3.2. Aerogels

Aerogels, exemplary photograph see figure 2.5, are an especially promising active material support option in applications of photocatalysis, see for instance [80, 81]. Aerogels are gas-filled, open porous, interconnected, and mechanically stable networks of nano-scale particles with extreme porosity ranging from 90 % up to 99.99%, see for instance [82]. Aerogels can be made
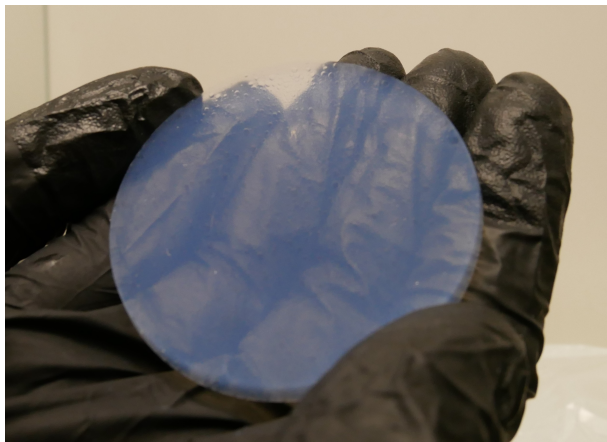
Figure 2.5.: Photograph of a silica aerogel monolith employed as active material support showing a slight blue haze emanating from Rayleigh scattering.

based on various materials, for instance silica [83], titania [31], carbon [82], or organic polymers [84]. They have, if the materials are chosen properly, a good thermal stability and are chemically stable in many chemical environments. Specific surface areas of aerogels are huge, typically in the range of several hundred square meters per gram, see for instance [83, 31, 85]. The advantageous huge specific surface area emanates from the high porosity and nano-sized pores, whose size typically lies between 10 nm and 100 nm, see for instance [85, 86]. Due to the small pore size, fluid transport in the gel structure is, depending on the pressure or the mean free path length, respectively, dominated either by diffusion or a superposition of diffusion and viscous flow [85]. Diffusion coefficients are in the range of 10^{-5} m^2 s^{-1}, which is in the range of gas diffusion coefficients [85]. This is favorable, but sets a limit for the size of aerogel monoliths employed as catalyst supports. The thermal conductivity of aerogels is exceptionally low, see for instance [84]. Aerogel supports, therefore, thermally decouple the active material from the reactor, which may be an advantage in photocatalytic processes in which solar heat (partially) drives the chemical reaction. For examples of corresponding active material systems please refer to section 2.1.2.

As active material support in solar fuel applications, silica aerogels are especially promising due to their high transparency, or low scattering and absorption coefficients, respectively, throughout the UV and Vis band, see
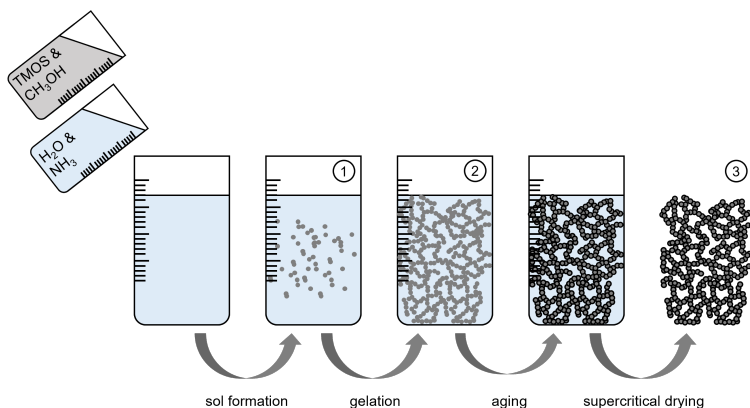
Figure 2.6.: Scheme depicting a standard silica aerogel synthesis in a sol-gel route starting from the silica precursor tetra methyl ortho silicate (TMOS) dissolved in methanol (CH_3OH) and ammonia as catalyst (NH_3) dissolved in water (H_2O) and comprising the steps of sol formation, gelation, aging, and supercritical drying. The numbers indicate steps in the synthesis in which an active material can be impregnated onto the gel. (1) refers to mixing active material particles into the reacting sol, (2) refers to wet impregnation of an active material precursor into the alcogel, and (3) refers to mixing an aerogel powder with an active material powder. Figure derived from [83].

for instance [87]. Light penetration depths into pure silica aerogels are in the range of centimeters to meters, depending on the wavelength. However, Rayleigh scattering in the nano-sized pores/primary particles induces an increase of the scattering coefficient with decreasing wavelength, resulting in a slight blue haze of silica aerogel monoliths [86], see also figure 2.5, and sets a limit to the application of silica aerogel supports with active materials using deep UV photons.

The synthesis of silica aerogels follows established sol-gel procedures comprising sol formation, gelation, aging, and supercritical drying. For an illustration of a typical synthesis process please refer to figure 2.6. The standard synthesis depicted in figure 2.6 opens up basically three ways for active material impregnation. First, active material particles can be added during the sol formation before gelation, compare for instance [31, 83]. Second, an active material precursor can be impregnated into the alcogel by adding the precursor solution to the reacting sol, or during aging [81]. And third, the already dried aerogel can be ground and mixed with a powder of the active material.

2.2. Photoreactors

A photoreactor provides suitable operating conditions for the employed photocatalyst. It ensures photon absorption, provides a suitable temperature, and governs the reactant supply and product extraction. In a very general perspective, photoreactors comprise a reaction volume shaped by a reactor body and an optical access to the reaction volume, for instance via a window. In applications employing artificial light sources, the light source may be considered as a part of the photoreactor as well. Literature reported photoreactors can be grouped in photoreactors that are intended and designed for research applications and photoreactors that are intended and designed for production scenarios either using sunlight or artificial light sources. The requirements and thereof resulting designs for research and production photoreactors differ significantly.

2.2.1. Research photoreactors

Research photoreactors are the workhorses of the development of high efficiency photocatalytic processes. They are employed for the essential tasks of catalyst screening, reaction kinetic and quantum yield measurements, and mechanistic studies. Photoreactors for mechanistic studies are exclusively tailor-made, addressing the requirements of the respective analysis method, therefore, show a broad design variance, and will not be discussed in detail in this place.

2.2.1.1. Catalyst screening

Photoreactors for catalyst screening are the most commonly employed research tool in the search for suitable active materials. They often are rather simple systems that are designed to be convenient in use, especially with regard to the catalyst exchange. Well-defined operating conditions, temperature, reactant concentrations, local volumetric rate of photon absorption, and wavelength of the employed light are of course desired but often not feasible within the simple designs employed. For a brief discussion of this challenge, see for instance [61].
In a broad view, the most frequently reported photoreactors for catalyst screening can be grouped in two categories. The first category comprises
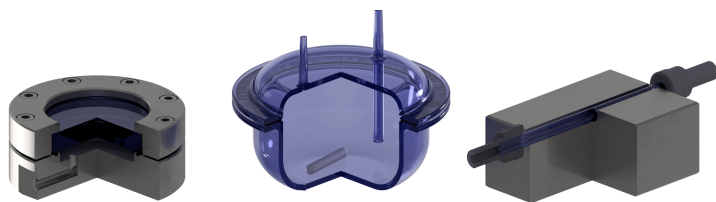
Figure 2.7.: CAD model renderings of three typical photoreactor types employed for photocatalyst screening: two vessel-type reactors (left and centre) and one capillary reactor. In all three depicted photoreactors, photons would be coupled into the reactor from above. The Batch reactor CAD model (left) is derived from design indications in [62] and comprises a two-part reactor body and a quartz glass window that together surround the reaction volume. Reactants and products are fed/extracted over the fluid connector bore. The stirred tank reactor CAD model (centre) is derived from design indications in [35] and comprises a two-part glass vessel with two fluid connectors for purge gas supply and product extraction and a stirring rod. The capillary reactor model is derived from design indications in [63] and comprises a quartz glass capillary with two commercial fluid connectors and a heating block for temperature control.

simple, sometimes stirred vessels, either for batch operation, see for instance [62], or continuous operation, see for instance [35, 57]. The second category comprises glass capillary reactors exclusively for continuous operation, see for instance [88, 63, 31]. For an illustration of exemplary systems representing the two categories, see figure 2.7.

For the sake of simplicity, illumination in both categories is realized in most cases via external light sources. In case of vessel-type reactors, photons are coupled into the reaction volume either through a window, see for instance [62] or, if the vessel is made from glass, through the reactor wall, see for instance [35]. Common light sources are xenon short arc lamps, see for instance [62], halogen lamps, see for instance [55], mercury-vapour lamps, see for instance [57, 38, 56], and light emitting diodes (LEDs), see for instance [89]. Noteworthy, the latter two light source types, mercury-vapour lamps and LEDs, are narrow band light sources, whereas the named thermal light sources, xenon short arc lamps and halogen lamps, are polychromatic light sources with an emission spectrum typically ranging from the UV over the Vis to the IR band. With polychromatic light sources, narrow band pass filters can be used to control the wavelength of photons sent into the reactor, see for instance [38]. With narrow band light sources narrow band pass filters are obsolete, but an exchange of the light source is necessary to modify the wavelength of incident photons. Noteworthy, the number of absorbed photons,

or even the local volumetric rate of photon absorption, is hard to determine with accuracy in such simple vessel-type reactors. For a discussion of this issue, see for instance [61]. With regard to the optical operating conditions most simple vessel-type reactors are, therefore, poorly defined.

Additionally, in batch systems, the reactants are fed previously to the reaction into the reactor, and gas phase/liquid samples are taken after a defined illumination time to test the conversion, see for instance [62]. Inherent to batch reactors is, therefore, a change of the reactant/product concentration during the experiment time. Depending on the achieved conversion, these changes can be significant. With regard to the reactant concentration, batch reactors, therefore, are also poorly defined.

Concluding, most employed screening reactors only give limited insight into the photocatalytic performance of photocatalysts. Due to the poorly defined operating conditions, both on the optical and the reactant concentration side, results obtained in such systems often do not allow meaningful comparisons between works of different working groups. In extreme cases, in which the optical properties differ significantly between photocatalysts, even comparisons between photocatalysts tested in the same photoreactor may not be reasonable. This is because in such systems rather radiation transport than the photocatalytic performance determine the system behaviour, and observations made do not indicate catalytic performance metrics but radiation transport phenomena.

2.2.1.2. Reaction kinetic and quantum yield measurements

Photoreactors for reaction kinetic and quantum yield measurements are the essential tool in active material and photocatalyst engineering. Reaction kinetics and quantum yields derived with the help of such devices are the fundamental and indispensable basis of the development of high efficiency photoreactors and processes [90, 91]. For a detailed discussion of this need, please refer to section 2.2.2. Photoreactors for reaction kinetic and quantum yield measurements must provide well-defined operating conditions, including temperature, reactant concentration, wavelength of absorbed photons, and the local volumetric rate of photon absorption [90, 91]. A well-defined local volumetric rate of photon absorption is, thereby, of outstanding importance, since only rate law expressions modelling the reaction rate as function of the local volumetric rate of photon absorption are a valid tool for photoreactor design tasks [91]. If considered, the requirement of well-defined operating

conditions results in rather complex photoreactor designs. However, from a fundamental view, it is important to note that well-defined operating conditions represent the necessary precondition for comparable and meaningful measurements [92, 93, 94].

Quantum yield measurements require both experimental access to the number of production events, and experimental or simulative access to the number of photons that are absorbed by the photocatalyst. For clarification, refer to equation (2.7). The number of production events, thereby, is proportional to the product formation rate or the reaction rate, respectively. Measuring the reaction rate or examining the reaction kinetics, respectively, is therefore, an essential part of quantum yield measurements. Any approach suitable for quantum yield measurements, consequently, implies a suitability for reaction kinetic measurements. If the operating conditions are well-defined, reaction kinetics can easily be derived from a measurement of the amount of product molecules at the photoreactor outlet with standard analytical methods, for instance via UV Vis spectroscopy, or liquid/gas chromatography, see for instance [93, 94].

The challenge of quantum yield measurements typically arises from the determination of the number of photons absorbed by the catalyst system. This holds especially for heterogeneously catalysed photoreactions in which scattering complicates the radiation transport problem [27, 35]. For the sake of the complexity of both experimental and simulative approaches that give access to the number of absorbed photons in a photocatalytic experiment, most literature works reporting quantum yields relate the number of production events to the number of incident photons rather than to the number of absorbed photons. These works indirectly assume that the number of absorbed photons equals the number of incident photons. However, the number of incident and absorbed photons can differ significantly, see for instance [94, 95]. According to IUPAC recommendations, quantum yields that are derived under the assumption that the number of absorbed photons equals the number of incident photons should be tagged as *apparent* quantum yields [27].

The most simplistic photoreactors for *apparent* quantum yield measurements are vessel-type stirred reactors illuminated from one side, typically from the top [35, 57], scheme see figure 2.7, centre. Either narrow band light sources or the employment of narrow band pass filters is mandatory since the quantum yield is a spectral property defined at a specific wavelength, see equation (2.7). The number of incident photons in these experiments is typically determined either via actinometry, see for instance [57], or with photodiode power

sensors, see for instance [35]. Besides the critical assumption made regarding the number of absorbed photons, the employed vessel-type photoreactors additionally exhibit high gradients in the local volumetric rate of photon absorption that emanate from the unilateral illumination that obviously does not penetrate the whole reaction volume. If the illumination penetrated the whole reaction volume, photons would leave the photoreactor at the side opposite to the illuminated side and the assumption of full photon absorption would be taken ad absurdum. This nonuniform illumination represents an error source if the reaction rate does not scale linearly with the local volumetric rate of photon absorption or with other words if the quantum yield is a function of the local volumetric rate of photon absorption, discussion see for instance [96].

Black-body photoreactors for quantum yield measurements are an advancement compared to the described simplistic vessel-type photoreactors for *apparent* quantum yield measurements. In these black-body systems, the photocatalyst is placed in a reaction volume that surrounds a cavity, for illustration see 2.8, left. The cavity has an opening, that is very small compared to the inner surface of the cavity. Through the opening photons are coupled into the cavity. Assuming the reaction volume surrounding the cavity was opaque, or with other words, the photocatalyst absorbs/scatters light strong enough in order to avoid any transmittance, indeed any photon sent into the cavity is finally absorbed by the catalyst. Photon losses through the cavity opening are negligible as long as the opening is small in comparison to the cavity's inner surface. Parasitic absorption by the cavity walls is negligible as long as the material is chosen properly with a low absorption coefficient in the relevant optical band. Practical implementations of such black body photoreactors are for instance photoreactors with either a light source or an optical fibre connected to an according cavity immersed in the reaction volume, see for instance [96]. Still these black-body reactors exhibit high gradients in local volumetric rate of photon absorption and, therefore, are only suitable for photocatalysts, in which the quantum yield is independent of the local volumetric rate of photon absorption.

Integrating sphere photoreactors are another advancement in quantum yield measurements, example see for instance [97, 98, 99]. In these setups, a cuvette containing the photocatalyst with reactants, or a flow cell, is placed in an integrating sphere and illuminated through an opening in the integrating sphere surface, illustration see figure 2.8, right. Simplified, the integrating sphere collects all photons that are either transmitted or scattered by the photocatalyst in the cuvette/flow cell. A sensor on the integrating sphere's
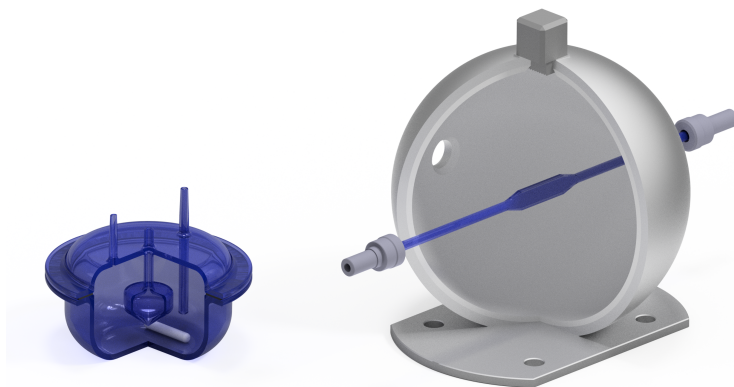
Figure 2.8.: CAD model renderings of two typical photoreactor types employed for quantum yield measurements, one black body type photoreactor (left) and one integrating sphere type photoreactor (right). The black body type photoreactor comprises a cavity that is immersed in the reaction volume. Provided that the reaction volume was opaque, all photons coupled into the cavity, for instance via an optical fibre, are absorbed by the reaction volume regardless of scattering effects in the reaction volume. The CAD model was derived based on details given in [96]. The integrating sphere type photoreactor comprises a flow cell placed in an integrating sphere. The flow cell is illuminated through the light source port in the surface of the integrating sphere. The detector mounted of axis detects the intensity of light that is not absorbed by the photocatalyst in the flow cell and, therewith, gives access to the number of absorbed photons. The CAD model was derived based on details given in [97].

inner surface lastly detects this photon flux. By comparing an integrating sphere measurement of the photocatalyst sample in the sample cell under illumination with a reference measurement without the photocatalyst in place, the number of absorbed photons can be derived experimentally. If the characteristic dimensions and the absorption and scattering coefficients of the reaction volume, or of the photocatalyst respectively, are chosen/tuned properly, the assumption of an approximately uniform distribution of light in the reaction volume or a uniform local volumetric rate of photon absorption is valid. If designed and conducted properly, quantum yield measurements in integrating sphere photoreactors are, therefore, highly reliable. Drawbacks of integrating sphere photoreactors are their complex and expensive design, the sensitivity of integrating spheres and the limited space in standard setups typically comprised in desktop UV Vis spectrometers. The latter limits the

feasibility of complex studies addressing other operating conditions than wavelength and local volumetric rate of photon absorption.

2.2.2. Production photoreactors

Production photoreactors suitable for solar fuel production ensure a high photocatalytic efficiency under the constraint of a low area-specific cost of the resulting system. Achieving both, high photocatalytic efficiency and low-cost at the same time is the crucial prerequisite for a reasonable and commercially feasible implementation of a solar fuel processes. For a brief discussion of this issue see chapter 1.

Maximizing the photocatalytic efficiency of a photocatalytic process is a photoreaction engineering challenge. Presumed a photocatalyst exhibiting a high quantum yield in a relevant optical band was available, and the light source was not variable, the photoreactor optimization task addressing the photocatalytic efficiency focuses on two aspects. First, the photoreactor must provide the operating conditions, temperature, reactant concentrations, local volumetric rate of photon absorption, and to some extent the wavelength of absorbed light, under which the quantum yield peaks. And second, the photoreactor must guide incident photons towards the photocatalyst with minimized photon losses [100]. The latter occur for instance through parasitic absorption by reactor components, mirrors, windows, lenses, etc., or reflective losses through 'misguided' photons missing the reaction volume [94]. For these two reasons, the need of tailored optical operating conditions and the need for efficient radiation transport, high efficiency photoreactor design is based on a precise radiation transport model, or a suitable radiation transport equation, respectively, mapping radiation transport from the photoreactor aperture into the reaction volume [27]. The dependency of high efficiency photoreactor design on a suitable radiation transport model also finds its representation in the general photoreactor design equation, equation (2.9), that returns the achieved photocatalytic efficiency. It relates the number of production events, the wavelength and volume integral of the product of local volumetric rate of photon absorption and quantum yield in the reaction volume (V), to the number of incident photons, the wavelength and area integral of the spectral photon irradiance ($E_{p,\lambda}$) in the reactor aperture (A). The

photoreactor design equation is, therewith, a reformulation of the definition of the photocatalytic efficiency, equation (1.2).

$$\eta_p = \frac{\iint L_{p,\lambda}^a \Phi(T, c_i, \lambda, L_{p,\lambda}^a) d\lambda dV}{\iint E_{p,\lambda} d\lambda dA} \tag{2.9}$$

In order to evaluate the local volumetric rate of photon absorption in the reaction volume, the mentioned radiation transport model is mandatory. Noteworthy, the evaluation of local temperature and concentration fields demand for suitable heat and mass transport models that may indirectly demand for a momentum transport model (fluid dynamic model). The level of complexity in the different aspects, radiation, heat, mass and momentum transport, needed in order to succeed with a photoreactor design task, thereby, largely depends on the sensitivity of the quantum yield towards the respective operating conditions. If the quantum yield is strongly influenced by optical operating conditions, wavelength and local volumetric rate of photon absorption, the implementation of a precise, and most likely complex radiation transport model is necessary. If, on the other hand, temperature and/or reactant concentration only mildly influence the quantum yield, the implementation of complex fluid dynamic, or heat and mass transport models is optional/not advisable. In many photoelectro catalytic systems, the latter is the case [100]. A further complicating design constraint in the design of high efficiency photoreactors for solar applications is a moving light source, or the moving sun, respectively. The employed photoreactor must be able to ensure a high photocatalytic efficiency not only in one irradiation scenario, but throughout the course of the day and year with an according variation of the direction of incident light, which might represent a substantial challenge [94].

Achieving low area-specific cost of a photoreactor employed in a solar fuel process is a multi-faceted challenge. Of course the term 'area-specific cost' addresses capital and operational cost. Achieving low capital costs starts with an appropriate choice of materials. The main reactor body should be made from the cheapest materials possible, for instance polymers, and still should be as lightweight as possible, having in mind, that rather square kilometers than square meters must be covered with 'photoreactor aperture' in order to be able the generate a significant production, see for instance [52, 24]. Expensive materials, for instance the photocatalyst, should be employed as sparingly as possible. The catalyst usage must, therefore, be maximized in most systems [24]. Further, low capital cost can be achieved by a suitable design that is manufacturable with established, low-cost techniques, for instance polymer

injection molding, polymer extrusion, or film blowing. Beyond that, complex and costly components in best case are avoided. This could for instance include sun tracking mechanics that appear to be an elegant mean to address the aforementioned challenge of a varying position of the sun throughout the day and year, but are known for dominating the costs of sunlight harvesting systems, for instance in the field of concentrated photovoltaics [101] or concentrated solar power [102]. Lastly, low capital cost can be achieved by a standardized and modular design that allows easy adaptation to various use cases, and expansion of existing installations.

A modular design, further, is a mean to reduce operational cost. Modules that don't show the desired performance metrics anymore can be exchanged easily without shutting down a whole plant. Further, operational costs can be reduced by a high degree of system integration and automation that both reduce labor intensive works to an absolute minimum necessary. In the perspective of low operational cost, again, simple designs that do not rely on complex and sensitive components, such as sun tracking mechanics, are favorable, if possible.

There is a multitude of different production photoreactors proposed for solar fuels applications. They differ significantly in their design and represent attempts to address the discussed challenge of achieving high photocatalytic efficiency under the constraint of low area-specific cost. As discussed, most designs are, thereby, strongly influenced by the reaction engineering properties of the employed photocatalyst.

2.2.2.1. Highly concentrating systems

Highly concentrating production photoreactors, example see figure 2.9, are typically designed for either solar-driven thermal or photothermal photocatalysts. Light concentration mainly is employed to achieve the desired reaction temperatures. 'Highly concentrating', thereby, refers to a geometric concentration ratio of at least several hundred to more than two thousand multiples of the solar irradiance, see for instance [22, 40].

Typical systems comprise mirror-based concentrating optics like parabolic troughs, paraboloids and, in a bigger scale heliostat fields that guide incident sunlight into a cavity receiver containing the photocatalyst, see for instance [100, 102, 22]. Noteworthy, even though seemingly exotic at a first glance, concentrating optics reaching such high concentration ratios are well understood, highly efficient and already in large-scale commercial use in concentrated

Figure 2.9.: Highly concentrating photoreactor at the ETH Zürich employed to operate a solar-driven thermal catalyst system splitting carbon dioxide and water to yield synthesis gas in a high temperature redox cycle. Reprinted with permission from Springer Nature, [22], Copyright 2021.

solar power plants for instance in Quarzazate, Morocco, Almeria, Spain, or Invanpah, California [102]. Sun tracking is mandatory for highly concentrating systems [102]. The law of etendue conservation, equation (2.10), describes a clear thermodynamic limit for the acceptance angle (θ) that concentrating optics in air reaching a certain concentration ratio (C) may reach at maximum [103]. The higher the concentration ratio, the more precise tracking must be. The high precision of the required tracking optics induces a significant cost penalty for highly concentrating photoreactors [102]. For instance, for solar hydrogen from a high temperature redox cycle implemented in a heliostat field, the cost for the concentrating optics are estimated to contribute roughly 80 % of the final hydrogen cost [40].

$$C \leq \frac{1}{sin^m(\theta)} \quad m = \begin{cases} 1 & \text{for line concentration} \\ 2 & \text{for point concentration} \end{cases} \quad (2.10)$$

In addition to the tracking requirement, highly concentrating systems face a challenge with regard to typical process temperatures. As described in

section 2.1.2, typical temperatures needed to drive the thermochemical conversions are in the range of 1000 ℃ to 1500 ℃. Handling such temperatures demands substantial efforts on the engineering side. On the one hand, these temperatures are challenging with regard to available construction materials, for instance the window material of the cavity receiver [22]. On the other side the extreme temperatures impact significantly the achievable efficiencies through (1) radiative heat losses [40], (2) the heat losses that are induced by reactants flowing through the reactor [42], and (3) the heating duty necessary to cycle the reactor temperature [42]. It is also for the extreme temperature and the complex handling of those, that highly concentrating systems are only economically feasible within large-scale applications [102]. Modular designs, adaptable to different use cases, maybe even including small-scale decentral use, are hard to imagine in such high temperature processes.

2.2.2.2. Panel-like systems

Panel-like photoreactors, example see figure 2.10, are especially suited for ambient temperature photoelectrocatalysts, see for instance [23]. Panel-like, thereby, refers to a thin, slab-like geometry of the photoreactor that allows a modular plant design. Similar panel-like systems are known from photovoltaic applications and, on a side note, kick-started the photovoltaic sector. The most simplistic panel-like production photoreactors are plates, for instance frosted glass plates, coated with the photocatalyst and covered with a transparent window, for instance Pyrex or quartz glass sheets, see [23, 104]. Reactants are either fed into the volume between photocatalyst layer and transparent cover [23] or, in case the photoreactor is a simple inclined plate, flow in a thin film on the catalyst layer [100]. Such straight forward and simple designs theoretically allow mass fabrication of the photoreactor panels and, thereby, production at scale. Further the lack of any concentrating optics induces favorable acceptance characteristics with a broad acceptance angle region that allows an implementation without sun tracking mechanics. This drastically reduces the system cost compared to highly concentrating photoreactors that depend on precise sun tracking. However, the lacking optical design freedom of a simple plate limits reachable photocatalytic efficiencies. Photons either being scattered by or being transmitted through the photocatalyst layer are lost, meaning they are no longer available for production. Additionally, if transmission losses are minimized by increasing the optical thickness of the photocatalyst layer, which is reasonable, gradients

Figure 2.10.: Panel like production photoreactor with photoelectro chemical photocatalyst splitting water to hydrogen and oxygen. Reprinted with permission from Springer Nature, [23], Copyright 2021.

in the local volumetric rate of photon absorption and a low catalyst usage are indispensable.

Scattering and transmission losses can be reduced with slightly more complex photoreactor panel assemblies. There are, for instance, panel-like photoreactors that are derived from tube bundle reactors, [105]. In these assemblies a bundle of transparent tubes shapes a slab-like reaction volume comprising the tubes and the photocatalyst in the tubes. The tubing walls, thereby, act as light guides, that allow photons to penetrate deep into the the reaction volume. If photons are transmitted or scattered in the photocatalyst in one of the tubes, the likelihood for another absorption chance in one of the neighbouring tubes is rather high [105]. These multiple passages of photons through different or one and the same reaction volumes increase the chance of absorption and consequently the achievable photocatalytic efficiency. Proper dimensioning of the tube wall thickness and tube inner diameter are essential tasks of a successful design of a tube bundle-derived photoreactor panel that ensures a homogeneous local volumetric rate of photon absorption, high catalyst usage, and satisfactory photocatalytic efficiency. On a side note, geometric dimensions of photocatalyst layers that are still partially transparent, or with other words photocatalyst layers that can be illuminated in a way that the local volumetric rate of photon absorption does not possess high gradients, are rather small. Typically they lie more in the range of several dozens of

micro metres to millimeters than in the range of centimeters to meters, even if the active material is supported on a transparent support, see for instance [23].

A significant drawback of tube bundle derived photoreactor panels is the rather intensive construction material use and complicated fluid distribution and collection in tube bundles. If glass is used as construction material, the resulting photoreactors are rather heavy, seen as an area-specific weight. The same holds for photoreactor panels build from frosted glass substrates and transparent glass covers. Due to the outstanding importance of the reactor component cost, see [24], the use of tube-bundle derived photoreactors, or even more general the use of photoreactors made from glass, for large scale solar fuel synthesis is, therefore, questionable.

2.2.2.3. Low-cost systems

Low-cost production photoreactors are designed with regard to a maximum simplicity and lowest possible cost. Often this entails a penalty with regard to the achievable photocatalytic efficiency. In 2022 such systems only exist as concepts. Low-cost construction materials like polymers, the avoidance of costly components meaning, for instance, no sun tracking, mild process conditions, such as in photoelectro catalysis, and the suitability for mass fabrication are mandatory.

The most popular example of a low-cost photocatalytic production reactor are plastic bags, filled with a photoelectro catalyst and operated at ambient temperature, so called 'baggie' reactors, see for instance [24, 52, 106] and scheme figure 2.11. The envisaged application of 'baggie' reactors is solar hydrogen production via photoelectro catalytic water splitting. The most simplistic scheme of a baggie reactor comprises one plastic bag with a dual function photocatalyst, both reducing protons and oxidizing water. In this scenario, a potentially explosive mixture of hydrogen and oxygen is formed in the plastic bag. To avoid this hazardous characteristic, a further development of the baggie reactor concept foresees the employment of a z-scheme photocatalyst system comprising separate reduction and oxidation catalysts that are operated in two baggie reactors and connected via a diaphragm allowing a redox shuttle to mediate between the two catalyst systems [106]. In this concept, hydrogen and oxygen are obtained in two separate baggies and explosive gas mixtures are avoided. The realization of the two connected baggies remains to be demonstrated, however.
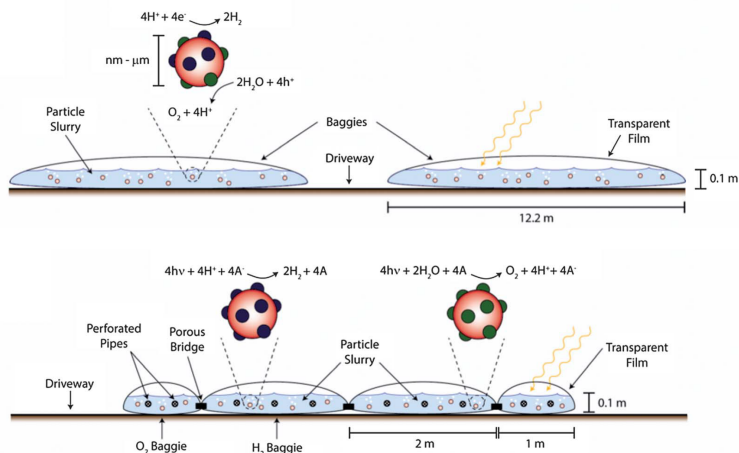
Figure 2.11.: Scheme of two envisioned low-cost 'baggie' production photoreactors being built from polymer plastic bags, filled with photoelectro catalyst slurry and employed for water splitting. The scheme on top represents a 'baggie' reactor with one photoelectro catalyst both reducing protons to hydrogen and oxidizing water to oxygen. Hydrogen and oxygen are obtained as mixture in one baggie reactor. The bottom scheme comprises two baggie reactors in which separately protons are reduced and water is oxidized. The two bags are connected with a diaphragm that allows a redox shuttle to permeate and mediate between the two photocatalysts. Hydrogen and oxygen are obtained separately in this approach. Reprinted with permission from RSC Publishing, [52], Copyright 2015.

On the radiation transport side, for baggie-like photoreactors the same challenges as for simplistic panel-like photoreactors arise. Scattered and transmitted photons are lost, and, if the catalyst suspension is optically thick to avoid transmission losses, high gradients in the local volumetric rate of photon absorption are indispensable. Consequently, achievable photocatalytic efficiencies are expected to be lower than in more sophisticated reactor concepts including optics [24]. Additionally, handling of explosive mixtures in macroscopic structures entails an impressive explosion hazard, that renders single baggie reactors with a dual function photocatalyst a rather risky concept.

3. Outline of the work

According to the introduced photoreactor design equation, equation 2.9, and as already stated in chapter 1, the development of a high efficiency solar fuel process relies on two core components: (1) a photocatalyst using UV and Vis photons efficiently to drive a relevant chemical reaction of carbon dioxide and/or water and (2) a photoreactor providing optimal operating conditions for the photocatalyst and a high efficiency in radiation transport from the photoreactor aperture to the photocatalyst deposited in the reaction volume. Photocatalysts using photons efficiently to drive chemical reactions of water and carbon dioxide to energy carriers are indeed reported, but complex, precisely engineered material systems. Roughly grouping, there are systems that are operated at medium to extreme temperature, photothermal, and solar-driven thermal catalysts, and systems that are operated at ambient temperature, photoelectro catalysts.

The design of production photoreactors is strongly influenced by the photocatalyst's properties. Decisive is the operating temperature and the therefrom resulting requirements for the optical components. Roughly grouping, there are photoreactor concepts that highly concentrate sunlight and that are designed for extreme process temperatures and panel-like or baggie-like photoreactor concepts without concentrating optics that are designed for ambient temperature operation.

The cost of a solar fuel technology is predominantly shaped by the capital cost of the employed photoreaction technology. Key to a low-cost concept are, therefore, the employment of cheap construction materials for the photoreactor and a design that is manufacturable with low-cost, standard techniques. The employment of technically complex and expensive components, like, for instance, sun tracking mechanics, must be avoided if possible. Costly materials, like, for instance, the photocatalyst, must be used sparingly but especially efficiently. A high catalyst usage is, consquently, mandatory.

To contribute to the endeavour of the development of a high efficiency and low-cost solar fuel process, the present work, consequently, aims to develop and demonstrate a polymer photoreactor concept with a design that allows

fabrication via polymer extrusion. The concept shall be panel-like and modular and explicitly excludes the option to employ sun tracking. Even though statically aligned to the sun path, the concept shall ensure a high photocatalytic efficiency for any photocatalyst exhibiting a high quantum yield in the relevant UV Vis band. This explicitly includes heterogeneous photocatalysts that tend to scatter light intensively. Achieving a high photocatalytic efficiency under these conditions, static alignment to the sun path and scattering photocatalysts, demand a design concept that combines the features of highly concentrating photoreactor concepts comprising light concentration and trapping in cavities with the broad acceptance characteristics of simple panel-like or baggie-like photoreactors. All together the envisioned characteristics not only favour an economic implementation in solar farms but also allow to imagine small-scale, decentral applications that may represent a way to establish new technologies in the energy market [107].

The use of polymers as construction material limits the suitability of the envisioned photoreactors to low temperature photocatalysts. Such photocatalysts are photoelectro catalysts. Besides the overarching aim to contribute to the endeavour of the development of a high efficiency and low-cost solar fuel process via the design of suitable photoreactors, the second aim of the present work is, therefore, the development of a model photoelectro catalyst system that can be employed to demonstrate the functionality of the envisioned photoreactor concept. Besides the active material development the efforts in the field of photoelectro catalyst system development shall explicitly include suitable active material support strategies that can be employed to control radiation transport on the photocatalyst level. The latter is necessary to avoid radiation transport hindrances in the catalyst bed and, thereby, opens ways towards a high catalyst usage.

The photoreactor design equation, equation 2.9, also highlights, that two skills are key to success in the development of a high efficiency solar fuel process: (1) the ability to determine quantum yields in photoreactions as a function of the operating conditions, including temperature, reactant concentration, wavelength and especially the local volumetric rate of photon absorption, and (2) the ability to model radiation, heat, mass, and momentum transport in a photoreactor.

The third aim of the present work is, consequently, the development of a method for the precise determination of quantum yields in gas, liquid and multi-phase photoreactions. The focus shall be the precise knowledge and definition of the local volumetric rate of photon absorption in the experiments. To the best of the author's knowledge, this operating condition, the local
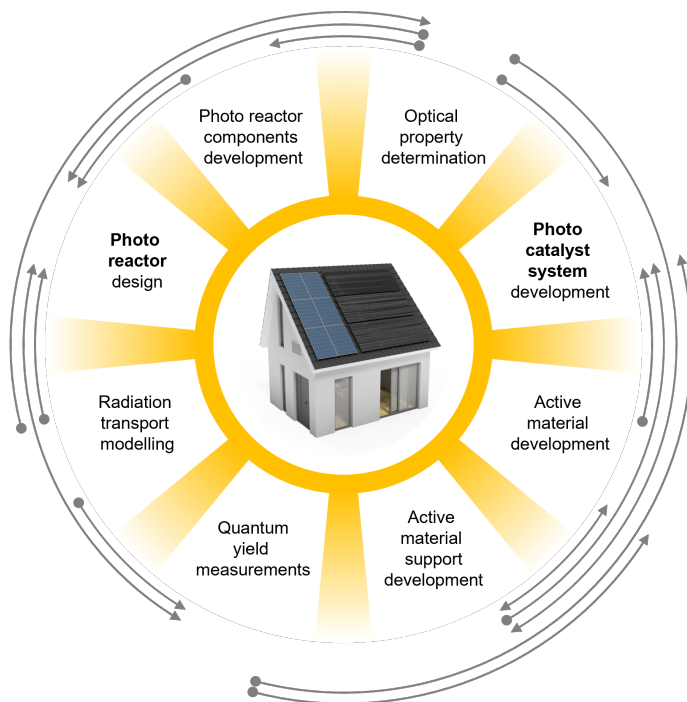
Figure 3.1.: Scheme of the overall challenge of the design of a low cost high efficiency photocatalytic process using carbon dioxide, water, and sunlight to deliver a solar fuel. The Scheme depicts the main development tasks and methods (text boxes) together with their dependencies (grey arrows).

volumetric rate of photon absorption, translating to the process intensity, is only sparingly examined as a parameter influencing the quantum yield in photoreactions. This is even though the local volumetric rate of photon absorption is considered as the most suitable variable to express the influence of 'light intensity' in photoreaction kinetics [91]. Besides its importance for photoreactor design, the envisaged method, therewith, also allows interesting scientific insights into the nature of quantum yields in photoreactions.

And lastly, since the quantum yield is expected to be only slightly sensitive towards temperature and reactant concentration in photoelectro catalyst systems, the fourth aim of the present work is the development of a precise radiation transport model for photoreactors (that can be combined with heat,

mass and momentum transport models). The envisioned radiation transport model shall be able to map radiation transport in multi-component systems with high accuracy but at a reasonable computational cost. The latter opens the way towards numerical design optimizations. Of course, mapping radiation transport with a radiation transport model is only reasonable with the knowledge of optical transport properties, like refractive indices, absorption and scattering coefficients, reflectivity and reflection characteristics, etc.. The determination of these transport properties is, consequently, a supplementary topic of the present work.

Summarizing, the present work addresses the overall challenge of high efficiency low-cost photoreactor design illustrated in figure 3.1 and discusses the following topics in detail (in order as described in the following):

1. Development and validation of a radiation transport model for multi component systems

2. Development of a test environment for reaction engineering experiments with materials and and components of solar fuel processes

3. Development of pathways of photoreactor prototype fabrication

4. Development of methods for the determination of optical transport properties

5. Development of a model photocatalyst comprising active material and support

6. Development of a method for the precise determination of quantum yields and its application in a detailed examination of the interdependencies of local volumetric rate of photon absorption and the quantum yield

7. Development and demonstration of a low-cost photoreactor design concept for a simple photocatalytic model reaction and detailed examination of its performance metrics

4. Radiation transport modelling

The radiation transport model developed for the tasks in the present work shall be able to map radiation transport in three dimensions in multi-component systems. More concretely, this means that the radiation transport model shall be able to map radiation transport in photoreactor assemblies comprising transparent components like windows or lenses, translucent (turbid) components like particulate catalyst beds, and opaque components like mirror optics or reactor component walls.

A restriction made before all considerations, is that the mapped components do not show gradients in their optical properties. A transparent window for example would have a constant refractive index and absorption coefficient throughout its whole volume. As will be lined out, this assumption facilitates the considerations and implementation significantly.

4.1. Physical basis

In theory, Maxwell's equations entirely describe the propagation of light in any system [108]. Applying Maxwell's equations on a radiation transport problem would allow to assess any imaginable radiation transport performance metric in any imaginable detail level, including, for instance, the local volumetric rate of photon absorption in a photocatalyst placed in the reaction volume of a photoreactor. The resulting complexity and computational effort, however, render this approach in most cases impractical [109]. A simplification is needed in order to deal complex macroscopic multi-component systems, systems like photoreactors, with acceptable computational effort. Geometric optics represent such a simplification [108, 109]. The following, very brief introduction into geometric optics is based on the text books referenced in [108, 109].

4.1.1. Geometric optics

Geometric optics are applicable if the characteristic dimensions of both the objects in which light travels and the objects with which light interacts are way bigger than the wavelength of the mapped light [109]. In this special case Fermat's principle is applicable and light can be mapped as propagating rays [109].

If the refractive index is constant along a ray path, compare the fundamental assumption made in the introduction of this chapter, light rays are propagating in straight lines [109, 108]. The optical path length of light traveling from point A to B in a medium with constant refractive index, therefore, equals the geometric distance between A and B [109].

If rays cross phase boundaries with a change in refractive index, the propagation direction of the rays is altered [109, 108]. Thereby, the incident ray vector, the refracted ray vector and the phase boundary surface normal vector in the intersection point of ray and phase boundary are coplanar [109]. Figure 4.1 depicts an exemplary path of a ray crossing a phase boundary with a change in the refractive index from n_0 (originating medium) to n_1. Its change in propagation direction can be derived from Fermat's principle and results in Snell's law, equation (4.1) [109, 108]. The change in direction, thereby, depends on the incident angle α (relative to the phase boundary surface normal in the ray phase boundary intersection point) and the change in refractive index from n_0 (originating medium) to n_1. The direction change is expressed in form of a refraction angle β (relative to the phase boundary surface normal vector in the intersection point of ray and phase boundary), equation (4.1). In case $n_0 > n_1$, total reflection will occur if the incident angle is above the critical angle α_{crit}, equation (4.2) [109, 108].

$$n_0 \sin \alpha = n_1 \sin \beta \tag{4.1}$$

$$\alpha_{crit} = \arcsin \frac{n_1}{n_0} \tag{4.2}$$

On any phase boundary with a change in refractive index, in addition to refraction, partial specular reflection will occur [109, 108]. Specular reflection of rays on phase boundaries can be mapped as a special case of refraction, in which the refractive index changes its sign [109]. Incident and reflection angle equal each other. Incident ray, reflected ray, and the phase boundary surface normal vector are again coplanar. The reflectivity R of the phase boundary, being the ratio between reflected ray intensity and incident ray intensity,
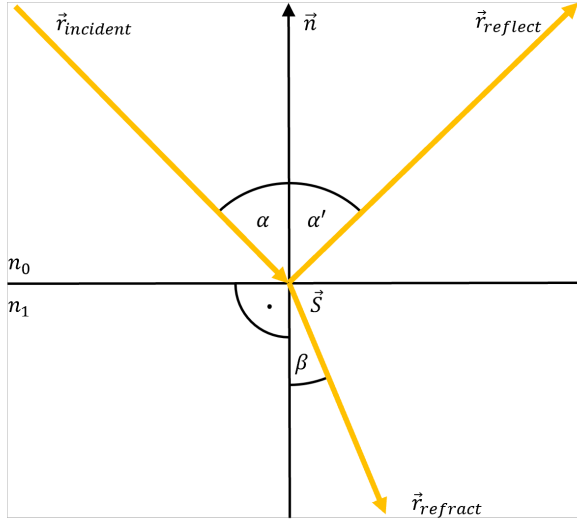
Figure 4.1.: Exemplary path of a ray (yellow arrows) propagating over a phase boundary (horizontal solid line) with a change in refractive index from n_0 (originating medium) to n_1. The incident angle α is defined as angle between the incident ray vector $\vec{r}_{incident}$ and the phase boundary normal vector $\vec{n}$ in the intersection point of ray and phase boundary $\vec{S}$. The reflection angle α' is defined equally between the reflected ray vector $\vec{r}_{reflect}$ and $\vec{n}$. The refraction angle β is defined as the angle between the refracted ray vector $\vec{r}_{refract}$ and $-\vec{n}$ ($\vec{n}$ pointing into the entering medium).

depends on the incident angle and the refractive indices of the two media being in contact at the phase boundary and can be calculated for natural light with the Fresnel equations given with equations (4.3) [109, 108].

$$R = \begin{cases} \frac{1}{2} \left[\frac{\sin^2{(\alpha-\beta)}}{\sin^2{(\alpha+\beta)}} + \frac{\tan^2{(\alpha-\beta)}}{\tan^2{(\alpha+\beta)}} \right] & \alpha \in (0, \pi] \\ \left(\frac{n_1-n_0}{n_1+n_0} \right)^2 & \alpha = 0 \end{cases} \tag{4.3}$$

4.1.2. Volume and surface interaction

The introduced basic principles of geometric optics provide the basis for a model describing light propagating in multi component systems in which each component is transparent and homogeneous with regard to its refractive

index. Briefly summarizing, ray paths in such systems are sequences of straight lines whose connecting points lie on phase boundaries. Further modelling is needed in order to map volume absorption, volume scattering, the superposition of both, and the interaction of rays on opaque surfaces.

Rays traveling through an absorbing medium with constant refractive index and constant absorption coefficient experience an attenuation which can be described with a Lambert-Beer law approach, equation (4.4) [108, 110]. Thereby I refers to the energy transported by the ray, L corresponds to the ray path length and σ_a corresponds to the absorption coefficient.

$$\partial I = -\sigma_a I \partial L \tag{4.4}$$

Additionally, the Lambert Beer type approach can be extended to include scattering. The introduced absorption coefficient is replaced by the extinction coefficient being the sum of absorption and scattering coefficient ($\sigma_{ext} = \sigma_a + \sigma_s$). Noteworthy, in this case of simultaneously occurring absorption and scattering the ray attenuation calculated with the Lambert Beer type approach does no longer equal the absorption intensity because the fraction of scattered light (σ_s/σ_{ext}) propagates through the medium with altered direction. In order to map the influence of scattering onto the radiation transport problem, the scattering characteristics of the scattering events must be defined. The scattering characteristics describe the intensity distribution of scattered rays around the scattering centre (volume element, that scatters light). Generally these scattering characteristics are complex and depend on the nature (material, size, and shape) of the scattering centers (or particles/pores respectively) [108]. The most simplistic assumption that can be made regarding this scattering characteristic is isotropic scattering into the whole sphere around the scattering centre.

The interaction of rays with opaque surfaces can be modelled with a reflection law correlating the intensity of the reflected ray to the intensity of the incident ray via the reflectivity of the opaque surface, which, thereby, is equally defined as the reflectivity of phase boundaries introduced earlier, equation (4.5), [108].

$$I_R = R I_{inc} \tag{4.5}$$

In order to map the influence of reflection events onto the radiation transport problem, in addition to the reflection law, equation (4.5), the reflection characteristics must be defined. The reflection characteristics describe the intensity distribution of reflected rays above the reflecting surface. Generally, these characteristics are complex and depend on the nature of the reflecting surface

(material and surface structure, or more precisely the pore structure of the near surface volume). The most simplistic models that can be applied are ideal specular reflection, which is mapped in analogy to partial reflection of rays on phase boundaries, see subsection 4.1.1, and ideal diffuse reflection which can be mapped with Lambert's cosine law, equation (4.6), [111]. In Lambert's cosine law γ is the polar angle of the reflected ray, which is defined relative to the surface normal in the intersection point of ray and surface, and I_{max} the intensity of rays in direction of the surface normal, which can be shown to equal the incident ray intensity I_{inc} divided by π. For Lambertian reflection, the intensity distribution with regard to the azimuth angle is homogeneous, or with other words, for one fix polar angle, the intensity does not vary for different azimuth angles.

$$I(\gamma) = \cos(\gamma)I_{max} = \cos(\gamma)\frac{I_{inc}}{\pi} \qquad (4.6)$$

In practice, the reflection characteristics of opaque surfaces are commonly approximated as a superposition of specular and ideal diffuse reflection with a defined specular share. Noteworthy, this represents a drastic simplification. Its validity must be assessed on a case to case basis.

4.2. Monte Carlo ray tracing

Monte Carlo ray tracing is a collective term for Monte Carlo integration techniques for radiation transport problems. The origins of Monte Carlo ray tracing go back to lighting problems in computer graphics. First publications on Monte Carlo ray tracing go back to the sixties of the last century, see for instance [112]. From a very general perspective, Monte Carlo ray tracing techniques are implementations of the geometric optics simplification introduced briefly above. Basically, rays, generated in a source, are traced through a simulation domain comprising one or multiple objects that interact with the ray. On their way through the simulation domain the ray-object interactions are modeled according to the assumed physical models. Typically, the modelled interaction comprises interaction at phase boundaries, namely refraction, reflection and absorption, and interaction in volumes, namely absorption and scattering. For an illustration of a general ray tracing procedure see figure 4.2.
Depending on the level of detail of the interaction models implemented
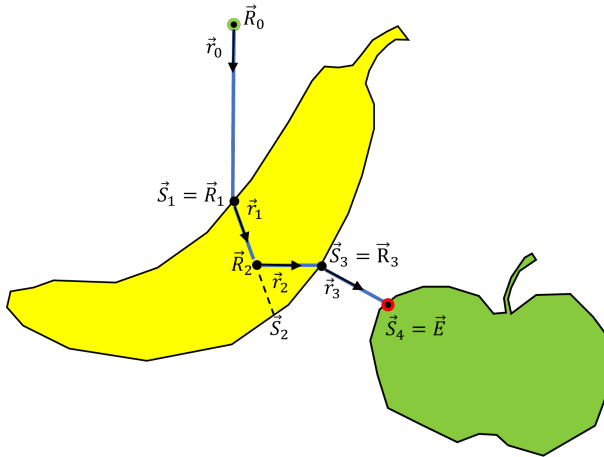
Figure 4.2.: Graphical representation of the ray tracing procedure implemented in this work in an exemplary simulation domain comprising a translucent banana and an opaque apple. The initial ray is generated in a 'light source' (point highlighted in green) and gets assigned an initial ray foot point $\vec{R}_0$ and an initial ray direction vector $\vec{r}_0$. The ray is then traced in its initial direction until it hits an object comprised in the simulation domain. In the ray object intersection $\vec{S}_1$ the ray object interaction is modelled. In the exemplary presentation the ray is refracted and enters the translucent banana volume and gets assigned a new ray foot point $\vec{R}_1$ and a new ray direction vector $\vec{r}_1$. The ray is then traced through the banana volume. On its way through the banana the physical interaction, absorption and/or scattering, is modelled according to the underlying absorption/scattering models. In the exemplary case, the ray is scattered in $\vec{R}_2$ and gets assigned a new ray foot point and a new ray direction vector $\vec{r}_2$. This procedure is repeated until the ray either misses any object in the simulation domain or is absorbed. In the exemplary presentation the ray leaves the translucent banana in $\vec{S}_3$ and gets finally absorbed on the surface of the opaque apple, the ray end point $\vec{E}$ (point highlighted in red).

and depending on the ray tracing technique applied, ray tracing delivers photorealistic image renderings, or in the case of an engineering problem, realistic approximations to the solution of the radiation transport problem to be solved. However, ray tracing techniques are computationally rather costly techniques. In order to map the lighting situation/the radiation transport problem properly, not one but a 'large' number of rays must be traced through the simulation domain over various interactions. The precise number of rays needed depends on the individual case setup and target metric and must be determined on a case to case basis in ray studies. For examples of such ray studies, refer to chapters 6, 7, and 8.

4.3. Implementation

In computer graphics applications of ray tracing the direction of ray tracing typically goes from the view point (eye) into the simulation domain. This facilitates the efficient solution of the rendering equation or efficient generation of images, respectively. The Monte Carlo ray tracing implementation developed for the present work of course does not aim for the efficient generation of images. The aim is to map radiation transport from the light source(s) into the simulation domain with a special focus on absorption phenomena. The question of interest in almost all applications of ray tracing in the present work is: Where in the simulation domain photons are 'deposited' or absorbed? Therefore, the ray tracing direction in the implementation of the present work is the from a physicist's point of view more intuitive direction from the light source(s) into the simulation domain.

4.3.1. General procedure

The general procedure realized with the implementation is graphically summarized in figure 4.2 and depicted in more detail in the flow chart in figure 4.3. The initial step of each ray tracing iteration is the generation of a ray with a pseudo-random location on the light source surface and a pseudo random direction. Thereby, the pseudo-random location and direction are chosen in a way that a large number of rays generated from the light source surface precisely map the assumed shape and emission characteristics of the light source. Subsequently, the closest intersection of the ray with the objects in the simulation domain is determined. Since the refractive index is assumed to be constant in all objects/the environment around the objects, this intersection search is a 'simple' geometric problem equal to the search of an intersection of a straight line with the surfaces of the objects in the simulation domain (compare section 4.1.1). With the closest intersection of the ray found, first, the ray volume interaction on the newly defined ray path segment is modelled. This modelling checks if an absorption or scattering event occurred on the ray path segment, and, if yes, where on the ray path segment it occurred. These two decisions are derived in a way that a large number of rays passing through the mapped volume precisely map the assumed ray attenuation model. With the determined position of the interaction, the type of interaction, absorption or scattering, is determined. If absorption occurred,
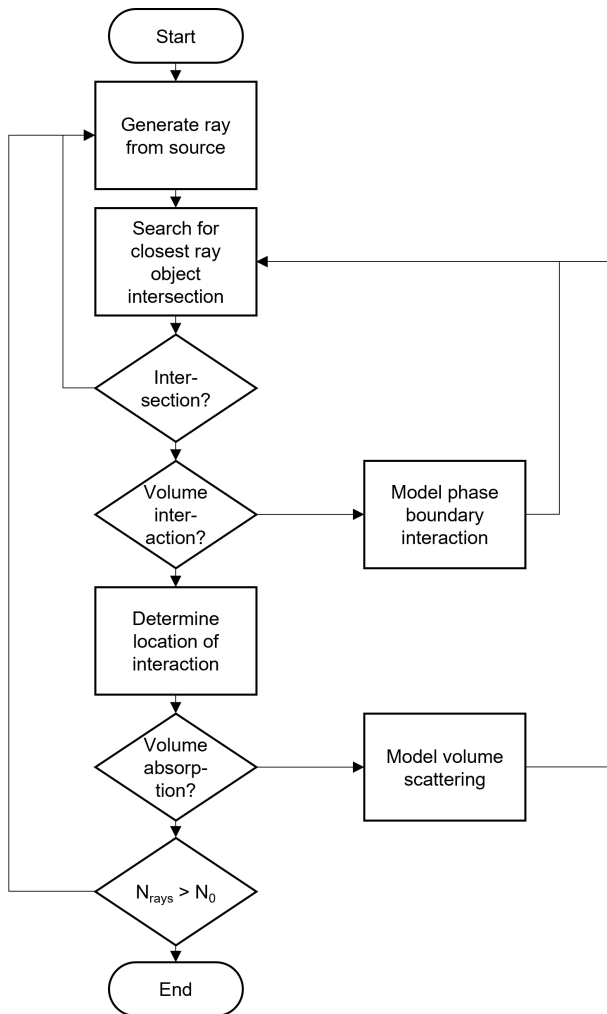
Figure 4.3.: Flow chart of the implemented Monte Carlo ray tracing procedure mapping radiation transport from the radiation source(s) into the simulation domain by tracing a number of N_0 rays through the simulation domain. The procedure comprises ray generation in the source, search for ray object intersections, modelling of volume absorption and scattering, and modelling of phase boundary interactions. Flow chart derived in accordance to DIN66001 [113]. Decision diamonds are 'Yes' in vertical direction and 'No' in horizontal direction.

the ray iteration is stopped and a new ray iteration is started in the light source. If instead scattering occurred, a new ray is derived that has its foot point in the derived scattering position on the ray path segment and a new, pseudo-random direction. Thereby, the pseudo-random scattering direction is chosen in a way that a large number of rays scattered in the same scattering centre precisely map the assumed scattering characteristics. If no volume interaction at all occurs, the interaction of the ray in the phase boundary is modelled according to the phase boundary type, either phase boundaries between two translucent objects or phase boundaries between a transparent and an opaque object, and according to the assumed interaction models. If the phase boundary interaction results in an absorption event, the ray iteration is stopped and a new ray iteration is started in the light source. In case of refraction or reflection, a new pseudo-random ray direction vector is assigned to a new ray with its foot point on the phase boundary intersection. Thereby, again, the pseudo-random direction is derived in a way, that a large number of rays interacting on the phase boundary map the assumed reflection character-istics (or refraction characteristics, respectively). From this point onward the procedure is repeated until either the ray is absorbed, the ray misses any of the objects in the simulation domain, or a maximum number of ray iterations is achieved. The last of the named interrupt criteria is necessary to avoid 'lock-in' situations in which rays are caught in infinite reflection scenarios, for instance, in opposite mirrors or internal total reflection scenarios in non absorbing/scattering objects. Such 'lock-ins' would entail an infinite run time. A complete ray tracing simulation with the implementation developed in the present work traces a predefined number of rays and primarily returns the derived ray paths. Additionally, during the solution process the ray end points of absorbed rays together with the properties of the absorbed rays (wave-length and number of absorbed photons/quantity of absorbed energy) are saved. The latter facilitates the evaluation with respect to the local volumetric rate of photon absorption. Noteworthy, the implementation also allows to chose the option to not save any ray paths which reduces the main memory occupancy during the solution process. In many cases this is recommendable since the individual ray paths are of secondary/no interest.

4.3.2. Interaction models

Objects in the simulation domain in ray tracing implementation in the present work can be assigned two interaction models. One interaction model repre-

sents an opaque object with a reflecting surface with a defined reflectivity. Of course the reflectivity can also equal zero which represents a perfect black absorber. Applications of such black objects may be probing surfaces in the simulation domain probing a radiation flux in a certain position/orientation etc., see for instance section 4.3.6. The reflection characteristics can be chosen to be ideally specular, ideally diffuse or a superposition of both with a defined specular share, detail see section 4.1.2. The second interaction model represents a translucent object with a defined refractive index and absorption and scattering coefficient. Ray attenuation in the volume is modelled with a Lambert Beer type approach. Scattering is assumed to be isotropic, for details see section 4.1.2. Scattering and/or absorption coefficients can be set to zero in order to model perfectly transparent objects. Interactions at phase boundaries between two translucent objects or between translucent objects and the environment are modelled according to Snell's law and Fresnel equations, details see section 4.1.1. For the evaluation of the Fresnel equations, light is assumed to be naturally polarized. The environment in the simulation domain is assumed to be homogeneous with respect to its user-defined refractive index and assumed to be non-scattering and non-absorbing.

4.3.3. Light source models

Light sources in the ray tracing implementation in the present work can be mapped as surfaces that either emit ideally diffuse light (Lambertian emission characteristics) or collimated light with a preferential direction and a defined divergence angle. One simulation case can comprise an arbitrary number of light sources of different shape and with different emission characteristics. Each light source will generate the same number of rays during the simulation. The total emission power of the light sources, however, can be assigned individually.

4.3.4. Implemented acceleration techniques

As mentioned, Monte Carlo ray tracing methods are a computationally rather costly methods. Monte Carlo ray tracing implementations, therefore, heavily depend on acceleration techniques that speed up the solution process.

4.3.4.1. Bounding volume acceleration

The run time determining step in any Monte Carlo ray tracing implementation is the search for ray object surface intersections. Acceleration techniques for this step in particular are, in consequence, mandatory.
In the Monte Carlo ray tracing implementation in the present work, the surface of objects is described with discrete surface elements. In principle ray object intersections can be found by testing every surface element of every object comprised in the simulation domain for a ray intersection, see figure 4.4, left, for illustration. There is no mistaking that this approach is computationally extremely costly, especially for complex simulation domains with many objects and complex shapes. More precisely, the computational effort for this direct search approach is proportional to the number of surface elements in the simulation domain, see dashed line figure 4.5. The implementation in the present work, therefore, comprises a bounding volume acceleration approach that reduces the number of ray surface element intersection tests that are necessary to find an intersection. The idea behind bounding volume acceleration is to run the intersection search on a sorted data set. The surface elements are thereby sorted into a defined set of bounding volumes subdividing the space in the simulation domain. The search strategy in ray object intersection search accelerated with bounding volumes does now no longer test all surface elements for a ray intersection, but only those who are in a bounding volume that has a ray intersection. This precondition of a ray intersection of the bounding volume is the necessary precondition that a surface element in the bounding volume may have a ray intersection. In order that a bounding volume search strategy represents an acceleration technique, the surface of the bounding volumes must be easy to test for ray intersections. More precisely, the intersection test conducted with the bounding volume surface must be computationally less expensive than testing all surface elements in the bounding volume for an intersection. The bounding volume shape must, therefore, be primitive.
In addition to the sorting of surface elements into bounding volumes, bounding volumes can be nested in hierarchies, so bounding volumes can be built around bounding volumes in order to reduce the necessary number of intersection tests of rays with bounding volumes. For illustration of a hierarchical bounding volume search strategy with two hierarchy levels, see figure 4.4, right.
The implementation in the present work comprises a bounding volume search
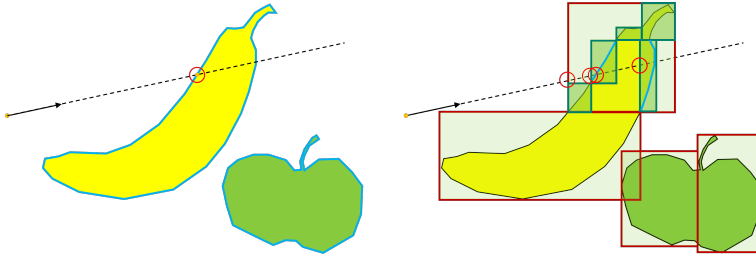
Figure 4.4.: Representation of the implemented strategy of bounding volume acceleration in ray object intersection search. In the left scenario all surface elements of banana and apple are tested against a ray intersection. In contrast in the right scenario, bounding volumes are employed to reduce the number of necessary tests to find the closest intersection. The bounding volumes are organised in two levels (red and green bounding volumes). All surface elements are sorted into the second level bounding volumes (depicted in green, for the sake of clarity not all second level bounding volumes are depicted). The surface elements in each second level bounding volume are only tested, if there is a ray intersection with the surface of the second level bounding volume that surrounds them. The second level bounding volumes are only considered in the search if the first level bounding volume surrounding them has a ray intersection. Consequently, less tests for ray surface element tests are necessary in order to find the ray object intersection (compare blue fractions of the banana and apple surface in left and right presentation).

strategy with bounding volumes nested in two hierarchies. Bounding volumes are simple boxes defined around the sorted group of surface elements or the sorted group of higher level bounding volumes, respectively. The number of bounding volumes in one hierarchy level is set depending on the number of surface elements, see equation (4.7). Under the assumption that every surface element has the same likelihood for an intersection, the number of bounding volumes per level calculated with equation (4.7) represents an optimum with a minimum number of ray surface element intersection tests expected.

$$N_{bV} = \left(\frac{N_{elements}}{4} \right)^{\frac{1}{3}} \tag{4.7}$$

Sorting of surface elements into bounding volumes is executed previously to the ray tracing procedure. Briefly summarizing the search strategy during the solution process comprises the following three steps: (1) search for intersections of the current ray with first level bounding volumes (depicted in red in figure 4.4, right). (2) If there are intersections of the ray with one of the first level bounding volumes, continue the search in the second step with a search for ray intersections with second level bounding volumes (depicted in green
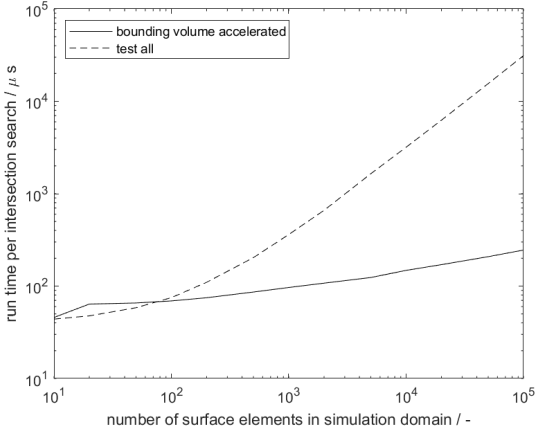
Figure 4.5.: Average run time per intersection search in an exemplary simulation case as function of the number of surface elements in the simulation domain. The dashed line represents data derived with an intersection search strategy testing all surface elements. The solid line represents data derived from a bounding volume accelerated search strategy with rectangular bounding volumes nested in two hierarchies. Note the logarithmic scale of the two axes. The computation was executed with the single core solver on a standard desktop computer (Intel®Core™i5-7500 CPU). Values represent an average of roughly 6000 function calls. For details on the two named search strategies, compare figure 4.4.

in figure 4.4, right). (3) Only if there are intersections with a second level bounding volume, test the surface elements sorted into these second level bounding volumes for a ray intersection (depicted in light blue in figure 4.4, right). The illustration in figure 4.4, thereby, clearly highlights that through the application of bounding volumes the fraction of surface elements tested for a ray intersection is drastically reduced compared to a 'test all' search strategy.

A simple performance test comparing run times needed to find an intersection with a 'test all' search strategy against the implemented bounding volume search strategy clearly lines out the effect of bounding volume acceleration, see figure 4.5. Only for simulation domains with less than roughly one hundred surface elements, the bounding volume strategy represents a slight disadvantage compared to the 'test all' strategy. This seeming 'disadvantage' of bounding volume accelerated search, occurring in simulation domains with a very low number of surface elements, is induced by a computational over-

head resulting from the need to go through the bounding volume hierarchy. For realistic numbers of surface elements in the simulation domain (several thousands to tens of thousands) the bounding volume accelerated search strategy, however, represents a clear advantage being computationally more efficient by orders of magnitude. Noteworthy, to highlight the importance of this acceleration, the intersection search is conducted for each simulated ray and especially in each ray iteration step, so for typical simulation cases hundreds of millions of times. Depending on the simulation domain and chosen interaction models, the share of the overall run time induced by the intersection search typically lies between 30 % and 90 %. A reduction of the average search time for one ray object intersection is, therefore, crucial.

4.3.4.2. Geometry projection

In addition to bounding volume acceleration, it is recommendable to reduce the complexity of the geometry description as far as possible, or with other words it is recommendable to reduce the number of surface elements as far as possible. Since the geometries mapped in simulations in the present work are channel-like geometries or extrudeable geometries, respectively, the geometry description in the ray tracing implementation is reduced to a two dimensional projection of the geometry. For an illustration, see figure 4.6. The surface of all objects are consequently closed lines and comprise significantly less surface elements (line segments) than a full three dimensional description (in which the geometry would be built from plane segments). Additionally, with this geometry projection implemented, the ray object intersection search can be conducted with projections of rays into the geometry description plane rather than in three dimensions. The implemented simplification of the geometry description, therefore, does not only simplify the object surface description but also reduces the dimension of the linear equation system that is solved repeatedly in ray intersection tests from three to two which represents another run time advantage. Noteworthy, this does not affect the accuracy of the ray tracing procedure. Rays are still traced and radiation transport is still mapped in three dimensions. The only change is that geometry description and the intersection search are conducted in a two dimensional projection of the three dimensional, channel-like geometry.
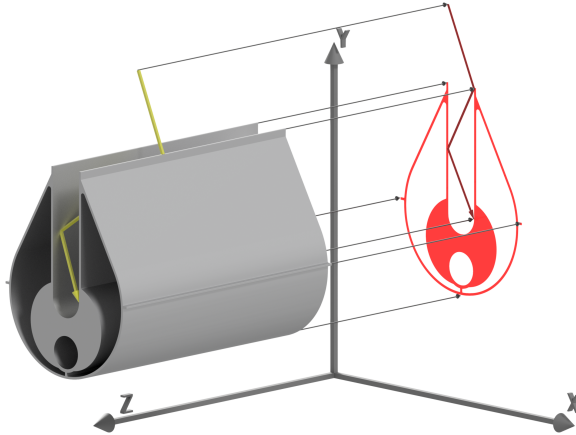
Figure 4.6.: Illustration of the projection (red) of channel-like geometries (grey body) and traced rays (yellow ray) into a plane in the developed Monte Carlo ray tracing environment phoRex. The projection is in direction of the z-axis and into the x-y- plane.

4.3.4.3. Parallel computing

Ray tracing is especially easy to parallelize because every ray is independent of all other rays. So basically, copying the ray tracing case and running it with a fraction of all rays on multiple workers in parallel is a simple but valid strategy to access the result of a simulation comprising a large number of rays in an acceptable time. The overall solution is derived via simple superposition of solutions of the individual workers.

To exploit the benefits of modern multi-core computing architectures, the ray tracing implementation of the present work can be run on multiple workers in parallel with a built-in parallel solver handling all tasks of copying, transferring to the workers, retransferring to the host, and recombining automatically.

Theoretically, the run time of a simulation case should be inversely proportional to the number of workers employed in the solution process. A double-logarithmic plot of the simulation run time over the number of workers should deliver a straight line with a slope equal to minus one. In reality copying, transferring to the workers, retransferring, and recombining the simulation cases induces a computational overhead. Consequently, depend-
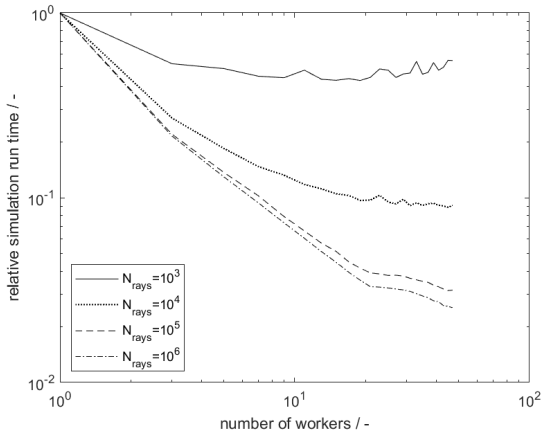
Figure 4.7.: Relative simulation run times of an exemplary simulation as function of the number of workers employed in the ray tracing step for simulations with different numbers of rays to simulate. The computation was executed on a work station equipped with an AMD Ryzen™ Threatripper™ 3960X CPU using between one and all 48 available workers for the solution process.

ing on the number of rays in a simulation case, there might be a domain in which rather the parallel overhead than the number of rays dominates the run time. The latter would be apparent in a slope deviating from minus one in a double-logarithmic plot of the simulation run time over the number of workers. This undesired 'parallel overhead effect' can be observed in the Monte Carlo ray tracing implementation of the present work, see figure 4.7. However, it only occurs for simulation cases with a small number of rays to simulate (approx. $<10^5$ rays), which is seldomly reasonable. Typically, the number of rays in a conducted simulation lies around one million rays.

4.3.4.4. Retracing

In practise polychromatic light may be especially hard to map in ray tracing simulations. This is, if optical properties show a distinct dispersion, or with other words, if for instance the refractive index or the scattering coefficient show a strong dependency on the wavelength. In these cases, for each wavelength to be mapped, an individual ray tracing case must be set up and

conducted. There is one exception that holds if only the optical properties that shape the probability of absorption, absorption coefficient and reflectivity, but not the optical properties that shape the direction of ray propagation, refractive index, specular share and scattering coefficient, are dependent on the wavelength. In these cases it is possible to derive an arbitrary number of ray tracing results with different values of absorption coefficient and reflectivity from one previously ran ray tracing case conducted under the assumption of no absorption. The strategy in these cases is to retrace the existing ray paths and only calculate the probability of absorption on each ray path segment. The computationally costly ray object intersection search can, thereby, be circumvented. At the same time, the obtained converged simulation results are the same. The ray tracing implementation in the present work comprises such a 'retracing algorithm'. It's applicability should be assessed on a case to case basis depending on the materials' optical properties and optical bands mapped in the simulations. For an example of such an assessment, see for instance chapter 8.

4.3.5. Code structure

The Monte Carlo ray tracing implementation in the present work comprises multiple thousand lines of code. It is written object-oriented in the programming language MATLAB® and summarized in a MATLAB® toolbox named phoRex (photoreactor engineering toolbox). The following is a brief overview of the code structure and the basic functionalities of the toolbox. The overview given intends to give a brief introduction into the code and its usage. Any details can be found in the extensively commented source code and examples published via KITopenData [114]. Figure 4.8 gives an overview of the most important class definitions, including a list of the most important properties and methods, and the dependencies between the class definitions via inheritance and nesting.

The recommended workflow in an optical simulation using the Monte Carlo ray tracing implementation of the present work comprises three steps, the simulation preparation (preprocessing), the solution process (processing), and the result analysis (postprocessing).

The preprocessing step is script-based and aims to provide all necessary information for the solution process in a structured, and especially reproducible way. There is no graphical user interface. At the end of the preprocessing step an instance of the class CASE is built. This instance of CASE comprises
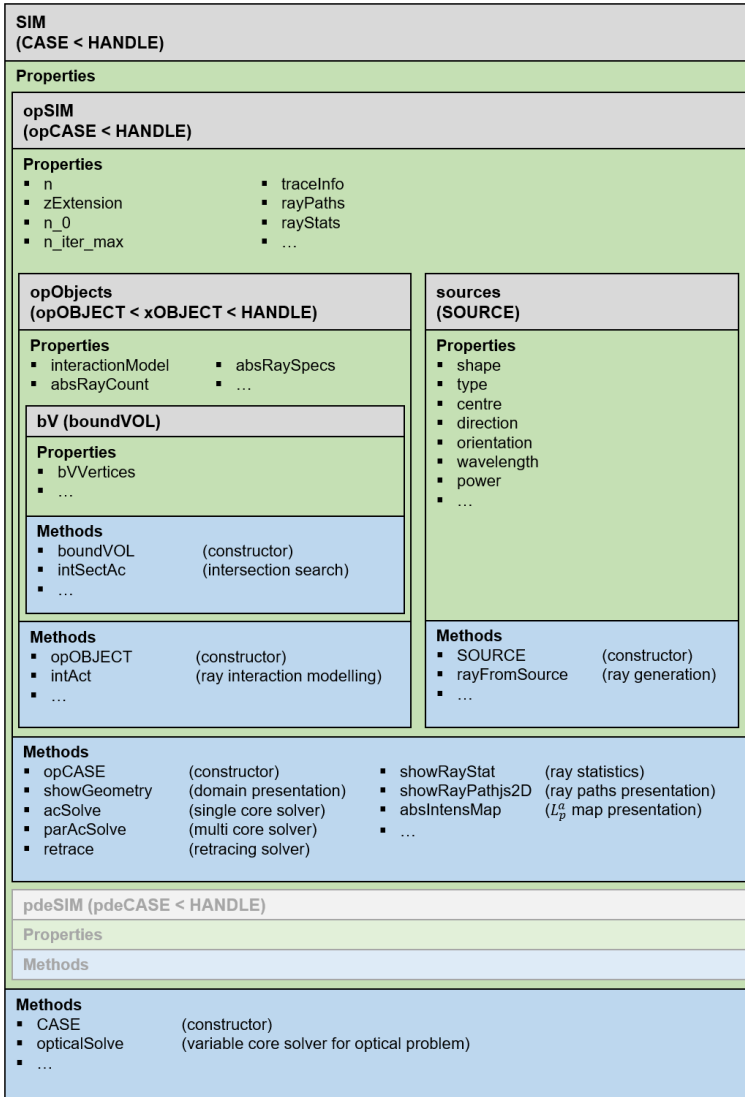
Figure 4.8.: Graphical presentation of the code structure of the developed Monte Carlo ray tracing environment phoRex. Properties of the comprised classes are placed in green boxes, the corresponding methods in blue boxes. Dependencies between classes via inheritance are depicted via the < symbol, dependencies via properties via the nested structure.

a property `opSIM`, which is an instance of the class `opCASE`. The class definition of `opCASE` defines all properties and methods that are needed for the preparation, execution, and evaluation of a Monte Carlo ray tracing simulation. On a side note, the class definition of `CASE` also provides an interface to the MATLAB® partial differential equation toolbox (via its property `pdeSIM`, which is an instance of the class `pdeCASE`). This interface can be used to run coupled radiation and heat transport simulations. However, this feature is not employed in the present work and not described in any detail in this place.

The most important properties of the class `opCASE` describe the simulation domain, the light sources, the solver parameters, and the solution structures. More precisely they are: (1a) `opObjects`, an array of instances of the class `opOBJECT` that together shape the simulation domain, (1b) `n` and `zExtension`, floating point numbers indicating the refractive index of the environment and the extension of the simulation domain in extrusion direction (details see section 4.3.4), (2) `sources`, an array of instances of the class `SOURCE` that represent the light sources in the simulation domain, (3) `n_0` and `n_iter_max`, integers indicating the number of rays to simulate and the maximum number of iterations per rays (meaning see section 4.3), and lastly (4) `traceInfo`, `rayPaths`, and `rayStats`, solution structures and arrays containing preliminary results necessary for retracing (details see section 4.3.4), the derived ray paths, and ray counts representing a rough ray statistic (simulated, absorbed, missed, and interrupted rays).

The most important methods of the class `opCASE` guide through the steps of preprocessing, processing, and postprocessing. All preprocessing steps, including the built up of the simulation domain and definition of light sources is done by calling the constructor `opCASE`. Input, encoding the simulation setup, is expected via a set of name value pairs. The solution process can be started by calling `acSolve` (single core solver) or `parAcSolve` (multi core solver basically calling `acSolve` on multiple cores and managing the superposition of the single core solutions). The default in most work flows should be `parAcSolve`. Additional solver parameters, like for instance the number of workers to be used during processing or the solver mode (ray tracing or retracing, details see section 4.3.4), can be handed over via name value pairs. The class definition of `opCASE` also comprises a large set of methods for postprocessing. Calling `showGeometry` will, for instance, open a report window illustrating the simulation domain with all objects and light sources in a two dimensional projection. `showRayPaths2D` and `showRayPaths3D` will generate ray path diagrams in a two dimensional projection and in three dimensions respectively. `showRayStat` will open a report window presenting

the ray statistics meaning a presentation of the number of rays that were absorbed (including by which object they are absorbed), how many rays finally missed any object, how many ray iterations were interrupted due to the interrupt criterion, and lastly how many rays have been simulated overall. Noteworthy, partial solutions that adhere to the objects in the simulation domain are properties of the instances of `opOBJECT` stored in the `opCASE` property `opObjects`.

Properties of `opOBJECT` comprise, for instance, a count indicating the number of rays absorbed by the object (`absRayCount`), which is useful for the calculation of ray statistics. Further, the properties `absRayEnds` and `absRaySpecs` comprise information of the location of rays absorbed by the object and the according ray specifications (wavelength, transported energy). Besides the properties containing solution related information, properties of `opOBJECT` comprise information on the geometry and the interaction model (with assigned radiation transport properties). The most important property of `opOBJECT` is the property `bV`, which is an instance of the class `boundVOL`, a class definition that represents an implementation of a bounding volume accelerated ray object intersection search strategy, details see section 4.3.4.

The most important method of `opOBJECT` is `intAct`, a method that is called during the solution process and models the interaction based on the interaction model chosen for the object, details see section 4.3.2. Intersection search during the solution process is realized via calling the `boundVOL` method `intSectAc`.

4.3.6. Validation against literature models

The Monte Carlo ray tracing implementation was validated against literature models for typical radiation transport problems. Those comprise refraction on a phase boundary, specular reflection on a phase boundary, partial absorption in volumes, reflection on a window, and diffuse reflection of an optically thick turbid layer under diffuse irradiation.

4.3.6.1. Refraction on phase boundaries

Refraction on a phase boundary can be mapped with Snell's law, equation (4.1). In order to test the simulation environment against Snell's law, a set of one hundred rays, with incident angles between 0 and $\pi/4$, were sent from a
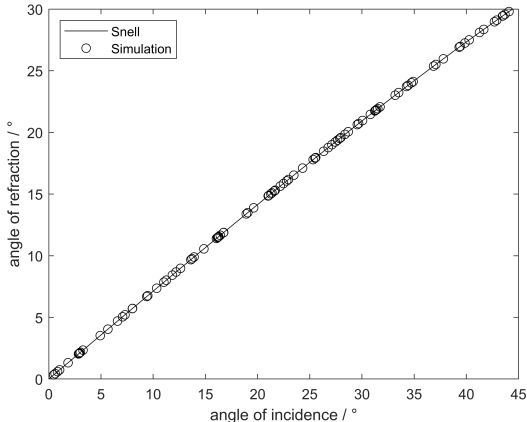
Figure 4.9.: Validation of the Monte Carlo ray tracing implementation against Snell's law (refraction) via a comparison of refraction angles extracted from a simulation of one hundred rays sent onto a phase boundary with a refractive index change from $n_0 = 1$ to $n_1 = 1.4$ (empty circles) with values derived via Snell's law (solid line).

point light source onto a phase boundary with a refractive index change from $n_0 = 1$ to $n_1 = 1.4$. The simulated angle of refraction was determined from the angle between the phase boundary normal vector and the ray direction vector after the refraction event at the phase boundary. The analysis shows an excellent agreement between Snell's law and the refraction angles in the Monte Carlo ray tracing simulation, figure 4.9.

4.3.6.2. Reflection on phase boundaries

Reflection of natural light on phase boundaries as a function of the incidence angle can be mapped with the Fresnel equations, equations (4.3). Validation of the Monte Carlo ray tracing implementation against the Fresnel equations was realized via simulations of a collimated beam sent onto a phase boundary with a refractive index change from $n_0 = 1$ to $n_1 = 1.4$. The reflectivity was derived from absorption ray counts of an ideally black probe in the reflection ray path related to the number of simulated rays (= the number of rays sent onto the phase boundary). The analysis shows an excellent agreement of
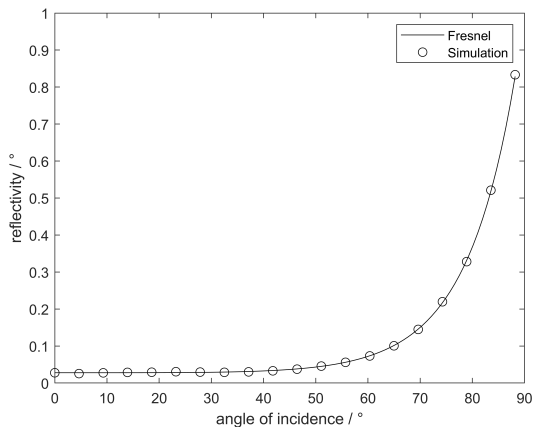
Figure 4.10.: Validation of the Monte Carlo ray tracing implementation against the Fresnel equations (partial reflection on phase boundaries) via simulations of a collimated beam sent onto a phase boundary with a refractive index change from $n_0 = 1$ to $n_1 = 1.4$. The reflectivity was derived from absorption ray counts of a black probe in the reflection ray path related to the number of simulated rays. Empty circles represent values from the simulation, values derived via the Fresnel equations are depicted with a solid line.

simulated reflectivity and values derived via the Fresnel equations, figure 4.10.

4.3.6.3. Absorption in volumes

Absorption in volumes can be mapped with a Lambert Beer type approach, equation (4.4). The Monte Carlo ray tracing implementation was tested against Lambert Beer's law via simulations of an absorbing layer with an absorption coefficient of 10 m^{-1} and varying thickness between 1 cm and 1 m. The transmission through the layer was detected in the simulations with a black probe on the unilluminated side of the absorbing layer. The light source was a collimated light source shining its light perpendicular onto the absorbing layer. The optical path length, therefore, equalled the geometric thickness of the layer. The refractive index of the layer was set to equal the refractive index of the environment ($n_1 = 1$) in order to avoid an influence of partial reflection on the layer surface onto the detected transmission. The
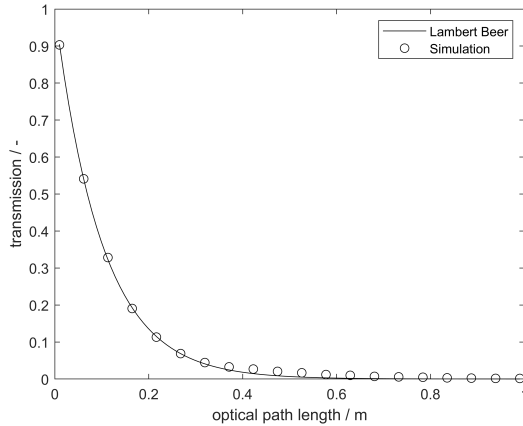
Figure 4.11.: Validation of the Monte Carlo ray tracing implementation against Lambert Beer's law (absorption in volumes) via comparison of simulated values of the transmission of an absorbing layer with an absorption coefficient of $10 \ m^{-1}$ and varying thickness with transmission values derived via Lambert Beer's law. Empty circles represent values from the simulation, values derived via the Lambert Beer's law are depicted with a solid line.

analysis shows an excellent agreement between simulated data and data derived from Lambert Beer's law, figure 4.11.

4.3.6.4. Reflection on windows

The reflectivity of a window (two consecutive phase boundaries) under illumination with natural light can be derived via the Fresnel equations and some additional considerations regarding the occurring window internal reflections, see for instance [115], equation (4.8). $R(\alpha)$, thereby, stands for the incidence angle-dependent reflectivity of the single phase boundary derived via the Fresnel equations, see equation (4.3).

$$R_{window} = \frac{2R(\alpha)}{1 + R(\alpha)} \tag{4.8}$$

The Monte Carlo ray tracing implementation was validated against this simple model of the reflectivity of a window via simulations of a transparent
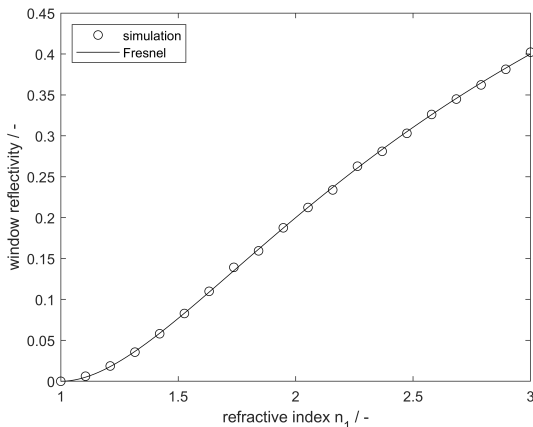
Figure 4.12.: Validation of the Monte Carlo ray tracing implementation against a model describing the reflectivity of a window (two consecutive phase boundaries) via simulation of the reflectivity of a transparent layer with a refractive index between $n_1 = 1$ and $n_1 = 3$ under perpendicular irradiation with a collimated beam and comparison of the derived values with the model equation, see equation 4.8. Empty circles represent values from the simulation. Values derived via equation 4.8 are depicted as solid line.

layer with a refractive index ranging from $n_1 = 1$ to $n_1 = 3$ under perpendicular illumination with a collimated beam. The reflectivity was derived from absorption ray counts of a black probe in the reflection ray path related to the number of simulated rays. The analysis of the obtained data reveals an excellent agreement between simulated values and the values obtained via equation (4.8), see figure 4.12.

4.3.6.5. Albedo of turbid layers

The albedo (= diffuse reflectivity) of an absorbing and scattering (= turbid) layer under diffuse illumination from one side can be mapped with the Kubelka Munk model [116, 117]. The model basically describes propagation of two diffuse light fluxes, one traveling from the illuminated towards to unilluminated side and the other vice versa. The model comprises two simple differential equations, one for each diffuse light flux, mapping the influence of absorption and radiation exchange between the two mapped fluxes. Scattering is

assumed to be isotropic, as is the case in the Monte Carlo ray tracing implementation. For an optically thick layer, meaning that there is no transmission, the solution of the Kubelka Munk differential equations deliver equation (4.9) describing the albedo of the layer.

$$R_{KM,layer} = 1 + 2\frac{\sigma_a}{\sigma_s} - 2\sqrt{\left(\frac{\sigma_a}{\sigma_s}\right)^2 + \frac{\sigma_a}{\sigma_s}} \qquad (4.9)$$

The Monte Carlo ray tracing implementation was validated against the Kubelka Munk model by simulation of an optically thick absorbing and scattering layer with an absorption coefficient of 5 m^{-1} and varying ratios between absorption and scattering coefficient under diffuse illumination. The refractive index of the layer was set to equal the refractive index of the environment ($n_1 = 1$) to avoid influences of partial reflection phenomena on the layer surface. The albedo was derived from absorbed ray counts of a black probe counting the number of diffusely reflected rays and relating to the number of simulated rays. The analysis reveals an excellent agreement between simulated data and values from the Kubelka Munk model, see figure 4.13.

4.4. Interim summary

The developed and successfully implemented Monte Carlo Ray tracing simulation environment allows at a reasonable computational cost the simulation of radiation transport in three dimensional simulation domains comprising multiple components with complex shapes and different optical interaction models. The two predefined interaction models foresee opaque objects with a defined reflectivity and reflection characteristic on their surface and translucent objects exhibiting refraction and partial reflection on their surface according to Snell's law and the Fresnel equations and absorption and scattering in their volume according to a Lambert Beer's law and an isotropic scattering model. Limitations of the implementation are the solely applicability to extruded or channel-like geometries and the lacking capability of modelling of objects with non-homogeneous optical transport properties.

Altogether the presented validation cases highlight the reliability of the implementation. The most relevant interactions between propagating light and
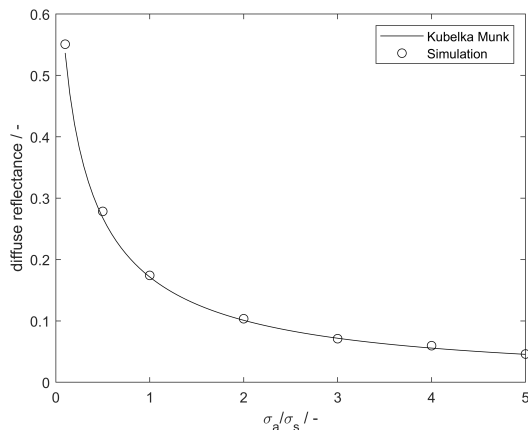
Figure 4.13.: Validation of the Monte Carlo ray tracing implementation against the Kubelka Munk model (radiation transport in absorbing and scattering layers under diffuse illumination from one side) via comparison of simulated values of the albedo of an optically thick layer with an absorption coefficient of 5 m^{-1} and various ratios between absorption and scattering coefficient with values of the albedo derived via the Kubelka Munk model. Empty circles represent values from the simulation. Values derived via the Kubelka Munk model are depicted as solid line.

objects in the simulation domain are precisely mapped. This includes refraction and reflection on phase boundaries between transparent/translucent objects, reflection and absorption on phase boundaries between translucent/transparent and opaque objects, and absorption and isotropic scattering in volumes. The simulation environment can consequently be employed for a broad variety of radiation transport problems encountered in photochemical engineering. This explicitly includes the envisioned tasks of the present work, data evaluation in complex optical measurements, and the design, assessment, detailed analysis, and optimization of photoreactors.

5. Experiment environment

The development of a low-cost, high efficiency photocatalytic processes demands for a reliable experimental environment providing the basis for reaction engineering examination of both photocatalysts and photoreactors.

Roughly, there are three core functionalities that a suitable environment for reaction engineering examinations of photocatalysts and photoreactors must have: (1) the environment must be able to provide a well-defined reactant feed for the employed photoreactors, (2) the environment must be able to provide either well-defined radiation in the photoreactor aperture or an electronic interface to drive light sources included in the photoreactor, and (3) the environment must provide suitable analytics to detect precisely the reactant/product concentrations in the reactor effluent.

Since detailed photocatalyst and/or photoreactor studies comprise large sets of experiments that may take long time to execute and a maximum reproducibility is hard to guarantee under under human operation in such time consuming studies, it is further desirable to realize a high degree of automation that allows to conduct automated experiments without user interaction. The latter entails that for the sake of security in automated experiments, the environment must include self-surveillance functionalities.

5.1. System design

The experiment environment developed, built, commissioned, and finally employed in the present work is a complex test rig designed for both gas phase and liquid phase photocatalytic experiments conducted under simulated solar irradiation or with reactor internal light sources providing narrow band light. The test rig is built from modules that aggregate related functionalities and facilitate the assembly/maintenance. For illustration, see a photograph of the test rig in figure 5.1. The integrated LabVIEW®-based measurement and control system allows both manual and fully automated operation. All

safety-relevant process parameters are supervised electronically and linked to a central safety shut down functionality. The latter allows long term experiments without user presence and even remote operation if conducted in accordance to current legal work safety regulations. A MATLAB®-based data handling tool provides an user-friendly interface to large data sets resulting from automated long-term experiments.

5.1.1. System description

5.1.1.1. Gas phase feed conditioning and analysis

The gas phase feed and analysis included in the test rig is built to be operated between ambient temperature and 200 °C and system pressures between ambient pressure and 3 MPa. It comprises a gas feed module handling five feed gases, namely argon, nitrogen, hydrogen, carbon dioxide and carbon monoxide, a saturator used to saturate the feed gas stream with vapours of liquids, a cold trap used to condense reactant and/or product vapour, a pressure regulating valve used to adjust the reactor pressure, a gas chromatograph used to detect reactant/product concentrations, and an exhaust system safely guiding the reactant/product gas mixture to the ventilation system. All tubing is made from stainless steel Swagelok® components and heated electrically from the saturator down stream to prevent any species to condense. The exhaust stream is not heated but can be flushed with pressurized air instead. The tubing setup allows convenient bypass of all major components, saturator, reactor, cold trap, and gas chromatograph. An overview over the gas feed and analysis system is given with the P&ID in figure 5.2.

The gas feed module (tagged with (1) in figure 5.1) receives gas from the house grid at a maximum pressure of 24 MPa, filters the incoming gas streams through sinter metal filtering elements (filter size 7 μm), and adjusts constant system feed pressures with back pressure regulators (range 0-3.5 MPa). There are two hydrogen feed pressure regulators, one for the gas chromatograph gas supply and one for the reactor feed supply. Argon is only fed to the gas chromatograph. The gas feed module further comprises four thermal mass flow controllers that dose the reactant gases (flow range 0-200 mL$_N$ min^{-1} for hydrogen and 0-50 mL$_N$ min^{-1} for nitrogen, carbon dioxide, and carbon monoxide), which are subsequently mixed in a manifold. Check valves after the mass flow controllers in each of the four gas feed lines prevent any gases to flow back into the house grid. A relief valve in the manifold adjusted
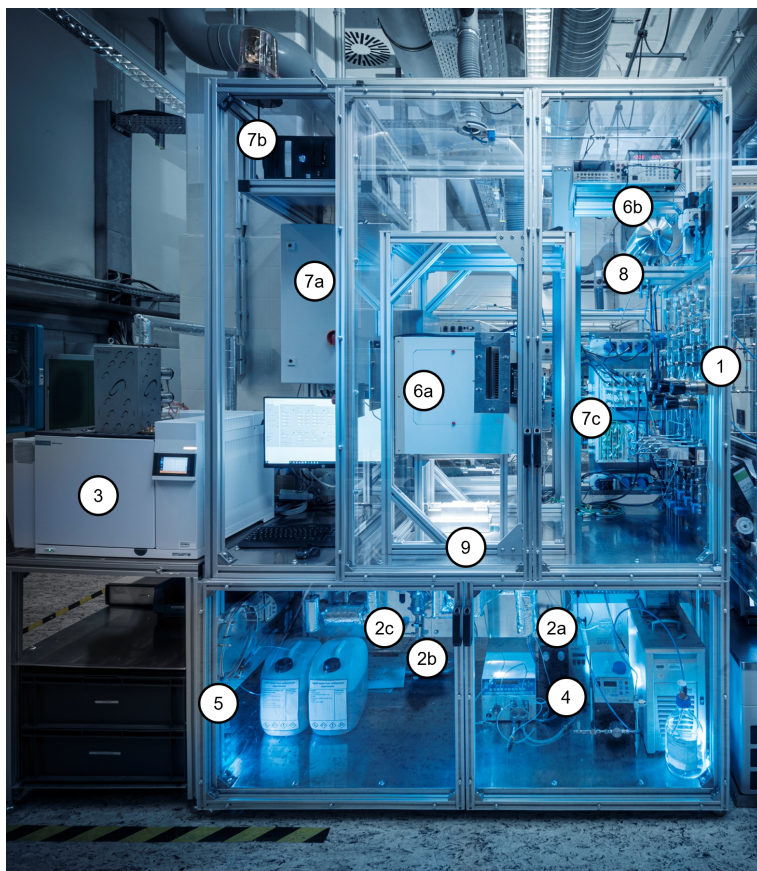
Figure 5.1.: Photograph of the developed, built, commissioned, and finally operational photoreactor test rig employed in the present work. The highlighted main modules and components are: (1) a gas feed module, (2) a gas phase process module with a saturator, a cold trap, and a pressure regulating valve, (3) a gas chromatograph for gas phase analysis, (4) a liquid feed module comprising two pumps and liquid storage vessels, (5) a UV Vis spectroscopy module with liquid flow cell, UV Vis light source, and spectrometer, (6a) a collimated class ABA solar simulator, (6b) a DC electric interface for power supply of photoreactor internal light sources with a high accuracy current metre, (7a) a switching cabinet with real time target, power electronics, and various digital interfaces, (7b) a host computer with LabVIEW®measurement and control system, (7c) an interface module for analogue sensor signals, and auxiliary power supply of components, (8) and a pressurized air module for pressurized air supply of components. The experiment space in which the photoreactor is placed is below the solar simulator in the target plane of the latter, see tag (9). Photo: Amadeus Bramsiepe, KIT.
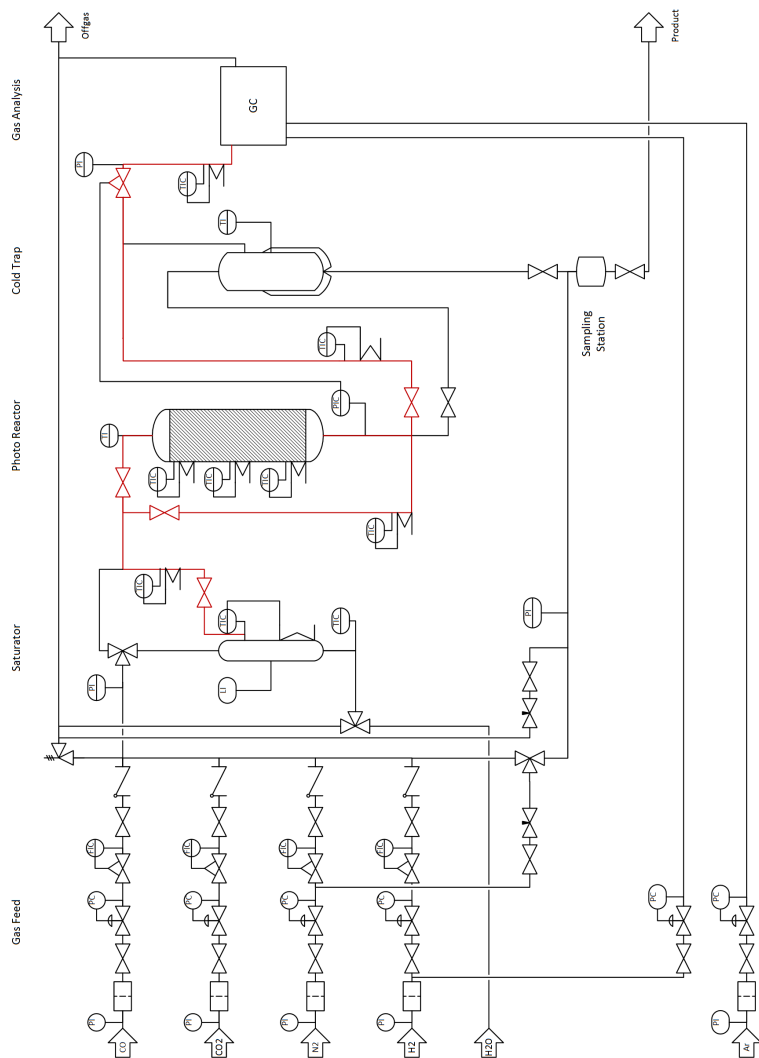
Figure 5.2.: P&ID of the gas phase side of the employed experiment environment. The environment comprises a gas feed system conditioning and dosing gases in to the test rig, a saturator used for dosing vapour, a cold trap condensing any reactant/product vapour, a pressure regulating valve, and a gas chromatograph. Red lines are lines that are heated electrically to prevent vapour condensation.

to open at 3 MPa ensures the test rig is never operated at pressures above the design pressure. A bypass of the nitrogen dosing mass flow controller equipped with a ball valve in series with a fine needle regulating valve allows to dose larger amounts of nitrogen into the tubing for flushing purposes (larger than the maximum 50 mL$_N$ min^{-1} from the mass flow controller). The same 'undefined' nitrogen feed can also be redirected with a three way valve in order to pressurize the flood gate below the cold trap prior to sampling. This feature allows liquid sampling without large pressure fluctuations in the system.

The saturator, the cold trap, and the pressure regulating valve are grouped on the process module in the lower segment of the test rig (for illustration see tag (2) in figure 5.1).

The saturator is built from Swagelok®components and is basically a liquid filled packed bed with a gas feed at the lower end. Gas bubbles meander through the fixed bed made from 2x2 mm glass Raschig rings and leave the saturator saturated with the liquid vapour at the upper end. The temperature of the saturator is measured in the gas phase just before the exit and in the liquid phase at the gas feed position at the bottom of the packed bed. The heating is realized with an electrical heating wrapped around the assembly. For cooling of the saturator, a liquid cooling coil is wound around the assembly. The PID temperature control loop controls the gas phase temperature.

The cold trap is similarly built from Swagelok®components and basically is a tube in tube annular gap design with a gas feed through the inner tube entering the annular gap at the lower end of the cold trap. The gas feed in the annular gap flows upwards and is cooled at the outer wall of the annular gap. Condensable species condense at the wall and accumulate in the annular gap while saturated permanent gases leave the cold trap at the top. Cooling of the assembly is realized with a 3D-printed cooler body with an internal channel structure that is clamped onto the tubing pieces. The cooling water supply is realized with a thermostat.

The pressure regulating valve is designed to be able to maintain pressures up to 3 MPa at flow rates as low as 50 mL$_N$ min^{-1} and ambient effluent pressure. At lower system pressures the flow rates that can be controlled are smaller respectively.

The gas chromatograph included in the test rig (for illustration see tag (3) in figure 5.1) is a customized system with an external heated valve box (maximum temperature 200 °C). It is designed to detect permanent gases (nitrogen, carbon dioxide, carbon monoxide, hydrogen, etc.), water vapour, light alcohols, and hydrocarbons. The gas chromatograph setup comprises two parallel

sample loops and corresponding column setups in one oven. The two sample loops are flushed consecutively with the gas sample. A stop flow valve in the gas chromatograph's feed line ensures ambient pressure in the sample loops before sampling even at increased sample gas flow rates. The latter ensures that the sample amount in the sample loops and, thereby, the calibration factors of the gas chromatograph are constant under all operating conditions. The first sample loop/column setup is designed to separate and detect water vapour, light alcohols, and hydrocarbons via a thermal conductivity detector, and a flame ionisation detector that are included in series at the column outlet. The detected species are separated on a Rt-Q-Bond column. The second sample loop/column setup first separates permanent gases from water, light alcohols and hydrocarbons on a HaysepQ column and subsequently separates the different permanent gases on a 5A mole sieve column. Detection in this column setup is realized with a thermal conductivity sensor mounted at the column outlet. For illustration of the gas chromatograph setup also see figure 5.3. The detection limit for carbonaceous burnable species and hydrogen lies around 10 ppm. The detection limit for other permanent gases and water lies around 100 ppm.

5.1.1.2. Liquid phase feed and analysis

The liquid phase feed and analysis is built to be operated at ambient temperature and only slightly increased pressure (ambient pressure at the outlet). It comprises a liquid feed module dosing liquids into the system (tagged with (4) in figure 5.1), and a UV Vis spectroscopy module for online analysis of the liquid system effluent (tagged with (5) in figure 5.1). Filters, valves, and piping adaptors are made from Swagelok®stainless steel components. The 1/8" tubing is made from PTFE . An overview of the liquid feed and analysis system is given with the P&ID in figure 5.4.

The liquid feed module comprises two storage tanks, one for the feed solution, and one for water employed for flushing purposes. Each storage tank is connected to one feed pump of which each is connected to the reactor feed line. The feed pump for water is a gear pump with a feed rate up to 500 mL min^{-1}. The feed pump for the feed solution is a precision tandem syringe pump with a maximum feed rate of 4 mL min^{-1}.

The UV Vis spectroscopy module comprises a flow cell allowing for online UV Vis spectroscopy of the reactor effluent. The flow cell is connected to a UV Vis light source and a UV Vis spectrometer via two short optical fibres.
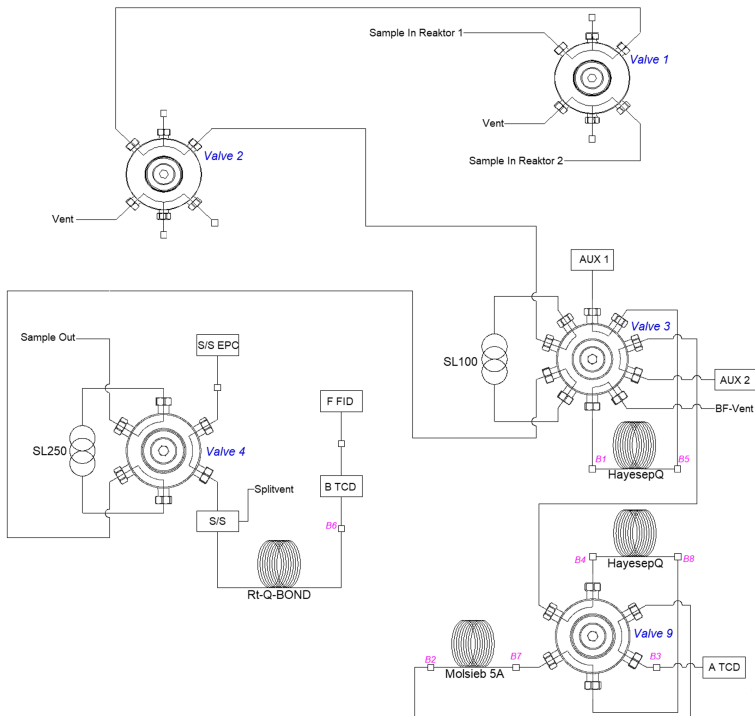
Figure 5.3.: Gas chromatograph wiring diagram including two sample loops with two parallel analysis channels. The first analysis channel is used to detect water, light alcohols, and hydrocarbons (left). The second analysis channel is used to detect permanent gases like nitrogen, hydrogen, carbon dioxide, and carbon monoxide (right).

The flow cell effluent can either be collected for further analysis or be fed into a waste tank.

5.1.1.3. Light sources

The employed test rig comprises a commercial class ABA highly collimated solar simulator providing AM1.5D solar irradiation in its target plane being roughly 200 mm in diameter (for illustration see tag (6a) in figure 5.1). The classification ABA is defined by ASTM standard E927-10, see [118], and addresses spectral match, spatial homogeneity, and temporal stability of the
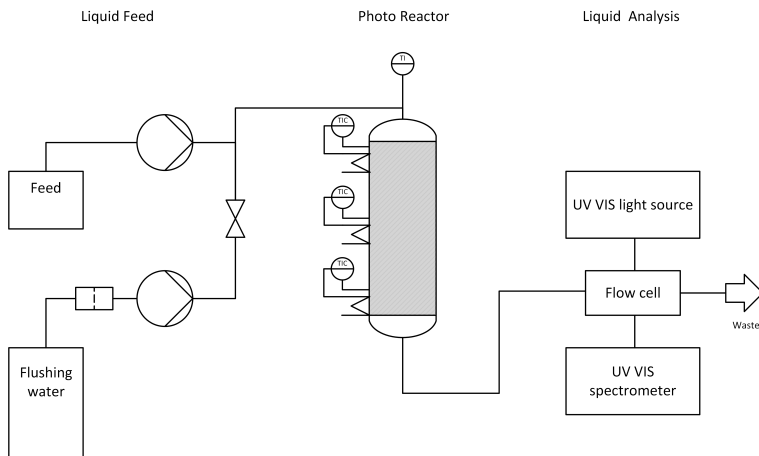
Figure 5.4.: P&ID of the liquid feed and analysis system of the employed experiment environment comprising two storage vessels and two feed pumps and a UV Vis Spectroscopy setup with light source, flow cell, and spectrometer.

emitted light.

The solar simulator is basically a xenon short arc lamp in line with a condenser lens, an air mass filter, and a Fresnel collimating lens. In addition to the air mass filter, a polymer intensity mask on the back side of the Fresnel lens is included and ensures the class B intensity homogeneity in the target plane. The AM1.5D irradiation can be dimmed down to 10 % of the nominal intensity by using both the power setting of the short arc and neutral density mesh filters inserted into the beam line after the condenser lens.

To verify the manufacturer indications on power settings and neutral density filters in the beam line necessary to achieve a certain irradiance, the irradiance in the target plane in the test rig is measured with a thermopile-based power sensor equipped with a well defined aperture and a USB-based live link to the test rig measurement and control system.

In addition to the solar simulator, the employed test rig provides a low voltage (max. 18 VDC) current supply (max. 20 A) with precise current measurement (for illustration see tag (6b) in figure 5.1). The current supply can be used for the power supply of reactor internal light sources, for instance light sources based on light emitting diodes (LEDs). The supply current is detected with a precision current meter mounted electrically in series with the current supply

and the employed light source. Both current supply and current meter are included in the measurement and control system via a live link based on RS232 serial communication.

5.1.1.4. Measurement and control system

The measurement and control system implemented in the test rig employed in the present work masters four main tasks: (1) it provides a user-friendly interface to the experiment setup presenting the current system state and the current set values of all controls, (2) it ensures safe operation by supervising safety-relevant process variables, (3) it runs automated experiments on user request, and lastly (4) it ensures structured data logging during any experiment. The measurement and control system comprises a large set of hardware components and software.

The hardware side of the measurement and control system employed provides analogue and digital interfaces for all sensors and components. Analogue input channels comprised are sixteen thermovoltage inputs for the use with thermocouples and eight DC current inputs for the use with standard industrial sensors. Analogue output channels comprised are eight DC current outputs for standard industrial actors and eight counter outputs for solid state relays control. The latter are employed to control the heating power of 230 VAC heating elements via pulse width modulation. Digital interfaces range from Ethernet connections over USB connections to RS485 and RS232 connections. The core components of the measurement and control hardware are aggregated in a switching cabinet (compare tag (7a) in figure 5.1). The most important pieces of hardware are a real time target, basically a computer running a Linux-based real time operating system, and a host computer running a Windows operating system (for illustration see tag (7b) in figure 5.1). The real time target provides all analogue input and outputs of the measurement and control system and runs all control loops controlling the tubing and reactor temperatures and the system pressure. The physical analogue input/output interface, which comprises industry standard plugs for all input/output channels, is realized on an interface module in the experiment chamber of the test rig (compare tag (7c) in figure 5.1). The host computer is in the centre of the measurement and control system managing the communication with all devices and running the software of the measurement and control system. The scheme in figure 5.5 gives a brief overview of the measurement and control system's hardware with the real time target and
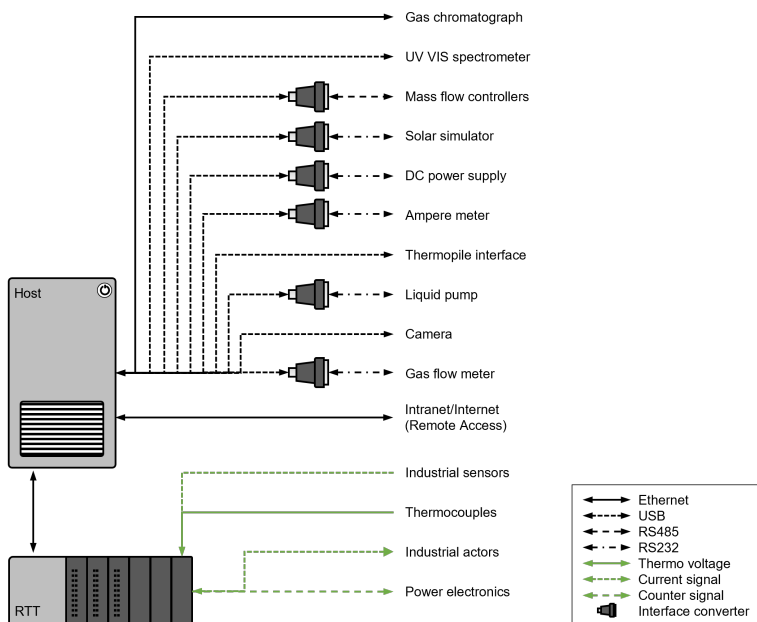
Figure 5.5.: Overview of the measurement and control system's hardware including all digital (black lines) and analogue (green lines) interfaces and connected components.

the host computer as core components.

The software side of the measurement and control system is implemented in LabVIEW®and is split in two main processes. One main process is running on the real time target, the other on the host computer. Both main processes are implementations of an input-process-output-model-based control system. After an initialization step switching on the power supply of the heating elements, the main process on the real time target goes repeatedly through the steps of process variable update, check of safety shut down conditions, and update of control variables. The update frequency lies in the range of 10-20 Hz. The main process on the real time target is an infinitely executed loop terminated only by a user command entered over the graphical user interface on the host computer. A lost connection to the host computer does not affect the execution of the main process on the real time target.

The main process on the host computer is built similarly to the main process on the real time target. In its initialization step, the serial communication

interfaces are initialized, and communication with all devices is established. Afterwards, the main process on the host computer, in analogy to the main process on the real time target, goes repeatedly through the steps of process variable update, check of safety shut down conditions, graphical user interface update, and control variable update. A speciality of the main update loop of the main process on the host is that especially slow communication processes, like, for instance, communication with the camera and the UV Vis spectrometer, are run in individual update loops in order to keep the most important updates, namely the process variable updates, in time. Implemented that way the update frequency of the main update loop on the host computer lies in the range of 5 Hz. In addition to the main update loop, the main process on the host computer comprises a user defined data recording loop, a user-independent backup data recording loop, a UV Vis spectra saving loop, an image saving loop, and an automation loop updating the automation setpoints if automated operation is active. Automation setpoints are, thereby, read from an automation file, that is provided by the user and that comprises an arbitrary number of system states (= sets of setpoints) with corresponding hold times. The automation basically goes through this list in the automation file, sets the automation setpoints read from the file, and holds them for the indicated hold time.

The graphical user interface, screenshot see figure 5.6, is implemented in a way that all process variables and setpoints are presented in both numerical indicators as well as trends. Additionally, online UV Vis analysis results, and the images of the camera are displayed. Importantly, when automation is active, automation setpoints are written onto the graphical user interface controls rather than being directly communicated to the test rig components. Implemented in that way, the user always is able to see the current setpoints on the graphical user interface, no matter if the setpoints are entered manually or by an automation running in the background, and priority conflicts between user commands and automation are avoided. Noteworthy, setpoints from the graphical user interface are only communicated to the test rig components, if the safety shut down status is negative. If the latter is positive the safety shut down commands defined previous to the system start up are communicated, and the orange signal on the top of the test rig is switched on. A safety shutdown is triggered if one of the following criteria is fulfilled: (1) any of the detected temperatures is higher than its safety shut down temperature, (2) any of the thermocouples detecting process temperatures shows a malfunction, (3) any detected pressure is higher than its respective safety shut down value, (4) the doors are opened with an activated door guard, (5)

the ventilation system shows a malfunction,or (6) the kill switch mounted next to the user work place is hit. Safety shut down values, namely shut down temperatures and pressures, are defined in a spreadsheet previous to the system start up and can be updated during run time via a button in the 'Commands' tab of the graphical user interface. Same holds for the safety shut down commands (control variable values in safety mode). Since it is practicable to remove the reactor from the test rig during handling, for instance, during filling with catalyst, the thermocouple malfunction guard of the five thermocouple interfaces, to which the reactor thermocouples are connected, can be deactivated in the graphical user interface in the status tab. With active thermocouple guard, disconnecting the thermocouples comprised in the reactor would be interpreted as a malfunction and would induce a safety shut down. For safety reasons it is of utmost importance to activate the reactor thermocouple guard as soon as the reactor is included into the test rig and before the reactor heating is connected/activated.

The host computer has intranet/internet access. With the Windows Remote Desktop Tool this allows remote control and operation in accordance to the effective legal regulations.

5.1.1.5. Data handling

Following one of the experiment instructions for automated experiments, see appendix B, data recorded in an experiment executed in the test rig is sorted in a reproducible way into a predefined folder structure. This data sorting structure is the prerequisite that the developed MATLAB®-based data handling tool can be used to conduct a raw analysis of the recorded data.

Primarily, the executed raw analysis has two objectives: (1) providing the base for an online presentation of long term trends during the experiment (in addition to the short term trends in the graphical user interface of the measurement and control system). (2) merging of different data types, images, gas chromatography reports, system logs, in one data set and especially on one time axis.

The MATLAB®-based tool is written object-oriented. If used as intended, the tool delivers a single object being an instance of the class `PRTR`. The object comprises in its properties basic information on the experiment as well as the experiment and automation data. Its methods are used for data extraction (which are the five methods named `extractExperimentLog`, `extractGCLog`,
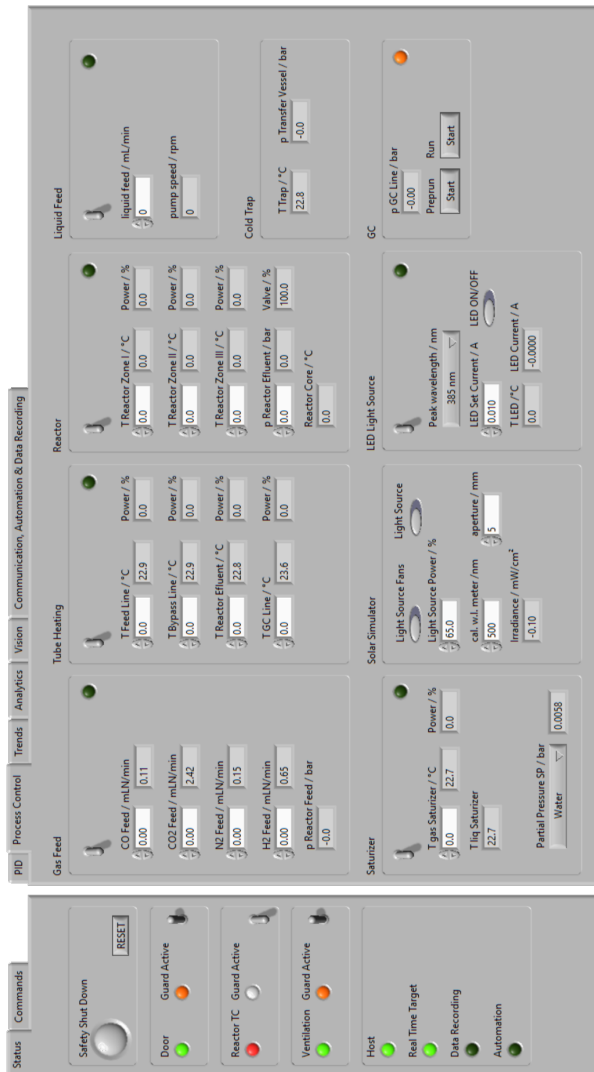
Figure 5.6.: Screenshot of the measurement and control system software graphical user interface presenting in the current tab all process variable and control variable indicators and setpoint controls.

extractCameraTakes, extractAutomation, and update), data analysis (for instance in the method extractCameraTakes or writeGCReport), and graphical and text-based reports (for instance in the methods LEDWaterSplittingReport or writeGCReport).

5.1.2. System components

A detailed list of components with manufacturer and type indications is part of the appendix of the present work, see appendix A.

5.2. System commissioning

During system commissioning the basic functionalities of the test rig were tested, and all components were put into operation. The main objectives on the instrumentation side were the characterization of the solar simulator emission spectrum and the calibration of the gas chromatograph.

5.2.1. Light source characterization

5.2.1.1. Materials and methods

For the characterization of the emission spectrum of the test rig-internal solar simulator, a calibrated UV Vis spectrometer (CAS 140 CT from Instrument Systems) equipped with an EOP 120 diffusor sensor head was employed. Measurements were conducted in the target plane of the solar simulator (300 mm distance measured from the Fresnel lens surface) in the 20x80 mm area, in which in later experiments the photoreactor aperture is placed (shaded area in figure 5.7). The diffusor sensor head, thereby, had a diameter slightly larger than the width of the target area but significantly smaller than the length of the target area (see red circles in figure 5.7). Measurements were, therefore, conducted in four positions, P1 to P4. In each position, ten spectra were recorded and averaged. The optical band covered in the measurements ranged from 360 nm to 800 nm. The spectral resolution was 1 nm.
Data sets were recorded with two different power settings of the short arc of

the solar simulator (82.7 % and 72.5 %) and with and without a 34 % transmission neutral density filter in place.

If not stated else wise, reported spectra are the average of all forty spectra resulting from ten repeat measurements in the four positions P1 to P4 and, thereby, represent a temporal and spatial mean value. Indicated standard deviations are empirical standard deviations calculated based on the four repeat measurements in positions P1 to P4. The data evaluation is implemented in a class definition (LIGHT) in MATLAB® and results, if applied as indented, in an object which stores in its properties the raw and averaged spectra with adherent information. Methods comprised in the class definition of LIGHT are the constructor that governs both, data reading, and averaging and presentation methods building figures of the raw and evaluated data sets. Further the class definition comprises methods that allow the calculation of band emission powers at user-defined short arc power settings and neutral density filters via linear interpolation between the derived mean spectra. Instances of LIGHT, therewith, also represent an interface to the Monte Carlo ray tracing environment developed in the present work (see chapter 4) by delivering spectrally resolved information on light sources mapped in simulations.

5.2.1.2. Results and discussion

Figure 5.8 depicts an exemplary data set of the four recorded temporally averaged spectra in position P1 to P4 for a short arc power setting of 82.7 % and no filter in place (100 % transmittance). The deviations between the spectra recorded in the four positions indicate a spatial inhomogeneity in the irradiance in the target plane. The maximum relative deviation from the mean value of the four measurements equals roughly 6 % which indicates an approximate accordance of the employed solar simulator to the ASTM class B homogeneity requirements for solar simulators (max. 5 % relative spatial inhomogeneity in the total irradiance [118]). Noteworthy, the employed diffusor sensor head did not meet the ASTM standard precisely, and, therefore, an assessment of the accordance of the spatial inhomogeneity of the solar simulator's irradiance to the ASTM standard is strictly speaking not accurate with the employed equipment. Figure 5.9 further depicts the temporally and spatially averaged emission spectra for different short arc power settings and neutral density filters in the beam line. A comparison of recorded spectra with and without neutral density filters in place clearly highlights the neutral filtering characteristics of the mesh filters employed (no wavelength dependent
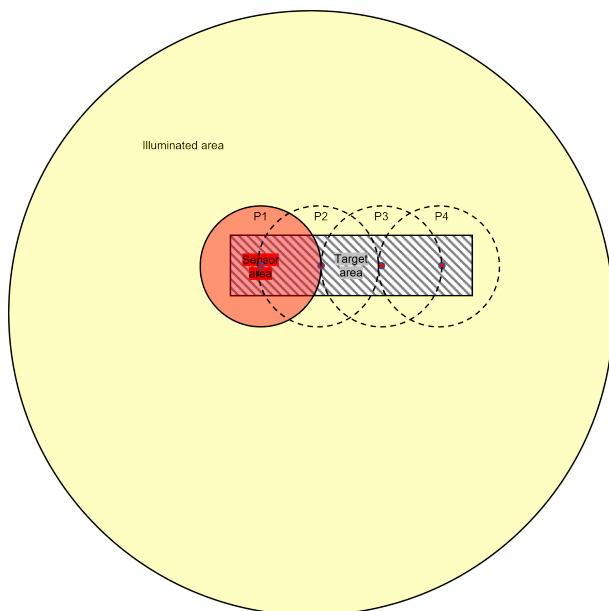
Figure 5.7.: Scheme visualizing the positions of the spectrometer sensor head during the characterization of the solar simulator emission spectrum. The illuminated area is illustrated in yellow. The target area in which in later experiments the photoreactor aperture is placed, is depicted in grey shades. The diffusor sensor head area is highlighted in red.

transmission characteristics). Further the manufacturer indications on the transmittance of the neutral density filters are satisfactory fulfilled. The filter with a manufacturer indication of 34 % transmission results in a spectraly averaged transmission of 36.95±0.17 %. Lastly, figure 5.10 depicts the recorded and normalized solar simulator spectrum together with a normalized ASTM AM1.5D reference spectrum highlighting the spectral match of the simulated solar light from the solar simulator. The emission peaks in the solar simulator emission spectrum at approximately 460 nm and 760 nm are system inherent emission peaks resulting from the xenon atmosphere around the short arc.
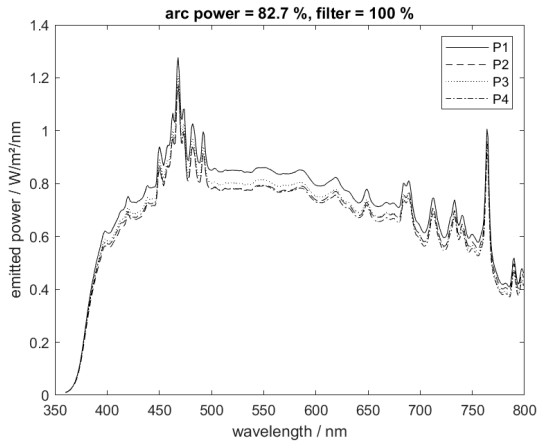
Figure 5.8.: Solar simulator emission spectrum raw data at 82.7 % short arc power setting and no filter in place.
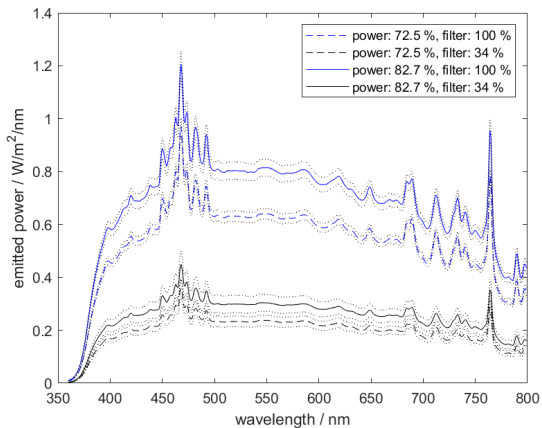
Figure 5.9.: Spatial and temporal average solar simulator emission spectra for different short arc power settings and neutral density filters in place. The color indicates different neutral density filters (blue corresponds to no filter, black to a 34 % transmittance filter). The line style indicates different power settings (solid line corresponds to 82.7 % and dashed line corresponds to 72.5 % short arc power setting). Dotted lines represent one empirical standard deviation.
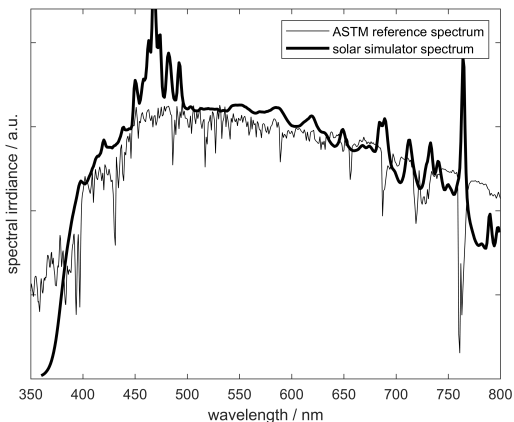
Figure 5.10.: Normalized solar simulator and ASTM AM1.5D reference spectrum. The thin solid line corresponds to the ASTM AM1.5D reference spectrum, the bold solid line to the recorded solar simulator spectrum.

5.2.2. Gas chromatograph calibration

The calibration of the gas chromatograph links the molar fraction of a species i in the analyte (y_i) with the gas chromatograph response, or more precisely the signal peak area assigned to the species ($A_{GC,i}$), via the calibration factor of the species ($q_{cal,i}$), compare equation (5.1). The calibration of the gas chromatograph, therefore, relies on well defined gas mixtures with known composition.

$$y_i = \frac{A_{GC,i}}{q_{cal,i}} \tag{5.1}$$

5.2.2.1. Materials and methods

The gas chromatograph was calibrated for permanent gases, namely hydrogen, nitrogen, carbon dioxide, and carbon monoxide, using commercial calibration gases. Details on the employed calibration gases, designation and indicated molar fractions, are listed in table 5.1.

Each calibration gas mixture was injected three times into the sample loops of the gas chromatograph and analysed with a method developed by TECKSO

Table 5.1.: Calibration gas mixtures employed for the gas chromatograph calibration.

Calibration gas	$y_{H_2}/\%$	$y_{N_2}/\%$	$y_{CO_2}/\%$	$y_{CO}/\%$
SG23988	-	20.06	79.94	-
SG25488	79.96	20.04	-	-
SG26779	59.85	20.07	20.08	-
SG24438	-	-	-	5.021
SG26777	14.070	-	0.995	-
SG26774	1.001	49.465	30.28	14.00

GmbH for the specific analysis tasks of the present work. The gas chromatograph response was subsequently averaged throughout these three repeat measurements and added with the corresponding molar fraction to the calibration table. Calibration factors were derived from a linear fit through all points in the calibration table recorded for one species.

Further, the gas chromatograph was calibrated for water and methanol vapour with a nitrogen stream saturated with water or methanol in the saturator (details on the saturator and experimental setup, see section 5.1.1). Previous to the calibration, the saturator was dried with pressurized air and subsequently filled with water (deionized with Milli-Q from Merck KGaA) or methanol (Carl Roth GmbH&Co KG). The according molar fractions of water and methanol were calculated via equation (5.2). Thereby, $p_{S,i}$ refers to the vapour pressure of water or methanol at the saturator temperature and p_{System} to the system pressure during the calibration. For the calculation of the vapour pressure, a Wagner equation with corresponding parameters taken from [119], and the measured gas phase temperature at the saturator outlet, were employed.

$$y_i = \frac{p_{S,i}(T)}{p_{System}} \tag{5.2}$$

Equation (5.2) lines out that both, a system pressure variation, and a variation of the saturator temperature, are means to adjust different molar fractions of methanol or water. This system property can be used to verify the assumption of a thermodynamic equilibrium at the saturator outlet: Calibration factors can be derived from a linear fit of the experimental gas chromatograph response and the corresponding vapour molar fractions adjusted over a system pressure variation. Only if calibration factors derived from a pressure variation at different saturator temperatures equal each other, the assumption of

thermodynamic equilibrium is valid.

Lastly, the gas chromatograph was calibrated for methyl formate and formalde-hyde via a direct injection of well defined liquid mixtures of methanol (Carl Roth GmbH&Co KG) and methyl formate (Arcos Organics) or formaldehyde (Merck KGaA) into the split injector of the gas chromatograph (for details on gas chromatograph setup, see figure 5.3). The corresponding gas phase molar fractions were calculated via equation (5.3). Thereby x_i refers to the molar fraction in the liquid sample injected into the split injector.

$$y_i = y_{CH_3OH} \frac{x_i}{x_{CH_3OH}} \tag{5.3}$$

The employed indirect procedure for the calibration of methyl formate and formaldehyde requires an existing calibration of the gas chromatograph for methanol. Otherwise the methanol molar fraction y_{CH_3OH} in equation (5.3) would be unknown. Additionally, the indirect calibration procedure via the split injector is less accurate compared to a direct calibration via a well-defined gas feed for the sake of error propagation from the methanol calibration to the calibration of methyl formate and formaldehyde. The approach was chosen nevertheless, because methyl formate evaporates extremely fast form-ing explosive mixtures in air (boiling temperature at ambient pressure is roughly 32 °C) and, therefore, is hard to handle in a standard lab environment. Formaldehyde is not stable without water and/or methanol as stabilizer and, therefore, commercially not available as pure substance.

5.2.2.2. Results and discussion

The calibration for permanent gases resulted in the calibration factors listed in table 5.2.

The calibration of the gas chromatograph for water was executed at different saturator temperatures (37 °C, 50 °C, and 60 °C) in order to validate the as-sumption of thermodynamic equilibrium at the saturator outlet. The system pressure was varied at each saturator temperature from 0.2 MPa, over 0.3 MPa and 0.4 MPa to 0.5 MPa. Each operating point was measured twice. The mea-sured gas chromatograph responses are plotted over the molar fractions derived via equation (5.2) in figure 5.11. The excellent linearity ($R^2 = 0.998$) of the calibration curve resulting from a fit of all 24 measured points, which is obviously independent of the saturator temperature, underlines the validity of the assumption of thermodynamic equilibrium of at the saturator gas outlet
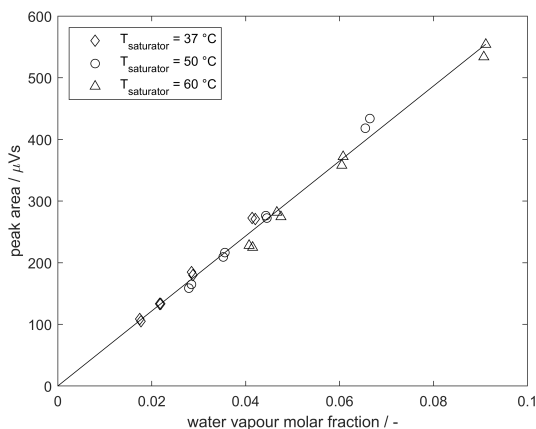
Figure 5.11.: Experimental gas chromatograph response drawn over the water vapour molar fraction in the gaseous analyte calculated via (5.2). Different symbols refer to experiments with different saturator temperatures between 37 °C and 60 °C. For details see the legend.

and, thereby, validates the calibration approach.

The calibration for methanol was executed similarly at saturator temperatures of 35 °C and 40 °C, and a pressure variation from 0.3 MPa over 0.4 MPa to 0.5 MPa.

The derived calibration factors for water and methanol are listed in table 5.2. The calibration for methyl formate and formaldehyde was executed subsequently to the methanol calibration and resulted in the calibration factors listed in 5.2.

5.3. Interim summary

The developed, built, and lastly successfully commissioned photoreactor test rig represents a robust basis for the further reaction engineering experiments of the present work. Its gas and liquid phase feed systems, thereby, allow the conduction of gas, liquid, and heterogeneous multi-phase photocatalytic experiments. The included online gas and liquid phase analysis together with a sophisticated measurement and control system, being able to conduct automated experiments, provide the basis for long term experiments scanning

Table 5.2.: Derived gas chromatograph calibration factors.

Species	calibration factor
H_2	58260 µV s
N_2	6430 µV s
CO_2	7960 µV s
CO	6736 µV s
H_2O	6204 µV s
CH_3OH	120813 pA s
$CHOOCH_3$	122906 pA s
CH_2O	1753 pA s

wide ranges of different operating variables. The developed MATLAB®-based data handling tool facilitates data handling. Lastly, the included two options of lighting, a solar simulator and an electrical interface for reactor internal light sources, open ways towards both experiments under simulated solar irradiation and detailed reaction engineering experiments with narrow band light. The detailed characterisation of the emission spectrum of the solar simulator, thereby, is the essential basis for meaningful evaluation of conducted experiments.

6. Material development

The development of a low-cost, high efficiency photocatalytic process relies on suitable materials, both photoreactor component materials, and photocatalysts, and the precise knowledge of their optical and reaction engineering properties.

6.1. Photoreactor component materials

On the reactor component materials side, structural materials, like, for instance, steel or polymers, as well as transparent window materials, like, for instance, glass or polymers, and optical coating materials, like, for instance, aluminum or silver are essential for successful photoreactor designs. In the present work, structural components were fabricated from 316L stainless steel via additive manufacturing. Window materials were commercial quartz glass parts with predefined shape. Optical coatings were silver-based and applied on structural components made from 316L stainless steel. On a side note, for the sake of the availability of manufacturing techniques in metal in the present work, reactor prototypes were not polymer-based as would be favorable to reduce the system costs in large scale production, see brief discussion in section 2.2.2 and chapter 3. However, as will be lined out in chapter 8, the design of production photoreactors in the present work was developed in a way that the components would be manufacturable with established low-cost manufacturing techniques in polymers.

The challenges faced on the reactor components material side in the present work mainly lay in the field of the preparation of optical coatings on the 3D-printed stainless steel parts via adequate post treatment of printed raw parts. A second focus was the determination of optical transport properties of the materials needed for optical simulation and numerical optimisation of photoreactor assemblies. This comprises the reflectivity and reflection

characteristics of structural components and applied optical coatings as well as refractive indices and absorption coefficients of window materials.

6.1.1. Materials and methods

6.1.1.1. Additive manufacturing of structural components

The structural components of photoreactors developed and employed in the present work have complex shapes, see for instance figures 6.5, 8.2, and 7.1. Especially the employed optical components in the case of developed high efficiency photoreactors are free-form geometries. Traditional subtractive manufacturing of such geometries is time consuming and sets limits to the complexity of the geometry. The structural and optical components of photoreactors in the present work were, therefore, manufactured via 3D-printing of stainless steel, more precisely via powder bed fusion with laser beams of stainless steel.

The typical work flow in additive manufacturing comprises the design process based on computer aided design (CAD) , subsequent slicing of the created CAD model with a slicing software, and lastly, the layer-wise built up of the component via the printing method of choice. For a more detailed description of both the typical work flow and powder bed fusion additive manufacturing technologies see for instance [120].

In the present work, all components were designed using AUTODESK™ IN-VENTOR®. Slicing was executed with RDesigner from DMG MORI. The slice thickness was set to 50 μm for all print jobs. The components were subsequently printed on a Realizer SLM 125 powder bed fusion machine from DMG MORI. The stainless steel powder employed was 316L powder with a particle size of 10-45 μm purchased from Carpenter Additive®. Post treatment of the printed components in a first step was limited on the removal of the support structures via traditional milling.

6.1.1.2. Roughness reduction of additively manufactured components

Raw parts from powder bed fusion with laser beams of metals typically have a mean surface roughness value between 5 μm and 30 μm. Even though the roughness is typically evenly distributed, the roughness may represent a challenge for printed optical surfaces. Rough surfaces exhibit diffuse reflection

characteristics rather than specular reflection characteristics. In some cases, this is desirable. For concentrating optics, however, or precise radiation transport control, respectively, specular reflection characteristics of optical surfaces are essential. In order that a surface exhibits specular reflection characteristics, its mean surface roughness must be well below the wavelength of reflected light. For UV and Vis photons this means that the mean surface roughness must be well below 100 nm.

In order to reduce the roughness of optical surfaces after the printing process, in the present work a two-step procedure was employed. In the first step, the surface was smoothed via multipass milling on a high precision KERN HSPC milling machine. In the second step the milled surfaces were polished in a four step manual polishing procedure with poly-crystalline diamond suspensions (DIA Complete Poly from QATM GmbH) and textile polishing cloth. The crystallite size of the polishing suspensions was reduced stepwise from 6 μm over 3 μm and 1 μm to 0.25 μm in the four polishing rounds.

6.1.1.3. Surface roughness measurements

Mean surface roughness measurements were conducted with an S neox optical profilometer from SENSOFAR Metrology. The profilometer was operated with a DI 10X objective in interferometry mode. The evaluation of the obtained 3D surface scans was executed with SensoVIEW, a software tool from SENSOFAR Metrology. The evaluation comprised in a first step a form removal, in which unavoidable inclinations of the measured surfaces were corrected. In the second step the mean surface roughness value was determined on the form corrected surface in accordance to DIN ISO 25178. For details on the proceeding, see [121].

6.1.1.4. Application of optical coatings

3D-printed raw parts and parts with reduced surface roughness employed as optical components were coated with silver in order to increase the reflectivity of the optical surfaces in the relevant optical band (in the experiments reported in the present work the relevant optical band lies approximately between 350 nm and 500 nm). The coatings were applied by a commercial provider (C. Jentner GmbH) and comprise three layers, an adhesion promoter (nickel), the silver coating, and a tarnish protection. Nickel was applied in

an electroless coating procedure, whereas silver was coated galvanically, and the tarnish protection in a wet chemical coating procedure. Details on the coating procedures are intellectual property of C. Jentner GmbH.

6.1.1.5. Determination of optical transport properties

Refractive indices and absorption coefficients of windows

The refractive index and absorption coefficient of employed quartz glass components (ILMASIL PN from QSIL GmbH) was derived from transmission data of quartz glass samples with varying thickness. In the evaluation, reflections on the phase boundaries between quartz glass and the environment were mapped according to Fresnel equations, see equation (4.3). Absorption was modeled with a Lambert Beer law approach, see equation (4.4). Assuming perpendicular illumination of the quartz glass sample during the manufacturer's measurements, algebraic reformulations deliver equation (6.1) for the transmission of a quartz glass window (T_{window}) which is an appropriate model for the sample in the transmission measurement. Thereby R is the reflectivity of a single phase boundary under perpendicular irradiation calculated with the Fresnel equations, equation (4.3), d the thickness of the quartz glass sample, and σ_a the quartz glass absorption coefficient.

$$T_{window} = \frac{(1 - R)^2 \, exp \, (-\sigma_a d)}{1 - [exp \, (-\sigma_a d) \, R]^2} \qquad (6.1)$$

The absorption coefficient and refractive index were lastly estimated with the MATLAB® standard optimizer `fminsearch` minimizing the sum of residual squares between indications on transmission of quartz glass samples and the model values calculated for the different sample thicknesses via equation (6.1).

Reflectivity and specular share of optical surfaces

The total reflectivity (R_{total}) of optical surfaces was determined with a Lambda 1050 UV Vis spectrometer from Perkin Elmer equipped with an integrating sphere assembly. In order to derive accurate values, reflectivity measurements were taken relative to a PTB-traceable Zenith polymer diffuse reflection

standard from Sphere Optics GmbH. The according correction of the recorded raw data was done via equation (6.2).

$$R_{total}(\lambda) = R_{raw}(\lambda)R_{standard}(\lambda) \qquad (6.2)$$

The specular share (S, definition see chapter 4.3) in the total reflectivity was estimated from a comparison of reflectivity measurements with a specular trap in the integrating sphere in place, or with other words a measurement of the diffuse reflectivity ($R_{diffuse}$), with the total reflectivity. The specular share was derived accordingly via equation (6.3).

$$S(\lambda) = \frac{R_{total}(\lambda) - R_{diffuse}(\lambda)}{R_{total}(\lambda)} \qquad (6.3)$$

If not indicated otherwise, the mapped optical band in the measurements ranged from 300 nm to 800 nm, and the spectral resolution was 1 nm. Measurements where taken three times, and indicated values are the average of these three repeat measurements.

6.1.2. Results and discussion

6.1.2.1. Structural components

3D printed stainless steel parts were fabricated as described in section 6.1.1.1. After the printing, raw parts typically show a shape accuracy of roughly 200 μm and mean surface roughness of roughly 5 μm. The reflection on the surface raw parts is perfectly diffuse with a limited reflectivity (<30 % in the blue band and <20 % in the UV band), see figure 6.1. The employed post-treatment strategy to reduce the mean surface roughness value results in a mean surface roughness value of roughly 160 nm after the multipass milling step and a mean surface roughness value of roughly 50 nm after the four step manual polishing procedure. For illustration of the effect of the post treatment procedure see photographs of photoreactor components after multipass milling and polishing in figure 6.2.

6.1.2.2. Optical coatings

Optical coatings were applied on 3D-printed parts both, before, and after the post treatment reducing the mean surface roughness value in accordance
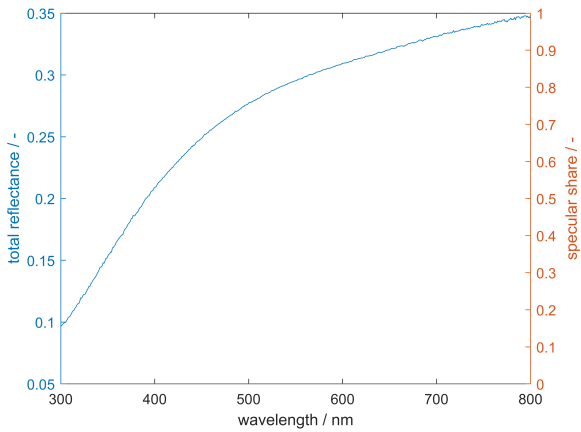
Figure 6.1.: Reflectivity and specular share of a stainless steel surface after 3D printing.
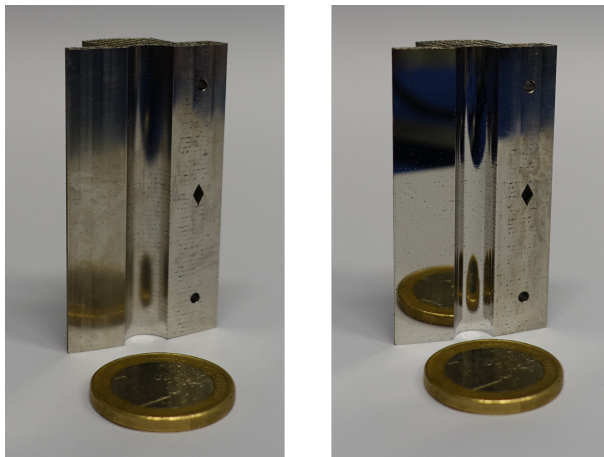
Figure 6.2.: Photographs of 3D-printed optical photoreactor structural components after multipass milling (left) and subsequent manual four step polishing (right).
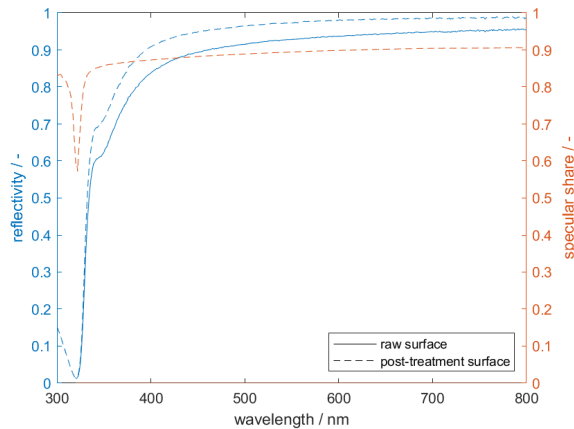
Figure 6.3.: Reflectivity (blue) and specular share (orange) of optical silver coatings on raw surface from 3D printing (solid line) and polished surface after the post treatment (dashed line).

to the proceeding described in 6.1.1.4. Optically coated parts with no post treatment exhibit a perfectly diffuse reflection characteristic, whereas optically coated parts with reduced surface roughness exhibit an almost perfectly specular reflection characteristic (with a specular share >90 %), compare orange lines in figure 6.3. The imperfection of the reflection characteristic of the silver coating on polished surfaces can be attributed to small surface defects resulting from unavoidable pores resulting in power bed fusion with laser beams of metals, see dark surface defects in the polished surfaces in the photographs in figure 6.2.

The reflectivity of applied optical silver coatings is, as expected, high (>90 %) throughout the Vis band with a step decrease in the UV band (<400 nm) and an almost diminishing reflectivity at approximately 325 nm, compare blue lines in figure 6.3. The course of the reflectivity in the UV band is a consequence of the electronic structure of silver and, therefore, a characteristic indicator for standard silver coatings, compare for instance data given in [122].

The slightly lower apparent reflectivity of optical coatings on parts without a roughness reducing post treatment can be attributed to ray attenuation through multiple reflection events occurring in the spandrels on the rough surface before an incident ray is redirected towards the hemisphere above the reflecting surface.
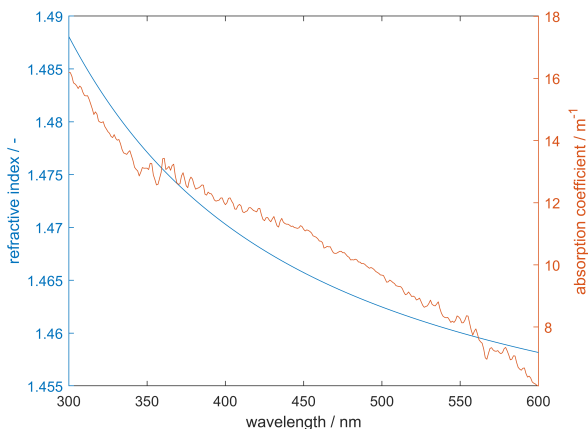
Figure 6.4.: Refractive index and Napierian absorption coefficient of ILMASIL PN quartz glass.

6.1.2.3. Windows

The refractive index and absorption coefficient of employed quartz glass components were determined with manufacturer indications on the optical transmission of three samples with thicknesses of 1.0 mm, 1.5 mm, and 2.0 mm and in accordance to the described proceeding in chapter 6.1.1.5. The refractive index lies in a typical range for quartz glass with a value of approximately 1.470 at 400 nm, compare for instance with indications in [123]. The determined absorption coefficient is slightly higher than comparable literature values (see for instance indication in [123]), which might be attributed to quartz glass impurities, small enclosed air bubbles, or an imperfect alignment of the samples in the manufacturer's measurement.

6.2. Photocatalyst development

On the photocatalyst side, both, active materials as well as suitable supports, are key factors to successful process designs. The challenges faced on the photocatalyst level in the present work lie mainly in the development of model active materials showing a clear photocatalytic reaction mechanism,

the development of a practicable active material support strategy, and the determination of optical transport properties of liquid and particulate photocatalysts. This especially addresses the effective absorption and scattering coefficients of particulate fixed beds.

The first photocatalytic model system employed in the present work is a homogeneous liquid phase photocatalytic reaction with well known reaction engineering properties, the potassium ferrioxalate photoreduction, equation(6.4), which yields Fe^{II+} as reaction product. Especially, for this reaction the quantum yield and its spectral dependency is well known, see for instance [124]. The knowledge of the latter is, according to the photoreactor design equation (equation (2.9)), and as discussed in chapter 3, the necessary information on the photocatalyst level needed to design high efficiency photocatalytic processes. Noteworthy, one absorbed photon in the potassium ferrioxalate system may induce two reduction events. So, theoretically, the quantum yield as defined in equation (2.7) could peak at a value of two. In reality the quantum yield for the potassium ferrioxalate photoreduction lies in the range of 1.0-1.2 in the optical band from 250 nm to 500 nm.

$$[Fe^{III+}(C_2O_4)_3]^{3-} \xrightarrow{h\nu} [Fe^{II+}(C_2O_4)_2]^{2-} + C_2O_4{}^{\cdot-}$$
$$[Fe^{III+}(C_2O_4)_3]^{3-} + C_2O_4{}^{\cdot-} \xrightarrow{\Delta} [Fe^{II+}(C_2O_4)_2]^{2-} + 2\,CO_2 + C_2O_4{}^{2-} \tag{6.4}$$
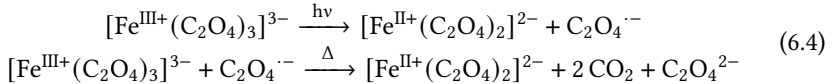
The potassium ferrioxalate photoreduction is employed in the present work to experimentally validate the developed Monte Carlo ray tracing environment and the developed photoreactor designs.

The second photocatalytic model used in the present work is a titania-based catalyst system driving the gas-phase methanol photoreforming reaction, compare equation (2.6). A titania-based system is chosen, because of the often simple synthesis routes yielding promising active materials and many literature reports of clear photocatalytic reaction mechanisms. The titania-based photocatalyst is employed to validate the chosen photocatalyst support strategy and to examine the expected but rarely reported interdependencies between process conditions and the quantum yield in gas phase photocatalytic reactions.

The titania-based active material, thereby, in some experiments is supported on a silica aerogel-based active material support in order to control radiation transport on a photocatalyst level while avoiding limitations on the radiation transport side.

6.2.1. Materials and methods

6.2.1.1. Synthesis of titania-based active material

As described in [93], in the present work, the synthesis route to yield a methanol photoreforming-active, titania-based active material was a modified literature-reported wet impregnation method. The corresponding literature references are [125, 126].

Briefly, according to the literature report, a commercial titania powder was suspended in water and mixed with a palladium nitrate solution. After drying, calcination, and reduction in a hydrogen atmosphere, the active material was ready for use.

In a standard synthesis in the present work, AEROXIDE® titania P25 from Evonik Industries was dispersed in deionized water (MilliQ from Merck) in a water bath at 80 °C under continuous stirring. Using a syringe, palladium-(II)-nitrate-hydrate (ARCOS Organics) dissolved in deionized water (MilliQ from Merck) at 80 °C was added drop-wise to the stirred and tempered titania suspension. The resulting suspension was then further stirred at 80 °C until a paste-like texture was achieved. To remove water residues, the paste was subsequently dried at 110 °C under static air in a M110 muffle furnace from Thermo Scientific. Heating and cooling rates were 5 K min^{-1}, with no active cooling. Subsequently, the active material powder was calcined for three hours. Heating and cooling rates in the calcination step were 10 K min^{-1}, again without active cooling. The calcinated active material was ground by hand using a mortar and sieved several times with an Analysette 3 PRO sieving machine from FRITSCH GmbH to isolate active material particles with a defined particle size. For reaction engineering experiments with pure active material in a photoreactor, the sieves in the sieving step were chosen to ensure a particle size between 50 μm and 200 μm. For reaction engineering experiments with supported active material, the sieves were chosen to ensure a particle size between 15 μm and 25 μm.

Both, the calcination temperature and the precise recipe, were varied in the present work yielding active materials with different palladium loading and thermal history with the aim to identify the most promising active material. Details on the optimization strategy, see chapter 6.2.1.3.

6.2.1.2. Reaction engineering characterization

Synthesized active materials were tested for their methanol photoreforming activity in a modular photoreactor assembly. For an illustration of the latter, see figure 6.5. The assembly is made from 3D-printed, laser-cut and commercial parts only and basically comprises a reactor body, commercial fluid connectors (Swagelok) holding a commercial 1/4" quartz glass capillary (QSIL GmbH) in place, and three electrically heated drums that establish an isothermal zone in the center drum enclosing the reaction volume. The center drum has optics included that concentrate light ($C \approx 2$) with the help of commercial mirror insets (Edmund Optics) and guide it into a silver coated cavity. The cavity surrounds the quartz glass capillary shaping the cylindrical reaction volume. Heating cartridges with included thermocouples (Horst GmbH) inserted into foreseen bores in the heated drums allow temperature control in the three heating zones. A fourth thermocouple can be inserted into the reaction volume. The inserted thermocouple detects the reaction zone temperature in the conducted experiments. The maximum operating pressure of the reactor is 1 MPa. For safety reasons operation under pressure must be conducted under full enclosure and surveillance of the latter. The maximum temperature of the reactor should not exceed 300 °C. Noteworthy, even though no structural or functional failure is expected at elevated temperatures, the mirror insets and silver coatings degrade when operated for longer periods of time at higher temperatures.

In a standard experiment conducted to test an active material for its methanol photoreforming activity, roughly 200 mg of active material were filled into the quartz glass capillary and held in place with quartz wool plugs. The position of the active material in the quartz glass capillary was chosen in a way, that the active material was precisely in the center drum with included optics after the assembly of the photoreactor. For illustration, see figure 6.5. Lastly, the assembled reactor was mounted into its foreseen place below the solar simulator in the test environment described in chapter 5. Prior to the experiment start, the tubing connecting the reactor to the gas feed and analysis system of the experiment environment was insulated with mineral wool half shells and glass silk straps to prevent condensation of reactants in the feed or reactor effluent line.

The experiment routine conducted with each active material comprised basically three phases. In the first phase the active material was reduced for 3 h at 260 °C under 20 $mL_N\,min^{-1}$ hydrogen flow and a target system pressure
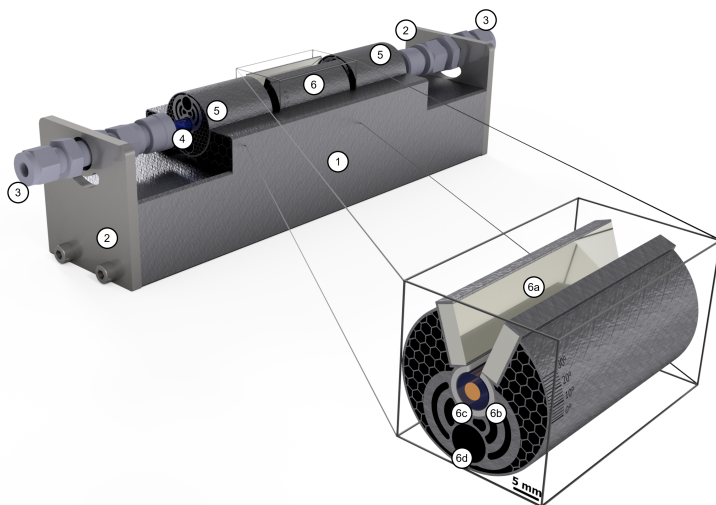
Figure 6.5.: Rendering of a CAD model of the modular photoreactor assembly employed in this work. The assembly is made up of a 3D-printed reactor body (1), clamped between laser-cut front and back plates (2) onto a milled metal back bone structure (not visible). The commercial tubing connectors (3) hold a commercial 1/4" quartz glass capillary (4) in place that goes through the 3D-printed inlet and outlet heating drums (5) and a 3D-printed and heated optics module (6). The optics module (zoom in) comprises commercial mirror insets (6a) that shape a narrowing gap concentrator guiding incident light into a silver coated cavity (6b) in which the quartz glass tube surrounds the reaction volume depicted in orange (6c). Heating in the inlet and outlet heating drums and the optics module is realized via electrical heating cartridges (not depicted) in foreseen heating cartridge bores (6d).

of 1 MPa. Heating rates were 5 $K\,min^{-1}$, and pressure change rates were 20 $kPa\,min^{-1}$. The pressure before the reduction was ambient, the pressure at the end of the activation phase was 50 kPa.

In the second phase of a typical experiment, the complete system was purged with nitrogen to remove any detectable traces of hydrogen from the activation. This was necessary because in the subsequent methanol photoreforming experiments, hydrogen was the product of interest and likely to be detected in traces only, thus a hydrogen free atmosphere had to be guaranteed prior to the main experiment phase. The nitrogen purge procedure was a pressure swing purge conducted with a large nitrogen flow dosed in pulses (frequency roughly 1 min^{-1}) over the nitrogen mass flow controller bypass (details see

chapter 5). Only, if the gas analysis indicated no detectable traces of hydrogen, the main experiment phase was initiated.

In this third phase, 5 mL$_N$ min^{-1} nitrogen were fed to the saturator filled with a mixture of methanol (Carl Roth GmbH&Co.KG) and water (MilliQ from Merck) with a methanol mass fraction of 17.1 wt %. The saturator effluent was fed directly to the gas chromatograph via the reactor bypass and the cold trap bypass. Only, if the saturator effluent showed a stationary composition with a molar ratio of methanol and water of roughly 1:1, the saturator effluent was directed to the reactor and the main experiment could start. In this main experiment the active material was operated under four different reactor temperatures (60 ℃, 80 ℃, 100 ℃, and 140 ℃), and with and without the solar simulator switched on. The solar simulator was operated with a power setting of the short arc of 82.7 % and with no neutral density filter in the beam line. Every operating point was held for 90 min. At each operating point, three samples were taken with the gas chromatograph. After the total of eight operating points (four with and four without light), a last reference operating point (80 ℃ and lights switched on) was measured to check the active material for deactivation. The main experiment was conducted with an automation without user interaction ensuring a maximum degree of reproducibility/comparability between different characterization runs. A graphical summary of the experiment procedure is given in figure 6.6.

The mean hydrogen activity (a_{H_2}) as measure for the catalyst performance was derived from the experiment raw data via equation (6.5). Thereby, $\dot{N}_{N_2}$ is the molar nitrogen feed detected by the nitrogen mass flow controller's thermal mass flow sensor and m_{cat} is the catalyst mass in the photoreactor determined with a balance (Kern ABJ NM/ABS-N) previously to the experiment. Indicated standard deviations for the mean hydrogen activity are empirical standard deviations derived via Gaussian error propagation from the estimated errors in the hydrogen and nitrogen molar fraction in the reactor effluent and the estimated error in the nitrogen feed. The error estimation in the relevant process parameters was based on empirical standard deviations derived from the three conducted repeat measurements.

$$a_{H_2} = \frac{y_{H_2} \dot{N}_{N_2,Feed}}{y_{N_2} m_{cat}} \tag{6.5}$$
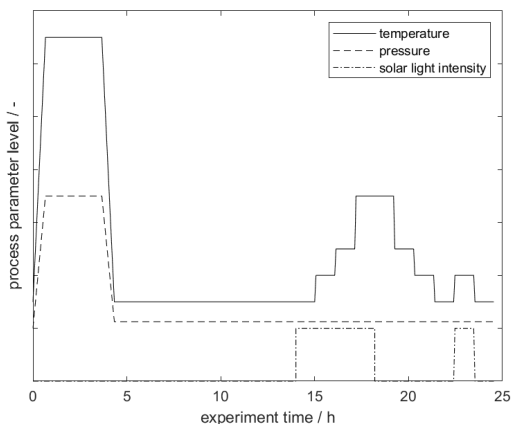
Figure 6.6.: Graphical presentation of the experiment routine employed to test developed active materials for their methanol photoreforming activity. The experiment routine basically comprises three phases, a high temperature high pressure reduction phase in which the active material is reduced (from 0 h to 4 h), a subsequent purge phase in which hydrogen is removed from the system (from 4 h to 13 h) and, lastly, the experiment phase in which the active material is operated at four different temperatures, and with and without simulated solar irradiation (from 13 h to 25 h).

6.2.1.3. Active material optimization

The active material was optimized with regard to its photocatalytic performance in a pattern search-based experimental optimization strategy. The influencing parameters addressed in the optimization were the palladium loading of the active material and the temperature during the calcination of the active material in the active material synthesis (for details on the active material synthesis, see chapter 6.2.1.1).

The photocatalytic performance (= the objective function of the optimization) was defined as the difference between light and dark frequency factors of a simplified hydrogen reaction rate law, equation (6.6). The higher that difference the more dominant is the photocatalytic contribution in the overall reaction rate. The assumed hydrogen reaction rate law is first order in light intensity and the reactant concentrations. It maps the temperature dependency of the reaction rate via two Arrhenius-like terms describing a 'light contribution' and a 'dark contribution' to the overall reaction rate. The assumption

of first order in reactant concentrations and light intensity is questionable but unavoidable since the experimental data basis for the rate law parameter estimation did not comprise a concentration and/or light intensity variation (for details on the experiment design see chapter 6.2.1.2).

$$
\dot{r}_{H_2} = \left[\frac{E_p}{E_{ref,p}} k_{ref,light} \exp\left[-\frac{E_{a,light}}{R} \left(\frac{1}{T} - \frac{1}{T_{ref}} \right) \right] \right.
$$
$$
\left. + k_{ref,dark} \exp\left[-\frac{E_{a,dark}}{R} \left(\frac{1}{T} - \frac{1}{T_{ref}} \right) \right] \right] c_{CH_3OH} c_{H_2O}
$$

(6.6)

Since the chosen objective function depends on the temperature and different active materials may have a maximum in the objective function at different temperatures, a comparison of different active materials at a fixed temperature would deliver a distorted picture. The light-dark frequency factor difference considered in the optimization was, therefore, determined as the difference between light and dark frequency factor at an individual optimal temperature at which the frequency factor difference has its individual maximum. Mathematically, the objective function value was derived via equation (6.7), with the optimal temperature calculated via equation (6.8).

$$
k_{H_2,diff} = \frac{E_p}{E_{ref,p}} k_{ref,light} \exp\left[-\frac{E_{a,light}}{R} \left(\frac{1}{T_{opt}} - \frac{1}{T_{ref}} \right) \right]
$$
$$
- k_{ref,dark} \exp\left[-\frac{E_{a,dark}}{R} \left(\frac{1}{T_{opt}} - \frac{1}{T_{ref}} \right) \right]
$$

(6.7)

$$
\frac{1}{T_{opt}} = \frac{1}{T_{ref}} + \frac{R}{E_{a,light} - E_{a,dark}} ln\left[\frac{k_{ref,light} E_{a,light}}{k_{ref,dark} E_{a,dark}} \right]
$$

(6.8)

$E_{a,light}$ and $E_{a,dark}$ and $k_{ref,light}$ and $k_{ref,dark}$ in equations (6.6), (6.7) and (6.8), are, thereby, the light and dark activation energy and reference frequency factors of the assumed hydrogen reaction rate law, respectively. These kinetic parameters were determined via a parameter estimation, fitting the experimental hydrogen molar fraction in the reactor effluent to a simple plug flow reactor model, equation (6.9).

$$
\frac{\partial \dot{N}_{H_2}}{\partial m_{cat}} = \dot{r}_{H_2}
$$

(6.9)

In the parameter estimation, the reactor design equation was solved using the MATLAB® ordinary differential equation solver `ode15s`, a variable step,

variable order solver typically employed for stiff problems. For details on the algorithm, see [127]. The parameter estimation itself was conducted using the MATLAB® non-linear least square minimization tool `lsqnonlin` with the default method based on a trust-region-reflective algorithm. For details on the algorithm, see [128, 129]. To reduce the likelihood of a local minimum/an influence of the start parameters in the optimization, a multi start approach was employed restarting the optimization one thousand times with randomly chosen start parameters. The parameter set resulting in the smallest sum of residual squares was defined as the 'global' optimum.

Standard deviations of the estimated parameters were derived via a linear approximation model and calculated as the square root of the ith element of the covariance matrix Cov calculated via equation (6.10). Thereby, $\hat{J}$ is the jacobian matrix in the optimum, estimated by `lsqnonlin`, and s^2 the estimate of the variance of the residuals (= sum of residual squares divided by the difference between number of data points and number of estimated parameters).

$$Cov = s^2 \left(\hat{J}' \hat{J} \right)^{-1} \tag{6.10}$$

The employed pattern search-based experimental optimization strategy started from a selected center with values for the influencing parameters, namely palladium loading and calcination temperature, considered as promising by pre-evaluation. After the determination of the objective function value in the center, a pattern of variations of the center with a defined variation width of the influencing parameters was created and scanned for possible improvements in the objective function value. Noteworthy, every scanned variation represented a complete active material synthesis, a reaction engineering characterization of the resulting active material, and the subsequent evaluation via kinetic parameter fitting and the calculation of the objective function value. If one of the scanned variations had a higher value in the objective function value, the respective variation was defined as new center for the optimization and the procedure was started from new, by experiment and evaluation. Generally, locking onto a new center may be done directly if an improvement is found or after a full scan of the pattern only. In the present work, a full scan strategy was employed. If multiple variations showed an improvement in the objective function value, the variation with the best objective function value was chosen as new center. In theory, a reduction of the pattern variation width can be employed to reduce the resolution around a center, if necessary. On a side note, the search strategy was inspired by the MATLAB® global optimization toolbox optimization tool `patternsearch`.

6.2.1.4. Catalyst support synthesis

As described in [93], the catalyst support employed in the present work, a silica aerogel, was synthesised in a standard sol-gel synthesis route with subsequent supercritical drying of the resulting alcogel. The synthesis was adapted from literature, see [83]. The synthesis in a first step delivered aerogel monoliths that were ground and mixed with active material powders to yield a photocatalyst with tuned active material loading and consequently tuned optical transport properties.

A standard synthesis started by mixing 7.835 g TMOS (Arcos Organics) with 4.946 g methanol as solvent (Carl Roth GmbH) resulting in a molar ratio of TMOS and methanol of 1:3. In a second beaker 0.567 g of 25 wt % ammonia solution were mixed with 150 g deionized water (MilliQ from Merck) to yield a molar ratio of ammonia and water of 0.001:1. 3.723 g of the prepared ammonia solution were subsequently dropped in approx. 60 s into the prepared TMOS solution under rigorous stirring resulting in a TMOS to methanol to water to ammonia ratio of 1:3:4:0.004. Immediately after mixing was completed, the reacting sol was poured into methanol wetted polytetrafluoroethylene moulds that were subsequently covered with a watch glass until gelation occurred (approximately after 7-9 min at room temperature). Directly after gelation, the moulds with the gels were submerged in a large quantity of fresh methanol (Carl Roth GmbH) and aged for seven days. The methanol supernatant was exchanged after two and four days of aging. In the last step the aged silica alcogel was removed from the methanol bath and dried for 20 h in a supercritical carbon dioxide atmosphere (12 MPa, 60 °C) using a HPE-300 supercritical drier from EUROTECHNICA GmbH. During drying, a continuous flow of carbon dioxide (200 $\mathrm{L\,h^{-1}}$) was pumped through the drying chamber.

The obtained aerogel monoliths, for illustration see figure 2.5, were ground by hand using a mortar and sieved with an Analysette 3 PRO sieving machine from Fritsch GmbH to isolate silica aerogel particles with a size between 100 µm and 200 µm.

6.2.1.5. Optical property determination

Liquids

Absorption coefficients of liquid homogeneous solutions, such as potassium ferrioxalate solutions employed in the experiments reported in chapters 7 and 8, were determined from absorbance measurements conducted with an Agilent 8453 UV Vis desktop spectrometer. For water born solutions, a sample of the solution was filled into an optical quartz glass cuvette with an optical path length of 10 mm and its absorbance was measured relative to the same quartz glass cuvette filled with deionized water. The chosen reference, deionized water in the same quartz glass cuvette, facilitates the evaluation of the raw data drastically. Assuming the reference solution had the same refractive index than the sample solution, partial reflections on the phase boundaries between sample and quartz glass and between quartz glass and air are the exact same in reference and sample measurement and can, consequently, be neglected in the evaluation. The determined absorbance can be attributed to the sample absorption solely. Consequently, the absorption coefficient can be calculated from the determined absorbance via equation (6.11).

$$\sigma_a = A_e/L \qquad\qquad (6.11)$$

On a side note, most, if not all spectrometers return in their standard operation mode the decadic absorbance rather than the Napierian absorbance. The Monte Carlo ray tracing environment developped and employed in the present work (details see chapter 4) uses Napierian absorption coefficients. The absorbance raw data obtained from a spectrometer must, therefore, be corrected prior to the evaluation to yield the Napierian absorbance. The Napierian absorbance equals the decadic absorbance multiplied with the natural logarithm of ten ($A_e = ln(10)A_{10}$).

If not indicated else wise, the covered optical band in the measurements ranged from 350 nm to 550 nm and was conducted with a spectral resolution of 1 nm.

Powder beds

Effective absorption and scattering coefficients of powder beds were derived from total transmission and reflectance measurements of powder samples in

a 1/Q/2 Spectrosil® quartz glass cuvette from Starna Scientific with an optical path length of 2 mm. The measurements were conducted with a Lambda 1050 UV Vis spectrometer equipped with an integrating sphere assembly. Reflectance measurements were taken relative to a PTB traceable Zenith polymer diffuse reflection standard from Sphere Optics GmbH and corrected accordingly prior to further processing (details on the correction see chapter 6.1.1.5 and equation (6.2)). In a standard measurement, powder samples were filled into the cuvette, which subsequently was placed at the transmission port of the integrating sphere of the spectrometer. After the total transmission measurement, the cuvette was carefully removed from the transmission port and mounted on the reflection port of the integrating sphere to measure the corresponding total reflectance. This procedure was repeated three times to yield three data sets comprising total transmittance and reflectance data of the powder bed in the cuvette. Between the three repeat measurements, the cuvette with the powder sample was shaken to check for the influence of the random orientation and distribution of the particles in the cuvette. If not indicated else wise, measurements were taken in the optical band from 350 nm to 800 nm with a spectral resolution of 1 nm.

Due to the complex radiation transport phenomena during the measurement, including partial reflections at the phase boundaries between air and quartz glass cuvette, partial reflections at the phase boundaries between powder sample and quartz glass cuvette, and absorption and scattering in the powder sample itself, the evaluation of the total transmission and reflectance measurements aiming for effective transport properties of the powder bed is non-trivial.

In the present work, the evaluation was conducted based on optical simulations of the sample cell. For the simulations, the developed Monte Carlo ray tracing environment was employed, details see chapter 4. Briefly, the strategy in the evaluation was to find absorption and scattering coefficients of the powder bed in simulations that result in a close map of simulated and experimental transmittance and reflectance data.

In the optical simulations, the sample cell was modelled as a hollow cuboid with outer dimensions of 12.5 x 4.5 x 45 mm (width x thickness x length) with a wall thickness of 1.25 mm. These dimensions equal the manufacturer indications for the employed quartz glass cuvette. The hollow internal of the cuboid was modelled to be filled with a translucent (= scattering and absorbing) medium with a refractive index equal to unity. The filling represented the powder bed in the simulations. A refractive index equal to unity is a close approximation of the typical refractive index of silica aerogels, see for
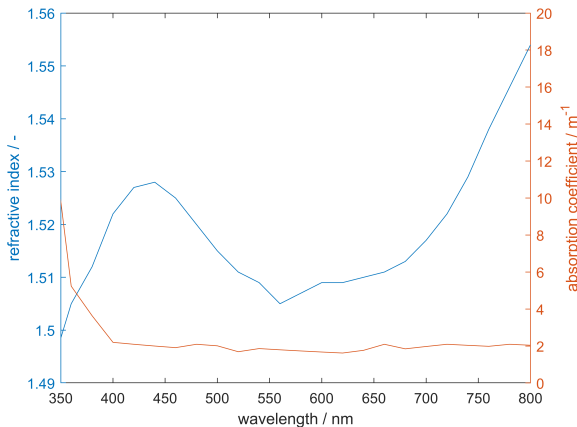
Figure 6.7.: Assumed refractive index and absorption coefficient for Spectrosil® quartz glass (material of UV Vis cuvettes). Data equals literature indications, see [123].

instance [130]. The cuboid itself was assumed to be transparent with a refractive index and absorption coefficient equal to literature indications for quartz glass, details see figure 6.7. The spectrometer light source was modelled in the simulation as a rectangular surface emitting an ideally collimated beam hitting the sample cell at the front face. The light source size was set to 3 x 14 mm, which equalled the determined spot size in the spectrometer setup. The target metrics of the simulation, total reflection and transmittance of the modelled sample cell, were determined from absorption ray counts of ideally black probes placed directly before and behind the cuboid front and back face in the simulation domain. Total transmittance and reflectance were determined by relating the number of rays absorbed by the two ideally black probes to the number of simulated rays.

Prior to all simulations the number of simulated rays necessary in order to achieve convergence in the target metrics was determined in a ray study assuming an exemplary absorption and scattering coefficient of the powder bed equal to 200 m^{-1}. In the ray study the sample cell was simulated with increasing number of simulated rays (starting from 1 k rays and increasing up to 100 k rays). For each number of simulated rays five repeat simulations were conducted. From the five repeat simulations the relative empirical standard deviation in the target metrics were derived. The necessary number of simu-
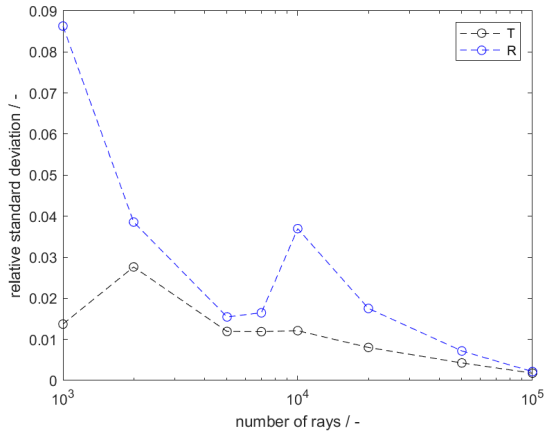
Figure 6.8.: Ray study conducted for the optical simulations of the UV Vis sample cell in UV Vis measurements of powder beds depicting the relative empirical standard deviation of simulated transmittance (black) and reflectance (blue) of the sample cell as function of the number of simulated rays. The simulations were conducted assuming light with a wavelength of 405 nm and absorption and scattering coefficient of the powder bed equal to 200 m^{-1}.

lated rays was finally chosen in a way that the relative empirical standard deviation in the target metrics was less than 1 %. According to the result of the ray study, see figure 6.8, this condition is given for simulations with more than 50 k rays. The number of rays in all simulations used for experimental data evaluation was therefore set to 50 k rays.

In order to reduce the computational effort in the parameter estimation aiming for a suitable estimate of absorption and scattering coefficients of a powder sample in a measurement, a sample cell characteristic was derived. This characteristic is a map comprising transmittance and reflectance data of the simulated sample cell for different absorption and scattering coefficients of the powder bed. The covered range in absorption and scattering coefficient in the derived map was 0 m^{-1} to 4 000 m^{-1} with a resolution of 20 m^{-1} resulting in a total number of 40 000 simulations to run. The computation time for these simulations was roughly six days on a work station equipped with an AMD Ryzen™ Threadripper™ 3960X CPU. For a presentation of the derived characteristic, see figure 6.9.

On a side note, the characteristic was derived for optical properties of quartz glass at 405 nm. Strictly speaking, for each relevant wavelength an own char-
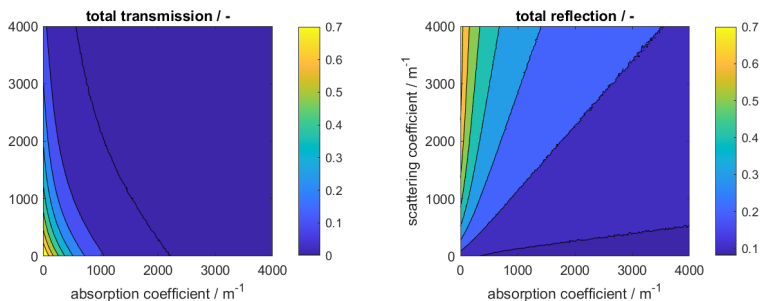
Figure 6.9.: Simulated characteristic of the UV Vis sample cell employed in UV Vis measurements of powder beds depicting the transmittance (left) and reflectance (right) of the sample cell for different absorption and scattering coefficients of the simulated powder bed. The 40 000 simulations underlying the characteristic were conducted assuming optical properties of quartz glass at 405 nm.

acteristic must be derived. However, in practice, the dispersion of the optical properties of quartz glass in the relevant UV Vis band is not pronounced. The influence of the optical property dispersion of the quartz glass was, nevertheless, checked in a dispersion study prior to the experiment data evaluation varying the mapped wavelength, or optical properties of quartz glass, respectively, for a powder bed with an absorption and scattering coefficient equal to 200 m^{-1}, see figure 6.10. Obviously, the influence of the dispersion of the optical properties of quartz glass on the target metrics is negligible and one single sample cell characteristic is sufficient for the envisaged data evaluation, as can be seen from the transmittance and reflectance steady behaviour for different wavelengths.

Absorption and scattering coefficients of powder beds finally were estimated using the derived sample cell characteristics and the MATLAB® non-linear least square minimization tool `lsqnonlin` with the default method based on a trust-region-reflective algorithm. For details on the algorithm, see [128, 129]. The optimization attempted to minimize the sum of residual squares of all three conducted repeat measurements at once. The simulated sample cell characteristic was linearly interpolated during the minimization using a linear fit derived with the MATLAB® fit tool `griddedInterpolant`. To reduce the likelihood of a local minimum/an influence of the start parameters in the parameter estimation, a multi start approach was employed restarting the optimization thirty times with randomly chosen start parameters in the range
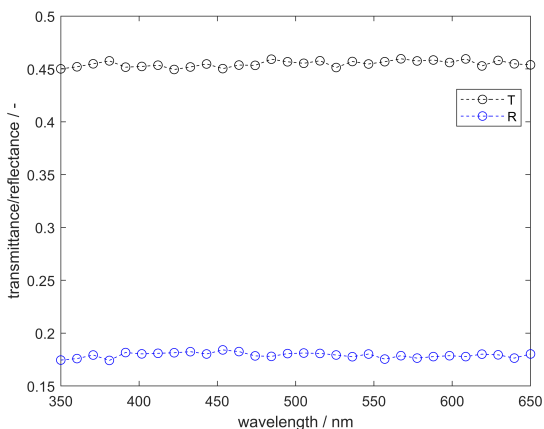
Figure 6.10.: Dispersion study of the sample cell in UV Vis transmittance and reflectance measurements of powder beds depicting the influence of the dispersion of the optical properties of quartz glass on the simulated transmittance (black) and reflectance (blue) of the sample cell. The absorption and scattering coefficient of the powder bed were set to 200 m^{-1} in the underlying simulations.

of 0 m^{-1} to 4 000 m^{-1}. The optical property set resulting in the smallest sum of residual squares was defined as the 'global' optimum.

Standard deviations of the estimated optical properties were derived via a linear approximation model and calculated as the square root of the ith element of the covariance matrix *Cov* calculated via equation (6.10). For further details on error estimation in parameter estimation, see analogue proceeding in kinetic parameter estimation in chapter 6.2.1.3.

6.2.2. Results and discussion

6.2.2.1. Active material development

The optimization of the titania-based active material model system employed in the present work (details on the material system synthesis, see chapter 6.2.1.1, and details on the optimization strategy, see chapter 6.2.1.3) started at a center of 0.5 wt % palladium loading and a calcination temperature of 375 °C. The variations around the center point in the first scanned pattern were
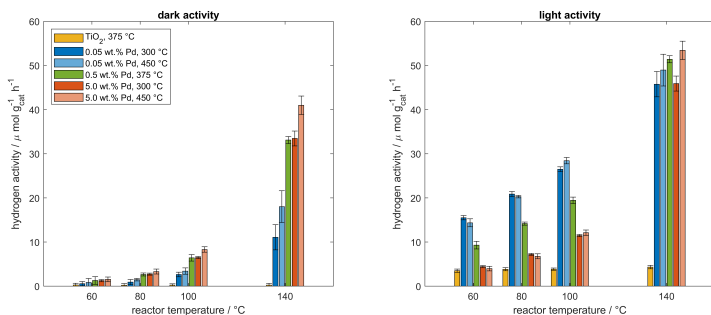
Figure 6.11.: Experimentally determined hydrogen activities in the dark (left) and under simulated solar irradiation (right) at varying reactor temperature and for different synthesized active materials. The drawn data sets represent the first pattern of the active material optimization process with a pattern center at a palladium loading of 0.5 wt % and a calcination temperature of 375 °C (green bars) and the corresponding center variations with 5 wt % (red bars) and 0.05 wt % (blue bars) palladium loading and calcination temperatures of 450 °C and 300 °C, respectively. The yellow bars represent the hydrogen activity of a reference titania catalyst without any palladium loading.

5 wt % and 0.05 wt % for the palladium loading and 450 °C and 300 °C for the calcination temperature. For details on the corresponding recipes, see table 6.1. For illustration of the scanned pattern, see dark red points in figure 6.13. On a side note, the muffle furnace employed in the active material calcination showed a significant but at least reproducible offset in the regulated target temperatures, resulting in significantly higher calcination temperatures than the desired set temperatures. As a consequence the active material indented to be calcined at 300 °C was calcined at approximately 360 °C. For set temperatures of 400 °C and 450 °C real temperatures of approximately 440 °C and 515 °C resulted.

The hydrogen activity (definition see equation (6.5)) at different reactor temperatures for the five active material variations of the first pattern in the optimization process is depicted in figure 6.11, determined in the dark and under simulated solar irradiation.

The comparison of the derived hydrogen activities with the activity of a reference active material, a pure titania powder without any co-catalyst, first of all lines out a drastic effect of the palladium co-catalyst. For illustration compare blue, green and red bars with yellow bars in figure 6.11. Throughout all active materials in the first scanned pattern, the activity of the active materials with

Table 6.1.: Recipes for titania-based active material synthesis yielding variants with different palladium loadings. $V_{H_2O,I}$ represents the water volume used for dispersing the titania precursor. $V_{H_2O,II}$ represents the water volume used for dissolving palladium nitrate hydrate. For details on the synthesis procedure, see chapter 6.2.1.1.

w_{Pd} / wt %	m_{TiO_2} / g	$m_{Pd(NO_3)_2}$ / g	$V_{H_2O,I}$ / mL	$V_{H_2O,II}$ / mL
5.0	8.112	1.005	20	8
0.5	4.248	0.053	10	3
0.1	12.909	0.030	35	3
0.05	12.909	0.015	35	3
0.025	17.200	0.010	43	3

palladium loading is significantly higher than the activity of the reference active material without any co-catalyst.

Compared to the clear effect of the palladium co-catalyst on the hydrogen activity of the examined active materials, the calcination temperature has a significantly weaker impact on the hydrogen activity. In the dark and at higher temperatures under simulated solar irradiation, a higher calcination temperature induces a slightly increased hydrogen activity. For illustration see bars in different color intensities in figure 6.11. At reactor temperatures below 100 °C and under simulated solar irradiation this picture inverts.

A comparison of the hydrogen activities determined with and without simulated solar irradiation further lines out a clear effect of light onto the hydrogen activity. For illustration compare left and right graph in figure 6.11. Especially for the active material variations with a low palladium loading and at temperatures below 100 °C reactor temperature, the irradiation drastically increases the observed hydrogen activity. The ratio between hydrogen activity under simulated solar irradiation and hydrogen activity in the dark for the active material with a palladium loading of 0.05 wt % and a calcination temperature of 300 °C for instance peaks at 60 °C reactor temperature with a value of approximately 27, meaning that the hydrogen activity is increased by a factor of 27 through illumination with AM1.5D simulated solar light under those conditions.

The temperature trends of the hydrogen activity derived for both dark conditions and for simulated solar irradiation indicate an approximately exponential increase of the hydrogen activity with increasing temperature. For

Table 6.2.: Estimated activation energies for the dark and light contribution in the overall reaction rate of hydrogen. For details on the assumed hydrogen reaction rate law, see chapter 6.2.1.3.

w_{Pd} / wt %	T_{calc} / °C	$E_{a,light}$ / kJ mol^{-1}	$E_{a,dark}$ / kJ mol^{-1}
0.05	300	17.4±0.7	63±6
0.05	450	17.70±0.11	57±5
0.5	375	13.91±0.08	63.4±1.3
5.0	300	17.3±0.4	67±3
5.0	450	26±5	66±2
0.025	225	19.2±0.6	37±4
0.025	375	18.7±0.8	43±5
0.1	225	18.5±1.0	48±2
0.1	375	15.9±0.8	53.0±1.5

illustration, see trends in bars in both graphs in figure 6.11. Noteworthy, the temperature dependency of the hydrogen activity is less pronounced for the activities derived under simulated solar irradiation. The latter also becomes evident in a comparison of derived activation energies for the light and dark contribution to the overall hydrogen reaction rate (for details on the assumed rate law and parameter estimation, see chapter 6.2.1.3). The activation energy for the dark contribution lies in the range of 50-70 kJ mol^{-1}, whereas the activation energy for the light contribution lies in the range of 10-30 kJ mol^{-1}, compare table 6.2. This difference in the dark and light activation energy is typical for photoreactions and can, therefore, be interpreted as another indication for a clear photoelectro chemical contribution underlying the reaction network.

In the first scanned pattern the active material variant with a palladium loading of 0.05 wt % and a calcination temperature of 300 °C shows the highest objective function value, see figure 6.13. Also, this variant shows the highest ratio between observed hydrogen activities under simulated solar light and hydrogen activities in the dark. To further improve the active material, a second pattern was spun with its center at 0.05 wt % and a calcination temperature of 300 °C. The variations around that second center were 0.025 wt % and 0.1 wt % for the palladium loading and 225 °C and 375 °C for the calcination temperature. For details on the corresponding recipes see table 6.1.

For illustration of the second pattern, see light red circles in figure 6.13. On a side note, again, the muffle furnace employed for the calcination in the active material synthesis route showed a significant but reproducible offset in the regulated temperature. For set temperatures of 225 °C and 375 °C real temperatures of approximately 280 °C and 445 °C resulted.

The hydrogen activities under dark conditions and under simulated solar light determined for the five active material variants in the second scanned pattern are depicted in figure 6.12. The resulting overall picture is similar to the picture in the first scanned pattern: (1) The palladium co-catalyst drastically increases the observable hydrogen activity compared to the reference active material without any catalyst loading. (2) Compared to the effect of the palladium loading, the calcination temperature has a significantly weaker effect on the hydrogen activity. (3) At reactor temperatures below 100 °C light significantly increases the hydrogen activity. And (4) the temperature trends in the hydrogen activity are exponential. Again the apparent activation energies derived for the light contribution to the overall reaction rate are with values below $20 \, \text{kJ} \, \text{mol}^{-1}$ significantly smaller than the activation energies determined for the dark contribution ($30\text{-}60 \, \text{kJ} \, \text{mol}^{-1}$), see table 6.2.

In the second pattern, the variant with a palladium loading of 0.025 wt % and a calcination temperature of 225 °C exhibits the highest value in the objective function of the optimization, see figure 6.13. Compared to the starting point of the optimization, the objective function value could be increased by a factor of roughly six through the two steps in the optimization. The found optimal active material with a palladium loading of 0.025 wt % and a calcination temperature of 225 °C further has a significant hydrogen activity and a clear activity boost induced by irradiation with solar light. Having achieved the overall aim to prepare an active material with a clear photocatalytic contribution in the underlying reaction mechanism, the optimization was stopped after the second scanned pattern.

Summarizing, palladium added as co-catalyst to the titania active material increases the observed hydrogen activities, whereas the calcination temperature is of secondary importance. A high palladium loading entails a significant hydrogen activity in the dark with the trend towards higher activities with increasing palladium loading, compare figures 6.11 and 6.12 left. The opposite is the case for the hydrogen activity under simulated solar irradiation. Here, a lower palladium loading increases the hydrogen activity, compare figures 6.11 and 6.12 right. The effect of palladium on the hydrogen activities in the dark could be explained by the generally good (thermo-) catalytic properties of the noble metal palladium. It is also employed as thermal catalyst in
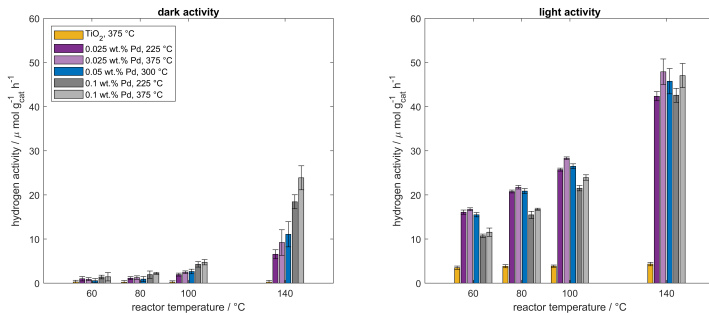
Figure 6.12.: Experimentally determined hydrogen activities in the dark (left) and under simulated solar irradiation (right) at varying reactor temperature and for different synthesized active materials. The depicted data sets represent the second pattern of the active material optimization process with a pattern center at a palladium loading of 0.05 wt % and a calcination temperature of 300 °C (blue bars) and the corresponding center variations with 0.1 wt % (grey bars) and 0.025 wt % (purple bars) palladium loading and calcination temperatures of 375 °C and 225 °C, respectively. The yellow bars represent the hydrogen activity of a reference titania catalyst without any palladium loading.
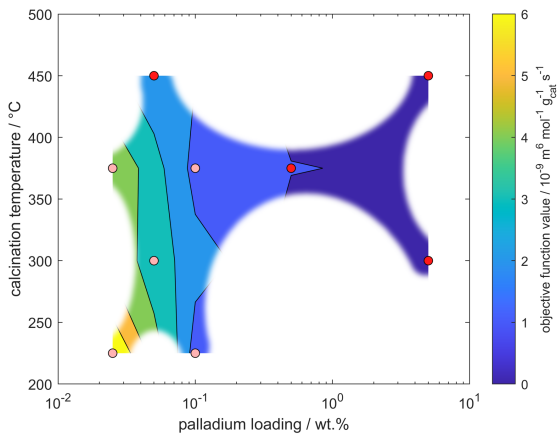
Figure 6.13.: Objective function in the active material optimization drawn over the two synthesis parameters, namely palladium loading and calcination temperature, addressed in the optimization. The dark and light red circles represent the center and center variations scanned in the first and second pattern of the optimization respectively. The color map depicts the objective function value experimentally determined for each point. Values of the color map between the points are linearly interpolated. The cutouts in the contour plot highlight that the objective function value is only known in the parameter space in which experiment were conducted.

methanol reforming at elevated temperatures [131]. The 'positive' effect of palladium on the hydrogen activity under simulated solar irradiation could be attributed to the provision of active sites with a low overpotential for hydrogen evolution, which, due to the band edge potentials, is difficult on pure titania (see discussion chapter 2.1.2.2). A shading effect of palladium particles on the surface of titania particles on the other hand could explain the observation, that increasing the palladium loading over a critical value induces a decrease of the hydrogen activity under simulated solar irradiation. However, these interpretations need further examination in detailed material scientific studies.

Importantly, it must be stated at this point that the derived kinetic parameters (activation energies and frequency factors) and the assumed hydrogen reaction rate law are of no value for photoreactor design. They have only been introduced to better distinguish between different active material variants. The employed photoreactor is badly defined with regard to its optical operating conditions, the wavelength of incident light, but especially the local volumetric rate of photon absorption. The derived photoreaction kinetics are, therefore, not transferable to other reactor geometries or illumination scenarios, respectively. For a detailed discussion of this general reaction engineering challenge in the field of active materials development, see chapter 2.2.1.

6.2.2.2. Optical properties of model photocatalysts

Potassium ferrioxalate

The absorption coefficient of the 2 mM potassium ferrioxalate solution (details on the preparation see section 7.2.3) employed in potassium ferrioxalate photoreduction experiments was determined as described in section 6.2.1.5. The determined absorption coefficient is depicted in figure 6.14 together with the assumed refractive index. The refractive index of the 2 mM potassium ferrioxalate solution is assumed to equal the refractive index of water and is taken from literature. For details, see [132].

The absorption coefficient of the 2 mM potassium ferrioxalate solution is strongly dependent on the wavelength with a steep increase of the absorption coefficient with decreasing wavelength below approximately 450 nm. For a wavelength of 500 nm and above, the absorption coefficient of the 2 mM potassium ferrioxalate solution almost diminishes. The latter indicates that
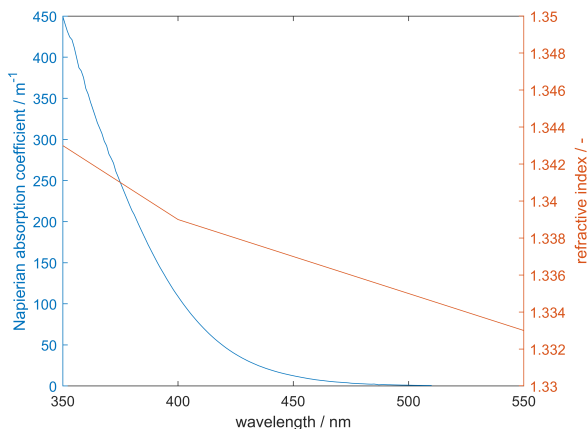
Figure 6.14.: Optical transport properties, absorption coefficient and refractive index, of 2 mM potassium ferrioxalate solution.

even though the quantum yield of the potassium ferrioxalate photoreduction is significantly different from zero up to a wavelength of 550 nm, see figure 6.15, it is hard to achieve a photoreduction with photons in the band from 500 nm to 550 nm due to the diminishing absorption.

Titania-based photocatalyst

Effective scattering and absorption coefficients of the silica aerogel powder (details on the synthesis see section 6.2.1.4) employed as active material support in the present work were determined as described in section 6.2.1.5. The total transmission and reflectance measurements underlying the analysis first of all revealed a good reproducibility of the measurements. This indicates a negligible influence of the precise but random alignment of the particles in the silica aerogel particle fixed bed on the effective radiation transport properties of the latter. All three data sets derived from the three conducted repeat measurements with a random agitation of the quartz glass cuvette between the repeat measurements lie less than 10 %rel apart, see figure 6.16. The derived effective absorption and scattering coefficients further highlight the pronounced suitability of the employed silica aerogel powder as active material support in solar driven photocatalysis. Even though the effective
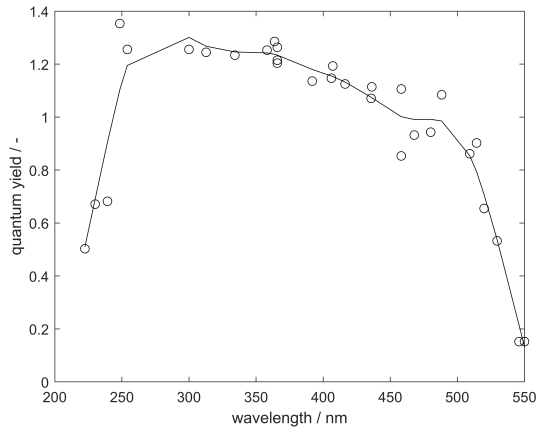
Figure 6.15.: Literature data for the quantum yield of the potassium ferrioxalate photoreduction in the optical band from 250 nm to 550 nm together with a smoothing fit facilitating data processing in reactor simulations. Data is taken from [124].
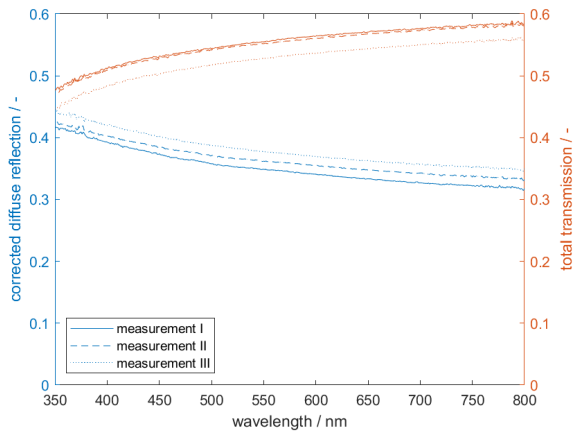
Figure 6.16.: Total transmittance (orange) and reflectance (blue) of the silica aerogel powder employed as active material support in a quartz glass cuvette with an optical path length of 2 mm. The three different line styles represent the three conducted repeat measurements.

119
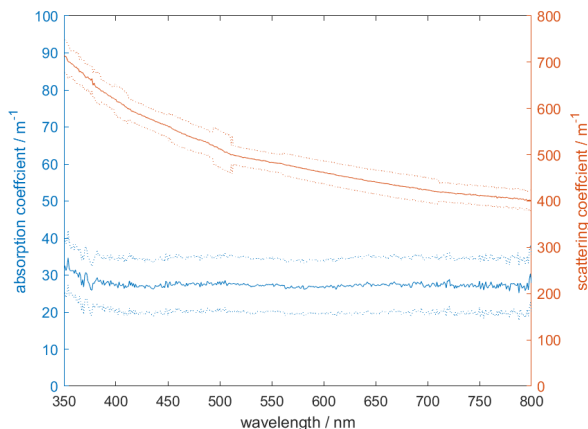
Figure 6.17.: Effective absorption (blue) and scattering (orange) coefficient of the silica aerogel powder employed as active material support in the present work. Solid lines represent the estimated value and dotted lines the estimated standard deviation.

scattering coefficient of the fixed bed is significant, the effective absorption coefficient is low in the UV and Vis band, see figure 6.17. The latter ensures negligible parasitic absorption by the support which is a necessary property of any photocatalyst support. For further discussion see chapter 2.1.3. On a side note, the increase of the scattering coefficient with decreasing wavelength is characteristic for nano-particulate systems with particle sizes well below the wavelength of incident light and may be explained by Rayleigh scattering. For further details, see for instance [86].

Effective optical transport properties of the employed methanol photo-reforming photocatalyst, the titania-based active material supported on the employed silica aerogel powder, were determined for four different volumetric active material loadings between $5 \, \mathrm{mg \, mL^{-1}}$ and $30 \, \mathrm{mg \, mL^{-1}}$. The proceeding in the measurement and evaluation was as described in section 6.2.1.5.

The examined samples were prepared by mixing 1 mL of prepared silica aerogel powder with according quantities of activated active material. The active material activation, or partial reduction of the raw material, respectively, was conducted as described in chapter 6.2.1.2 but without a reaction engineering characterization following the activation step.

For the reproducibility of the conducted transmission and reflectance mea-
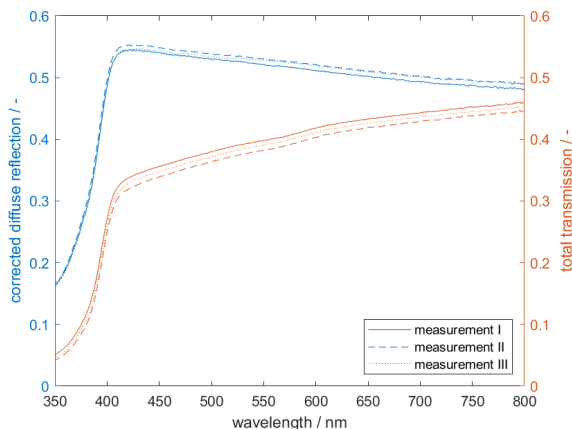
Figure 6.18.: Total transmittance (orange) and reflectance (blue) of the model photocatalyst employed in the present work in a quartz glass cuvette with an optical path length of 2 mm and a volumetric active material loading of 5 mg mL^{-1}. The three different line styles represent the three conducted repeat measurements.

surements, apparently, the same holds than for the pure aerogel powder. Repeat measurements do not lie further apart then 10 %rel, see figure 6.18. The dispersion of the active material, consequently, can be considered homogeneous and the precise but random alignment of the particles in the fixed bed, apparently, does not significantly influence the effective radiation transport in the latter.

A comparison of the total transmittance and reflectance data for the pure silica aerogel powder and the model photocatalyst already indicates significant differences in the system behaviour. Total reflectance is increased through the added active material, whereas the transmittance is decreased especially in the UV band. For illustration compare figures 6.16 and 6.18. Noteworthy, even though the dilution of the active material is high in the employed photocatalysts, the transmittance of the 2 mm thick fixed bed in the quartz glass cuvette is already below 10 % in the relevant UV band, even for the lowest of all examined volumetric active material loadings, see figure 6.18. This indicates that absorption and scattering coefficients take extreme values in the UV band and deep penetration of UV radiation into larger volumes of the examined photocatalyst is hard to achieve.

This preliminary conclusion is supported by the derived effective absorption
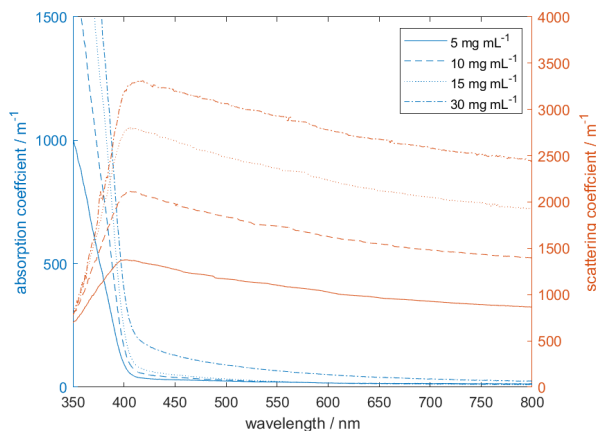
Figure 6.19.: Effective absorption (blue) and scattering (orange) coefficient of titania-based photocatalysts with different volumetric active material loading between 5 mg mL^{-1} and 30 mg mL^{-1}. For the sake of clarity standard deviations are not displayed.

and scattering coefficients, see figure 6.19. The scattering coefficient of prepared photocatalysts lies around 1 000 m^{-1} throughout the UV Vis band for an active material loading of 5 mg mL^{-1} and well above 1 000 m^{-1} for higher catalyst laodings. Interestingly, in the Vis band, the absorption coefficient of the photocatalysts is not significantly higher than the absorption coefficient of the pure aerogel support. This picture drastically changes in the UV band (below 400 nm), where the absorption coefficient takes impressive values sky-rocketing with decreasing wavelength. This characteristic absorption behaviour of the photocatalysts can be traced back to the absorptive properties of titania that, as any other semi-conductor, strongly absorbs photons that carry an energy equal to or greater than its band gap energy. From the onset of the absorption coefficient increase in the UV band evident in figure 6.19, therefore, the band gap energy can be estimated. For all four photocatalysts the onset lies in the range of 400 nm to 410 nm which equals a band gap energy of 3.02 eV to 3.09 eV. The latter is in good agreement with literature indications on the band gap of titania, see for instance data given in [133].

6.3. Interim summary

Summarizing, the developments in the field of reactor component materials mainly delivered a manufacturing pathway for 3D-printed structural components for photoreactors with complex shapes and optical silver coatings with high reflectivity in the relevant optical band. The described 3D-printing manufacturing pathways and post-print treatment strategies, thereby, allow a precise tuning of the reflection characteristics of the obtained optical surfaces ranging from perfectly diffuse to almost ideally specular reflection characteristics.

On the photocatalyst side, the developments primarily delivered a titania-based model active material with a distinct photocatalytic contribution in the overall reaction rate and a negligible dark activity. Additionally, a simple and straight forward active material support strategy was introduced that allows to tune the optical transport properties of a photocatalyst resulting from the optical dilution of an active material on a translucent active material support. Importantly, the material development presented in this chapter does not include the determination of the quantum yield achievable with the introduced titania-based photocatalyst. As mentioned, the knowledge of the latter as function of the operating conditions is the essential prerequisite for successful high efficiency photoreactor design. The determination of the latter, however, is a complex and challenging task being subject to an own chapter, see chapter 7.

As a side product, in this chapter, methods for the determination of optical transport properties including reflectivity and reflection characteristic of optical surfaces, refractive index and absorption coefficients of window materials, and absorption and scattering coefficients of photocatalysts were established/developed. Their application primarily delivers the material data basis for meaningful optical simulations of the reactor systems described in chapters 7 and 8. On an optical engineering point of view, further, the determined optical properties of photocatalyst fixed beds, effective absorption and scattering coefficients, indicate that even very dilute photocatalysts may possess extreme absorption and scattering coefficients. The latter might entail radiation transport hindrances in photocatalyst beds of larger geometrical dimensions. This conclusion points out, that photoreactors that guarantee a high catalyst usage likely include some sort of catalyst bed structuring with characteristic lengths in the range between millimeters and micrometers and, thereby, represent a sophisticated strategy to distribute photons in the whole

reaction volume.

7.   Quantum yield measurements

As evident from the photoreactor design equation, equation (2.9), and as discussed in section 2.2.2 and chapter 3, the knowledge of the quantum yield of a photocatalyst as function of the operating conditions, namely temperature, reactant concentration, wavelength, and local volumetric rate of photon absorption, is a necessary precondition for successful high efficiency photoreactor design. The quantum yield, thereby, represents the efficiency metric of the photocatalyst. It describes how efficient absorbed photons are used to contribute to the production.

Noteworthy, comparisons of different photocatalysts should also be made, if possible, based on quantum yield data rather than photocatalytic activities. This is because photocatalytic activities are no material intrinsic property but a system property resulting from the complex interplay of light source, radiation transport in the employed photoreactor, and the reaction engineering properties of the photocatalyst. Conclusions drawn from the evaluation of photocatalytic activities determined in different experimental setups, for instance, in setups of different working groups, therefore, may be misleading. The ability to precisely determine quantum yields in photocatalytic reactions as function of the operating conditions is, consequently, a key skill in the field of photochemical engineering. It requires special photoreactors that are able to precisely define all operating conditions with as low as possible gradients. To the author's knowledge, literature reported reactor systems employed for the determination of quantum yields especially exhibit a deficiency in the definition of the local volumetric rate of photon absorption. For a detailed discussion, see section 2.2.1. The concept introduced herein is an attempt to overcome this drawback by proposing an isophotonic photoreactor, a photoreactor with zero or small gradients in the local volumetric rate of photon absorption, and a precisely defined methodology for the determination of quantum yields in gas, liquid, and multi phase photoreactions.

In the following, in a first step, the approach is introduced and validated by the determination of the quantum yield of the potassium ferrioxalate photoreduction (details see section 6.2) and a subsequent comparison of the obtained

data to literature data. In a second step the approach is employed to determine the quantum yield of the optimized titania-based photocatalyst model system (details see section 6.2.2.1) as function of temperature, reactant concentration, wavelength, and local volumetric rate of photon absorption. The detailed information obtained in this analysis, lastly, allows a fundamental discussion of the influence of the reaction engineering properties of photocatalysts onto photoreactor design.

The presented concept and structure of explanations are in parallel to the corresponding journal publication, see [93].

7.1. Introduction

7.1.1. Approach

From a very basic point of view, the determination of quantum yields in photoreactions requires both the knowledge of the number of production events, in case of photoredox reaction the number of transferred electrons, and the number of absorbed photons at a specific wavelength, see definition of the quantum yield in equation (2.7).

The determination of the number of production events, in most cases, is straight forward, since the product concentrations are experimentally accessible via a measurement of product concentrations in the reactor effluent via standard analytical methods. Common analytical methods employed for this task include liquid or gas chromatography and UV Vis spectroscopy.

As already discussed in section 2.2.1, the challenge of quantum yield measurements typically arises from the need to determine the number of photons at a specific wavelength absorbed by the photocatalyst. For a brief discussion see also [27]. On a side note, 'photocatalyst' in the following context refers to the reactant mixture, if a homogeneous photocatalytic reaction is considered, like for instance the potassium ferrioxalate photoreduction, and to the particulate photocatalyst, if a heterogeneously catalysed photoreaction is considered, like, for instance, in titania-catalysed methanol photo-reforming.

In the approach presented herein, the number of photons absorbed at a specific wavelength by the photocatalyst is determined via spectrally resolved 3D optical simulations conducted with the introduced MATLAB®-based Monte Carlo ray tracing simulation environment. For details on the method, its MATLAB® implementation, and its validation via a comparison to literature
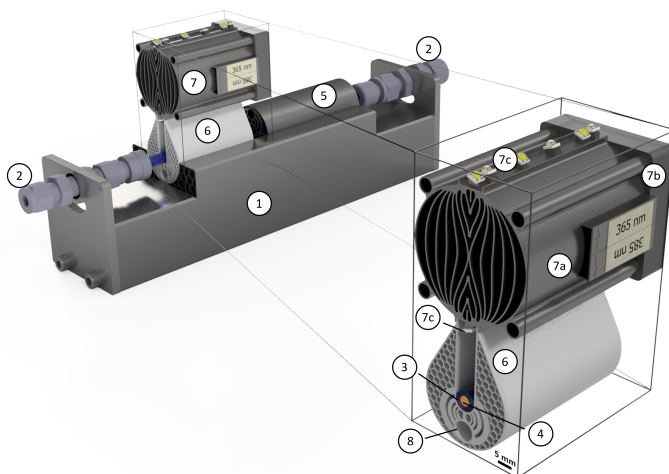
Figure 7.1.: Rendering of the CAD model of the isophotonic photoreactor developed and employed for the determination of quantum yields in liquid, gas, and multi phase photoreactions. The reactor assembly core components are a 3D printed reactor body (1), and commercial fluid connectors (2) that hold in place a commercial quartz glass capillary (3). The quartz glass capillary surrounds the reaction volume (4). Heating cartridges inserted into bores in 3D printed and removable heating brackets (5) and the 3D printed axially movable optics module (6) allow precise temperature control of the capillary. The custom LED light source module (7) is made up of a 3D printed cooler body (7a) equipped with a commercial cooler fan (7b), and two times six high power SMD LEDs (7c). Figure is reprinted from corresponding open access publication with CC-BY license, [93], Copyright 2022.

models for radiation transport in simple geometries, see chapter 4. The simulations are conducted assuming the precise geometry of the especially designed isophotonic photoreactor, figure 7.1, and the specific optical properties of the reactor components and the photocatalyst in the reaction zone. For details on the determination of the latter, see chapter 6. The simulations deliver the spectral radiation transport efficiency of the assembly that represents the ratio between the number of photons absorbed in the reaction volume at a specific wavelength and the number of photons sent into the reactor aperture by the employed LED light source modules at the same specific wavelength, equation (7.1). Mathematically, the spectral radiation transport efficiency equals the reaction volume integral of the local volumetric rate of photon
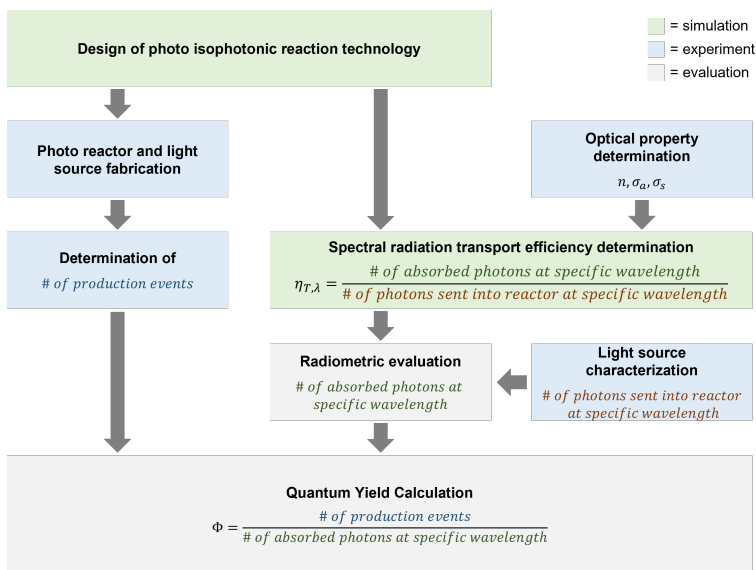
Figure 7.2.: Graphical summary of the steps of the developed approach for the determination of quantum yields in gas, liquid and multi-phase photoreactions. Figure is reprinted from corresponding open access publication with CC-BY license, [93], Copyright 2022.

absorption at a given wavelength ($L_{p,\lambda}^a$) related to the surface integral of the spectral irradiance ($E_{p,\lambda}$) in the reactor aperture at the same wavelength.

$$\eta_{T,\lambda} = \frac{\# \ of \ absorbed \ photons \ at \ specific \ wavelength}{\# \ of \ photons \ sent \ into \ reactor \ at \ specific \ wavelength}$$

$$= \frac{\int L_{p,\lambda}^a dV}{\int E_{p,\lambda} dA} \qquad (7.1)$$

In order to derive the number of photons absorbed by the photocatalyst at a specific wavelength from the spectral radiation transport efficiency, the number of photons sent into the reactor aperture by the light source must be determined via a radiometric characterization of the latter.

All experimental and simulative tasks and steps comprised by the approach are graphically summarized in figure 7.2.

7.1.2. Employed photoreactor

The isophotonic photoreactor developed and employed for quantum yield measurements in the present work comprises three core components: (1) a reactor body with fluid connectors and a quartz glass capillary surrounding the reaction volume, (2) an optics module, and (3) an LED light source module. For details on the assembly see figure 7.1. The LED light source module comprises two times six high power SMD LEDs mounted on a 3D-printed cooler body that shine their light into the optics module. The optics module is 3D-printed and silver coated without surface smoothing post-treatment of the 3D-printed raw part and, consequently, shows diffuse reflection characteristics. The optics module guides/distributes photons sent into the reactor by the LED light source module into the reaction volume comprising the examined photocatalyst. The position and orientation of the SMD LEDs on the LED light source module are numerically optimized in a way that the gradients in the local volumetric rate of photon absorption are minimal. For details on the proceeding in this optimization see section 7.2.1.2. The wavelength of absorbed photons can be varied by changing the LED light source module to another LED light source module with different SMD LEDs having different emission peak wavelengths. For a list of all LEDs with different peak wavelengths employed in the present work, see table 7.1.

The temperature of the photocatalyst can be controlled by heating cartridges in the optics module and movable heating brackets that are mounted around the quartz glass tubing. The temperature of the catalyst bed is additionally measured with a thermocouple that is axially inserted into the fixed bed.

7.2. Methods

7.2.1. Optical simulations

7.2.1.1. Simulation setup

The simulation domain in the conducted optical simulations of the reactor assembly comprised the optics module, the backing of LED cooler body, the quartz glass capillary, and the reaction volume. All together those components equal the presented components in the zoom in in figure 7.1. The optics module and the LED cooler body were modelled as opaque objects with a

Table 7.1.: List of manufacturer technical specifications on the SMD LEDS employed for quantum yield measurements. All LEDs were commercial parts provided by Würth Elektronik eiSos GmbH & Co. KG.

peak λ / nm	emission band half width / nm	model designation
365	15	WL-SUMW Ceramic Waterclear
385	15	WL-SUMW Ceramic Waterclear
395	15	WL-SUMW Ceramic Waterclear
405	15	WL-SUMW Ceramic Waterclear
450	15	WL-SMDC Horticulture
520	35	WL-SMDC Mono-color
590	15	WL-SMDC Mono-color
635	15	WL-SMDC Mono-color

wavelength-dependent reflectivity and ideal diffuse reflection characteristics throughout the whole mapped optical band. The assumed optical transport properties equal the ones given in figures 6.1 and 6.3. The quartz glass capillary was modelled as a transparent object with a wavelength-dependent refractive index and absorption coefficient. The assumed optical transport properties equal the ones given in figure 6.4. For the simulations of the validation experiment, the potassium ferrioxalate photoreduction, the reaction volume was modelled as a transparent object with wavelength-dependent refractive index and absorption coefficient. The assumed optical transport properties equal the ones illustrated in figure 6.14. In the simulation of the titania-based model photocatalyst, the reaction volume was modelled as a translucent object with wavelength-dependent absorption and scattering coefficient and a constant refractive index equal to unity. The assumed absorption and scattering coefficients equal the ones given in figure 6.19 for a volumetric active material loading of 10 mg mL^{-1}.

The six SMD LEDs of the LED light source modules were modelled as rectangular surfaces with an edge length of 1.8 mm showing Lambertian emission characteristics. Both the assumed dimensions and the emission characteristics were defined in accordance with the technical data sheets of the employed SMD LEDs.

The primary target metric of the simulations, the spectral radiation transport

efficiency, was determined from ray counts relating the number of rays absorbed by the reaction volume ($N^a_{rays,RV}$) to the number of simulated rays ($N_{rays,sim}$), which equals the number of emitted rays, equation (7.2).

$$\eta_{T,\lambda} = \frac{N^a_{rays,RV}}{N_{rays,sim}} \tag{7.2}$$

The second target metric of the simulations was the density distribution of the local volumetric rate of photon absorption in the reaction volume. This density distribution was derived from absorption ray counts in 6230 voxels that together shape the reaction volume. The local volumetric rate of photon absorption in one voxel was derived via relating the number of rays absorbed in the voxel to the total number of simulated rays (= the number of emitted rays) and the voxel's volume. Weighting of the derived values with the total spectral emission of the LED light source modules lastly delivers the local volumetric rate of photon absorption.

The number of rays needed in order to achieve convergence in the primary target metric was determined in a ray study previous to the simulations. In this ray study, simulations of the titania-based photocatalyst at 405 nm and with increasing number of simulated rays were conducted. The number of simulated rays was varied between 10 k rays and 5 M rays. For each number of simulated rays, five repeat simulations were conducted and the corresponding spectral radiation transport efficiency was derived. The number of rays was finally chosen in a way that the relative standard deviation in the determined five values of the spectral radiation transport efficiency was well below 1 %. This criterion is fulfilled for a number of rays higher than 500 k rays, see figure 7.3. The number of simulated rays was lastly set to 2 M rays in all simulations.

If not stated else wise the optical simulations were conducted in the band from 350 nm to 550 nm with a spectral resolution of 2.5 nm.

7.2.1.2. Numerical light source optimization & fabrication

The LED light source modules were optimized in order to achieve an isophotonic reaction volume. More precisely, the orientation and the axial positions of the six symmetrically aligned SMD LEDs were optimized. First, the SMD LEDs were alternatingly inclined for 20° to prevent a direct illumination of the reaction volume and distribute emitted photons via diffuse reflections
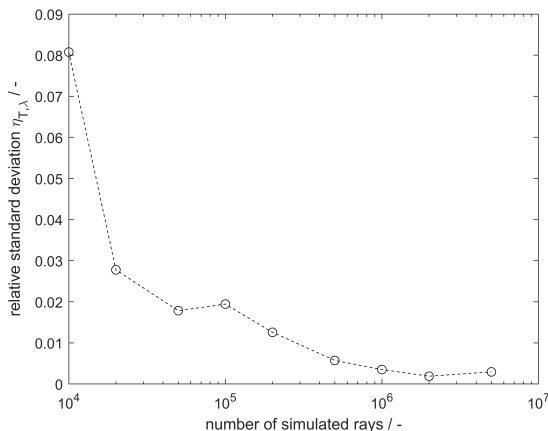
Figure 7.3.: Relative standard deviation in the spectral radiation transport efficiency in simulations of the photoreactor assembly employed for quantum yield measurements as a function of the number of simulated rays. For the reaction volume optical transport properties of the titania-based model photocatalyst were assumed. The simulated wavelength was 405 nm.

on the optics module cavity wall. For illustration of the inclined LEDs, see zoom in see figure 7.5. Second, the axial positions were optimized to reduce axial gradients in the radial mean value of the local volumetric rate of photon absorption to the smallest possible extend. This optimization task was conducted with the MATLAB® global optimization toolbox minimization tool `surrogateopt`. The objective function in the optimization was the variance of the radial mean value of the local volumetric rate of photon absorption calculated from the radial mean values in twenty equally thick slices of the reaction volume in the quartz glass capillary. For an illustration of the applied subdivision of the reaction volume, see figure 7.4. The optimal positions of the LEDs slightly depend on the optical transport properties of the photoreactor assembly. The LED positions realized in the present work were optimized assuming the optical transport properties of the photoreactor components at a wavelength of 405 nm and an absorption and scattering coefficient of the reaction volume equal to 200 m^{-1} and 400 m^{-1}, respectively.

The derived positions of the LEDs were lastly realized by designing small inclined pillars in the respective positions on the LED cooler body. For an illustration, see figure 7.5. After printing of the cooler body (details on the printing process see section 6.1.1), the LEDs were soldered to wires with de-
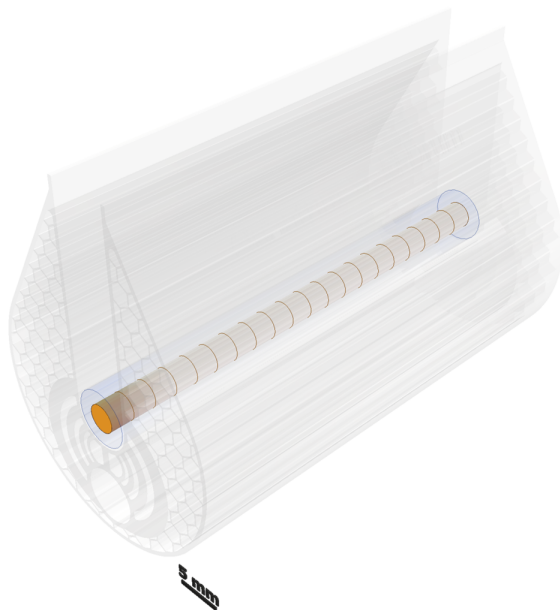
Figure 7.4.: Rendering of CAD model of the optics module of the photoreactor employed for quantum yield measurements with quartz glass capillary (blue) and reaction volume (orange) illustrating the reaction volume subdivision introduced for the LED light source module optimization. Figure is reprinted from corresponding open access publication with CC-BY license, [93], Copyright 2022.

fined length for the electrical connection and glued onto the pillar structures with thermally conducting glue (HERNON 746 from ALUTRONIC Kühlkörper GmbH & Co. KG).

7.2.2. Light source characterization

The total spectral emission (q_λ) of the employed LED light source modules was determined via a radiometric characterization of the LED light source modules using a RIGO801-300 photogoniometer from TechnoTeam GmbH. The goniometer was equipped with a calibrated UV Vis spectrometer measuring the spectral irradiance (E_λ) in the positions on the spherical cap scanned

Figure 7.5.: Rendering of a the CAD model of the LED light source modules shining their light into the optics module of the developed isophotonic photoreactor. The small inclined pillars on which the SMD LEDs are placed ensure the derived optimal inclination and positions of the LEDs resulting in an isophotonic reaction volume.

by the goniometer. The spherical cap scanned in the measurements covered an azimuth angle (Θ) from 0° to 360° and a polar angle (φ) from 0° (= perpendicular view onto the LED light source module) to 110° and had a radius of 310 mm. The step width in the azimuth and polar angle scan in the measurements was 5° resulting in a total number of roughly 3200 points on the scanned sphere cap to measure. The target metric, the total spectral emission, was finally derived from the measured spectral irradiance via a sphere surface integral, equation (7.3), approximated via a discrete sum over the 3200 points.

$$q_\lambda = \int E_\lambda dA = r_{goniometer}^2 \iint E_\lambda sin(\Theta)d\Theta d\varphi \qquad (7.3)$$

In a standard goniometer measurement, the LED light source modules were mounted into an especially designed and 3D printed holder in the goniometer's center and aligned to precisely meet the goniometer's center position, which equals the center of the scanned sphere cap. The LED light source modules were then supplied with a drive current by a high precision PTNhp

125-10 current source from Heinzinger electronic GmbH and operated at least for 10 min in order to achieve a stable temperature and light emission. The LED temperature was observed with a thermocouple glued onto the ceramic support of one of the six SMD LEDs on the LED light source modules. During the measurement, the LED drive current was additionally measured with a LMG95 precision power meter from ZES ZIMMER Electronic Systems GmbH. To avoid any influence of ambient light on the measurement, the goniometer measurements were conducted in a dark laboratory at the Institute of Light Technology at the Karlsruhe Institute of Technology.

UV Vis spectra were taken from 350 nm to 800 nm with a spectral resolution of 1 nm. To reduce the influence of measurement noise at the lower end of the measurement range (below 360 nm) raw spectra were fitted to a Gaussian curve and noisy data at the lower end of the measurement range was replaced by values derived from the fit function.

To map the conditions in the reaction engineering experiments as precise as possible, it is desirable to run goniometer measurements at each LED drive current setting used in the reaction engineering experiments. However, the time needed for one goniometer measurement yielding the total spectral emission of an LED light source module at one drive current setting renders this approach impractical. This especially holds in the present work, because of the large number of drive current settings in the reaction engineering experiments used (six) and the number of LED light source modules built for the experiments (eight).

To reduce the number of needed goniometer full scans, for each LED light source module a full scan was only conducted for the highest of all drive current settings. The total spectral emission of the LED light source modules at deviating drive current settings was subsequently estimated from the ratio of a single point spectral irradiance measurement at a polar angle of 0° at the individual drive current setting and the spectral irradiance in the same position in the full scan measurement. The total spectral emission was lastly calculated via equation (7.4).

$$q_\lambda\left(I_{LED}\right) = q_\lambda\left(I_{LED,scan}\right) \frac{E_{\lambda,\varphi=0°}\left(I_{LED}\right)}{E_{\lambda,\varphi=0°}\left(I_{LED,scan}\right)} \tag{7.4}$$

For convenient data handling, the determined emission spectra (= the wavelength course of the total spectral emission) of the LED light source modules were normalized to their area. This area equals the total emission of the LED light source modules (q) . The drive current course of the total emission

of the light source modules derived, is denoted as LED light source module characteristic. Values from the LED light source module characteristic acts a linear scaling factor for the area normalized LED light source emission spectra to yield emission spectra at any drive current setting.

Lastly, the energy-based data for the total spectral emission from the UV Vis measurements was converted to number-based data via equation 7.5. Thereby, h represents the Planck constant and ν the frequency of the corresponding wavelength.

$$q_{p,\lambda} = \frac{q_\lambda}{h\nu} \tag{7.5}$$

7.2.3. Potassium ferrioxalate photoreduction

As introduced in section 6.2, equation (6.4), potassium ferrioxalate undergoes a photoreduction when irradiated with photons with a wavelength in the band from roughly 250 nm to 550 nm. Since the first reported works of Hatchard and Parker in 1956 reporting the quantum yield for this reaction [134], numerous literature contributions addressed the various aspects of the potassium ferrioxalate photoreduction, see for instance contributions to discussions on common pitfalls [135], application limits [136], or analysis methods [137]. Especially, multiple groups reported detailed information on the quantum yield, see for instance [138]. This renders the potassium ferrioxalate photoreduction a suitable reaction system for the validation of the approach introduced herein.

The experimental procedure in the present work was adapted from the work of Lehóczki et al [137]. In a standard experiment 2 mM potassium ferrioxalate (Alfar Aesar) dissolved in 0.05 M sulfuric acid (Fisher Scientific) was pumped through the photoreactor (details on the setup, see section 5.1.1.2) and collected downstream of the reactor. The LED light source module drive current setting was, thereby, chosen in a way that an average local volumetric rate of photon absorption of 30 µeinstein m^{-3} s^{-1}[1] resulted. Assuming an average quantum yield equal to unity, which is a reasonable guess for the potassium ferrioxalate photoreduction, see figure 6.15, a reaction volume of 0.23 mL, and a flow rate of 2 mL min^{-1}, a local volumetric rate of photon absorption of 30 µeinstein m^{-3} s^{-1} ensures a maximum conversion of 20 %. The latter

---

[1] The unit einstein corresponds to one mol of photons and is used in the present work to distinguish between number of photons and number of molecules/atoms.

avoids precipitation of reaction products and a significant variation of optical transport properties of the reaction tube length, which would not be mapped in the conducted optical simulations.

The concentration of the reaction product, Fe^{II+}, was determined in a standard 1-10-phenanthroline assay. In this assay 8mL of collected reactor effluent were mixed with 3 mL of 0.1 wt % 1,10-phenanthroline solution (0.1 gram in 100 mL deionized water), 4 mL sodium acetate buffer solution (1 M Sodium acetate (Arcos Organics) in deionized water mixed with 0.5 M sulfuric acid (REAGECON) in a volume ratio of 100:63), and 5 mL deionized water in a 20 mL volumetric flask. The absorbance of the colour-intense Fe^{II+} 1,10-phenanthroline complex at 510 nm was determined after roughly 30 min colour development time with a 8453 UV Vis desktop spectrometer from Agilent. A calibration linking the measured absorbance to the desired Fe^{II+} concentration was conducted using Mohr's salt (Arcos organics) solutions with varying Fe^{II+} concentration.

In addition to the 1,10-phenanthroline assay, the potassium ferrioxalate conversion was determined with the online UV Vis spectrometer included in the liquid analysis of the employed test rig (details on the setup, see section 5.1.1.2). The calibration of the online UV Vis analysis linking the absorbance of the reactant solution at 375 nm to the desired Fe^{II+} concentration was conducted with synthesized rector effluent solutions with varying 'simulated' conversion. These solutions were prepared by mixing the 2 mM potassium ferrioxalate stock solution in varying ratio with a solution containing the commercially available reaction products iron-(II)-oxalate (Alfa Aesar), concentration 2 mM, and potassium oxalate (Arcos Organics), concentration 1 mM, in 0.05 M sulfuric acid (Fisher Scientific).

To accurately determine the volumetric production rate of Fe^{II+} in the photoreactor ($\dot{r}_{Fe^{II+}}$) the experiments were conducted at three different flow rates (2.0 mL min^{-1}, 2.6 mL min^{-1}, and 3.7 mL min^{-1}). The resulting three Fe^{II+} concentrations were drawn over the space time (τ) . According to a simple plug flow reactor design equation, equation (7.6), the slope of the resulting line corresponds to the Fe^{II+} production rate if the later is no function of the length of the reaction tube. This assumption is valid if both the quantum yield and the local volumetric rate of photon absorption are no function of the length of the reaction tube ($\dot{r}_{Fe^{II+}} = \Phi L_{p,\lambda}^{a}$).

$$dc_{Fe^{II+}} + \dot{r}_{Fe^{II+}} d\tau = 0 \qquad (7.6)$$

The mean quantum yield in the emission band of the employed LED light source modules was lastly calculated via equation (7.7) relating the rate of Fe^{II+} production events to the rate of photon absorption.

$$\bar{\Phi} = \frac{\dot{r}_{Fe^{II+}}V}{\int \eta_{T,\lambda} q_{p,\lambda} d\lambda} \tag{7.7}$$

Strictly speaking, the quantum yield is defined at a specific wavelength and not in an optical band. Even though the emission band of the employed LED light source modules is narrow, it is not strictly monochromatic and values calculated after equation (7.7) are closer to the definition of a photonic yield than a quantum yield [27]. Therefore, in addition to the calculated mean values, estimated values for the quantum yield in narrow bands are reported. These values are derived in a least square estimation reducing the sum of residual squares derived from the experimental mean values of the quantum yield in all conducted experiments and mean values estimated via equation (7.8). Thereby, $q_{p,i}$ is the photon flux in each of the considered narrow band, Φ_i the corresponding quantum yield, and q_p the total photon flux from the LED light source module.

$$\bar{\Phi}_{estimated} = \sum \frac{q_{p,i}\Phi_i}{q_p} \tag{7.8}$$

7.2.4. Methanol photo-reforming experiments

In the methanol reforming experiments aiming for a determination of the quantum yield as function of the operating conditions, the optimized titania-based active material with a palladium loading of 0.025 wt % and a calcination temperature of 225 °C was employed (details on the synthesis, see section 6.2.1.1, and details on the optimization, see sections 6.2.1.3 and 6.2.2.1). The active material was supported onto a silica aerogel powder with a target active material loading of 10 mg mL^{-1} (details on the catalyst support synthesis, see section 6.2.1.4) to realize an optical dilution of the active material and, thereby, avoid optical transport hindrances in the fixed bed. The desired active material loading was achieved by mixing 3.9 mg of the active material with a particle size of 15-25 μm with 66 mg (corresponds to 0.42 mL) of the prepared aerogel powder with a particle size of 100-200 μm in a precision syringe via rigorous shaking. 36.7 mg (corresponds to approximately 0.23 mL) of the prepared photocatalyst was subsequently transferred into the quartz glass

tubing of the isophotonic photoreactor and held in place by quartz glass wool plugs. The resulting active material mass in the reactor was approximately 2.1 mg.

The experiments were conducted in the test environment described in chapter 5. Gases were fed to the reactor via the gas feed module and conditioned in the gas processing module. The saturator in the gas processing module allowed precise control of the methanol and water vapour concentrations in the reactor feed. The pressure regulating valve downstream the reactor allowed precise pressure control. In the reaction engineering experiments the system pressure was 50 kPa and the nitrogen carrier gas feed was 5 mL_N/min. All species concentrations in the reactor effluent were detected with the calibrated gas chromatograph of the test environment. For details on the calibration of the gas chromatograph procedure see section 5.2.2.

Prior to any methanol reforming experiment, the photocatalyst was activated in situ in a hydrogen atmosphere at 1 MPa system pressure and 260 °C as described in section 6.2.1.2. To avoid high temperatures at the optics module the axially movable optics module's and the removable heating brackets' positions where interchanged during the activation step (for illustration of the optics module and the heating brackets, see rendering of the CAD model of the employed photoreactor in figure 7.1). Subsequent to the activation, the optics module's and heating brackets' positions were interchanged again to place the optics module precisely around the reaction volume with the photocatalyst in place. Importantly, the reactor remains gas tight during this operation which avoids air contact of the activated photocatalyst. Prior to any measurement the reactor and tubing system was purged with nitrogen in a pressure swing purge procedure to remove any detectable traces of hydrogen remaining in the system from the photocatalyst activation. After the gas chromatograph did not detect any hydrogen traces in the reactor effluent, the methanol reforming experiments were started.

To check for a possible influence of mass transport hindrances on the observed reaction rates and derived quantum yields respectively, prior to the kinetic measurements, a control experiment was executed. In this experiment the photocatalyst was operated at a reactor temperature of 80 °C, with the LED light source module with an emission peak wavelength of 395 nm in place, a drive current setting of 0.4 A and a methanol and water vapour feed molar fraction of approximately 4 mol%. The experiment was conducted twice, once with nitrogen and once with helium as carrier gas. Since the diffusion coefficient in helium is roughly three times higher than the diffusion coefficient in nitrogen [139], in case that mass transport hindrances affect the reaction
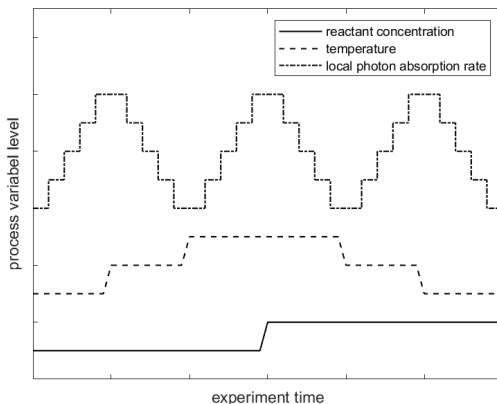
Figure 7.6.: Experiment design during the quantum yield determination of a titania-based photocatalyst varying the local volumetric rate of photon absorption in five levels (dotted line), the reactor temperature (dashed line), and the reactant feed molar fraction (solid line) for one single LED light source module (=one wavelength). Figure is reprinted from corresponding open access publication with CC-BY license, , [93], Copyright 2022.

rate, a difference in the photocatalyst performance should be observed in the two measurements conducted with different carrier gases. Reversely, if there is no observable difference in the photocatalyst performance, mass transport hindrances are negligible.

In the kinetic measurement, the mean local volumetric rate of photon absorption was varied through an LED light source module drive current variation in five levels between 0 µeinstein g_{cat}^{-1} s^{-1} and 100 µeinstein g_{cat}^{-1} s^{-1}. The reactor temperature was varied in three levels from 60 ℃ over 80 ℃ to 100 ℃. The reactant concentration was varied in two levels (3 mol% and 4 mol%) via a temperature variation of the saturator. The experiment design comprised a full factor variation resulting in a total number of 30 operating points per LED light source module. For an illustration of the defined experiment procedure, see figure 7.6. Each operating point was sampled three times with the gas chromatograph before the next operating point was set. The experiment execution was automated for each LED light source module.

To ensure a stable as possible reactant feed supply, the saturator was refilled with fresh methanol water mixture before each experiment procedure conducted with one LED light source module. Additionally, after each saturator
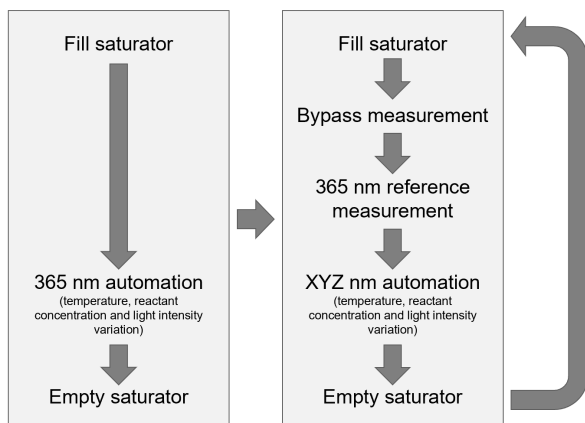
Figure 7.7.: Experiment routine of the conducted kinetic measurement comprising the saturator filling, the bypass measurement, the execution of the experiment automation for one LED light source module (for details on the automation, see figure 7.6), and the reference measurement.
Figure is reprinted from corresponding open access publication with CC-BY license, , [93], Copyright 2022.

refill, a bypass measurement was conducted to check the methanol and water vapour feed molar fractions to lie in the expected range.

To check the photocatalyst for a possible deactivation in the experiment routine, a reference measurement with the 365 nm LED light source module at 60 °C reactor temperature, a methanol and water vapour feed molar fraction of 3 mol% and a mean local volumetric rate of photon absorption of 20 µeinstein g_{cat}^{-1} s^{-1} was conducted after each experiment procedure conducted with one LED light source module.

All in all, the experiment routine as depicted in figure 7.7 was executed. Thereby, the LED light source modules with emission peak wavelength of 365 nm, 385 nm, 395 nm, 405 nm, and 450 nm were used.

The reported mean quantum yield ($\bar{\Phi}_{H_2}$) in the emission band of the employed LED light source modules was finally calculated via equation (7.9) which relates the rate of reduction events (= rate of hydrogen atom reductions) to the rate of photon absorption. Thereby, $\dot{N}_{N_2}$ corresponds to the nitrogen feed rate, and y_{H_2} and y_{N_2} to the hydrogen and nitrogen molar fraction, respectively.

The factor of two in the numerator results from the number of two atoms per hydrogen molecule.

$$\bar{\Phi}_{H_2} = \frac{2\dot{N}_{N_2}\frac{y_{H_2}}{y_{N_2}}}{\int \eta_{T,\lambda}q_{p,\lambda}d\lambda} \tag{7.9}$$

Reported hydrogen activities are calculated in analogy to the proceeding introduced in section 6.2.1.2 via equation (6.5) and relative to the active material mass.

7.3. Results and discussion

7.3.1. Optical simulations

7.3.1.1. Light source optimization

The optimization of the LED light source modules was conducted as described in section 7.2.1.2. The optimization resulted in an alignment of the six SMD LEDs showing a clustering of the LEDs at the front and back face of the LED light source module. For illustration see figure 7.5. More precisely, the derived optimal center positions of the SMD LEDS measured from the front and back face respectively are 1.7 mm, 6.5 mm, and 20.2 mm. The optimization algorithm, therewith, compensates photon losses of over the front and back face of the optics module and ensures an almost constant axial course of the radial mean value of the local volumetric rate of photon absorption, see figure 7.8.

7.3.1.2. System characteristics

Assuming the derived optimal alignment of the SMD LEDs on the LED light source modules as reported in section 7.3.1.1, the spectral course of the spectral radiation transport efficiency was derived in system simulations as described in section 7.2.1.1. Additionally, the simulation results were analysed with respect to the density distribution of the local volumetric rate of photon absorption in the reaction volume. The resulting system characteristics are depicted in figure 7.9 for the validation experiment, the potassium ferrioxalate reduction, and in figure 7.11 for the methanol reforming experiment.
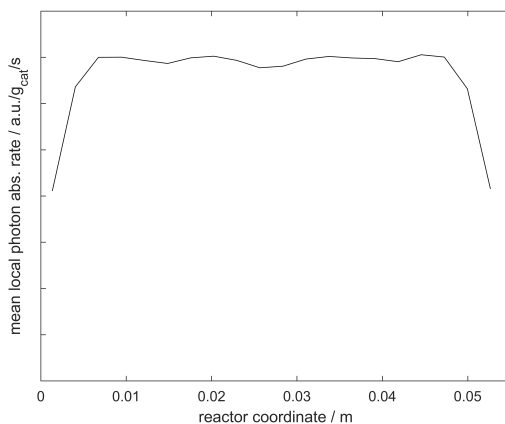
Figure 7.8.: Simulated axial course of the radial mean value of the local volumetric rate of photon absorption in the reaction volume resulting for exemplary optical properties at 405 nm and with optimized positions of the SMD LEDs on the LED light source module of the photoreactor employed for quantum yields measurements. Figure is reprinted from corresponding open access publication with CC-BY license, [93], Copyright 2022.

The spectral course of the spectral radiation transport efficiency for both the potassium ferrioxalate and the titania-based photocatalyst in tendency shows an increase of the spectral radiation transport efficiency with decreasing wavelength. For the titania-based photocatalyst, the increase is sharp, starting at a wavelength of approximately 400 nm, whereas, for the potassium ferrioxalate system, the increase is continuous starting from approximately 500 nm. For both systems, the spectral radiation transport efficiency peaks in the UV band below 400 nm. The observed characteristic spectral course of the spectral radiation transport efficiency emanates from the characteristic spectral courses of the optical properties of the reactor components and the photocatalyst in the reaction tube. Both simulated photocatalysts show a strong increase of the absorption coefficient with decreasing wavelength, see figures 6.14 and 6.19, which induces the tendency of an increasing spectral radiation transport efficiency with decreasing wavelength. At the same, time the reflectivity of the optical coating of the optics module in the UV band decreases with decreasing wavelength, see figure 6.3, which together with the increasing absorption coefficient of the photocatalysts systems entails the observed peak in the spectral course of the spectral radiation transport
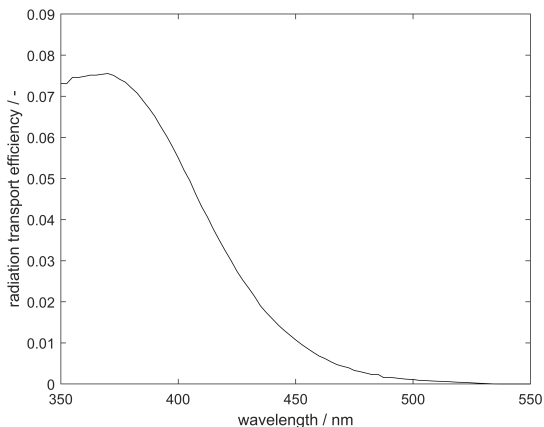
Figure 7.9.: Simulated spectral course of spectral radiation transport efficiency for the potassium ferrioxalate system in the isophotonic photoreactor employed for quantum yield measurements.

efficiency in the UV band.

The density distribution of the local volumetric rate of photon absorption is narrow and symmetrically distributed around its mean value for the potassium ferrioxalate system throughout the mapped optical band, see figure 7.10. The design goal of an isophotonic reaction volume is almost perfectly fulfilled. This is slightly different for the titania-based photocatalyst, see figure 7.12. Here, the density distribution of the local volumetric rate of photon absorption is slightly broadened in the UV band, especially below 370 nm and clearly asymmetrically distributed around its mean value. This indicates that the reaction volume exhibits a slight hot spot in the local volumetric rate of photon absorption likely resulting from the extreme absorption and scattering coefficient in the UV band, see figure 6.19, which hamper a full penetration of the reaction volume by incident photons. Nevertheless, the complete reaction volume is reached by photons. The density distribution does not possess any volume elements with a local volumetric rate of photon absorption equal to zero. Further, most of the volume elements have a volumetric rate of photon absorption close to the mean value. So concluding, even though the design goal of an isophotonic reaction volume is not perfectly achieved for the titania-based photocatalyst, the system is still illuminated
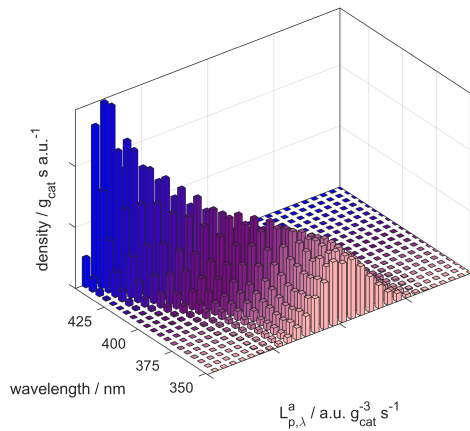
Figure 7.10.: Simulated spectral course of the density distribution of the local volumetric rate of photon absorption for the potassium ferrioxalate system in the isophotonic photoreactor employed for quantum yield measurements.
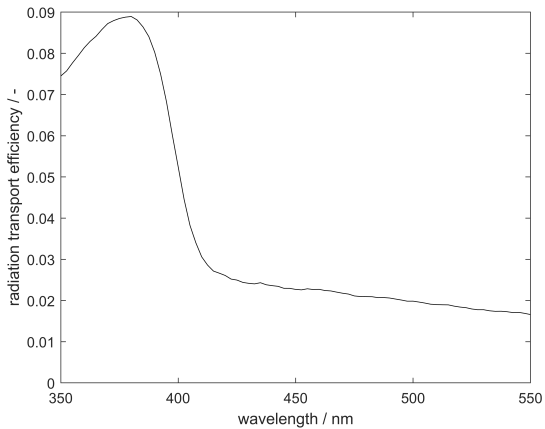
Figure 7.11.: Simulated spectral course of spectral radiation transport efficiency for the titania-based methanol photo-reforming system in the isophotonic photoreactor employed for quantum yield measurements.
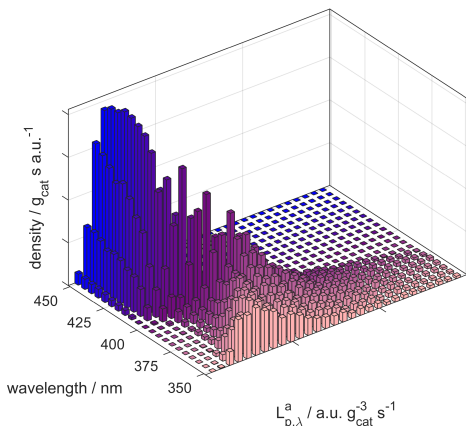
Figure 7.12.: Simulated spectral course of the density distribution of the local volumetric rate of photon absorption for the titania-based methanol photo-reforming system in the isophotonic photoreactor employed for quantum yield measurements.

completely with a narrow density distribution of the local volumetric rate of photon absorption.

7.3.2. Light source characterization

The LED light source module total spectral emission was determined as described in section 7.2.2. The recorded spectral courses of the spectral total emission for the LED light source modules employed in the reaction engineering experiments are depicted in figure 7.13. As indicated by the manufacturer, the emission is narrow banded and centered around emission peak wavelengths of approximately 365 nm, 385 nm, 395 nm, 405 nm, and 450 nm. The raw data shows significant noise at wavelength below 370 nm, see pale coloured spectra in the background in figure 7.13. For all LED light source modules with a peak wavelength above 370 nm this measurement noise is a negligible artefact. For the LED light source module with a emission peak wavelength of 365 nm, however, the employed noise reduction likely distorts the real picture and the obtained data must be handled with care. As introduced in section 7.2.2, the spectra of the total spectral emission depicted in figure 7.13 are normalized to their area. The drive current course of the total
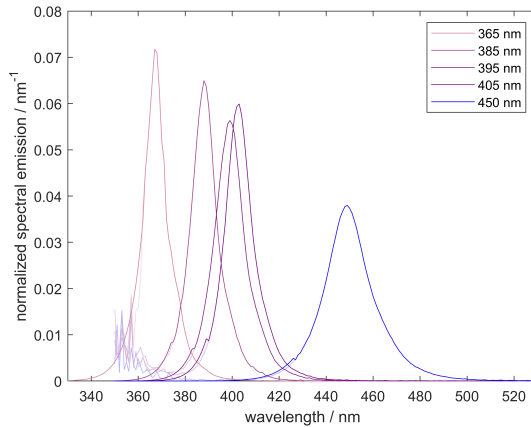
Figure 7.13.: Emission spectra of the LED light source modules employed in experiments for the determination of quantum yields. The spectra depicted in dark colors are noise reduced via a Gaussian curve fit replacing the noisy data at the lower end of the measurement range. The raw data is depicted in light colours in the background. Figure is reprinted from corresponding open access publication with CC-BY license, [93], Copyright 2022.

emission of the LED light source modules, which acts as linear scaling factor for the normalized total spectral emission spectra allowing the calculation of total spectral emission spectra at any drive current setting, was derived as described in section 7.2.2 and is depicted in figure 7.14. As expected for LEDs operated at low percentages of the nominal maximal drive current (which is 1000 mA for the employed SMD LEDs) the total emission of the employed LEDs is almost perfectly linearly dependent on the drive current.

On a side note, the observed linear dependency of the total emission on the LED drive current does not entail a constant LED efficiency as may be intuitively expected. The latter would only result if the LED drive voltage was no function of the LED drive current. However, LEDs typically have a strongly non-linear dependency between the drive current and drive voltage resulting in a non-linear drive current characteristic of the achieved efficiency. This can also be observed for the LEDs employed in the LED light source modules of the present work, see figure 7.15. For small drive currents, the efficiency of the employed LEDs first increases significantly with increasing drive current and subsequently peaks before it decays slowly with a further increase of the drive current. This course is characteristic for most UV LEDs
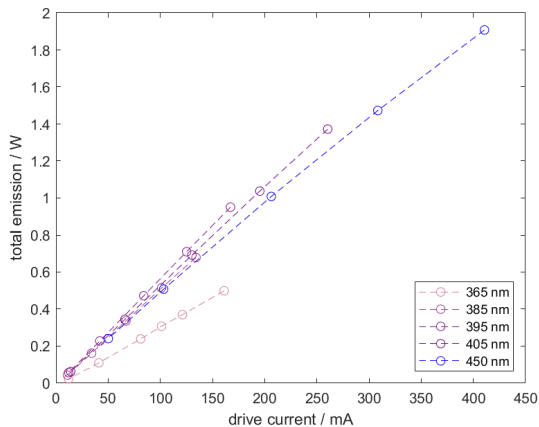
Figure 7.14.: Drive current course of the total emission of the LED light source modules employed for the determination of quantum yields. Figure is reprinted from corresponding open access publication with CC-BY license, [93], Copyright 2022.

and results from their complex electronic structure and multiple drive-current dependent non-radiative recombination mechanisms influencing the observed efficiencies. For a discussion of the quantum efficiency of typical UV LEDs, see for instance [140]. Interestingly, the efficiencies determined for the employed LED light source modules agree well with manufacturer indications (55 % at 500 mA for the SMD LEDs with 385 nm, 395 nm, 405 nm, and 450 nm emission peak wavelength) for all LED light source modules except the one with an emission peak wavelength of 365 nm. For the 365 nm SMD LEDs the manufacturer claims an efficiency of 45 % which is well above the observed value of roughly 30 %. This picture can be interpreted as another indication, that the radiometric characterisation of the LED light source modules at wavelengths below 370 nm must be handled with care. Further, it is likely that the radiometric characterisation underestimates the total emission of the 365 nm LEDs and quantum yields in this band will consequently be overestimated.
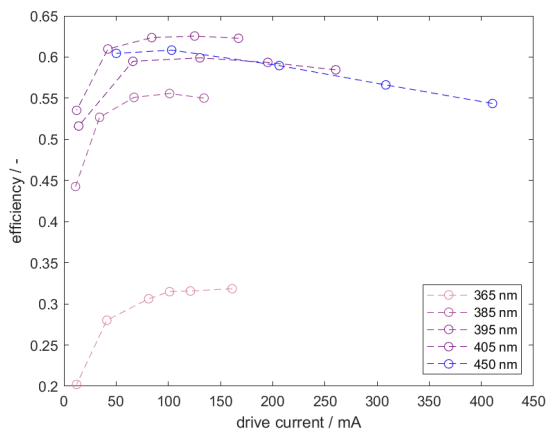
Figure 7.15.: Drive current course of the electrical efficiency of the LED light source modules employed for the determination of quantum yields.

7.3.3. Method validation

7.3.3.1. Calibration of analysis methods

The calibration of both the online and offline UV Vis analysis resulted in a strictly linear dependency of the measured absorbance at defined wavelengths of 375 nm (online analysis) and 510 nm (offline Fe^{II+} assay) and the target metric, the Fe^{II+} concentration or the potassium ferrioxalate conversion, respectively, see figures 7.16 and 7.17. The latter indicates that Lambert Beer's law holds which is to be expected for dilute solutions and, thereby, draws the picture of a valid calibration. Additionally, the molar decadic absorption coefficient of the Fe^{II+}-phenanthroline complex in the Fe^{II+}-assay can be derived from the slope of the calibration curve presented in figure 7.17 with the additional information of the optical path length of the employed cuvette (10 mm). It equals 11119 ± 105 L mol^{-1} cm^{-1} which is in good agreement with literature data, see for instance [124], which supports the conclusion of a successful calibration.
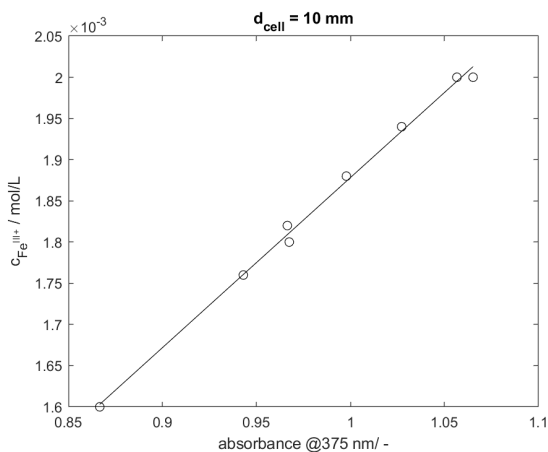
Figure 7.16.: Calibration of the online UV Vis spectroscopy linking the absorbance of the reactor effluent at 375 nm to the remaining concentration of potassium ferrioxalate in potassium ferrioxalate photoreduction experiments. Figure is reprinted from corresponding open access publication with CC-BY license, [93], Copyright 2022.
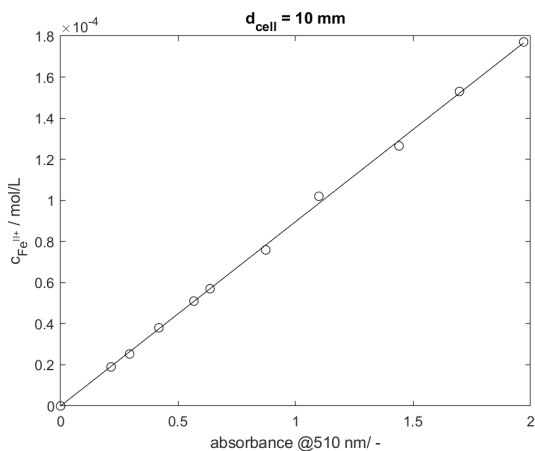
Figure 7.17.: Calibration of the Fe^{II+} assay linking the absorbance of the Fe^{II+}-phenanthroline complex to the concentration of Fe^{II+} in the analyte. Figure is reprinted from corresponding open access publication with CC-BY license, [93], Copyright 2022.

7.3.3.2. Potassium ferrioxalate photoreduction experiments

In a first step, the potassium ferrioxalate photoreduction experiment with subsequent evaluation returned experimental values for the mean quantum yield in the emission bands of the employed LED light source modules, see dark and light grey circles in figure 7.18. The comparison of the determined quantum yield mean values to literature data already indicates a good agreement of the quantum yield data determined via the approach introduced herein and values from literature, see grey circles and empty circles in figure 7.18. Beyond this first indication for a valid approach, the estimated values in 20 nm wide bands with their centers at 360 nm, 380 nm, 400 nm, and 420 nm show excellent agreement to literature data and, thereby, further support the picture of a valid approach, see red circles in figure 7.18. For details on the quantum yield estimation in narrow bands, see section 7.2.3.

The outlier at 360 nm might be a consequence of an underestimation of the total emission of the LED light source module with a peak wavelength of 365 nm emanating from metrological limitations in the employed goniometer setup (for a discussion and further information, see section 7.3.2). The large estimated standard deviation at 420 nm is a consequence of low spectral emissions in this band in all employed LED light source modules, see figure 7.13, and the thereof resulting reduced sensitivity of the estimation model in this band.

Nevertheless, with the presented data in mind, the approach introduced herein appears valid and can be applied to any other gas, liquid, or multi phase photocatalytic reaction system. Higher spectral resolution, or narrower bands in the quantum yield estimation, respectively, would only be possible with data sets comprising data from more LED light source modules with emission peak wavelengths different from those already employed.

7.3.4. Methanol photo-reforming

7.3.4.1. Mass transport hindrances

The experiment examining the influence of possible mass transport hindrances in the photoreaction kinetic measurements revealed a small influence of mass transport phenomena on the observed photocatalytic activities, see figure 7.19. With helium as carrier gas the observed activities are roughly 3 % higher than with nitrogen as carrier gas. The difference is statistically
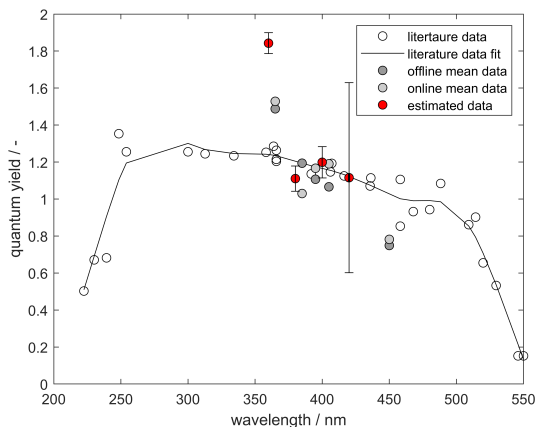
Figure 7.18.: Experimentally determined mean quantum yield data (dark and light grey circles) and estimated quantum yield data (red circles) for the potassium ferrioxalate photoreduction in comparison to literature data (empty circles and solid line). Figure is reprinted from corresponding open access publication with CC-BY license, [93], Copyright 2022.

significant with a significance level of 5 %. Nevertheless, as will be evident in the following, the sensitivity of the observed photocatalytic activity and, thereby, the sensitivity of the quantum yield towards the operating conditions, is significantly stronger than the influence of the carrier gas. Additionally, the Mears criterion, checking for an external mass transport limitation, and the Weisz-Prater criterion, checking for an internal mass transport limitation, are estimated to have values of 0.001 and 0.0002, respectively, which is well below the critical values of 0.15 and 1, respectively. Mass transport hindrances consequently are neglected in the following considerations.

7.3.4.2. Photocatalyst stability

The reference measurements conducted between the LED light source module changes during the kinetic measurement, checking the photocatalyst for a possible deactivation, revealed stable operation without any significant deactivation trend, see figure 7.20. Unfortunately, after the experiments with the 385 nm LED light source module, no reference measurement was conducted. With the first reference measurement with the 365 nm LED light
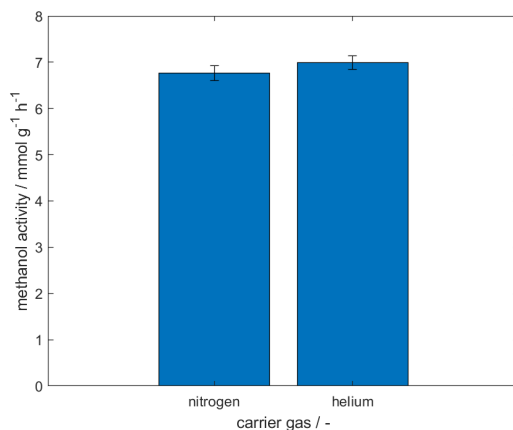
Figure 7.19.: Observed methanol photo-reforming activities with both nitrogen and helium as carrier gas. The experiment was conducted with the LED light source module with an emission peak wavelength of 395 nm, an LED drive current setting of 0.4 A, a reactor temperate of 80 °C and a reactant feed molar fraction of approximately 4 mol%. Figure is reprinted from corresponding open access publication with CC-BY license, [93], Copyright 2022.

source module in place as standard, except the reference activity determined after the 405 nm LED light source module, all observed activity differences are not statistically significant with a significance level of 5 %. Deactivation of the photocatalyst is consequently neglected in the following considerations. On a side note, the observed system stability throughout the whole experiment with 150 operating points can be interpreted as an indication that the model photocatalyst can be operated dynamically without the occurrence of dynamic effects, that accelerate, for instance, the aging of the active material. In the context of solar driven synthesis this property would be a huge advantage compared to thermal processes that typically cannot be operated with dynamic fluctuations at a second the minute time scale.

7.3.4.3. Quantum yield and operating conditions

In the experiments conducted to determine the mean quantum yield in methanol photo-reforming and its dependency on the operating condition, activities as high as 32 $mmol\,g_{cat}^{-1}\,h^{-1}$ and a negligible dark activity below
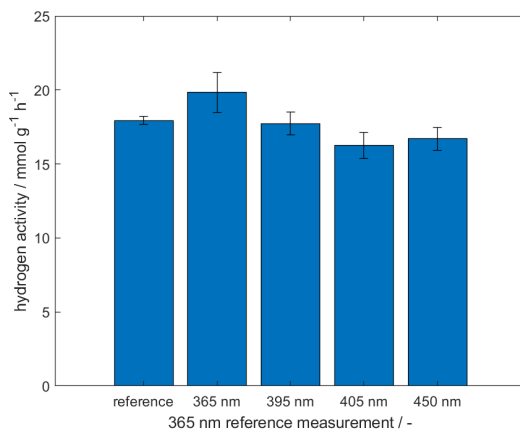
Figure 7.20.: Experimental values for the hydrogen activity in the reference measurements conducted in the course of the kinetic measurement to check for a possible photocatalyst deactivation. The activities were recorded with the 365 nm LED light source module in place operated to achieve a local volumetric rate of photon absorption equal to 20 µeinstein $g_{cat}^{-1}\,s^{-1}$, at a reactor temperature of 60 °C and a reactant feed molar fraction of roughly 3 mol%. Between two reference measurements the photocatalyst was operated roughly 100 h at 30 different operating points. Figure is reprinted from corresponding open access publication with CC-BY license, [93], Copyright 2022.

the detection limit of the employed gas chromatograph, which lies at the given catalyst mass at approximately 0.2 mmol $g_{cat}^{-1}\,h^{-1}$, were observed. On a side note, the lacking detection of a dark activity indirectly indicates that under the operating conditions resulting in an activity of 32 mmol $g_{cat}^{-1}\,h^{-1}$, 80 °C reactor temperature, a mean local volumetric rate of photon absorption of 55 µeinstein $g_{cat}^{-1}\,s^{-1}$, and a reactant feed molar fraction of approximately 4 mol%, the absorption of photons by the photocatalyst increased the methanol reforming activity of the latter by at least a factor of 160. Activity data from dark measurements with the same active material but without any active material support (compare section 6.2.2.1) even indicate a dark activity of only roughly 1 µmol $g_{cat}^{-1}\,h^{-1}$ at 80 °C and, thereby, an activity boost of more than four orders of magnitude through the absorption of photons. At the same time, a comparison of the the measured bulk temperature of the photocatalyst bed with and without the LED light source module switched on and the same reactor temperature setting and reactant feed molar fraction
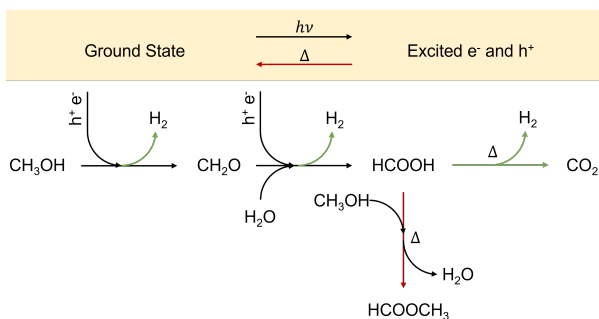
Figure 7.21.: Proposed reaction network for methanol photo-reforming on a semiconductor-based active material including charge carrier separation as preceding step (yellow box) and multiple subsequent electro chemical and thermal (marked with Δ) reactions. The network maps oxidation of methanol over formaldehyde to formic acid which subsequently reacts either with methanol to methyl formate or decomposes to carbon dioxide and hydrogen. Reactions that induce an increase of the determined quantum yield with increasing temperature are drawn with green reaction arrows. Reactions that induce a decrease of the observed quantum yield with increasing temperature are drawn with a red reaction arrow. Figure is reprinted from corresponding open access publication with CC-BY license, [93], Copyright 2022.

indicates an increase of the photocatalyst bed temperature of only 1.1 ℃ induced by the absorption of photons. This picture, a drastic increase of the activity through the absorption of photons without a significant change in the measured photocatalyst temperature, can be interpreted as another sign for a clear photocatalytic mechanism in the underlying reaction network.

The carbonaceous reaction products detected in the experiments were carbon dioxide, methyl formate with traces of formaldehyde in some operating points, together supporting the reaction network illustrated in figure 7.21.

The mean quantum yields derived via equation (7.9) from the recorded raw data are with values as high as 60 % astonishingly high and obviously depend on all varied operating conditions, see figures 7.22, 7.23, and 7.24. The nature of these dependencies is fairly complex.

The clearest influence on the mean quantum yield however, shows the wavelength, see figure 7.22. The clear trend is a decreasing mean quantum yield with increasing emission peak wavelength of the employed LED light source module. Whereas the mean quantum yield determined with the LED light source module with an emission peak wavelength of 365 nm lies in the range of 60 % to 30 %, the mean quantum yield determined with the LED light source module with an emission peak wavelength of 450 nm is equal to zero.
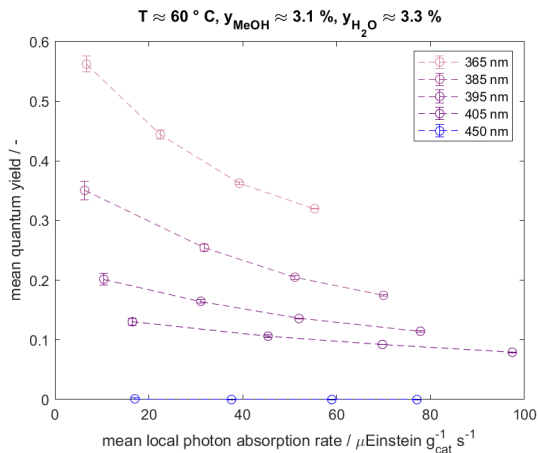
Figure 7.22.: Determined mean quantum yields in methanol photo-reforming as function of the mean local volumetric rate of photon absorption for different LED light source modules with different emission peak wavelength between 365 nm and 450 nm. Data was recorded at a reactor temperature of 60 °C and reactant feed molar fractions of approximately 3 mol%. Figure is reprinted from corresponding open access publication with CC-BY license, [93], Copyright 2022.

Knowing that the band gap of the employed titania-based active material lies just above 400 nm (details see section 6.2.2.2) this is to be expected since only photons with a wavelength smaller than 400 nm are able to excite electrons from the valence band to the conduction band and, consequently, induce a photoreaction. Photons emitted from the LED light source module with an emission peak wavelength of 450 nm all have a wavelength above 400 nm, see figure 7.13. Consequently, assuming a photoelectro chemical reaction mechanism, the experiments conducted with the LED light source module with an emission peak wavelength of 450 nm must result in an apparently inactive photocatalyst or a diminishing quantum yield, respectively. The position of the band gap might also explain to some extend the observed dependency of the mean quantum yield on the emission peak wavelength at emission peak wavelengths below 400 nm. Since the employed LED light source modules are not strictly monochromatic, see figure 7.13, with increasing emission peak wavelength, more and more of the emitted photons do not carry enough energy to surpass the band gap, consequently, do not induce any photoreaction, but nevertheless contribute to the derived photon absorption rate, which results in a smaller calculated quantum yield.
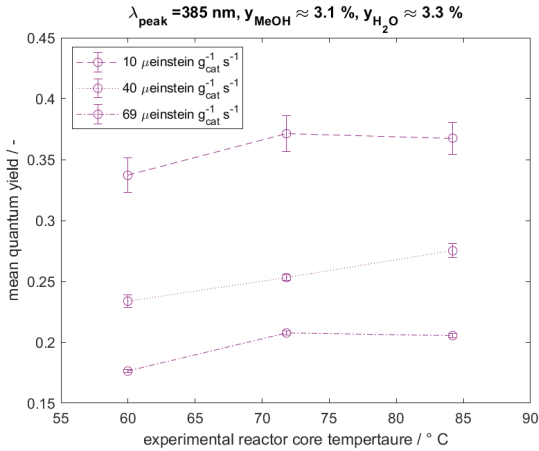
Figure 7.23.: Determined mean quantum yield in methanol -reforming as function of the photocatalyst bed temperature at different values of the mean local volumetric rate of photon absorption between 10 µeinstein g_{cat}^{-1} s^{-1} and 69 µeinstein g_{cat}^{-1} s^{-1}. Data was recorded with the LED light source module with an emission peak wavelength of 385 nm and reactant feed molar fractions of approximately 3 mol%. Figure is reprinted from corresponding open access publication with CC-BY license, [93], Copyright 2022.
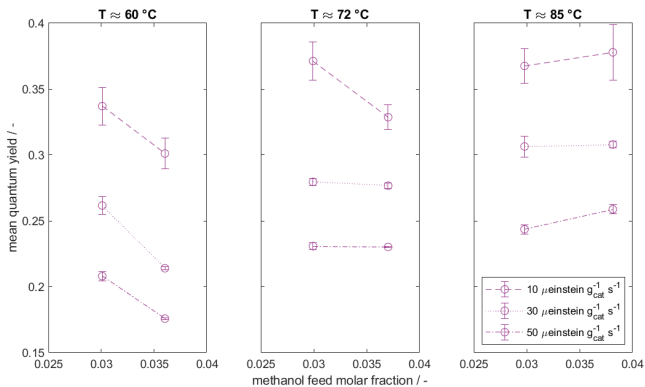
Figure 7.24.: Determined mean quantum yield in methanol photo-reforming as function of the methanol feed molar fraction for different mean local volumetric rates of photon absorption between 10 µeinstein g_{cat}^{-1} s^{-1} and 50 µeinstein g_{cat}^{-1} s^{-1} and different photocatalyst bed temperatures between 60 ℃ and 82 ℃. Data was recorded with the LED light source module with an emission peak wavelength of 385 nm. Figure is reprinted from corresponding open access publication with CC-BY license, [93], Copyright 2022.

157

Besides the obvious dependency of the mean quantum yield on the emission peak wavelength of the employed LED light source modules, the mean local volumetric rate of photon absorption exhibits the second strongest influence on the mean quantum yield, see figure 7.22. Throughout all conducted light source intensity variations, with all LED light source modules with different emission peak wavelengths, at all reactor temperatures, and at all reactant feed concentrations, increasing the mean local volumetric rate of photon absorption induces a decrease of the mean quantum yield. This observation could be the consequence of an intensification of non-radiative relaxation processes of induced charge carriers at higher excited charge carrier densities or local volumetric rates of photon absorption, respectively, see red reaction arrow in yellow box in figure 7.21. As discussed in section 2.1.2.2, even though this recombination mechanism and its influence on the observed quantum yield is not reported clearly for photocatalysts, is is known and well-described from semiconductors in other applications (photovoltaics), see for instance [53, 54].

The observed dependency of the mean quantum yield on the catalyst bed temperature is less straight forward than the dependency of the mean quantum yield on the mean local volumetric rate of photon absorption. Whereas in the exemplary data set presented in figure 7.23, the temperature course of the mean quantum yield shows an optimum for high (69 µeinstein g_{cat}^{-1} s^{-1}) and low (10 µeinstein g_{cat}^{-1} s^{-1}) values of the mean local volumetric rate of photon absorption, at an intermediate value (40 µeinstein g_{cat}^{-1} s^{-1}) of the mean local volumetric rate of photon absorption, the mean quantum yield increases monotonically with increasing temperature. This complex behaviour of the examined photocatalyst can be interpreted as an indication of a complex underlying reaction network with multiple competing thermally activated reactions, see coloured reaction arrows in figure 7.21. On the one hand, thermally activated desorption processes and the thermally activated decomposition of formic acid on the palladium co-catalyst induce an increasing quantum yield with increasing temperature (see green reaction arrows in figure 7.21). On the other hand, an intensification of non-radiative relaxation processes with increasing temperature and the intensification of the side reaction of the reaction intermediate formic acid to methyl formate with increasing temperature induce a decrease of the quantum yield with increasing temperature (see red reaction arrows in figure 7.21).

Both the decomposition of formic acid and the side reaction of formic acid to methyl formate are likely to be intensified by the process intensity or the local volumetric rate of photon absorption, respectively, because the con-

centration of the reaction intermediate formic acid will increase at higher photon-induced methanol reaction rates.

In the exemplary data set in figure 7.23, the temperature optimum of the mean quantum yield at a low value of the local volumetric rate of photon absorption could result from a thermal intensification of the side reaction of formic acid towards methyl formate with increasing temperature. Increasing the local volumetric rate of photon absorption from 10 µeinstein g_{cat}^{-1} s^{-1} to 40 µeinstein g_{cat}^{-1} s^{-1} apparently favours the decomposition reaction of formic acid towards carbon dioxide rather than the side reaction of formic acid to methyl formate, inducing the monotonous increase of the quantum yield with increasing temperature, and indicating different substrate concentration sensitivities of the two reactions that formic acid undergoes. A further increase of the mean local volumetric rate of photon absorption to 69 µeinstein g_{cat}^{-1} s^{-1} intensifies non-radiative relaxation processes whose temperature dependency could explain the observed decrease of the mean quantum yield at temperature above 80 °C.

The sensitivity of the mean quantum yield towards the methanol feed concentration depicted in figure 7.24 can be interpreted as another indication for the influence of the two reactions of the reaction intermediate formic acid on the observed mean quantum yield. At low catalyst bed temperatures and especially at low values of the mean local volumetric rate of photon absorption, increasing the methanol feed concentration induces a slight drop of the observed mean quantum yield. This could be an indication that under these reaction conditions the side reaction of formic acid towards methyl formate is favoured. Increasing the catalyst bed temperature, but especially the mean local volumetric rate of photon absorption inverts this trend. Under these reaction conditions, increasing the methanol feed concentration induces an increase of the observed mean quantum yield supporting the hypothesis that at higher process intensities the decomposition reaction of formic acid towards carbon dioxide is favoured rather than the side reaction of formic acid towards methyl formate.

The overall picture, however, clearly lines out, that the two photon-related operating conditions, wavelength and local volumetric rate of photon absorption, are the important operating conditions in the operation of the exemplary photocatalyst examined herein. Compared to temperature and reactant feed concentration, the influence of wavelength and local volumetric rate of photon absorption on the mean quantum yield is clearly dominant. In the varied ranges, temperature and reactant feed concentration play a minor role.

7.4. Interim summary

Summarizing, with the work presented herein, most importantly, a new approach for the precise determination of quantum yields in gas, liquid, and multi-phase photoreactions is introduced, validated, and subsequently applied to an exemplary heterogeneous photocatalyst. The approach is based on an isophotonic photoreactor and allows the variation of all important operating conditions, temperature, reactant concentrations, wavelength and local volumetric rate of photon absorption. In combination with the automated experiment environment described in chapter 5, the developed isophotonic photoreactor represents a powerful tool for detailed studies of photoreaction kinetics and quantum yields. As evident from the photoreactor design equation, equation (2.9), the knowledge of the dependencies of the quantum yield on the operating conditions is an essential precondition for successful high efficiency photoreactor design. The introduced approach, thus, not only supports the development of high efficiency photocatalysts but also represents a substantial contribution to the field of photochemical engineering.

The insights derived on the materials side further line out the importance of approaches for detailed and precise determination of quantum yields as function of the operating conditions. The significant dependency of the determined mean quantum yield on the mean local volumetric rate of photon absorption entails challenging optimization problems. On the one hand, expensive active materials should be used sparingly in photocatalytic processes in order to keep the capital costs low. This directly implies a high process intensity. On the other hand, if the quantum yield drops with increasing process intensity or with increasing local volumetric rate of photon absorption, respectively, it is favourable from an efficiency point of view to distribute incident photons to a larger amount of active material to avoid an disadvantageous drop of the photocatalytic efficiency of the overall system. Additionally, this optimization problem indicates, that high efficiency production photoreactor designs not only ensure efficient radiation transport from the reactor aperture into the reaction volume but also homogeneously distribute incident photons in the whole reaction volume.

From a material scientific point of view, the finding of the dependency of the mean quantum yield on the local volumetric rate of photon absorption entails that in all works reporting quantum yields, the local volumetric rate of photon absorption should be indicated. This claim is in line with recent works reporting that the quantum yield of the potassium ferrioxalate photoreduc-

tion drops under intense irradiation [136], and works that line out a decrease of the photocatalytic efficiency in photocatalytic processes with increasing light source intensity [141]. In best case quantum yields are determined in isophotonic photoreactors for a maximum meaningfulness, comparability, and reproducibility of the reported data.

Further development of the approach introduced herein should address the employed LED light source modules whose emission bands are narrow but, nevertheless, demand for cumbersome analysis delineating the influence of different wavelength onto the quantum yield. The application of filters mounted in front of the LEDs could be one option to accomplish this task. Further, elevated temperature and intensive UV radiation accelerated tarnishing of the employed silver coatings. The fabrication of the optics module in aluminium, for instance via wire-erosion, could be a promising option to circumvent the need for sensitive silver coatings on the optics module.

8. High efficiency photoreactors for solar-driven synthesis

As summarized in chapter 3 and as evident from the photoreactor design equation, equation (2.9), the design of a high efficiency photocatalytic solar-driven process relies on a set of core methods and pieces of information. This includes methods to map/understand radiation transport in photoreactor assemblies, and the indirectly resulting need for methods to determine optical transport properties of the various employed materials, or, alternatively, the knowledge of the latter. Further, successful design of high efficiency photocatalytic processes relies on methods for the manufacturing of reactor components and for the synthesis of an active material with a significant quantum yield in the UV band, but especially, in the Vis band, or the availability of such an active material, and a suitable support strategy employed to control radiation transport on a photocatalyst level. Lastly, either the knowledge of the quantum yield of the employed photocatalyst or the availability of a method to determine the latter precisely as function of the operating conditions is an absolutely necessary prerequisite for a successful photoreactor design process.

At this point of the present work all methods and pieces of information are given to go through the design process of a high efficiency photocatalytic process. The introduced Monte Carlo ray tracing-based radiation transport model allows detailed radiation transport modelling in three dimensions and multi-component photoreactors, see chapter 4. In chapter 6, not only methods for the fabrication of photoreactor prototypes, but especially a set of methods for the determination of optical transport properties of photoreactor components and photocatalysts are introduced. Further, active materials and suitable active material support strategies are presented in chapter 6. Lastly, in chapter 7 an approach for the precise determination of quantum yields in gas, liquid, and multi-phase photocatalytic reactions is introduced, validated, and lastly applied to the photocatalyst model system whose development and optimization are described in chapter 6.

Within this last main chapter of the present work, a photoreactor design concept is introduced and demonstrated. The design aims for a high photocatalytic efficiency in a sunlight-driven photocatalytic process. The design process is, thereby, constraint by the aim that the photoreactor design shall be low-cost both in fabrication and operation. This entails that the design must be manufacturable with low-cost standard techniques in low-cost materials and, additionally, must be able to operate throughout the day and year without sun tracking.

This chapter will introduce the basic design idea, describe its numerical optimization, and present experimental and simulative results underlining the validity of the chosen approach. A detailed analysis will line out achievable limits and reveal prevalent loss mechanisms shaping the photocatalytic performance of the system. Lastly, a simultaneous consideration of achievable limits and prevalent loss mechanisms will cumulate in a design guideline for reflective multi-pass photoreactors that paves the way for adaptation to other material systems, further development, and commercialization of the proposed photoreactor design.

The content and explanations in the following are in parallel to the corresponding publication, see [94].

8.1. Approach introduction

The proposed photoreactor design is depicted in figure 8.1 in an exemplary application scenario on the rooftop of a low-energy house. The basic concept of the design is a synthesis of the design aspects of highly concentrating photoreactors, panel-like photoreactors, and low-cost polymer-based baggie photoreactors (for details on / discussion off all three basic designs, see section 2.2.2).

To ensure a high efficiency of the radiation transport from the reactor aperture into the reaction volume, the proposed design concentrates light with a narrowing gap concentrator and guides the concentrated light into a channel-like optical cavity with mirror-coated walls. For an illustration of the geometry, see zoom in in figure 8.1. The optical cavities' volumes represent the reaction volumes, in which the photocatalyst is placed. The mirror coating of the optical cavities' walls ensures that light that is scattered by the photocatalyst or that is transmitted through the photocatalyst is redirected towards the
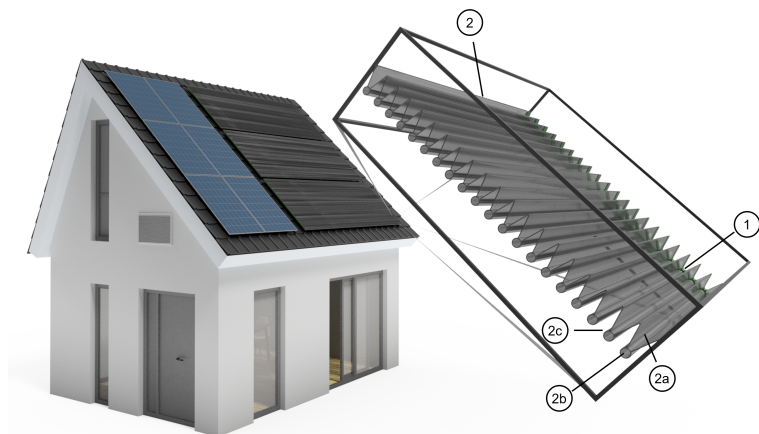
Figure 8.1.: Rendering of a CAD model of a low energy house equipped with envisioned low-cost and high efficiency solar fuel panels on its rooftop (dark grey panels). The panels are made from two polymer parts, a fluid distributor/collector (1) manufacturable via polymer injection moulding and an optics module manufacturable via polymer extrusion (2). The optics module basically is made from a large number of reaction channels of which each comprises a simple narrowing gap concentrator (2a) guiding incident light into an optical cavity (2b) in which the photocatalyst is placed. The fluid distributor/collector distributes the reactor feed to the numerous channels and collects the effluent at the channel outlets. The optics module is coated with a reflective coating from the bottom side, ensuring a high reflectivity of the concentrator and the optical cavity's walls (2c). Figure is reprinted from corresponding open access publication with CC-BY license, [94], Copyright 2022.

photocatalyst rather than being lost for the production process. This multi-pass strategy increases the achievable photocatalytic efficiency and allows the employment of optically dilute photocatalysts which is a prerequisite for a well-defined local volumetric rate of photon absorption throughout the whole reaction volume or a high catalyst usage/efficiency respectively. The combination of concentrating and trapping of incident light is, thereby, in analogy to sun-tracking concentrator-cavity photoreactor designs described in literature in the context of highly concentrating photoreactor systems employed mostly together with solar-driven thermal catalysts, see for instance [22]. The concentration ratio of the photoreactor optics proposed herein, however, is limited to a value that allows operation of the proposed photoreactor throughout the day and year without sun tracking. If statically

aligned with the sunpath at equinox [1], a line concentrator, which the proposed narrowing gap concentrators are, must have an acceptance angle of approximately 23.5° to be operational throughout the year. This precise value results from the obliquity of the ecliptic [2] and, therefore, of course is independent of the location on earth surface. From the obviously needed acceptance angle of a non-sun tracking photoreactor of approximately 23.5° and the law of etendue conservation introduced in section 2.2.2, equation (2.10), the maximum concentration ratio of a concentrating photoreactor design operational throughout the year can be determined to equal roughly 2.5. Noteworthy, any higher concentration ratio must result in a narrowed acceptance angle and a therefrom resulting limited functionality of a statically aligned photoreactor in the course of the year, or a need for sun tracking, respectively.

From a system perspective, the photoreactor design proposed herein is an array of parallel channels. For illustration see zoom in in figure 8.1. Therefrom, in analogy to photoreactors proposed in literature in the context of semi-conductor-based water splitting, see for instance [35], a panel-like photoreactor results. Its modular nature allows easy adaptation to different use cases, for instance applications on roof tops or in solar farms, and the straight forward extension of existing installations.

If built from polymers, for instance polymethylmethacrylat, as also proposed in low-cost baggie photoreactor concepts imagined for mass production of solar hydrogen, see for instance [24, 52, 106], the photoreactor design proposed herein is manufacturable via industry-established polymer extrusion with subsequent sputtering of a reflective layer on its backside. Interestingly, beyond the extruded optics module, the proposed design only needs one more part, a fluid distributor/collector, that distributes the reactor feed to the optics module, and collects the reactor effluent. For illustration see figure 8.1. The fluid distributor/collector is manufacturable via polymer injection moulding, a well-known industrial manufacturing technique widely applied in mass-fabrication of polymer parts.

To this point the introduced concept aims to be a panel-like and channel-based concentrator cavity reflective multi-pass photoreactor design manufacturable via industry-established techniques in polymers with an acceptance angle

---

[1] The sun path at equinox is the sun path in the sky at the day that day and night are equally long, thus the sun path at the 21st of March or the 23rd of September.

[2] The obliquity of the ecliptic is the inclination of the plane of earth's orbit relative to the earth's equatorial plane. It results from the inclination of the earths rotation axis relative to the earth's orbit plane.

that allows efficient operation throughout the year if properly aligned to the sunpath. However, the question remains, how the precise shape and dimensions of the channels' cross section must be chosen in order that the claimed high efficiency and acceptance characteristics are achieved. In the present work, this fundamental question is addressed via extensive optical modelling and numerical free-form geometry optimization tools. Further, the design is demonstrated in a single channel lab demonstrator depicted in figure 8.2. For the sake of convenient handling and a high quantum yield in the UV and Vis band, the photocatalyst considered in the design optimization and employed for the lab demonstration is the potassium ferrioxalate system introduced and characterized with respect to its optical transport properties in chapter 6.

8.2. Methods

8.2.1. Optical simulations

8.2.1.1. Simulation setup

The simulation domain in the optical simulations conducted during the design optimization and the subsequent detailed analysis mapped the zoom-in in figure 8.2 and comprised the optics module, the quartz glass capillary, and the reaction volume. The optics module was modelled as opaque object with a wavelength-dependent reflectivity and a wavelength-independent reflection characteristic. The assumed optical properties equal the ones determined for silver-coated 316L 3D-printed and post-print surface-treated optical components, see sections 6.1.1.5 and 6.1.2.2. For the determined values, see figure 6.3. The quartz glass capillary and the reaction volume were modelled as transparent objects with wavelength-dependent refractive indices and absorption coefficients. The assumed optical properties are the ones depicted in figures 6.4 and 6.14. For details on their determination, see sections 6.1.1.5, 6.1.2.3, 6.2.1.5, and 6.2.2.2. The quantum yield assumed for the photoreaction was derived from a fit to literature data for the the potassium ferrioxalate system, see solid line in figure 6.15.

Incident sunlight was modelled in the simulations via a rectangular light emitting surface virtually placed directly in the reactor aperture. The simulated
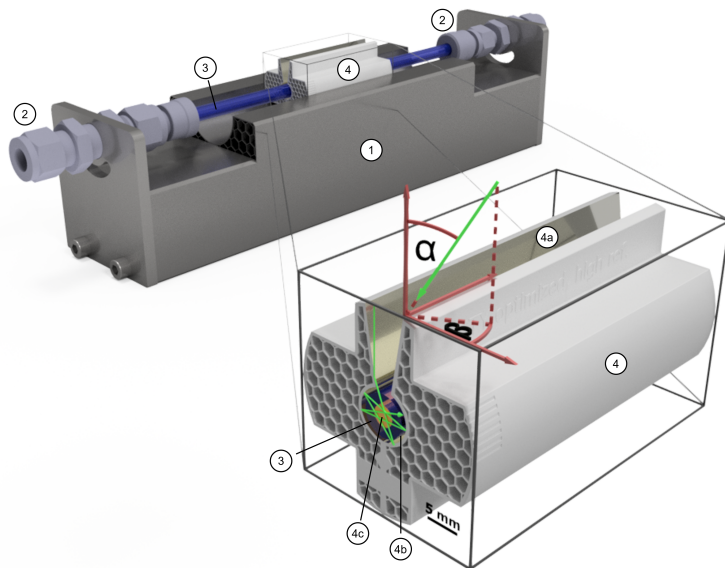
Figure 8.2.: Rendering of the CAD model of the single channel lab demonstrator developed to demonstrate the proposed photoreactor design concept for low-cast high efficiency photoreactor design. The lab demonstrator comprises a 3D printed reactor body (1) with commercial fluid connectors, a commercial quartz glass capillary (3), and an optics module (4) representing the channel geometry of the proposed photoreactor. The optics module comprises a narrowing gap concentrator (4a), an optical cavity (4b) with mirror-coated walls, and the quartz glass capillary (2) in its center surrounding the reaction volume (4c). The depicted polar coordinate system represents the coordinates referred to in the discussion of the present work. Figure is reprinted from corresponding open access publication with CC-BY license, [94], Copyright 2022.

light was divergent with a divergence half angle of 0.7°, which equals approximately the divergence of sunlight ($\approx 0.5°$) and the manufacturer indications on the divergence of the employed solar simulator. The incidence direction of the simulated light is defined in a polar coordinate system with a polar angle α and an azimuth angle β as defined in the zoom-in in figure 8.2.

The primary target metric of the simulations was the achieved photocatalytic efficiency derived via the numerical integration of the photoreactor design equation, equation (2.9). Thereby, a slightly reformulated form of the photoreactor design equation was applied, equation (8.1). For the reformulation it was assumed, that the quantum yield was no function of the local volumetric rate of photon absorption, or in other words no function of the position

within the reaction volume. This assumption may be a critical assumption in some reaction systems as shown in chapter 7, but at the same time is a valid and commonly applied assumption for the potassium ferrioxalate system at moderate values of the local volumetric rate of photon absorption. For a brief discussion of this topic see for instance [136]. The assumption of a quantum yield independent from the local volumetric rate of photon absorption allowed the approximation of the volume integral in the nominator of the photoreactor design equation via a simple product of incident spectral photon flux ($q_{p,\lambda}$), spectral radiation transport efficiency ($\eta_{T,\lambda}$), and quantum yield (Φ). The spectral radiation transport efficiency was, thereby, defined as introduced in chapter 7, see equation (7.1).

$$\eta_p = \frac{\int q_{p,\lambda}\eta_{T,\lambda}\Phi d\lambda}{\iint E_{p,\lambda}dA d\lambda} \tag{8.1}$$

The numerical solution of the wavelength integral in the numerator in equation (8.1) requires spectrally resolved simulations, meaning a set of simulations conducted at different wavelengths in the relevant optical band, delivering the spectral radiation transport efficiency as function of the wavelength. The wavelength resolution in the simulations was achieved via retracing. For details on this acceleration technique implemented in the Monte Carlo ray tracing environment developed in the present work, see section 4.3.4. The applicability of retracing was checked in an exemplary simulation set aiming for a calculation of the spectral radiation transport efficiency via full ray tracing and retracing as function of the wavelength. In the simulation set, an exemplary channel cross section with a narrowing gap concentrator with an aperture width of 5 mm and a cavity entry slit width of 1 mm and a cylindrical cavity with a diameter of 6.85 mm was mapped. Incident light entered the aperture under a polar incidence angle of 0°. For illustration of the geometry and a definition of the geometry parameters see figure 8.6. The simulations were conducted with 100 k rays per case. A comparison of the spectral radiation transport efficiency derived via retracing and via ray tracing does not reveal any significant differences, see figure 8.3, which confirms the applicability of retracing in the material system mapped in the simulations. On a side note, in the exemplary simulation set, the simulation time could be reduced by roughly 30 % through the application of retracing. The band covered in the spectrally resolved simulations ranged from 350 nm to 500 nm, which is the band in which both the employed solar simulator emits significant amounts of photons, and the quantum yield of the employed
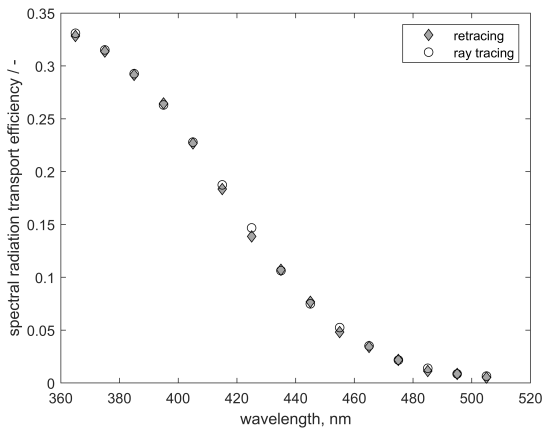
Figure 8.3.: Simulated spectral radiation transport efficiency of an exemplary high efficiency photoreactor channel cross section as function of the wavelength derived both via full ray tracing (circles) and retracing (diamonds). The assumed exemplary channel cross section was made from a narrowing gap concentrator with an aperture width of 5 mm, a cavity entry slit width of 1 mm, and a cylindrical cavity with a diameter of 6.85 mm.

potassium ferrioxalate system is different from zero, compare figures 5.10 and 6.15. The solution of the wavelength integral of the photoreactor design equation was lastly approximated as a discrete sum. The number of elements in the sum sets the number of simulations to be conducted and, thereby, defines the required simulation time. The number of elements in the sum should consequently be as low as possible to keep the simulation time low and allow the conduction of optimization studies relying on a large number of function evaluations. The number of elements in the sum needed for convergence in the objective function was, therefore, determined in a band width study varying the number of simulated wavelengths or the band width in the simulations respectively between 5 nm and 40 nm. The band width study was executed with an exemplary simulation case assuming a polar incidence angle of 0° and simulating 50 k rays in each simulated optical band. The mapped exemplary geometry comprised a channel cross section with a narrowing gap concentrator with an aperture width of 5 mm, a cavity entry slit width of 1.5 mm, and a cylindrical cavity with a diameter of 7 mm. For illustration of the geometry and a definition of the parameters see figure 8.6. The band width was finally chosen in a way, that the deviation of the target metric,
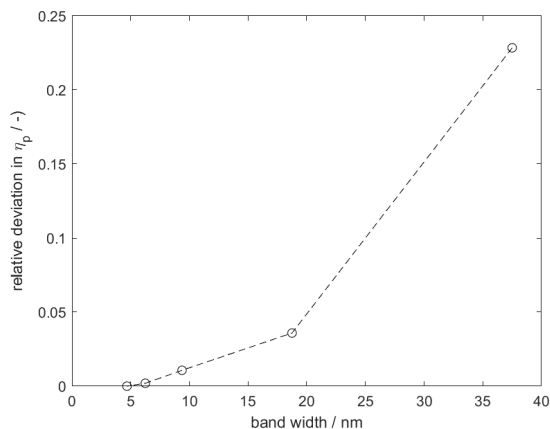
Figure 8.4.: Band width study conducted prior to polychromatic simulations underlying the numerical solution process of the photoreactor design equation necessary in the numerical optimization process of a high efficiency photoreactor. The study maps the relative deviation of the target metric, the photocatalytic efficiency, as function of the number of elements in the discrete sum used to approximate the wavelength-integral in the photoreactor design equation or the band width in the simulations respectively. Figure is reprinted from corresponding open access publication with CC-BY license, [94], Copyright 2022.

the photocatalytic efficiency, was well below 5 % relative to the simulation with the highest spectral resolution. According to this study, a band width $\leq$ 20 nm fullfills this criterion, see figure 8.4. The band width lastly chosen in the simulations was 18.75 nm, resulting in eight simulations for each numerical integration of the photoreactor design equation. All optical properties and the spectral photon flux in the reactor aperture $q_{p,\lambda}$ in the integral of the nominator in equation 8.1 were derived at the band center wavelength from a convolution of the original data with a rectangular function with an area equal to unity and a band with of 18.75 nm.

For the evaluation of the wavelength integral of the denominator in equation (8.1), the experimentally determined spectral irradiance ($E_{p,\lambda}$) in the solar simulator's target plane under experiment conditions (details see section 8.2.2) was assumed. The spectral resolution in the numerical integration was equal to the spectral resolution of the experimental data on the spectral irradiance (1 nm). The band considered in the integration ranged from 350 nm to 800 nm which equals the UV and Vis band. The number of rays per band needed for
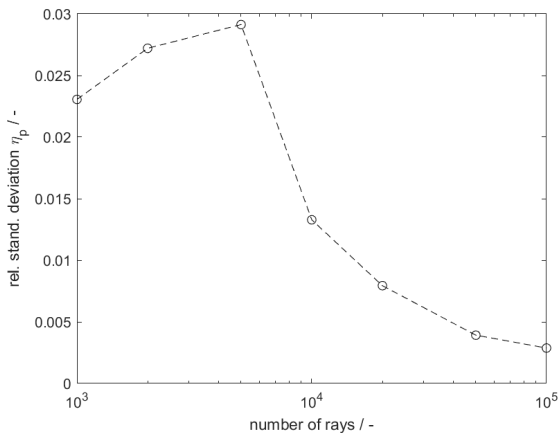
Figure 8.5.: Ray study result conducted prior to simulations underlying the numerical integration of the photoreactor design equation in the context of high efficiency photoreactor design. The ray study maps the relative standard deviation in the target metric, the photocatalytic efficiency, as function of the number of simulated rays derived from five repeat simulations conducted with a given number of simulated rays. Figure is reprinted from corresponding open access publication with CC-BY license, [94], Copyright 2022.

convergence in the photocatalytic efficiency was determined in analogy to the ray studies described in sections 6.2.1.5 and 7.2.1.1. In the conducted ray study, the number of simulated rays in each of the mapped bands was varied between 1 k rays and 100 k rays. The number of rays was finally chosen in a way, that the relative standard deviation in the target metric derived from five repeat simulations was well below 1 %. This criterion was fulfilled for a number of rays simulated per band larger than 20 k rays, see figure 8.5. The number of rays lastly chosen in the simulations was 50 k rays per optical band.

As secondary target metric in the conducted simulations, spectral absorption/loss shares were derived. These absorption/loss shares represent the fraction of photons at a specific wavelength coupled into the reactor aperture that were either absorbed by any of the objects, optics module, glass capillary, or reaction volume, or that were lost over open faces, the reactor aperture, or the front and back face of the optics module, after multiple internal reflections. The spectral absorption/loss shares were derived from counts of absorbed rays derived during the ray tracing procedure for all objects and an ideally

black virtual probe in the reactor aperture that were subsequently related to the total number of simulated rays.

8.2.1.2. Geometry optimization

The precise shape of the reaction channel cross section of the proposed photoreactor was optimized in a two step numerical optimization, aiming for a maximum feasible photocatalytic efficiency under perpendicular irradiation (polar incidence angle equal to 0°). All simulations during the optimization were conducted as described in section 8.2.1.1. In the first step of the optimization a parameterized description of the concentrator-cavity channel was optimized with the MATLAB® global optimization toolbox minimization tool `surrogateopt` addressing the cavity entry slit width (w_{cavity}) and the cavity diameter (d_{cavity}) and setting the negative photocatalytic efficiency as objective function. For an illustration of the definition of the two geometric parameters subject to optimization, see figure 8.6. The channel's aperture width was held constant in the optimization at a value of 5 mm.

In the second step of the optimization the geometry of the channel cross-section was altered by inducing free-form deformations in the cavity's wall aiming for further increase of the photocatalytic efficiency. The algorithm employed in this free-form optimization step was an in-house developed 'hammering' algorithm proceeding in two reiterated phases. The proceeding of the algorithm is summarized in the code flow chart in figure 8.8. In the first 'random search' phase the algorithm imposes random deformations on the initial geometry with a 'numerical hammer' altering the radial positions of the vertices spanning the cavity's surface. The 'numerical hammer', illustration see figure 8.7, thereby, 'hits' the cavity at a a random center vertex with index M and has a random width of W vertices. The random depth of the deformation in the center is D which is defined as a certain fraction of the radial position of the vertex with index M. The random deformation depth D decays exponentially with the distance from the center M ensuring a smooth geometry even after a large number of superimposed deformations. The radial positions r_i of the W vertices affected by a hammer hit are lastly calculated via equation (8.2) with i being the counting variable counting the vertices from the center vertex with index M.

$$r_i = r_{0,i} \left[1 + D \exp \left(\frac{i - M}{2W} \right)^2 \right] \qquad (8.2)$$

173
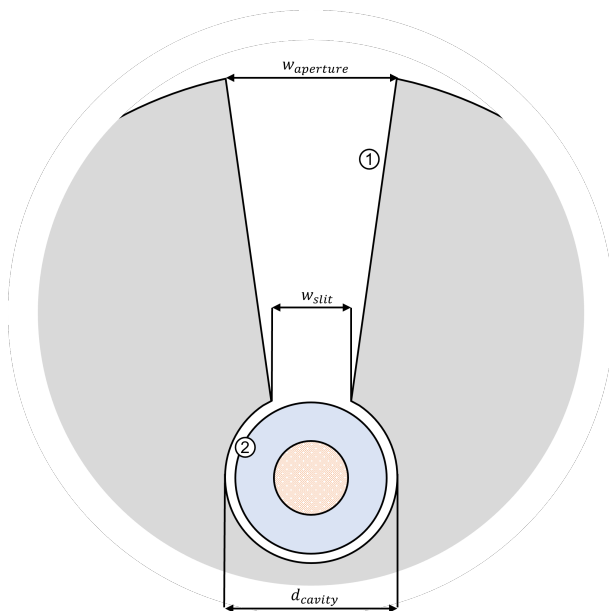
Figure 8.6.: Scheme of the parameterized geometry of the channel cross-section subject to optimization in the first step of the geometry optimization aiming for a photoreactor with a maximum achieved photocatalytic efficiency. The geometry parameters subject to optimization are the cavity entry slit width w_{cavity} and the cavity diameter d_{cavity} at a fixed channel aperture width ($w_{aperture}$) of 5 mm. Figure is reprinted from corresponding open access publication with CC-BY license, [94], Copyright 2022.

If one of the random deformations yields an improvement of the objective function, the algorithm continues with the second phase. In this second phase, the found successful deformation from the first phase characterized by the deformation parameters M, W, and D is subject to an optimization in a pattern search-based approach addressing the deformation parameters M, W, and D. In this pattern search optimization a pattern of variations of M, W, and D is spun around the initial values and scanned for possible improvements. If one of the variants yields an even higher value of the objective function, this combination of M, W, and D is set as new pattern center and a new pattern is spun around that new center. If a full pattern scan did not yield any improvement, the pattern is refined. After one refinement the pattern search is stopped, the deformation characterized by the found optimal M,
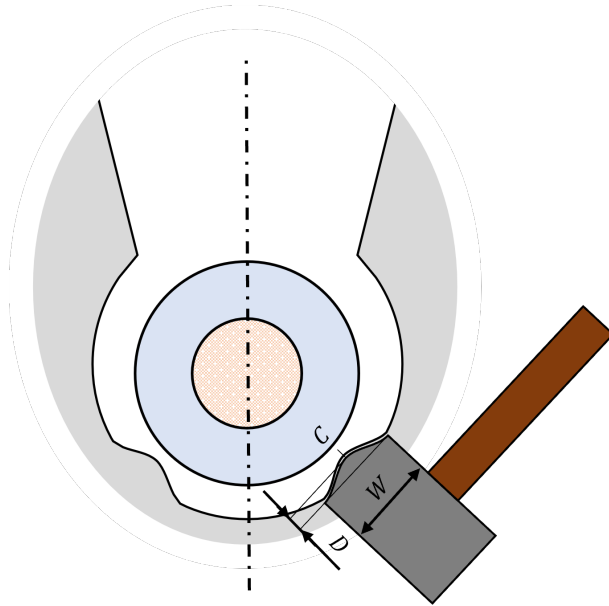
Figure 8.7.: Illustration of the 'numerical hammer' deformation strategy in the free-form geometry optimization of the cavity of a high efficiency reflective multi-pass photoreactor. The 'numerical hammer' (illustrated as 'real' hammer in the sketch) is an algorithm manipulating the radial position of the cavity's vertices around a center vertices (index C) in a width of W vertices and with a maximum deformation depth D. The deformation depth decays exponentially with the distance from the deformation center C ensuring a smooth geometry even after a large number of superimposed deformations.

W, and D is applied to the initial geometry, the altered geometry is set as new start geometry, and the algorithm switches back to the random search phase imposing random deformations until another 'promising' deformation is found. If a maximum number of 50 random deformations did not yield any improvement in the objective function, the maximum deformation depth is refined. The optimization stops if the maximum deformation depth undercuts a manufacturing accuracy limit ($\approx$ 10 μm) or a maximum number of 200 random deformations did not yield any improvement in the objective function.
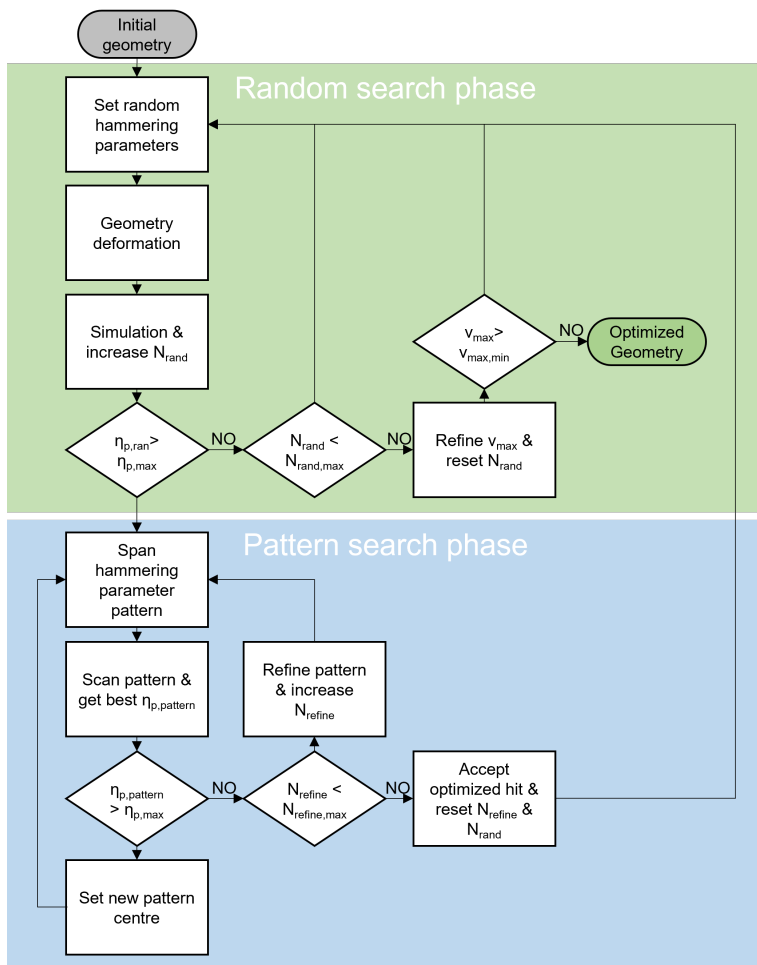
Figure 8.8.: Flow chart of the developed and employed 'hammering' free-form optimization algorithm. The algorithm repeatedly goes through a random search phase (green background) and a pattern search phase (blue background). In the random search phase random deformation are imposed onto a start geometry. If any of the random deformations entails a higher value of the objective function, the algorithm switches to the second pattern search phase where the successful random deformation is optimized. Figure is reprinted from corresponding open access publication with CC-BY license, [94], Copyright 2022.

8.2.2. Potassium ferrioxalate photoreduction

The experimental validation of the derived photoreactor design was executed with an additively manufactured optics module and the reaction system considered in the optimization, the potassium ferrioxalate system. For details on the optics manufacturing, see section 6.1.1.1. The potassium ferrioxalate photoreduction experiments were conducted in analogy to the potassium ferrioxalate photoreduction experiments described in section 7.2.3. Briefly, in an experiment a 2 mM potassium ferrioxalate (Alfa Aesar) solution in 0.05 M sulphuric acid (Fisher Scientific) was pumped through the reactor with three different flow rates (2.0 mL min^{-1}, 2.6 mL min^{-1}, and 3.7 mL min^{-1}), resulting in different space times. During the experiment, the reactor was illuminated with the test rig internal solar simulator from the top. For details on the solar simulator, please refer to section 5.1.1.3. The solar simulator was, thereby, operated at a short arc power setting of 72.5 % and with a 34 % filter in its beam line. For details on the resulting spectral irradiance in the target plane, please refer to section 5.2.1. Samples were collected at the reactor outlet and analysed with respect to their concentration of the reaction product Fe^{II+}. The analysis was conducted via a standard phenanthroline Fe^{II+} assay as described in section 7.2.3.

To derive the number of production events in the reaction volume, the derived Fe^{II+} concentrations were plotted over the varied space time. According to a simple plug flow reactor design equation, see equation (7.6), the slope of the resulting line corresponds to the potassium ferrioxalate reaction rate. For a brief discussion of the underlying assumptions, please refer to section 7.2.3. The achieved photocatalytic efficiency was lastly derived via equation (8.3) relating the number of production events in the reaction volume V to the number of incident photons in the reactor aperture. The integration of the wavelength integral of the denominator in equation (8.3) was conducted as described in section 8.2.1.1.

$$\eta_p = \frac{\dot{r}_{Fe^{II+}} V}{\iint E_{p,\lambda} dA d\lambda} \tag{8.3}$$

Potassium ferrioxalate photoreduction experiments were conducted under varying polar incidence angle at a fixed azimuth angle of 0°. The polar incidence angle variation was realized via a rotation of the cylindrical optics module in the cylindrical trough in the reactor body. For an accurate alignment angle marks were printed at the outer surface of the optics module. For

illustration, see figure 8.2. The polar angle range scanned in the experiments covered 0° to 20° with a step width of 4°.

8.3. Results and discussion

8.3.1. Optimal photoreactors

The geometry optimization of the channel cross-section of the proposed photoreactor design resulted in the geometry depicted in figure 8.9. For details on the optimization strategy, please refer to section 8.2.1.2. The first step of the optimization returned a cavity entry slit width of 2.3 mm and a cavity diameter of 7.8 mm. For an illustration of the optimized parameter-based geometry, see red line in figure 8.9. The second step altered the cavity's wall shape in a total number of seven optimized hits of the 'numerical hammer'. The finally derived optimal geometry has a cavity entry slit width of 2.6 mm which corresponds to a geometric concentration ratio of roughly 1.92 (aperture width set to 5.0 mm by default, see section 8.2.1.1). For an illustration of the resulting shape, see grey structure in figure 8.9.

Simulation data indicates that the optimized channel cross section yields a peak photocatalytic efficiency of 5.8 % under perpendicular irradiation (polar incidence angle equal to 0°), see y-intercept of solid line in figure 8.10. This value agrees well with the experimental value derived from the potassium ferrioxalate photoreduction experiments, see y-intercept of the free-form reference experiment (open circle, dotted line) in figure 8.10. Further, the polar incidence angle course at a fixed azimuth angle of 0° of the photocatalytic efficiency shows a satisfactory agreement between simulation and experiment underlining the reliability of the conducted simulations. A comparison of the achieved photocatalytic efficiency with a reference case of a simple quartz glass capillary without any optics mounted around the reaction volume reveals a more than fourfold improvement of the photocatalytic efficiency under perpendicular irradiation through the channel geometry underlining the value of the photoreactor design approach proposed herein, see dot dashed line (simulation) and dark grey circle (experiment) in figure 8.10. The observed performance boost by applying the optics module, thereby, clearly can be assigned to the repeated redirection of light through the reaction volume which entails multiple ray passes through the reaction volume. The latter add up to a significantly longer effective ray path in the reaction volume, resulting
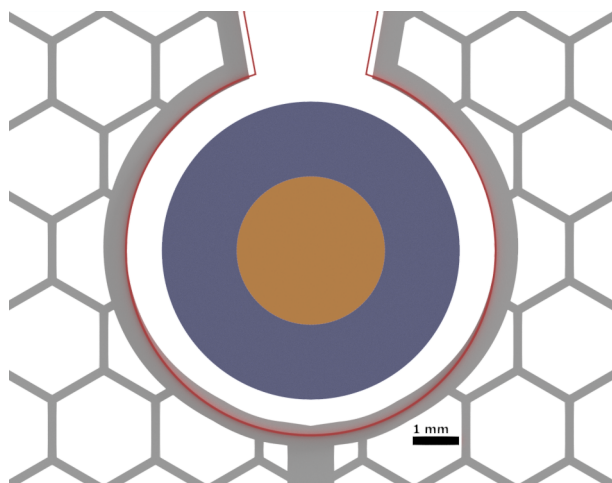
Figure 8.9.: Rendering of CAD model of the optimized channel cross section entailing a maximum photocatalytic efficiency for the potassium ferrioxalate photoreduction under perpendicular irradiation with simulated solar light. The orange object represents the reaction volume. The blue object represents the quartz glass capillary and the grey object the optics module. The red line indicates the optimal parameterized geometry derived in the first step of the optimization. Figure is reprinted from corresponding open access publication with CC-BY license, [94], Copyright 2022.

in a higher probability of absorption or an increased photocatalytic efficiency, respectively. Seen from this perspective, the overall goal of the optimization process is an extension of the effective ray path in the reaction volume by ensuring a maximum number of ray passes. The achieved peak photocatalytic efficiency might seem unimpressive at first glance but must be related to what actually can be achieved with the material system and light source considered. As is lined out in detail in section 8.3.2, the achieved peak photocatalytic efficiency of 5.8 % corresponds already to 62 % of what would actually be achievable for the sunlight driven photoreduction of potassium ferrioxalate within a reflective multi-pass photoreactor made from the materials used in the present work.

Most importantly, the derived optimal photoreactor design shows a pronounced tolerance towards a variation of the direction of incident light or a moving sun in the sky, respectively. As shown in figure 8.10, even for a polar incident angle α of up to 20° ($\beta = 0$°), photocatalytic efficiency does not fall below the value of a system without any optics module. Assuming

179
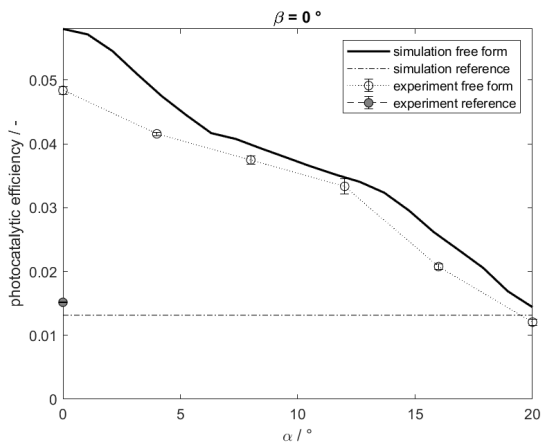
Figure 8.10.: Both simulated (solid line) and experimental values (dotted line) of the photocatalytic efficiency for the potassium ferrioxalate photoreduction in a photoreactor with optimized channel cross section as a function of polar incident angle α ($\beta = 0°$). The Dot dashed line and dark grey circle represent data for a simple capillary photoreactor without any optics surrounding the reaction volume. Figure is reprinted from corresponding open access publication with CC-BY license, [94], Copyright 2022.

an infinitely long reaction channel, or a reaction channel long enough that front and back face losses are negligible, that is optimally aligned to the sunpath, the derived optimal photoreactor design is operational throughout the day and year without sun tracking. The latter is evident from the simulated diurnal and annual course of the photocatalytic efficiency depicted in the sunpath diagram in figure 8.11. The assumed optimal alignment to the sunpath means an alignment of the photoreactor in a way that a projection of its channels into a horizontal plane is aligned with an east west axis and its aperture normal points towards the sunpath at equinox. This criterion of course entails a dependency of the optimal alignment on the geolocation, more precisely the latitude of the geolocation. The presentation in figure 8.11 assumes a photoreactor operated at 49° latitude which equals the latitude of Karlsruhe, Germany. The favourable acceptance characteristic of the derived optimal photoreactor, thereby, results from the low realized concentration ratio (for a detailed discussion see section 8.1) and the axial extension of the geometry. The acceptance characteristic does not only allow operation without sun tracking and a reduced CAPEX and OPEX , but also allows to
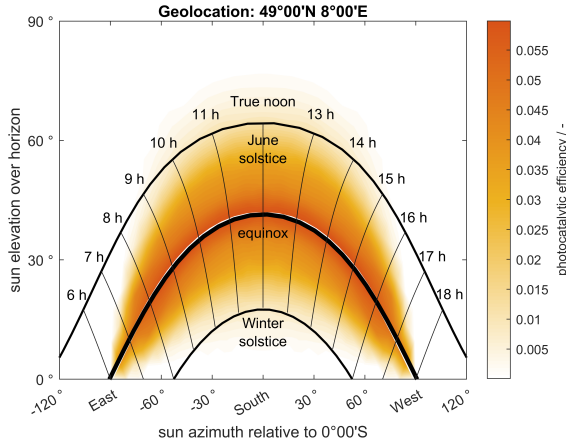
Figure 8.11.: Simulated photocatalytic efficiency of the derived optimal photoreactor in diurnal an annual course depicted in a sunpath diagram. For the simulations, an infinite channel being optimally aligned with the sun path was assumed. The incidence angle was varied in the simulations in a hemisphere above the photoreactor aperture. Optimal alignment means that a projection of the photoreactor channel in a horizontal plane is aligned with an East-West axis and the aperture normal points towards the sunpath at equinox. The sun path calculation underlying the graph is based in the astronomical algorithms by Meeus, for details see, for instance [142], and have been executed with the sun path calculator from the National Oceanic and Atmospheric Administration. Figure is reprinted from corresponding open access publication with CC-BY license, [94], Copyright 2022.

imagine decentral operation on rooftops with a potentially broad impact on the energy market as discussed for instance in [107].

8.3.2. Achievable limits

As also lined out in [94] in detail, the optimization of reflective multi-pass photoreactors with respect to the achieved photocatalytic efficiency is constrained from two sides. First of all, the quantum yield of the photocatalyst and its spectral dependency set an ultimate limit to the achievable photocatalytic efficiency in a solar-driven process. The potassium ferrioxalate system employed herein, for instance, is only able to use photons up to a wavelength of approximately 550 nm, see figure 6.15 and empty circles in figure 8.13. Photons that contribute to the production must consequently

have a wavelength smaller than 550 nm. Only roughly one third of all UV Vis photons in the sunlight spectrum fulfill this criterion. Noteworthy, and of utmost importance, a quantum yield different from zero is a necessary but not sufficient condition for any photocatalytic reaction to take place. The second necessary, obvious, but in the end non-trivial condition is absorption of photons by the photocatalytic system, which is determined by the radiation transport phenomena in the considered photoreactor/photocatalyst. Both the geometry and optical transport properties of employed materials determine this transport problem.

The efficiency of radiation transport from the reactor aperture into the reaction volume in reflective multi-pass photoreactors is constrained by inherent absorptive losses that occur when light travels through the reactor assembly. Even though the silver coating of the concentrator and the cavity wall have a high reflectivity throughout the relevant optical band and even though the glass tubing is highly transparent having only a small absorption coefficient, with each reflection on a wall and each passage through the glass tubing, a small share of a ray's photons is absorbed and dissipated to thermal energy. These parasitically absorbed photons of course can no longer contribute to the production in the reaction volume. However, there are optimal ray paths, on which parasitic absorption losses are minimal. These ray paths are characterized by two critical properties. First, they have a maximum ray path segment length in the reaction volume minimizing the number of reflections on the cavity wall needed to achieve full absorption and, thereby, reducing the parasitic absorption share of the cavity wall. Second, they have a high ratio between ray path segment length in the reaction volume and ray path segment length in the surrounding glass, minimizing the parasitic absorption share of the glass tubing. In a circular reaction volume, as is the case in the lab demonstrator subject to optimization in the presented work, optimal ray paths go through the center of the assembly, see black arrow in figure 8.12. The ideal absorption shares, meaning minimal parasitic absorption shares with a simultaneous maximum absorption share of the reaction volume, or in other words a maximum spectral radiation transport efficiency, can be derived by adding up the single interaction absorption shares of glass tubing, cavity wall, and reaction volume on an infinite series of ray passages through the assembly on an ideal ray path.

As lined out in [94], modelling the intensity of a ray on an ideal ray path after its reflection on the cavity wall via a simple reflection law, equation (4.5) and its decay in the glass tubing and reaction volume with Lambert Beer's law, equation (4.4), the intensity of the ray after its ith passage through the
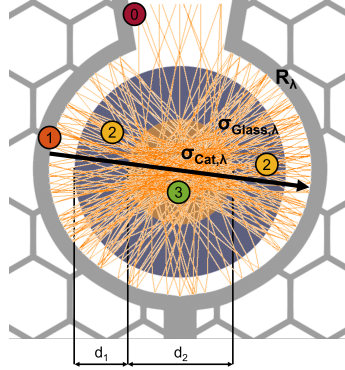
Figure 8.12.: Optimal ray path (black arrow) in the lab demonstrator subject to optimization in the presented work together with ten representative ray paths (orange lines) extracted from a simulation results. On an ideal ray path parasitic absorption losses by the concentrator (0) and the cavity wall (1) as well as parasitic absorption losses by the quartz glass tubing (2) are minimal compared to the absorption share in the reaction volume (3). Figure is reprinted from corresponding open access publication with CC-BY license, [94], Copyright 2022.

assembly on an ideal ray path can be expressed depending on its intensity in the preceding passage via equation (8.4). R_λ, $\sigma_{glass,\lambda}$, and $\sigma_{cat,\lambda}$ are the wavelength dependent wall reflectivity and glass and reaction volume absorption coefficient, respectively. d_1 and d_2 are the characteristic dimensions of the glass tubing and the reaction volume. For details on the definition of the latter two geometric properties, see figure 8.12. The absorption share by the reaction volume in a single passage can be expressed accordingly via equation (8.5).

$$I_i = I_{i-1} R_\lambda \exp\left(-2\sigma_{glass,\lambda} d_1\right) \exp\left(-\sigma_{cat,\lambda} d_2\right) := I_{i-1} f_1 \qquad (8.4)$$

$$I_i^a = I_{i-1} R_\lambda \exp\left(-\sigma_{glass,\lambda} d_1\right) \left[1 - \exp\left(-\sigma_{cat,\lambda} d_2\right)\right] := I_{i-1} f_2 \qquad (8.5)$$

Summing up the single passage absorption shares of the reaction volume calculated after equation (8.5) in an infinite sum results after some algebraic reformulations in equation (8.6) for the calculation of the reaction volume absorption share. The latter corresponds to the theoretical limit for the spectral radiation transport efficiency. The factor k, thereby, takes into account the effect of a missing primary ray attenuation if an incident ray is not reflected before its first passage through the core of the photoreactor assembly. k equals unity, if a ray passes through the tube and reaction volume before its first reflection on the concentrator or cavity wall, and zero, if the ray is

reflected on the concentrator/cavity wall before its first passage through the tube and reaction volume.

$$\eta_{T,limit,\lambda} = \left(\frac{1}{R_\lambda}\right)^k \frac{f_2}{1-f_1} \tag{8.6}$$

The minimal absorption shares of glass and cavity wall corresponding to the maximum feasible spectral radiation transport efficiency can be derived in analogy to the above mentioned. Their calculation finally is along the lines of equations (8.7) and (8.8) with the absorption share factors f_3 and f_4 calculated after equations (8.9) and (8.10).

$$\eta_{T,limit,glass} = \left(\frac{1}{R_\lambda}\right)^k \frac{f_3}{1-f_1} \tag{8.7}$$

$$\eta_{T,limit,wall} = \left(\frac{f_1}{R_\lambda}\right)^k \frac{f_4}{1-f_1} \tag{8.8}$$

$$f_3 = R_\lambda \left[1 - \exp\left(-\sigma_{glass,\lambda}d_1\right)\right]\left[1 + \exp\left(-\left(\sigma_{glass,\lambda}d_1 + \sigma_{cat,\lambda}d_2\right)\right)\right] \tag{8.9}$$

$$f_4 = (1 - R_\lambda) \tag{8.10}$$

Interestingly, the ideal absorption shares, calculated after equations, (8.6), (8.7), and (8.8) are only dependent on the optical transport properties of the employed materials and the characteristic dimensions of the glass tubing and the reaction volume. Thereby, they highlight the importance of the choice of appropriate materials and characteristic dimensions for the design of high efficiency photoreactors. The latter is underlined by the presentation in figure 8.13 that depicts the introduced ideal absorption shares derived for the exemplary material system in the introduced lab demonstrator as function of wavelength via a color coding. In the exemplary system, the spectral radiation transport efficiency limit is high in the UV and blue band but drops drastically in the green band (450-550 nm), see green area in figure 8.13. This system characteristic is highly undesired, since exactly in the green band, both the emission of the employed light source and the quantum yield are high, which is the basis for a significant contribution to the number of production events. This momentous characteristic of the exemplary system is induced by the spectral dependency of the optical properties of the potassium ferrioxalate system, whose absorption coefficient drops over two orders of magnitude from roughly 109 m^{-1} at 400 nm to 1.0 m^{-1} at 500 nm (see figure 6.14) making absorption in the green band hard to realize without a drastic increase of
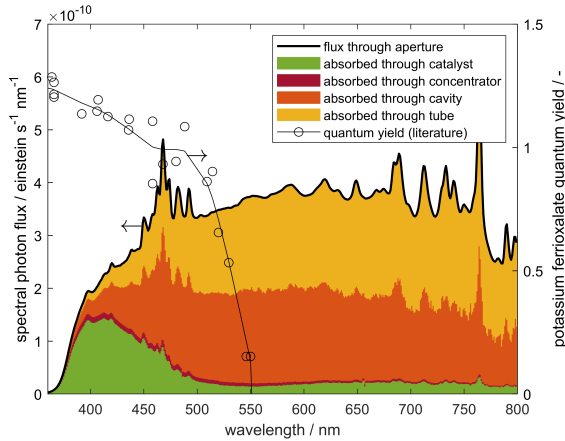
Figure 8.13.: Ideal spectral absorption shares for the patassium ferrioxalate system (coloured areas) drawn overlaid with the emission spectrum of the employed solar simulator (bold solid line) as a function of the wavelength. Empty circles with a thin solid line fit represent literature data on the quantum yield of the potassium ferrioxalate system, [124]. Figure is reprinted from corresponding open access publication with CC-BY license, [94], Copyright 2022.

the characteristic dimensions of the reaction volume. Consequently, the achievable photocatalytic efficiency within the lab demonstrator system is 'only' 9.8 %, highlighting that the practically realized photocatalytic efficiency of 5.8 % corresponds to 62 % of what is theoretically feasible.

On a side note, the data underlying the presentation in figure 8.13 was derived via a weighted sum of ideal absorption shares assuming direct ($k = 1$) and indirect ($k = 0$) illumination, see equation 8.11. The direct illumination share (ξ_{direct}) was chosen as the ratio between cavity entry slit width and aperture slit width.

$$\eta_{T,\lambda,\sim} = \xi_{direct}\eta_{T,\lambda,\sim}\left(k = 1\right) + \left(1 - \xi_{direct}\right)\eta_{T,\lambda,\sim}\left(k = 0\right) \tag{8.11}$$

The drawn concentrator absorption share was derived via equation (8.12). It must be subtracted from the cavity wall absorption share if considered separately.

$$\eta_{T,limit,conc} = \left(1 - \xi_{direct}\right)\left(1 - R_\lambda\right) \tag{8.12}$$

8.3.3. Loss mechanism analysis

Beyond the inherent absorptive losses on ideal ray paths that shape the achievable limits, in real systems, additional losses occur that explain the differences between what can theoretically be achieved and what actually is achieved. On the one hand those are absorptive losses that originate in non-ideal ray paths. Such non-ideal ray paths are also present in the derived optimal photoreactor, see ray paths in the presentation in figure 8.12. They entail a non-ideal absorption share of glass tubing, concentrator and cavity wall, with 'non-ideal' meaning an increased absorption share relative to the ideal minimal parasitic absorption share introduced above. On the other hand there are losses that result from rays that leave the photoreactor assembly after multiple internal reflections either through the photoreactor aperture or via the front and back face of the photoreactor channel without being attenuated significantly. Thus, the picture described in section 8.3.2 and depicted in figure 8.13, is not the full picture. A detailed analysis of the simulation data reveals that with increasing wavelength, ray losses through the aperture and via the channel faces get more and more important and even become the predominant loss mechanism at wavelengths above roughly 500 nm, see blue areas in figure 8.14. The number of ray passages that a photoreactor can guarantee before a ray is lost through the aperture, thereby, becomes a critical design property with outstanding importance in high efficiency reflective multi-pass photoreactor design. The free-form optimized shape derived above, apparently, is able to guarantee roughly seven ray passages before ray paths become unstable and leave the photoreactor assembly, see asymptote of thin solid line in figure 8.14. Noteworthy, the real number of ray passages needed in order to achieve significant total absorption may be significantly smaller than the maximum number of guaranteed reflections before a ray path becomes unstable. Whether this is applicable or not, again, heavily depends on the optical transport properties and the characteristic dimensions of the photoreactor assembly. Briefly, the absorption on a single passage on a ray path must be significant. For the free-form optimized lab demonstrator this is the case in the blue and UV band (<450 nm), see thin solid line in figure 8.14 and compare to the optical transport properties of the components in figures 6.3, 6.4, and 6.14.
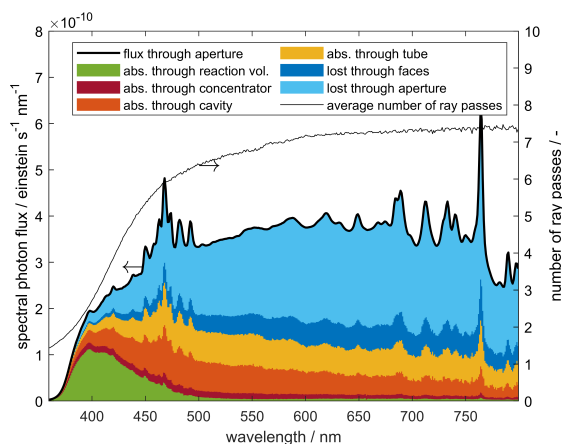
Figure 8.14.: Spectral photon flux send into the photoreactor aperture (bold solid line) together with simulated (real, non-ideal ray-path based!) spectral absorption shares of concentrator (dark red area), cavity wall (orange area), glass tubing (yellow area), and reaction volume (green area) and loss shares through the photoreactor aperture (light blue area) and the photoreactor faces (dark blue area). The thin solid line represents the average number of ray passages before a ray is either absorbed or lost through the aperture or faces of the photoreactor. Figure is reprinted from corresponding open access publication with CC-BY license, [94], Copyright 2022.

8.3.4. Design guideline

The considerations regarding the inherent absorptive losses occurring on ideal ray paths (see section 8.3.2) and the analysis of simulation data indicating that only a limited number of ray passages is feasible in real photoreactor assemblies (see section 8.3.3) together allow the derivation of a design guideline for reflective multi-pass photoreactors. The design guideline supports the selection of suitable materials and characteristic dimensions and starts from the two core conclusions that can be drawn from sections 8.3.2 and 8.3.3. First of all, materials and characteristic dimensions must be chosen in a way, that the spectral radiation transport efficiency limit is high throughout the relevant optical band. Secondly, the materials and characteristic dimensions must be chosen in a way, that a reasonable number of ray passages entails a significant ray attenuation or total absorption share, respectively. Thereby, 'reasonable' depends on the actual reactor geometry chosen. For the free-form optimized geometry described above 'reasonable' means a number of seven

ray passages. At the same time, a minimum number of ray passages is recommendable to ensure a good optical accessibility of the whole reaction volume or a high catalyst usage, respectively. On a side note, the lab demonstrator presented herein is sub-optimally designed with regard to both aspects. The materials and characteristic dimensions are chosen in a way that just in the band in which both the spectral emission of the employed solar simulator and the quantum yield are high, the spectral radiation transport efficiency is low and the maximum number of ray passes is no longer sufficient to ensure a significant absorption.

Mathematically, the Napierian absorbance of the reaction volume ($\sigma_{cat,\lambda}d_2$) necessary to ensure a desired spectral radiation transport efficiency at given Napierian absorbance of the glass tubing wall ($\sigma_{glass,\lambda}d_1$) and given cavity wall reflectivity (R_λ) can be derived via equation (8.13). Equation (8.13), thereby, is a reformulation of equation (8.6) expressing the spectral radiation transport efficiency limit as function of optical transport properties and characteristic dimensions.

$$\sigma_{cat,\lambda}d_2 = -\ln\left[\frac{R_\lambda \exp\left(-\sigma_{g,\lambda}d_1\right) - \eta_{T,\lambda,limit}}{R_\lambda \exp\left(-\sigma_{g,\lambda}d_1\right)\left[1 - \eta_{T,\lambda,limit}\exp\left(-\sigma_{g,\lambda}d_1\right)\right]}\right] \qquad (8.13)$$

Further, the number of ray passages on ideal ray paths necessary to ensure a desired total absorption share (Ω) can be derived via equation (8.14), which is derived from equation (8.4) describing the ray attenuation in one passage on an ideal ray path.

$$N_{min} = \frac{\ln\left(1 - \Omega\right)}{\ln\left(f_1\right)} \qquad (8.14)$$

The two design equations, equations 8.13 and 8.14, can be employed to derive a graphical presentation of the proposed design guideline, see figure 8.15. Equation 8.13, thereby, provides the basis for the calculation of the lines with constant cavity wall reflectivity. Equation 8.14 provides the basis for the calculation of the tick marks along the lines of constant cavity wall reflectivity. In the graphical presentation of the design guideline in figure 8.15, the lines with constant cavity wall reflectivity derived for different design spectral radiation transport efficiencies between 60 % and 90 % (see color coding), connect a given Napierian absorbance of the glass tube wall (y axis) and cavity wall reflectivity (see line labeling) with the Napierian absorbance of the reaction volume (x axis) necessary to ensure the desired spectral radiation transport efficiency. In case the absorption coefficient of the reaction volume is fixed, the derived necessary absorbance allows the estimation of a
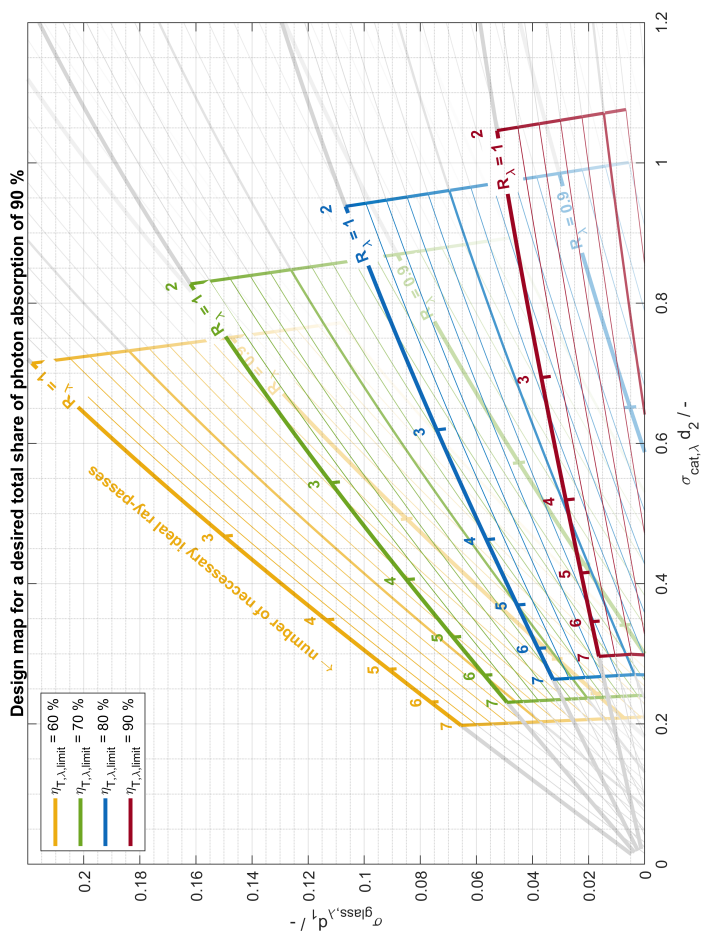
Figure 8.15.: Graphical representation of the design guideline for reflective multi-pass photoreactors aiming for a total absorption share of 90 %. The guideline connects the optical transport properties and characteristic dimensions of the employed components (x and y axis for glass tubing and reaction volume and iso-lines for the cavity wall reflectivity) with spectral radiation transport efficiency limit (color coding) and the number of passages on ideal ray paths needed to ensure the design total absorption share (ticks along iso-reflectivity lines). Figure is reprinted from corresponding open access publication with CC-BY license, [94], Copyright 2022.

suitable characteristic dimension of the reaction volume. In case the reaction volume dimensions are fixed, the derived necessary Napierian absorbance of the reaction volume can be used to derive the needed Napierian absorption coefficient or the catalyst concentration, respectively.

The ticks along the lines with constant cavity wall reflectivity further give an estimation of the number of ray passages on ideal ray paths that are necessary to ensure the desired total absorption share. The coloured area between two and seven ray passes, thereby, highlights the region in which the free-form optimized photoreactor presented herein has its working range. If for a given set of optical transport properties of glass tubing and cavity wall the point on the line with constant wall reflectivity lies outside the coloured area, the desired spectral radiation transport efficiency limit is not feasible within two to seven ray passages on ideal ray paths for the given set of material data.

On a side note, in most material systems, absorption coefficients show a pronounced wavelength dependency that might render a 'perfect' design ensuring a high spectral radiation efficiency and a high total absorption share within a reasonable number of ray passages on ideal ray paths throughout the relevant optical band impossible. The potassium ferrioxalate system in context of a sunlight driven synthesis is such a material system. In such cases trade-offs are needed that entail complex optimization tasks and highlight the need of polychromatic considerations/simulations.

Lastly to be noted, the guideline introduced herein only allows the determination of suitable characteristic dimensions or material properties and the estimation of the number of ray passages on ideal ray paths necessary to ensure the desired total absorption share. The optical design task that lastly ensures the number of needed ray passages on as ideal as possible ray paths, is a creative challenge that can be addressed by geometry optimization tools as demonstrated above.

8.4. Interim Summary

The way towards a commercial implementation of solar fuels demands for a low-cost and high efficiency photocatalytic process. Ensuring both at the same time is a coupled materials and photoreaction engineering challenge that relies on both materials with a high quantum yield in the 6 for a relevant chemical reaction and photoreactors providing suitable operating conditions and a high spectral radiation transport efficiency in the UV Vis band.

The reflective multi-pass photoreactor design introduced herein is one option to master the photoreaction engineering part of the overall challenge. The design can be made from cheap materials with established mass production techniques, and, if designed properly, exhibits a high spectral radiation transport efficiency. The derived design guideline, thereby, supports the selection of suitable materials and the determination of suitable characteristic dimensions resulting in a photoreactor suitable for a specific photocatalytic system. The design guideline, therewith, provides the basis for further development and adaptation of the proposed design to other photocatalytic systems. Even though demonstrated with a standard liquid phase photochemical reaction, the design approach is easily adaptable to photocatalytic reactions of all kinds, including gas, liquid and heterogeneous multi-phase catalysis in the fields of solar fuels, (waste) water treatment, or fine chemical synthesis.

9.   Summary and conclusions

With the work presented herein the multi-facetted materials and photochemical engineering challenge introduced in chapter 1 aiming for low-cost, high efficiency photocatalytic processes is discussed and analysed in detail.

Starting from an analysis of the status quo in chapter 2, the prerequisites and core challenges are worked out. Summarizing, the design of a high efficiency photocatalytic process is governed by the reaction engineering and optical properties of the light source, the photocatalyst, and the photoreactor. If the sun represents the light source, the design challenge naturally focuses on the photocatalyst and photoreactor. A suitable photocatalyst exhibits a high quantum yield throughout the relevant optical band that equals in case of a sunlight driven process the UV and Vis band. A suitable photoreactor ensures the operating conditions under which the quantum yield peaks and guides incident light into the reaction volume with as low as possible photon losses. Achieving low costs in both, fabrication and operation requires a reactor design that is manufacturable in cheap materials with standard, low-cost techniques. Additionally, the design must possess robust operating characteristics, especially with regard to the tolerance towards a varying direction of incident light resulting from a moving sun in the sky.

Further, the analysis in chapter 2 reveals that two core skills are essential in a photoreactor design process. Firstly, for the sake of the outstanding importance of the quantum yield of the employed photocatalyst, methods for the precise determination of the latter are indispensable. Of especial importance is, thereby, the ability to map the dependencies of the quantum yield on the operating conditions, namely temperature, reactant concentrations, wavelength, and local volumetric rate of photon absorption. These dependencies set the requirements on the photoreactor engineering side of the overall challenge. The second core skill is the ability to map radiation transport in complex multi-component systems such as photoreactors. The latter indirectly demands for the ability to determine optical transport properties, such as refractive indices, absorption and scattering coefficients, reflectivities, etc., of the employed photoreactor components and photocatalysts.

Within chapter 4 of the present work a precise and especially flexible radiation transport model is introduced. The model is implemented in MATLAB® and represents an implementation of a Monte Carlo ray tracing method. The implementation is in many aspects similar to methods in the family of Monte Carlo ray tracing methods known from rendering problems in computer graphics applications. The developed toolbox, thereby, allows to map radiation transport in three dimensions in multi-component systems built from transparent, translucent, and opaque objects. The simulation domain can comprise free-formed shapes with a high design freedom. However, the complexity of the geometry is constraint to extrudable geometries that can be projected into two dimensions. This seeming limitation is ideal for channel-like geometries and accelerates significantly the numerical solution process. Together with the three additionally implemented acceleration techniques, parallelization, bounding volumes, and retracing, a computationally cost-effective solution of different scientific and engineering issues is guaranteed. Validated via a set of literature-reported radiation transport problems with explicit solutions, the toolbox developed in the framework of the present work provides a robust basis for the various optical challenges encountered in the field of optical property determination, quantum yield measurements, and high efficiency photoreactor design.

To complete the introduced Monte Carlo Ray tracing toolbox and provide the basis for reasonable optical simulations using the environment, in chapter 6, a set of methods for the determination of optical transport properties is introduced and applied to both, a set of reactor component materials, and photocatalysts employed in the present work. Beyond the description of methods for the determination of optical transport properties of reactor component materials and photocatalysts, in chapter 6, additionally, methods for the fabrication of reactor components via additive manufacturing and the synthesis of both active materials and translucent active material supports are introduced. The fabrication of reactor components via powder bed fusion with laser beams of 316L stainless steel, thereby, turns out to show a limited suitability for the fabrication of optical components. The rather high mean surface roughness of the printed raw parts requires a time consuming post-treatment of printed optical surfaces via micro-milling and suspension-based polishing to achieve both high reflectivity and specular reflection characteristics as needed for high efficiency photoreactor design. In contrast, the described active material and photocatalyst support development resulted in a simple-to-synthesise active material for methanol photo-reforming with an evident photocatalytic contribution in the reaction mechanism and a photocatalyst support strategy

that is straight forward and based on well-known and easy to synthesize silica aerogels. Interestingly, the determined optical transport properties of prepared aerogel-supported photocatalysts imply that due to intense absorption and scattering, even in very dilute photocatalysts, the illumination of larger bulk volumes is impossible. Absorption and scattering coefficients are so high that typical penetration depths of photons into a photocatalyst bed lie more in the sub-millimeter to millimeter range than in the centimeter to meter range. The latter unambiguously underlines the need for micro process engineering in the field of photoreaction engineering.

In chapter 7 a hybrid approach for the precise determination of quantum yields in gas, liquid, and heterogeneously catalysed multi-phase reactions is introduced. 'Hybrid', thereby, refers to the combination of detailed experimentation delivering the number of production events and sophisticated optical simulations delivering the number of absorbed photons. The approach allows the variation of temperature, reactant concentrations, wavelength, and volumetric rate of photon absorption. The approach, therewith, allows a variation of all important operating conditions potentially influencing the quantum yield in a photoreaction. A special focus is laid on the design of the employed photoreactor that provides an isophotonic reaction volume, meaning a reaction volume with as low as possible gradients in the local volumetric rate of photon absorption. This unique system property is achieved by a numerical design optimization of the employed LED light source modules and the control of the optical density of the reaction volume via an optical dilution of the characterized active material. The approach is both validated via the determination of the quantum yield of the literature-known potassium ferrioxalate photoreduction and applied to the methanol photo-reforming photocatalyst described in chapter 6. The validation via the determination of the quantum yield of the potassium ferrioxalate photoreduction underlines the validity of the overall approach. The presented quantum yield data for the methanol reforming system further reveals interesting dependencies of the quantum yield on the operating conditions. These dependencies indicate a complex system behaviour being influenced by temperature, reactant concentration, wavelength, and local volumetric rate of photon absorption. The 'optical' operating conditions, wavelength and local volumetric rate of photon absorption, thereby, have the most significant impact on the quantum yield. Of utmost importance for photoreactor design is the observed dependency of the quantum yield on the local volumetric rate of photon absorption: The evident systematic decrease of the quantum yield with increasing local volumetric rate of photon absorption, or increased process

intensity, respectively, entails a trade-off situation demanding for a careful optimization in a photoreactor design process. A decreasing quantum yield with increasing local volumetric rate of photon absorption indicates that higher overall photocatalytic efficiencies can be achieved if incident photons are distributed to a larger amount of active material. For the sake of the high complexity of visible light active high quantum yield active materials it is to be expected that those materials are expensive and a spare but especially efficient use is necessary to ensure an overall low cost. The resulting trade off between high photocatalytic efficiency and low system cost will need a careful consideration on a case to case basis. A decreasing quantum yield with increasing local volumetric rate of photon absorption further demands for a sophisticated optical design ensuring a homogeneous distribution of incident photons into the reaction volume. Absorption hot spots would entail a local decrease of the quantum yield and a therefrom resulting decrease of the overall photocatalytic efficiency.

Lastly, in chapter 8, a low-cost and high efficiency photoreactor design is introduced, numerically optimized, and validated with a model photoreaction, the potassium ferrioxalate photoreduction. The design process relies on the methods and information introduced and described in chapters 4 and 6: (1) the validated radiation transport model, (2) the introduced manufacturing routes for photoreactor prototypes, (3) the synthesis routes for active materials and active material supports, (4) the set of methods for the determination of optical transport properties, and (5) the approach for the precise determination of quantum yields in photoreactions. Noteworthy, the introduced photoreactor design is not limited to an application in the field of homogeneous liquid phase photocatalysis, like for instance the potassium ferrioxalate photoreduction, but can easily be adopted to any gas, liquid, or heterogeneously catalysed multi-phase photocatalytic reaction. The proposed optical design is especially suited for photocatalysts that exhibit strong scattering. The photoreactor design, thereby, combines the beneficial radiation transport characteristics of literature-known concentrator cavity photoreactor designs and the low-cost and modular nature and broad acceptance angle characteristics of literature-reported polymer-based baggie and panel-like photoreactors. Despite the complex optical demands for a high efficiency photoreactor, the proposed design's basic geometry is still manufacturable via low-cost and established mass manufacturing techniques, polymer extrusion and polymer injection moulding. This paves the way for a potential commercialization of a photocatalytic process based on the proposed photoreactor design.

On an engineering point of view, the considerations regarding the achievable

limits for the photocatalytic efficiency in a photocatalytic process presented in chapter 8 not only support the interpretation of the performance of the optimized photoreactor but especially highlight once more the double challenge faced in high efficiency photoreactor design. It becomes clear that on the one hand, the quantum yield and its dependency on the wavelength set an ultimate limit for the achievable photocatalytic efficiency in any photocatalytic process. On the other hand, a theoretical limit for the efficiency of radiation transport from the reactor aperture into the reaction volume sets a second limit for any optimization. The achievable radiation transport efficiency limit, thereby, strongly depends on the optical transport properties of the employed materials and chosen characteristic dimensions of the photoreactor.

The conducted loss mechanism analysis that precisely delineates prevalent loss mechanisms in the proposed photoreactor design supports the interim conclusion of an outstanding importance of optical transport properties and characteristic dimensions for a successful high efficiency photoreactor. Only, if the latter are chosen properly, a photoreactor can guarantee a significant total absorption share which is the prerequisite for any photocatalytic reaction to take place.

Taken together, the considerations regarding the achievable limits and the loss mechanism analysis cumulate in a design guideline that supports the appropriate choice of materials and the determination of suitable characteristic dimensions. A detailed discussion further underlines that for most photocatalytic systems, polychromatic considerations are indispensable and trade-offs in between the performance in different optical bands are needed. The introduced geometry optimization tool delivering free-form optimized photoreactors, thereby, is one option to address these challenging trade-off situations.

Summarizing, the work presented herein first of all delivers a complete set of methods for the design of a high efficiency photocatalytic process. This includes (1) precise but computationally manageable methods for the simulation of radiation transport in multi component systems, (2) manufacturing techniques for photoreactor prototypes, (3) synthesis routes for model photocatalysts, including active materials and active material supports, (4) methods for the determination of optical transport properties, (5) methods for the reaction engineering characterization of photocatalysts, and (6) numerical free-form optimization tools for the optimization of photoreactors under the consideration of polychromatic sunlight. Beyond this method toolbox, the work presented herein outlines the complexity of high efficiency photoreactor design and sheds light on the pivotal roles of light source, photocatalyst, and

photoreactor. The presented quantum yield data of a model photoreaction highlights the need for diligent analysis of quantum yields in photoreactions and the careful definition of operating conditions in photocatalytic processes. Lastly, the proposed photoreactor design opens one way towards a low-cost photocatalytic process. Its potential is underlined by a patent application filed in summer 2022 [143]. The detailed analysis of the proposed design gives insights into the complex prevalent loss mechanisms and cumulates in a design guideline paving the way for adaption, further development, and potential commercial implementation of photocatalytic processes relying on the proposed reflective multi-pass photoreactor design.

10. Outlook

Undoubtedly, materials are one corner stone in high efficiency photocatalytic process design. This includes reactor component materials but especially addresses the photocatalyst. In the present work, model photocatalysts are employed to demonstrate the validity of proposed methods and high efficiency photoreactor design. The challenge of the synthesis of an active material driving a relevant chemical reaction, for instance, the water splitting reaction, is not addressed. The need for a high quantum yield in the UV and Vis band, thereby, represents the core challenge that is not fully mastered until today. Indeed, there are many promising active materials reported. This includes, for instance, active materials for the water splitting reaction from the group around Kazunari Domen at the University of Tokyo. Those materials exhibit quantum yields close to unity but unfortunately are only active in the close UV and not in the Vis band. The challenge of an extension of the photocatalytic activity from the UV into the Vis band, thereby, is a well-known hurdle in the field of solar fuels. Further development, for instance, via the employment of new materials, like perovskite-based materials or cubic silicon carbide-based materials with suitable band gap, is undoubtedly needed. An encouraging fact is that many mechanisms and strategies for the governance of charge carrier dynamics and partial reactions, for instance, through a well-defined deposition of co-catalysts, are well understood and likely can be transferred from the experiences with UV active materials to new materials showing an activity in the Vis band as well.

As outlined in the present work, it is recommendable to impregnate active materials on translucent active material supports to ensure a good optical accessibility of the whole employed active material and control the operating conditions throughout the whole reaction volume. The proposed methodology via mixing of active material powders with silica aerogel powders is simple, functional, and easy to adopt to other material systems. However, the resulting photocatalysts exhibit rather high scattering coefficients which makes the illumination of larger reaction volumes impossible. Even though this is not necessarily a tremendous drawback, it makes the design of a high

efficiency photocatalytic process more difficult since the optical design of the photoreactor becomes more challenging in case of a strongly scattering photocatalyst. An improvement could be achieved by varying the aerogel impregnation strategy. Imaginable are, for instance, altered synthesis routes in which the active material is impregnated onto a silica alcogel in a wet impregnation process prior to the supercritical alcogel drying. Another approach could represent synthesis routes in which an active material slurry is added to the reacting sol in the alcogel synthesis. Preliminary studies in the framework of the present work imply, that these strategies may result in a more homogeneous dispersion of the active material in the aerogel support and a drastically reduced scattering coefficient of the resulting photocatalyst. As discussed in detail, both the active material development and the design of high efficiency photoreactors relies on methods for the precise determination of quantum yields. The approach for the precise determination of quantum yields introduced in the present work focuses on the provision of an isophotonic reaction zone, which, as shown in detail, indeed is highly relevant. The employed LEDs, however, are narrow banded but do not emit monochromatic light, which results in the challenge to differentiate the contributions of different wavelengths in a post experiment analysis. More elegant and more straightforward would be the employment of even narrower banded light sources or the employment of narrow band pass filters in the setup. Likely, this will also slightly alter the optical design of the employed photoreactor. The basic design idea of a diffusely reflecting cavity and a geometry optimized light source module, however, might still be a promising approach. The proposed light source optimization strategies could, thereby, be applied as demonstrated in the present work.

The reflective multi-pass photoreactor design concept developed in the present work is demonstrated in an additively manufactured lab demonstrator. As evident from the discussions regarding suitability of the employed manufacturing routes, additive manufacturing in the employed variant is not able to deliver the needed surface qualities. Additionally, from its nature, additive manufacturing is not the manufacturing route that would be chosen for mass production of photoreactors. Further, the materials employed in the lab demonstrator, 316L stainless steel, quartz glass, and silver coatings, are expensive and likely not the materials of choice in a photoreactor design intended for mass-production. The proposed employment of polymers, for instance polymethylmetharylate, and the employment of mass manufacturing routes, polymer extrusion and polymer injection moulding, remain to be demonstrated. The challenges that might be encountered in this research and

development task are (a) the surface quality of the optics module, which must be smooth enough to show specular reflection characteristics, (b) the application of a reflective layer, likely an aluminum layer, on the bottom side of the optics module, (c) the integration of the photocatalyst in the photoreactor channels, and (d) multiple additional material related issues that address the long-term stability of reflective multi-pass reactors. Those are, for instance, the resistance of the employed polymer towards the reactants, the resistance of the employed polymers towards UV irradiation, or the long term stability of the employed photocatalyst under realistic operating characteristics including diurnal and annual variations of the sunlight intensity. Moreover, the photocatalyst and photoreactor together do not result in a full process. Especially for an application in residential environments, fully integrated systems are needed. Such systems include the reactant conditioning upstream of the photoreactor and the product purification downstream of the photoreactor. The integration of a working photocatalyst-photoreactor combination with the necessary reaction engineering devices remains another open challenge. Summarizing, the work presented herein represents a significant contribution to the field of photochemical engineering. Nevertheless, it is only a small step in the overall way leading towards a low cost, high efficiency solar fuel process representing a corner stone of a future energy economy.
A long way towards a reasonable, sustainably living world society remains to be mastered.

Nomenclature

Abbreviations

CB	conduction band
IPCC	Intergovernmental Panel on Climate Change
IR	infrared
IUPAC	International Union of Pure and Applied Chemistry
LED	light emitting diodes
UV	ultra violet
VB	valence band
Vis	visible
CAD	computer aided design
CAPEX	capital expenditure
LED	light emitting diode
OPEX	operating expenditure
P&ID	piping and instrumentation diagram
PTB	Physikalisch Technische Bundesanstalt
PTFE	polytetrafluoroethylene
SMD	surface mount device

Molecular formulae

CH_2O	formaldehyde
$CHOOCH_3$	methyl formate
Fe^{II+}	iron-(II)-ion
$Pd(NO_3)_2$	palladium nitrate hydrate
TiO_2	titania
CeO_2	cerium oxide
CH_3OH	methanol

CH_4	methane	
CO	carbon monoxide	
CO_2	carbon dioxide	
H_2	hydrogen	
H_2O	water	
MO_2	generic metal oxide	
$MO_{2-\delta}$	generic partially reduced metal oxide	
NH_3	ammonia	
O_2	oxygen	
$TMOS$	tetra methyl ortho silicate	

Symbols

α	incidence angle	°
β	angle of refraction	°
$\dot{N}_{i,Feed}$	molar reactor feed rate of species i	$\mathrm{mol\,s^{-1}}$
$\dot{r}_{H_2}$	apparent catalyst mass specific hydrogen reaction rate	$\mathrm{mol\,g_{catalyst}^{-1}\,s^{-1}}$
η_p	photocatalytic efficiency	-
η_{STF}	solar to fuel energy efficiency	-
$\eta_{T,\lambda}$	spectral radiation transport efficiency	-
$\eta_{T,limit,\lambda}$	spectral radiation transport efficiency limit	-
$\eta_{T,limit,conc}$	minimal spectral parasitic absorption share of concentrator	-
$\eta_{T,limit,glass}$	minimal spectral parasitic absorption share of glass tubing	-
$\eta_{T,limit,wall}$	minimal spectral parasitic absorption share of cavity wall	-
γ	angle of reflection of diffusely reflected ray	°
$\hat{J}$	jacobian matrix in optimum in parameter estimation	variable
λ	wavelength	nm
ν	photon frequency	Hz
Ω	total absorption share in design guideline	-
Φ	quantum yield	-

ϕ	azimuth angle	°
σ_a	Napierian absorption coefficient	m^{-1}
σ_{ext}	Napierian extinction coefficient	m^{-1}
σ_s	Napierian scattering coefficient	m^{-1}
τ	space time	min
Θ	polar angle	°
θ	acceptance angle	°
ξ_{direct}	direct illumination share in high efficiency photoreactor design guideline	-
A	aperture area	m^2
A_e	Napierian absorbance	-
$A_{GC,i}$	gas chromatograph response for species i	$\mu\text{V s}$
a_{H_2}	hydrogen activity	$\text{mol g}_{\text{catalyst}}^{-1}\,\text{s}^{-1}$
C	geometric concentration ratio	-
c_i	concentration of species i	mol m^{-3}
D	deformation depth in free-form optimization	-
d_1	characteristic length of glass tubing in high efficiency photoreactor design guideline	m
d_2	characteristic length of reaction volume in high efficiency photoreactor design guideline	m
d_{cavity}	cavity diameter	m
E_λ	spectral irradiance	$\text{W m}^{-2}\,\text{nm}^{-1}$
E_p	photon irradiance in rate law	$\text{einstein m}^{-2}\,\text{s}^{-1}$
$E_{a,dark}$	apparent activation energy for dark contribution in rate law	J mol^{-1}
$E_{a,light}$	apparent activation energy for light contribution in rate law	J mol^{-1}
$E_{p,\lambda}$	spectral photon irradiance	$\text{einstein m}^{-2}\,\text{s}^{-1}$
$E_{p,ref}$	photon irradiance reference in rate law	$\text{einstein m}^{-2}\,\text{s}^{-1}$
f_1	total attenuation factor in high efficiency photoreactor design guideline	-
f_2	reaction volume absorption factor in high efficiency photoreactor design guideline	-

f_3	glass tubing absorption factor in high efficiency photoreactor design guideline	-
f_4	cavity wall absorption factor in high efficiency photoreactor design guideline	-
h	Plank constant	J s
I	intensity of propagating ray	W
I_R	intensity of reflected ray	W
I_{inc}	intensity of incident ray	W
I_{LED}	LED drive current	A
I_{max}	intensity of reflected ray under normal direction (diffuse reflection)	W
k	first reflection factor in high efficiency photoreactor design guideline	-
$k_{H_2,diff}$	difference between light and dark frequency factor in hydrogen rate law	$m^3\,mol^{-1}\,s^{-1}$
$k_{ref,dark}$	apparent reference frequency factor for dark contribution in a rate law	$m^3\,mol^{-1}\,s^{-1}$
$k_{ref,light}$	apparent reference frequency factor for light contribution in a rate law	$m^3\,mol^{-1}\,s^{-1}$
L	optical path length	m
$L_{p,\lambda}^a$	spectral local volumetric rate of photon absorption	$einstein\,m^{-3}\,s^{-1}$
M	vertex index deformation center in free-form optimization	-
m_{cat}	catalyst mass in photoreactor	g
n_i	refractive index of phase i	-
N_{bV}	number of bounding volumes per hierarchy level	-
$N_{elements}$	number of surface elements	-
N_{min}	minimum number of ray passages in design guideline	-
$N_{rays,RV}^a$	number of simulated rays absorbed by the reaction volume	-
$N_{rays,sim}$	number of simulated rays	-

$p_{S,i}$	vapour pressure of species i	Pa
p_{System}	system pressure	Pa
q	total emission of light source	W
q_λ	total spectral emission of light source	$W\,nm^{-1}$
$q_{cal,i}$	gas chromatograph calibration factor for species i	$\mu V^{-1}\,s^{-1}$
R	reflectivity of phase boundary or opaque surface	-
$R_{diffuse}$	diffuse reflectivity	-
$r_{goniometer}$	radius of goniometer arm	m
$R_{KM,layer}$	albedo of an optically thick layer under diffuse illumination after Kubelka Munk model	-
R_{raw}	raw data of total/diffuse reflectivity in UV Vis reflectivity measurements	-
$R_{standard}$	reflection standard reflectivity in UV Vis reflectivity measurements	-
R_{window}	reflectivity of a window (two consecutive phase boundaries)	-
S	specular share in total reflectivity	-
s^2	estimated variance of residuals in parameter estimation	variable
T	temperature	°C
T_{calc}	calcination temperature	°C
T_{window}	transmission of window in air	-
V	reaction volume	m^3
W	deformation width in free-form optimization	-
$w_{aperture}$	channel aperture width	m
w_{Pd}	palladium loading of titania active material	%
w_{slit}	cavity entry slit width	m
x_i	molar fraction of species i in liquid phase	-
y_i	molar fraction of species i in gas phase	-

Bibliography

[1] V. P. Masson-Delmotte et al. *Climate Change 2021: The Physical Science Basis. Contribution of Working Group I to the Sixth Assessment Report of the Intergovernmental Panel on Climate Change: Summary for Policymakers*. Ed. by Cambridge University Press. 2021.

[2] Francisco M. Calafat et al. "Trends in Europe storm surge extremes match the rate of sea-level rise". In: *Nature* 603.7903 (2022), pp. 841–845. DOI: 10.1038/s41586-022-04426-5.

[3] Joana Figueiredo et al. "Global warming decreases connectivity among coral populations". In: *Nature Climate Change* 12.1 (2022), pp. 83–87. ISSN: 1758-678X. DOI: 10.1038/s41558-021-01248-7.

[4] Qian Wang, Chanon Pornrungroj, et al. "Strategies to improve light utilization in solar fuel synthesis". In: *Nature Energy* 7.1 (2022), pp. 13–24. DOI: 10.1038/s41560-021-00919-1.

[5] E. M. Fischer and R. Knutti. "Anthropogenic contribution to global occurrence of heavy-precipitation and high-temperature extremes". In: *Nature Climate Change* 5.6 (2015), pp. 560–564. ISSN: 1758-678X. DOI: 10.1038/nclimate2617.

[6] Ki-Hyun Kim, Ehsanul Kabir, and Shamin Ara Jahan. "A review of the consequences of global climate change on human health". In: *Journal of environmental science and health. Part C, Environmental carcinogenesis & ecotoxicology reviews* 32.3 (2014), pp. 299–318. DOI: 10.1080/10590501.2014.941279.

[7] Mathew E. Hauer. "Migration induced by sea-level rise could reshape the US population landscape". In: *Nature Climate Change* 7.5 (2017), pp. 321–325. ISSN: 1758-678X. DOI: 10.1038/nclimate3271.

[8] Christian Almer, Jérémy Laurent-Lucchetti, and Manuel Oechslin. "Water scarcity and rioting: Disaggregated evidence from Sub-Saharan Africa". In: *Journal of Environmental Economics and Management* 86 (2017), pp. 193–209. ISSN: 00950696. DOI: 10.1016/j.jeem.2017.06. 002.

[9] Devin C. Bowles, Colin D. Butler, and Neil Morisetti. "Climate change, conflict and health". In: *Journal of the Royal Society of Medicine* 108.10 (2015), pp. 390–395. DOI: 10.1177/0141076815603234.

[10] Pierre Friedlingstein et al. "Global Carbon Budget 2020". In: *Earth System Science Data* 12.4 (2020), pp. 3269–3340. ISSN: 1866-3516. DOI: 10.5194/essd-12-3269-2020.

[11] Timothy M. Lenton et al. "Tipping elements in the Earth's climate system". In: *Proceedings of the National Academy of Sciences of the United States of America* 105.6 (2008), pp. 1786–1793. DOI: 10.1073/ pnas.0705414105.

[12] UN. *Paris Agreement*. Paris, 2015. URL: https://unfccc.int/process- and-meetings/the-paris-agreement/the-paris-agreement (visited on 10/26/2018).

[13] Myles Allen et al. *Global Warming of 1.5 ℃*. Incheon, Korea, 2018. URL: http://www.ipcc.ch/report/sr15/ (visited on 10/18/2018).

[14] Jan C. Minx et al. "A comprehensive and synthetic dataset for global, regional, and national greenhouse gas emissions by sector 1970–2018 with an extension to 2019". In: *Earth System Science Data* 13.11 (2021), pp. 5213–5252. ISSN: 1866-3516. DOI: 10.5194/essd-13-5213-2021.

[15] BP plc, ed. *BP Statistical Review of World Energy*. London, 2021.

[16] BP plc, ed. *BP Statistical Review of World Energy*. London, 2018.

[17] Falko Ueckerdt et al. "Potential and risks of hydrogen-based e-fuels in climate change mitigation". In: *Nature Climate Change* 11.5 (2021), pp. 384–393. ISSN: 1758-678X. DOI: 10.1038/s41558-021-01032-7.

[18] Francisco Vidal Vázquez et al. "Power-to-X technology using renewable electricity and carbon dioxide from ambient air: SOLETAIR proof-of-concept and improved process concept". In: *Journal of CO2 Utilization* 28 (2018), pp. 235–246. ISSN: 22129820. DOI: 10.1016/j.jcou. 2018.09.026.

[19]   Jordi Guilera et al. "Synthetic natural gas production from biogas in a waste water treatment plant". In: *Renewable Energy* 146 (2020), pp. 1301–1308. ISSN: 09601481. DOI: 10.1016/j.renene.2019.07.044.

[20]   Arne Kätelhön et al. "Climate change mitigation potential of carbon capture and utilization in the chemical industry". In: *Proceedings of the National Academy of Sciences of the United States of America* (2019). DOI: 10.1073/pnas.1821029116.

[21]   Nicola Armaroli and Vincenzo Balzani. "Solar Electricity and Solar Fuels: Status and Perspectives in the Context of the Energy Transition". In: *Chemistry (Weinheim an der Bergstrasse, Germany)* 22.1 (2016), pp. 32–57. DOI: 10.1002/chem.201503580.

[22]   Remo Schäppi et al. "Drop-in Fuels from Sunlight and Air". In: *Nature* (2021). DOI: 10.1038/s41586-021-04174-y.

[23]   Hiroshi Nishiyama et al. "Photocatalytic solar hydrogen production from water on a 100-m2 scale". In: *Nature* 598.7880 (2021), pp. 304–307. DOI: 10.1038/s41586-021-03907-3.

[24]   Blaise A. Pinaud et al. "Technical and economic feasibility of centralized facilities for solar hydrogen production via photocatalysis and photoelectrochemistry". In: *Energy & Environmental Science* 6.7 (2013), p. 1983. ISSN: 1754-5692. DOI: 10.1039/c3ee40831k.

[25]   Deutscher Wetterdienst. *Jahresgang Globalstrahlung 2021.* 2021.

[26]   Mineralölwirtschaftsverband e.V., ed. *Jahresbericht 2018.* Berlin, 2018.

[27]   Silvia E. Braslavsky et al. "Glossary of terms used in photocatalysis and radiation catalysis (IUPAC Recommendations 2011)". In: *Pure and Applied Chemistry* 83.4 (2011), pp. 931–1014. ISSN: 1365-3075. DOI: 10.1351/PAC-REC-09-09-36.

[28]   Dennis Y. C. Leung et al. "Hydrogen production over titania-based photocatalysts". In: *ChemSusChem* 3.6 (2010), pp. 681–694. DOI: 10.1002/cssc.201000014.

[29]   S. Bhatta, D. Nagassou, and J. P. Trelles. "Solar photo-thermochemical reactor design for carbon dioxide processing". In: *Solar Energy* 142 (2017), pp. 253–266. ISSN: 0038092X. DOI: 10.1016/j.solener.2016.12.031.

[30]   Athanasios A. Tountas, Geoffrey A. Ozin, and Mohini M. Sain. "Solar methanol energy storage". In: *Nature Catalysis* 4.11 (2021), pp. 934–942. DOI: 10.1038/s41929-021-00696-w.

[31] Felix Rechberger and Markus Niederberger. "Translucent nanoparticle-based aerogel monoliths as 3-dimensional photocatalysts for the selective photoreduction of CO 2 to methanol in a continuous flow reactor". In: *Materials Horizons* 4.6 (2017), pp. 1115–1121. ISSN: 2051-6347. DOI: 10.1039/C7MH00423K.

[32] Samar Al Jitan, Giovanni Palmisano, and Corrado Garlisi. "Synthesis and Surface Modification of TiO2-Based Photocatalysts for the Conversion of CO2". In: *Catalysts* 10.2 (2020), p. 227. DOI: 10.3390/catal10020227.

[33] Wenguang Tu et al. "Au@TiO$_2$ yolk-shell hollow spheres for plasmon-induced photocatalytic reduction of CO$_2$ to solar fuel via a local electromagnetic field". In: *Nanoscale* 7.34 (2015), pp. 14232–14236. DOI: 10.1039/c5nr02943k.

[34] William C. Chueh et al. "High-flux solar-driven thermochemical dissociation of CO2 and H2O using nonstoichiometric ceria". In: *Science (New York, N.Y.)* 330.6012 (2010), pp. 1797–1801. DOI: 10.1126/science.1197834.

[35] Tsuyoshi Takata et al. "Photocatalytic water splitting with a quantum efficiency of almost unity". In: *Nature* 581.7809 (2020), pp. 411–414. DOI: 10.1038/s41586-020-2278-9.

[36] Yohei Cho et al. "Visible-light-driven dry reforming of methane using a semiconductor-supported catalyst". In: *Chemical communications (Cambridge, England)* 56.33 (2020), pp. 4611–4614. DOI: 10.1039/D0CC00729C.

[37] Hong Wang, Jia Jia, et al. "Heterostructure Engineering of a Reverse Water Gas Shift Photocatalyst". In: *Advanced science (Weinheim, Baden-Wurttemberg, Germany)* 6.22 (2019), p. 1902170. ISSN: 2198-3844. DOI: 10.1002/advs.201902170.

[38] Mariana P. Languer et al. "Photo-induced reforming of alcohols with improved hydrogen apparent quantum yield on TiO2 nanotubes loaded with ultra-small Pt nanoparticles". In: *International Journal of Hydrogen Energy* 38.34 (2013), pp. 14440–14450. ISSN: 03603199. DOI: 10.1016/j.ijhydene.2013.09.018.

[39] ASTM International. *Standard Tables for Reference Solar Spectral Irradiances: Direct Normal and Hemispherical on 37° Tilted Surface.* London, 2020.

[40] Christopher Perkins and Alan W. Weimer. "Solar-thermal production of renewable hydrogen". In: *AIChE Journal* 55.2 (2009), pp. 286–293. ISSN: 00011541. DOI: 10.1002/aic.11810.

[41] A. Stamatiou, P. G. Loutzenhiser, and A. Steinfeld. "Solar Syngas Production via H 2 O/CO 2 -Splitting Thermochemical Cycles with Zn/ZnO and FeO/Fe 3 O 4 Redox Reactions". In: *Chemistry of Materials* 22.3 (2010), pp. 851–859. ISSN: 0897-4756. DOI: 10.1021/cm9016529.

[42] Christopher L. Muhich et al. "Comparing the solar-to-fuel energy conversion efficiency of ceria and perovskite based thermochemical redox cycles for splitting H2O and CO2". In: *International Journal of Hydrogen Energy* 43.41 (2018), pp. 18814–18831. ISSN: 03603199. DOI: 10.1016/j.ijhydene.2018.08.137.

[43] Michael R. Hoffmann et al. "Environmental Applications of Semiconductor Photocatalysis". In: *Chemical Reviews* 95.1 (1995), pp. 69–96. ISSN: 0009-2665. DOI: 10.1021/cr00033a004.

[44] Yoshihisa Sakata et al. "Remarkably high apparent quantum yield of the overall photocatalytic H2O splitting achieved by utilizing Zn ion added Ga2O3 prepared using dilute CaCl2 solution". In: *Chemical communications (Cambridge, England)* 51.65 (2015), pp. 12935–12938. DOI: 10.1039/C5CC03483C.

[45] Caixian Zhao et al. "A novel composite of TiO2 nanotubes with remarkably high efficiency for hydrogen production in solar-driven water splitting". In: *Energy & Environmental Science* 7.5 (2014), p. 1700. ISSN: 1754-5692. DOI: 10.1039/c3ee43165g.

[46] R. Dholam et al. "Hydrogen production by photocatalytic water-splitting using Cr- or Fe-doped TiO2 composite thin films photocatalyst". In: *International Journal of Hydrogen Energy* 34.13 (2009), pp. 5337–5346. ISSN: 03603199. DOI: 10.1016/j.ijhydene.2009.05.011.

[47] R. Asahi et al. "Visible-light photocatalysis in nitrogen-doped titanium oxides". In: *Science (New York, N.Y.)* 293.5528 (2001), pp. 269–271. DOI: 10.1126/science.1061051.

[48] Jum Suk Jang et al. "Location and State of Pt in Platinized CdS/TiO 2 Photocatalysts for Hydrogen Production from Water under Visible Light". In: *The Journal of Physical Chemistry C* 112.44 (2008), pp. 17200–17205. ISSN: 1932-7447. DOI: 10.1021/jp804699c.

[49]   Jie Zhang et al. "Photogeneration of hydrogen from water using an integrated system based on TiO2 and platinum(II) diimine dithiolate sensitizers". In: *Journal of the American Chemical Society* 129.25 (2007), pp. 7726–7727. DOI: 10.1021/ja071789h.

[50]   Wei Wang, Yao Zhang, et al. "Reverse water gas shift over In 2 O 3 –CeO 2 catalysts". In: *Catalysis Today* 259 (2016), pp. 402–408. ISSN: 09205861. DOI: 10.1016/j.cattod.2015.04.032.

[51]   K. Sayama et al. "Stoichiometric water splitting into H2 and O2 using a mixture of two different photocatalysts and an IO3-/I- shuttle redox mediator under visible light irradiation". In: *Chemical communications (Cambridge, England)* 23 (2001), pp. 2416–2417. DOI: 10.1039/b107673f.

[52]   David M. Fabian et al. "Particle suspension reactors and materials for solar-driven water splitting". In: *Energy & Environmental Science* 8.10 (2015), pp. 2825–2850. ISSN: 1754-5692. DOI: 10.1039/c5ee01434d.

[53]   Rebecca L. Milot et al. "Temperature–Dependent Charge–Carrier Dynamics in CH 3 NH 3 PbI 3 Perovskite Thin Films". In: *Advanced Functional Materials* 25.39 (2015), pp. 6218–6227. ISSN: 1616-301X. DOI: 10.1002/adfm.201502340.

[54]   Michael B. Johnston and Laura M. Herz. "Hybrid Perovskites for Photovoltaics: Charge-Carrier Recombination, Diffusion, and Radiative Efficiencies". In: *Accounts of chemical research* 49.1 (2016), pp. 146–154. DOI: 10.1021/acs.accounts.5b00411.

[55]   Wen-Churng Lin et al. "Hydrogen Production from Methanol/Water Photocatalytic Decomposition Using Pt/TiO 2− x N x Catalyst". In: *Energy & Fuels* 23.4 (2009), pp. 2192–2196. ISSN: 0887-0624. DOI: 10.1021/ef801091p.

[56]   Salvador Escobedo Salas, Benito Serrano Rosales, and Hugo de Lasa. "Quantum yield with platinum modified TiO2 photocatalyst for hydrogen production". In: *Applied Catalysis B: Environmental* 140-141 (2013), pp. 523–536. ISSN: 09263373. DOI: 10.1016/j.apcatb.2013.04.016.

[57]   Olga Fontelles-Carceller, Mario J. Muñoz-Batista, José Carlos Conesa, et al. "UV and visible hydrogen photo-production using Pt promoted Nb-doped TiO 2 photo-catalysts: Interpreting quantum efficiency". In: *Applied Catalysis B: Environmental* 216 (2017), pp. 133–145. ISSN: 09263373. DOI: 10.1016/j.apcatb.2017.05.022.

[58] A. Emeline, A. Salinaro, and N. Serpone. "Spectral Dependence and Wavelength Selectivity in Heterogeneous Photocatalysis. I. Experimental Evidence from the Photocatalyzed Transformation of Phenols". In: *The Journal of Physical Chemistry B* 104.47 (2000), pp. 11202–11210. ISSN: 1520-6106. DOI: 10.1021/jp001927o.

[59] Fabio Dionigi et al. "Gas phase photocatalytic water splitting with Rh2−yCryO3/GaN:ZnO in micro-reactors". In: *Energy & Environmental Science* 4.8 (2011), p. 2937. ISSN: 1754-5692. DOI: 10.1039/c1ee01242h.

[60] Mireille Ghoussoub et al. "Principles of photothermal gas-phase heterogeneous CO 2 catalysis". In: *Energy & Environmental Science* 52 (2019), p. 7372. ISSN: 1754-5692. DOI: 10.1039/c8ee02790k.

[61] Yuchan Dong et al. "Shining light on CO2: from materials discovery to photocatalyst, photoreactor and process engineering". In: *Chemical Society reviews* (2020). DOI: 10.1039/d0cs00597e.

[62] Laura B. Hoch et al. "Nanostructured Indium Oxide Coated Silicon Nanowire Arrays: A Hybrid Photothermal/Photochemical Approach to Solar Fuels". In: *ACS nano* 10.9 (2016), pp. 9017–9025. DOI: 10.1021/acsnano.6b05416.

[63] Jia Jia et al. "Photothermal Catalyst Engineering: Hydrogenation of Gaseous CO2 with High Activity and Tailored Selectivity". In: *Advanced science (Weinheim, Baden-Wurttemberg, Germany)* 4.10 (2017), p. 1700252. ISSN: 2198-3844. DOI: 10.1002/advs.201700252.

[64] Lourdes Hurtado et al. "Solar CO2hydrogenation by photocatalytic foams". In: *Chemical Engineering Journal* 435 (2022), p. 134864. ISSN: 13858947. DOI: 10.1016/j.cej.2022.134864.

[65] Joel Y. Y. Loh et al. "Waveguide photoreactor enhances solar fuels photon utilization towards maximal optoelectronic - photocatalytic synergy". In: *Nature communications* 12.1 (2021), p. 402. DOI: 10.1038/s41467-020-20613-2.

[66] Qian Wang, Takashi Hisatomi, et al. "Scalable water splitting on particulate photocatalyst sheets with a solar-to-hydrogen energy conversion efficiency exceeding 1". In: *Nature materials* 15.6 (2016), pp. 611–615. ISSN: 1476-1122. DOI: 10.1038/nmat4589.

[67]   Baowang Lu and Katsuya Kawamoto. "Preparation of monodispersed NiO particles in SBA-15, and its enhanced selectivity for reverse water gas shift reaction". In: *Journal of Environmental Chemical Engineering* 1.3 (2013), pp. 300–309. ISSN: 22133437. DOI: 10.1016/j.jece.2013.05.008.

[68]   Le He et al. "Spatial Separation of Charge Carriers in In2O3-x(OH)y Nanocrystal Superstructures for Enhanced Gas-Phase Photocatalytic Activity". In: *ACS nano* 10.5 (2016), pp. 5578–5586. DOI: 10.1021/acsnano.6b02346.

[69]   Andreas Jess and Peter Wasserscheid. *Chemical technology: An integral textbook*. Weinheim: Wiley-VCH, 2013. ISBN: 978-3-527-30446-2.

[70]   Xinbin Yu and Christopher T. Williams. "Recent advances in the applications of mesoporous silica in heterogeneous catalysis". In: *Catalysis Science & Technology* 12.19 (2022), pp. 5765–5794. ISSN: 2044-4753. DOI: 10.1039/d2cy00001f.

[71]   Li-Ying Shi et al. "Fabrication of highly dispersed nickel in nanoconfined spaces of as-made SBA-15 for dry reforming of methane with carbon dioxide". In: *Chemical Engineering Journal* 390 (2020), p. 124491. ISSN: 13858947. DOI: 10.1016/j.cej.2020.124491.

[72]   Yu Kou and Lin-Bing Sun. "Size Regulation of Platinum Nanoparticles by Using Confined Spaces for the Low-Temperature Oxidation of Ethylene". In: *Inorganic chemistry* 57.3 (2018), pp. 1645–1650. DOI: 10.1021/acs.inorgchem.7b02988.

[73]   Zhijie Wu et al. "Hydrothermal synthesis of LTA-encapsulated metal clusters and consequences for catalyst stability, reactivity, and selectivity". In: *Journal of Catalysis* 311 (2014), pp. 458–468. ISSN: 00219517. DOI: 10.1016/j.jcat.2013.12.021.

[74]   Xiaoliu Wang, Lingjun Zhu, et al. "Enhancement of CO 2 Methanation over La-Modified Ni/SBA-15 Catalysts Prepared by Different Doping Methods". In: *ACS Sustainable Chemistry & Engineering* 7.17 (2019), pp. 14647–14660. ISSN: 2168-0485. DOI: 10.1021/acssuschemeng.9b02563.

[75]   Vijayanand Subramanian et al. "The Role of Steric Effects and Acidity in the Direct Synthesis of iso -Paraffins from Syngas on Cobalt Zeolite Catalysts". In: *ChemCatChem* 8.2 (2016), pp. 380–389. ISSN: 18673880. DOI: 10.1002/cctc.201500777.

[76] Philipp Furler et al. "Solar Thermochemical CO2 Splitting Utilizing a Reticulated Porous Ceria Redox System". In: *Energy & Fuels* 26.11 (2012), pp. 7051–7059. ISSN: 0887-0624. DOI: 10.1021/ef3013757.

[77] Rajnish Changrani and Gregory B. Raupp. "Monte Carlo simulation of the radiation field in a reticulated foam photocatalytic reactor". In: *AIChE Journal* 45.5 (1999), pp. 1085–1094. ISSN: 00011541. DOI: 10.1002/aic.690450516.

[78] M. V. Twigg and J. T. Richardson. "Theory and Applications of Ceramic Foam Catalysts". In: *Chemical Engineering Research and Design* 80.2 (2002), pp. 183–189. ISSN: 02638762. DOI: 10.1205/026387602753501906.

[79] Nobuyuki Gokon et al. "Ferrite/zirconia-coated foam device prepared by spin coating for solar demonstration of thermochemical water-splitting". In: *International Journal of Hydrogen Energy* 36.3 (2011), pp. 2014–2028. ISSN: 03603199. DOI: 10.1016/j.ijhydene.2010.11.034.

[80] Sergio Muñoz et al. "Carbon Dioxide Hydrogenation by Means of Plasmonic Resonance Activation in Silica Aerogel Media". In: *Materials (Basel, Switzerland)* 11.11 (2018). ISSN: 1996-1944. DOI: 10.3390/ma11112134.

[81] Ahmad Jonoidi Jafari et al. "Synthesis and characterization of Ag-TiO2-composite aerogel for enhanced adsorption and photo-catalytic degradation of toluene from the gas phase". In: *Chemical Engineering Research and Design* 150 (2019), pp. 1–13. ISSN: 02638762. DOI: 10.1016/j.cherd.2019.07.017.

[82] Matthias Mecklenburg et al. "Aerographite: ultra lightweight, flexible nanowall, carbon microtube material with outstanding mechanical performance". In: *Advanced materials (Deerfield Beach, Fla.)* 24.26 (2012), pp. 3486–3490. DOI: 10.1002/adma.201200491.

[83] Luis Miguel Sanz-Moral et al. "View cell investigation of silica aerogels during supercritical drying: Analysis of size variation and mass transfer mechanisms". In: *The Journal of Supercritical Fluids* 92 (2014), pp. 24–30. ISSN: 08968446. DOI: 10.1016/j.supflu.2014.05.004.

[84] X. Lu, M. C. Arduini-Schuster, et al. "Thermal conductivity of monolithic organic aerogels". In: *Science (New York, N.Y.)* 255.5047 (1992), pp. 971–972. DOI: 10.1126/science.255.5047.971.

[85] B. Hosticka et al. "Gas flow through aerogels". In: *Journal of Non-Crystalline Solids* 225 (1998), pp. 293–297. ISSN: 00223093. DOI: 10.1016/S0022-3093(98)00130-6.

[86] Chandana Mandal et al. "Light scattering and haze in TMOS-co-APTES silica aerogels". In: *Journal of Sol-Gel Science and Technology* 90.1 (2019), pp. 127–139. ISSN: 09280707. DOI: 10.1007/s10971-018-4801-0.

[87] Tairan Fu et al. "Scattering and absorption coefficients of silica-doped alumina aerogels". In: *Applied optics* 55.4 (2016), pp. 705–711. DOI: 10.1364/AO.55.000705.

[88] Lu Wang, Yuchan Dong, et al. "Black indium oxide a photothermal CO2 hydrogenation catalyst". In: *Nature communications* 11.1 (2020), p. 2432. DOI: 10.1038/s41467-020-16336-z.

[89] Murielle Schreck et al. "3D Printed Scaffolds for Monolithic Aerogel Photocatalysts with Complex Geometries". In: *Small (Weinheim an der Bergstrasse, Germany)* 17.50 (2021), e2104089. DOI: 10.1002/smll.202104089.

[90] G. Camera-Roda et al. "Guidelines for the assessment of the rate law of slurry photocatalytic reactions". In: *Catalysis Today* 281 (2017), pp. 221–230. ISSN: 09205861. DOI: 10.1016/j.cattod.2016.06.050.

[91] R. J. Brandi, O. M. Alfano, and A. E. Cassano. "Evaluation of Radiation Absorption in Slurry Photocatalytic Reactors. 1. Assessment of Methods in Use and New Proposal". In: *Environmental Science & Technology* 34.12 (2000), pp. 2623–2630. ISSN: 0013-936X. DOI: 10.1021/es9909428.

[92] R. J. Brandi, O. M. Alfano, and A. E. Cassano. "Evaluation of Radiation Absorption in Slurry Photocatalytic Reactors. 2. Experimental Verification of the Proposed Method". In: *Environmental Science & Technology* 34.12 (2000), pp. 2631–2639. ISSN: 0013-936X. DOI: 10.1021/es9909430.

[93] Paul Kant, Laura Trinkies, et al. "Isophotonic photo reactor for the precise determination of quantum yields in gas, liquid, and multi pahse photo reactions". In: *Chemical Engineering Journal* 452 (2023). ISSN: 13858947. DOI: 10.1016/j.cej.2022.139204.

[94] Paul Kant, Shengzhi Liang, et al. "Low-cost photo reactors for high efficiency solar driven synthesis". In: (2022).

[95] Nick Serpone and Angela Salinaro. "Terminology, relative photonic efficiencies and quantum yields in heterogeneous photocatalysis. Part I: Suggested protocol". In: *Pure and Applied Chemistry* 71.2 (1999), pp. 303–320. ISSN: 1365-3075. DOI: 10.1351/pac199971020303.

[96] A. V. Emeline, X. Zhang, et al. "Application of a "black body" like reactor for measurements of quantum yields of photochemical reactions in heterogeneous systems". In: *The Journal of Physical Chemistry B* 110.14 (2006), pp. 7409–7413. ISSN: 1520-6106. DOI: 10.1021/jp057115f.

[97] Dengwei Jing et al. "Determination of the real quantum yield of the heterogeneous photocatalytic H 2 production reaction and insights". In: *Measurement Science and Technology* 32.4 (2021), p. 045901. ISSN: 0957-0233. DOI: 10.1088/1361-6501/abcff5.

[98] Angela Salinaro et al. "Terminology, relative photonic efficiencies and quantum yields in heterogeneous photocatalysis. Part II: Experimental determination of quantum yields". In: *Pure and Applied Chemistry* 71.2 (1999), pp. 321–335. ISSN: 1365-3075. DOI: 10.1351/pac199971020321.

[99] Lizhong Sun and James R. Bolton. "Determination of the Quantum Yield for the Photochemical Generation of Hydroxyl Radicals in TiO 2 Suspensions". In: *The Journal of Physical Chemistry* 100.10 (1996), pp. 4127–4134. ISSN: 0022-3654. DOI: 10.1021/jp9505800.

[100] Rowan J. Braham and Andrew T. Harris. "Review of Major Design and Scale-up Considerations for Solar Photocatalytic Reactors". In: *Industrial & engineering chemistry research* 48.19 (2009), pp. 8890–8905. ISSN: 0888-5885. DOI: 10.1021/ie900859z.

[101] Harry Apostoleris, Marco Stefancich, and Matteo Chiesa. "Tracking-integrated systems for concentrating photovoltaics". In: *Nature Energy* 1.4 (2016). DOI: 10.1038/nenergy.2016.18.

[102] Nick Jelley and Thomas Smith. "Concentrated solar power: Recent developments and future challenges". In: *Proceedings of the Institution of Mechanical Engineers, Part A: Journal of Power and Energy* 229.7 (2015), pp. 693–713. ISSN: 0957-6509. DOI: 10.1177/0957650914566895.

[103] G. Smestad et al. "The thermodynamic limits of light concentrators". In: *Solar Energy Materials* 21.2-3 (1990), pp. 99–111. ISSN: 01651633. DOI: 10.1016/0165-1633(90)90047-5.

[104]   Ali M. Qureshy, Mahmoud Ahmed, and Ibrahim Dincer. "Simulation of transport phenomena in a photo-electrochemical reactor for solar hydrogen production". In: *International Journal of Hydrogen Energy* 41.19 (2016), pp. 8020–8031. ISSN: 03603199. DOI: `10.1016/j.ijhydene.2015.12.218`.

[105]   Christian Sattler, Christian Jung, and Hans Jürgen Bigus. "Fotoreaktor: European Patent". EP 1 848 5 28 B1. 2011.

[106]   Rohini Bala Chandran et al. "Evaluating particle-suspension reactor designs for Z-scheme solar water splitting via transport and kinetic modeling". In: *Energy & Environmental Science* 11.1 (2018), pp. 115–135. ISSN: 1754-5692. DOI: `10.1039/c7ee01360d`.

[107]   Roland Dittmeyer et al. "Crowd oil not crude oil". In: *Nature communications* 10.1 (2019), p. 1818. DOI: `10.1038/s41467-019-09685-x`.

[108]   Wolfgang Demtröder. *Electrodynamics and Optics*. Cham: Springer International Publishing, 2019. ISBN: 978-3-030-02289-1. DOI: `10.1007/978-3-030-02291-4`.

[109]   Antonio Romano. *Geometric Optics: Theory and Design of Astronomical Optical Systems Using Mathematica®*. Modeling and Simulation in Science, Engineering and Technology. Boston: Birkhäuser Boston, 2010. ISBN: 978-0-8176-4871-8. DOI: `10.1007/978-0-8176-4872-5`. URL: `http://site.ebrary.com/lib/alltitles/docDetail.action?docID=10351832`.

[110]   William W. Parson. *Modern Optical Spectroscopy*. Berlin, Heidelberg: Springer Berlin Heidelberg, 2015. ISBN: 978-3-662-46776-3. DOI: `10.1007/978-3-662-46777-0`.

[111]   Frank L. Pedrotti and Leno S. Pedrotti. *Introduction to optics*. Englewood Cliffs, N.J.: Prentice-Hall, 1987. ISBN: 0-13-491465-1.

[112]   G. H. Spencer and M. V. R. K. Murty. "General Ray-Tracing Procedure†". In: *Journal of the Optical Society of America* 52.6 (1962), p. 672. DOI: `10.1364/JOSA.52.000672`.

[113]   Deutsches Institut für Normung. *Infromationsverarbeitung: Sinnbilder und ihre Anwendung*. Berlin, 1983.

[114]   Paul Kant. *phoRex & QY photoreactor - Monte Carlo ray tracing in MATLAB® & quantum yield measurements*. Karlsruhe, 2022. DOI: `10.5445/IR/1000150817`.

[115] Gustav Kortüm. *Reflexionsspektroskopie: Grundlagen, Methodik, Anwendungen*. Heidelberg, 1969.

[116] Paul Kubelka and Frank Munk. "Ein Beitrag zur Optik der Farbanstriche". In: *Zeitschrift für Technische Physik* 12 (1931), pp. 593–601.

[117] Paul Kubelka. "New Contributions to the Optics of Intensely Light-Scattering Materials. Part I". In: *Journal of the Optical Society of America* 38.5 (1947), pp. 448–457.

[118] ASTM International. *Standard Specification for Solar Simulation for Photovoltaic Testing*. London, 2015.

[119] *VDI Heat Atlas*. Berlin, Heidelberg: Springer Berlin Heidelberg, 2010. ISBN: 978-3-540-77876-9. DOI: 10.1007/978-3-540-77877-6.

[120] Ian Gibson, David Rosen, and Brent Stucker. *Additive manufacturing technologies: 3D printing, rapid prototyping and direct digital manufacturing*. Second Edition. New York et al.: Springer, 2015. ISBN: 978-1-4939-2113-3. URL: https://www.loc.gov/catdir/enhancements/fy1617/2014953293-b.html.

[121] International Organization for Standardization. *Geometrical Product Specifications*. Geneva, 2010.

[122] R. E. Hummel. "Reflectivity of silver- and aluminium-based alloys for solar reflectors". In: *Solar Energy* 27.6 (1981), pp. 449–455. ISSN: 0038092X. DOI: 10.1016/0038-092X(81)90040-2.

[123] M. A. Khashan and A. Y. Nassif. "Dispersion of the optical constants of quartz and polymethyl methacrylate glasses in a wide spectral range: 200–3000 nm". In: *Optics Communications* 188.1-4 (2001), pp. 129–139. ISSN: 00304018. DOI: 10.1016/S0030-4018(00)01152-4.

[124] Marco Montalti et al. *Handbook of photochemistry*. Third edition. Boca Raton: CRC/Taylor & Francis, 2020. ISBN: 9780367577902.

[125] Tomoya Inoue, Martin A. Schmidt, and Klavs F. Jensen. "Microfabricated Multiphase Reactors for the Direct Synthesis of Hydrogen Peroxide from Hydrogen and Oxygen". In: *Industrial & engineering chemistry research* 46.4 (2007), pp. 1153–1160. ISSN: 0888-5885. DOI: 10.1021/ie061277w.

[126] Manuel Selinsek et al. "Revealing the Structure and Mechanism of Palladium during Direct Synthesis of Hydrogen Peroxide in Continuous Flow Using Operando Spectroscopy". In: *ACS Catalysis* 8.3 (2018), pp. 2546–2557. ISSN: 2155-5435. DOI: 10.1021/acscatal.7b03514.

[127] Lawrence F. Shampine and Mark W. Reichelt. "The MATLAB ODE Suite". In: *SIAM Journal on Scientific Computing* 18.1 (1997), pp. 1–22. ISSN: 1064-8275. DOI: `10.1137/S1064827594276424`.

[128] Thomas F. Coleman and Yuying Li. "On the convergence of interior-reflective Newton methods for nonlinear minimization subject to bounds". In: *Mathematical Programming* 67.1-3 (1994), pp. 189–224. ISSN: 0025-5610. DOI: `10.1007/BF01582221`.

[129] Thomas F. Coleman and Yuying Li. "An Interior Trust Region Approach for Nonlinear Minimization Subject to Bounds". In: *SIAM Journal on Optimization* 6.2 (1996), pp. 418–445. ISSN: 1052-6234. DOI: `10.1137/0806023`.

[130] E. Aschenauer et al. "Optical characterization of n=1.03 silica aerogel used as radiator in the RICH of HERMES". In: *Nuclear Instruments and Methods in Physics Research Section A: Accelerators, Spectrometers, Detectors and Associated Equipment* 440.2 (2000), pp. 338–347. ISSN: 01689002. DOI: `10.1016/S0168-9002(99)00923-7`.

[131] Xinhai Xu, Kaipeng Shuai, and Ben Xu. "Review on Copper and Palladium Based Catalysts for Methanol Steam Reforming to Produce Hydrogen". In: *Catalysts* 7.6 (2017), p. 183. DOI: `10.3390/catal7060183`.

[132] George M. Hale and Marvin R. Querry. "Optical Constants of Water in the 200-nm to 200-mum Wavelength Region". In: *Applied Optics* 12.3 (1973), p. 555. ISSN: 0003-6935. DOI: `10.1364/AO.12.000555`.

[133] D. Reyes-Coronado et al. "Phase-pure TiO2 nanoparticles: anatase, brookite and rutile". In: *Nanotechnology* 19.14 (2008), p. 145605. DOI: `10.1088/0957-4484/19/14/145605`.

[134] C. G. Hatchard and C. A. Parker. "A new sensitive chemical actinometer - II. Potassium ferrioxalate as a standard chemical actinometer". In: *Proceedings of the Royal Society of London. Series A. Mathematical and Physical Sciences* 235.1203 (1956), pp. 518–536. ISSN: 0080-4630. DOI: `10.1098/rspa.1956.0102`.

[135] Benjamin Wriedt and Dirk Ziegenbalg. "Common pitfalls in chemical actinometry". In: *Journal of Flow Chemistry* 10.1 (2020), pp. 295–306. ISSN: 2062-249X. DOI: `10.1007/s41981-019-00072-7`.

[136] Benjamin Wriedt and Dirk Ziegenbalg. "Application Limits of the Ferrioxalate Actinometer**". In: *ChemPhotoChem* (2021). ISSN: 23670932. DOI: `10.1002/cptc.202100122`.

[137]   Tímea Lehóczki, Éva Józsa, and Katalin Ősz. "Ferrioxalate actinome-
         try with online spectrophotometric detection". In: *Journal of Photo-
         chemistry and Photobiology A: Chemistry* 251 (2013), pp. 63–68. ISSN:
         10106030. DOI: 10.1016/j.jphotochem.2012.10.005.

[138]   David E. Nicodem and Oscar M.V. Aquilera. "Standardization of the
         potassium ferrioxalate actinometer over the temperature range 5 –
         80 °C". In: *Journal of Photochemistry* 21.2 (1983), pp. 189–193. ISSN:
         00472670. DOI: 10.1016/0047-2670(83)80022-7.

[139]   Dieter Richter. *Mechanik der Gase.* Berlin, Heidelberg: Springer Berlin
         Heidelberg, 2010. ISBN: 978-3-642-12722-9. DOI: 10.1007/978-3-642-
         12723-6.

[140]   Yi-Chia Tsai, Can Bayram, and Jean-Pierre Leburton. "Effect of Auger
         Electron–Hole Asymmetry on the Efficiency Droop in InGaN Quan-
         tum Well Light-Emitting Diodes". In: *IEEE Journal of Quantum Elec-
         tronics* 58.1 (2022), pp. 1–9. ISSN: 0018-9197. DOI: 10.1109/JQE.2021.
         3137822.

[141]   Olga Fontelles-Carceller, Mario J. Muñoz-Batista, Enrique Rodríguez-
         Castellón, et al. "Measuring and interpreting quantum efficiency for
         hydrogen photo-production using Pt-titania catalysts". In: *Journal
         of Catalysis* 347 (2017), pp. 157–169. ISSN: 00219517. DOI: 10.1016/j.
         jcat.2017.01.012.

[142]   Jean Meeus. *Astronomical algorithms.* 2. engl. ed. Richmond, Va.:
         Willmann-Bell, 1998. ISBN: 978-0-943396-61-3.

[143]   Paul Kant, Michael Rubin, et al. "Kostengünstige und effiziente Fo-
         toreaktoren für Fotosynthesen mit Sonnenlicht". 2022.

List of Figures

List of Tables

List of publications

2023   Low-cost photoreactors for highly photon/energy-efficient solar-driven synthesis, Kant et al, Joule, DOI:10.1016/j.joule.2023.05.006.

2022   Isophotonic photoreactor for the precise determination of quantum yields in gas-, liquid-, and multiphase photoreactions, Kant et al, Chem. Eng. J., DOI:10.1016/j.cej.2022.139204.

2022   phoRex & QY photoreactor - Monte Carlo ray tracing in MATLAB®& quantum yield measurements, Kant et al, KitopenData, DOI:10.5445/IR/1000150817.

2022   Kostengünstige und effiziente Fotoreaktoren für Fotosynthesen mit Sonnenlicht, Kant et al, German patent application, No. 102022123109.

2020   Shining light on CO_2: from materials discovery to photocatalyst, photoreactor and process engineering, Dong et al, Chem. Soc. Rev., DOI:10.1039/D0CS00597E.

2019   Crowd Oil not Crude Oil, Dittmeyer et al, Nat. Commun., DOI:10.1038/s41467-019-09685-x.

2019   Crowd Oil – building-integrated CO_2 capture and conversion, Kant et al, ICCDU, conference contribution.

2018   Recent Developments in Compact Membrane Reactors with Hydrogen Separation, Wunsch et al, Membranes, DOI: 10.3390/membranes8040107.

A. Test environment components

The test environment described in detail in chapter 5 is built from a large set of commercial parts. The core components are listed in tables A.1, A.2, and A.3. The table explicitly does not include the hundreds of tubing pieces, valves and tube fittings and adaptors that together shape the gas phase and liquid phase tubing system of the test environment.

Table A.1.: Component list of the employed test environment comprising the main components.

Component	Manufacturer	Type
Hydrogen back pressure regulator	TESCOM	44-2214-241-010
Carbon dioxide back pressure regulator	TESCOM	44-2214-241-010
Carbon monoxide back pressure regulator	TESCOM	44-2214-241-010
Nitrogen back pressure regulator	TESCOM	44-2214-241-010
Argon back pressure regulator (GC)	BASI	HP302
Hydrogen back pressure regulator (GC)	BASI	HP302
Hydrogen mass flow controller	Brooks Instruments	SLA5850
Carbon dioxide mass flow controller	Brooks Instruments	SLA5850
Carbon monoxide mass flow controller	Brooks Instruments	SLA5850

Table A.2.: Component list of the employed test environment comprising the main components. Continuation of table A.1.

Component	Manufacturer	Type
Nitrogen mass flow controller	Brooks Instruments	SLA5850
Pressure transducers 0-4 MPa	WIKA GmbH	S-20
Pressure transducer 0-0.25 MPa	WIKA GmbH	S-20
Pressure transducer 0-10 kPa	WIKA GmbH	A2G-55
Pressure regulating valve	FLOWSERVE ESSEN GmbH	SamllFlow 0802P1
Thermocouples (tube heating)	CONNATEX GmbH	T029135
Thermocouples (reactor)	CONNATEX GmbH	T029137
Heating tape (tube heating)	HORST GmbH	020103
Gas Chromatograph	Agilent	G2790A
Liquid feed pump	ISMATEC	MCP-Z
Precision liquid feed pump	HITEC ZHANG	SyrDos™
UV Vis flow cell	Ocean Optics	FIA-Z-SMA-ULT
UV Vis spectrometer	Ocean Optics	USB4000
UV Vis spectrometer light source	Mikropak	DT-MINI-2-GS
Solar simulator	Sciencetech	SS1.6KXeFR-B
Irradiance sensor	Thorlabs	S401C
Irradiance sensor USB interface	Thorlabs	PM101R
LED power supply	AIM TTi	TSX1820P
Precision power meter	Keithley	2701
Host computer	TAROX	-
Real time target	National Instruments	cRIO 9056
Current input module	National Instruments	9203

Table A.3.: Component list of the employed test environment comprising the main components. Continuation of table A.2.

Component	Manufacturer	Type
Current output module	National Instruments	9266
Thermovoltage input module	National Instruments	9213
Counter output module	National Instruments	9472
Solid state relais (power electronics)	Crydom	DR24D06
Low voltage supply	Siemens	SITOP PSU100S
FI/LS	Siemens	5SV1316-6KK16
FI/LS	Kopp	741610012
Thermostat	Julabo	ED/F25

B.   Experiment instructions

The experiment environment described in detail in chapter 5 allows auto-mated long-term experiments. This feature entails some challenges in the experiment preparation and evaluation. First of all, the user absence during the experiment demands for a rigorous planning that ensures that during the experiment time no errors occur that either result in a malfunction or a safety shut down of the test environment. Secondly, the large data sets generated by different test rig components – the measurement and control system log, the gas chromatograph's reports, the UV Vis spectra, camera takes, etc. – must be saved in a structured and especially lucid way. In best case, the data structure can be machine-read and pre-evaluated before a manual evaluation of larger data sets is conducted.

The automation checklists in figures B.1 and B.2 have been developed in the present work and were employed in the reaction technological experiments with the developed titania-based photo catalyst system described in chapters 6 and 7. Following the check lists ensures, that the experiment is conducted without interruptions and all experiment data is saved in a structured way accessible by the data scraper briefly described in section 5. The check lists are no scientific or engineering result but are a strong support for future work with the test environment by providing a detailed idea of the sum of steps and prerequisites that are necessary to ensure a safe and successful conduction of automated long term experiments.

Figure B.1.: Automation checklist for experiments in the test environment using the solar simulator. The checklist was developed for the reaction technological experiments in the framework of the titania-based active material development described in chapter 6.

Figure B.2.: Automation checklist for experiments in the test environment using reactor internal light sources. The checklist was developed for the reaction technological experiments in the framework of the quantum yield determination described in chapter 7.